



Comparison of Cardiac Anatomy and Function: Statistics on Fibre Architecture from DT-MRI and Registration of 4D CT Images

Jean-Marc Peyrat

► To cite this version:

Jean-Marc Peyrat. Comparison of Cardiac Anatomy and Function: Statistics on Fibre Architecture from DT-MRI and Registration of 4D CT Images. Computer Science [cs]. Université Nice Sophia Antipolis, 2009. English. NNT: . tel-00633206

HAL Id: tel-00633206

<https://theses.hal.science/tel-00633206>

Submitted on 19 Oct 2011

HAL is a multi-disciplinary open access archive for the deposit and dissemination of scientific research documents, whether they are published or not. The documents may come from teaching and research institutions in France or abroad, or from public or private research centers.

L'archive ouverte pluridisciplinaire **HAL**, est destinée au dépôt et à la diffusion de documents scientifiques de niveau recherche, publiés ou non, émanant des établissements d'enseignement et de recherche français ou étrangers, des laboratoires publics ou privés.

NICE - SOPHIA ANTIPOLIS UNIVERSITY

GRADUATE SCHOOL STIC
INFORMATION AND COMMUNICATION TECHNOLOGIES AND SCIENCES

T H E S I S

to fulfill the requirements for the degree of

Doctor of Philosophy - Ph.D.

from the Nice - Sophia Antipolis University

Specialized in : CONTROL, SIGNAL AND IMAGE PROCESSING

presented and defended by

Jean-Marc PEYRAT

Comparison of Cardiac Anatomy and Function: Statistics on Fibre Architecture from DT-MRI and Registration of 4D CT Images

Thesis supervised by

Nicholas AYACHE and Hervé DELINGETTE,
defended the 27th of November, 2009.

Jury :

<i>Reviewers :</i>	Philip BATCHELOR	King's College London
	Patrick CLARYSSE	CNRS-INSERM - Creatis
	Boudewijn LELIEVELDT	Leiden University Medical Center
<i>Supervisor :</i>	Nicholas AYACHE,	INRIA - Asclepios
<i>Co-Supervisor :</i>	Hervé DELINGETTE,	INRIA - Asclepios
<i>Examiners :</i>	Rachid DERICHE	INRIA - Odyssée
<i>Invited Members:</i>	Maxime SERMESANT	INRIA - Asclepios
	Chenyang XU,	Siemens Corporate Research

UNIVERSITÉ DE NICE - SOPHIA ANTIPOLIS

ÉCOLE DOCTORALE STIC
SCIENCES ET TECHNOLOGIES DE L'INFORMATION ET DE LA
COMMUNICATION

T H È S E

pour obtenir le titre de

Docteur en Sciences

de l'Université Nice - Sophia Antipolis

Mention : AUTOMATIQUE, TRAITEMENT DU SIGNAL ET DES IMAGES

présentée et soutenue par

Jean-Marc PEYRAT

**Comparaison de l'Anatomie et de la Fonction
Cardiaque: Statistiques sur l'Architecture des
Fibres et Recalage d'Images 4D CT**

Thèse dirigée par Nicholas AYACHE et Hervé DELINGETTE,
soutenue le 27 Novembre, 2009.

Jury :

<i>Rapporteurs :</i>	Philip BATCHELOR	King's College London
	Patrick CLARYSSE	CNRS-INSERM - Creatis
	Boudewijn LELIEVELDT	Leiden University Medical Center
<i>Directeur :</i>	Nicholas AYACHE,	INRIA - Asclepios
<i>Co-Directeur :</i>	Hervé DELINGETTE,	INRIA - Asclepios
<i>Examineurs :</i>	Rachid DERICHE	INRIA - Odyssée
<i>Invités:</i>	Maxime SERMESANT	INRIA - Asclepios
	Chenyang XU,	Siemens Corporate Research

ABSTRACT

In this thesis, we addressed the problem of comparing cardiac anatomy and function from medical images. The first part focuses on cardiac anatomy with a statistical study of cardiac fiber architecture from diffusion tensor magnetic resonance imaging (DT-MRI). The second part focuses on a joint comparison of cardiac anatomy and function with the non-linear spatio-temporal registration of two sequences of 4D CT sequences of different patients or of the same patient at different times.

Cardiac muscle fibers are locally bound to form a plane called the laminar sheets. Moreover, the orientation of fibers and laminar sheets is spatially variable in the myocardium. This complex organisation of cardiac muscle fibers has an important influence on the electromechanical behaviour of the heart, and thus on cardiac function. We performed a study of this cardiac fiber architecture from DT-MRI. To achieve it, we proposed novel computational tools for the statistical analysis of a population of diffusion tensors based on the Log-Euclidean metric. The novelty of this approach lies in a statistical analysis performed directly on diffusion tensors (symmetric definite positive matrices) by analyzing their covariance matrix giving the variability of fiber and laminar sheet directions among the population.

We applied this computational framework to a dataset of canine DT-MRI acquired *ex vivo* not only providing an average model (or atlas) of cardiac fiber architecture but also revealing a consistency of fiber orientation and a higher variability of laminar sheet orientations. Then, this atlas of canine hearts is compared to a human heart and a synthetic model currently used for electromechanical simulations or image analysis. The human heart had similarities in fiber orientation whereas discrepancies in laminar sheet orientation. The synthetic model was too simple to describe in details to describe properly the complexity of fiber architecture.

The acquisition of time-series of cardiac images gives the opportunity to observe cardiac motion and thus its function in addition to its anatomy. In order to compare this cardiac function, we proposed a novel non-linear spatio-temporal registration algorithm of sequences of images. The spatio-temporal registration is decoupled into a temporal registration that aims at mapping corresponding physiological events and into a spatial registration that aims at mapping corresponding anatomical points ensuring a consistency with their respective motion. This consistency is ensured by defining *trajectory constraints* linking intra-sequence transformations describing cardiac motion to inter-sequence transformations describing anatomical differences over time. Under these trajectory constraints, the 4D spatial registration problem can be simplified to 3D multichannel registration problem solved using a new version of the *Diffeomorphic Demons* called the *Multichannel Diffeomorphic Demons*.

This new registration method is applied to the inter-subject registration of 4D cardiac CT sequences for evaluation. Its comparison to other possible methods showed that it was the best compromise between accuracy, spatial and temporal regularization, and computation times. A possible clinical application of the spatiotemporal nonlinear registration is proposed by comparing cardiac anatomy and function before and after therapy by studying the *remodeling strains* over a cardiac cycle.

RÉSUMÉ

Ce travail de thèse s'est consacré à la comparaison de l'anatomie et de la fonction cardiaques à partir d'images médicales. Une première partie se concentre sur l'anatomie cardiaque avec une étude statistique de l'architecture des fibres musculaires du cœur à partir d'IRM de tenseur de diffusion. Dans la deuxième partie est proposée une comparaison la fonction cardiaque de différents patients ou du même patient à différents instants par le recalage spatiotemporel de séquences 4D CT.

La complexe organisation des fibres musculaires cardiaques a un rôle très important dans le comportement électrique et mécanique du cœur. Pour étudier cette architecture des fibres, nous avons proposé de nouveaux outils algorithmiques d'analyse statistique d'IRM de tenseurs de diffusion. La nouveauté de cette approche est de réaliser cette analyse statistique directement sur les tenseurs de diffusion l'a où la plupart des études statistiques se font sur des vecteurs ou angles d'orientation décrivant les directions des fibres et des feuillets. La variabilité de l'orientation des fibres et des feuillets est ensuite directement donnée par la matrice de covariance des tenseurs de diffusion de laquelle sont extraites les variabilités des vecteurs propres.

L'application de ces outils à une base de données d'IRM de tenseur de diffusion de cœurs de chiens acquis *ex vivo* a permis d'obtenir un atlas de l'architecture des fibres mais aussi de révéler une cohérence de l'orientation des fibres et une plus grande variabilité de l'orientation des feuillets. Ensuite, nous avons comparé l'atlas de cœurs de chien à un cœur humain et un modèle synthétique couramment utilisé pour des simulations électromécaniques ou l'analyse d'images cardiaques. Le cœur humain s'est révélé plus proche des cœurs de chien au niveau de l'orientation des fibres que de celle des feuillets. Le modèle synthétique quant à lui s'est montré trop simple pour décrire en détails la complexité de l'architecture des fibres.

L'acquisition de séquences d'images cardiaques permet d'observer le mouvement cardiaque et donc sa fonction. Nous avons proposé un nouvel algorithme de recalage non-linéaire spatiotemporel de séquences d'images qui permet de comparer cette fonction cardiaque. Le recalage temporel assure la mise en correspondance d'instantanés physiologiques similaires. Le recalage spatial quant à lui doit assurer une cohérence entre le mouvement des points physiques intra-séquence et leur mise en correspondance inter-séquence. Cette cohérence est assurée par les *contraintes de trajectoires* liant les transformations intra-séquences décrivant le mouvement cardiaque aux transformations inter-séquences décrivant les différences anatomiques au cours du temps. Sous ces contraintes de trajectoires, le recalage spatial 4D est simplifié en un recalage multicanal 3D résolu avec une nouvelle version des *Demons Diffeomorphes Multicanaux*.

Cette méthode de recalage spatiotemporel est appliquée au recalage inter-sujet de séquences 4D CT pour évaluation. Comparée à d'autres techniques existantes, cette technique de recalage s'est révélée le meilleur compromis en terme de précision, de régularité spatiale et temporelle, mais aussi de temps de calcul. Un exemple d'application possible du recalage spatiotemporel est proposé avec la comparaison de l'anatomie et de la fonction cardiaques avant et après thérapie.

“Anyone whose goal is ‘something higher’ must expect someday to suffer vertigo. What is vertigo? Fear of falling? No, vertigo is something other than fear of falling. It is the voice of the emptiness below us which tempts and lures us, it is the desire to fall, against which, terrified, we defend ourselves.” - Milan Kundera

ACKNOWLEDGEMENTS

First of all I would like to thank my advisor, Nicholas Ayache, for supervising my research and for giving me the opportunity to work in his group for the last four years. I am particularly grateful to him for supporting not only my work but also myself when I was overwhelmed by my doubts.

I would like to thank my co-advisor, Hervé Delingette for his great help during my research. He was always here to give wise advices when needed.

I would also like to thank my industrial co-advisor, Chenyang Xu, for giving me the opportunity to collaborate with Siemens Corporate Research in a fruitful environment, for transmitting his energy to his co-workers, and for sharing his hindsight on research and life.

I should not forget to thank Maxime Sermesant and Xavier Pennec for their precious help in my research work.

I express my gratitude to the jury members, Philip Batchelor, Patrick Clarysse, Rachid Deriche, and Boudewijn Lelieveldt, for accepting their duty by giving time and attention to my work and also for their relevant comments and encouraging compliments.

A special thank to people without whom this PhD period would not have been the same and without whom I would be a different person. First of all, I would like to thank Ender Konukoglu for being more than an officemate, for being the closest friend during this period of doubts, for showing me the “burning light in the dark”. I would like to thank Heike Hufnagel for her kindness and sense of humour, for the thoughts we shared. I would like to thank Olivier Clatz for his straightforwardness, for his ability to push up people when needed, for his positive state of mind, and for opening me up to new experiences. I would like to thank Tommaso Mansi for always being available when I needed some help, for all the “Demoniac” discussions in front of the white board that gave me the opportunity to escape from my thesis writing from time to time. Thank you for your support and friendship that turned this difficult period into a positive one.

I take this opportunity to thank all my family for their influence and support in my life that made the man I am today.

And last but not the least, I thank my friends and colleagues from INRIA and SCR that made easier this journey in daily life: Isabelle Strobant, Barbara André, Florence Billet, Aurélie Canale, Florence Dru, Stéphanie Marchesseau, Sapna Nundloll, Liliane Ramus, Antoine Azar, Daniel Barbeau, François Chung, Olivier Commowick, Stanley Durrleman, Romain Fernandez, Pierre Fillard, Ezequiel Geremia, François Hébert (*“comment on fait?”*), Tobias Heimann, Hans Lamecker, Grégoire Malandain, Bjoern Menze, Sébastien Novellas, Erik Pernod (*“un petit plongeon?”*), Alexander Schmidt-Richberg, Jean-Christophe Souplet, Nicolas Toussaint, Tom Vercauteren, Thomas Yeo, Marie-Pierre Jolly, Kinda Saddi, Fred Azar, Michaël Caylus, Christoph Guetter, David Lesage, Hervé Lombaert, Julien Abi-Nahed, Jérôme Piovano, Mikaël Rousson, Guillaume Stordeur, Maxime Taron. I apologize to everyone whose names I forgot to mention.

Thank you everyone, my PhD is also yours!

CONTENTS

PART I - INTRODUCTION	1
1 INTRODUCTION	3
1.1 Importance of Cardiovascular Diseases	3
1.2 Towards a Better Understanding of the Heart	5
1.3 Overview and Contributions	5
2 FROM MICROSTRUCTURE TO FUNCTION OF THE HEART	9
2.1 At the Heart of the Cardiovascular System	9
2.1.1 Cardiac Anatomy	11
2.1.2 Cardiac Myofibres	14
2.1.3 Cardiac Fibre Architecture	15
2.1.4 Cardiac Function	17
2.2 Cardiac Imaging	20
2.2.1 4D Computed Tomography (CT)	22
2.2.2 Diffusion Tensor Magnetic Resonance Imaging (DT-MRI) . .	25
PART II - COMPARISON OF CARDIAC FIBRE ARCHITECTURE FROM DT-MRI	31
3 STATISTICAL ANALYSIS OF CARDIAC DT-MRI	33
3.1 Introduction	33
3.2 Atlas Building	38
3.2.1 Introduction to Atlas Building	38
3.2.2 Pairwise Registration	41
3.2.3 Groupwise Registration	44
3.3 Transformation of Cardiac Diffusion Tensors	45
3.3.1 Finite Strain (FS)	47
3.3.2 Preservation of the Principal Direction (PPD)	49
3.3.3 Comparison of the Reorientation Strategies	51
3.4 Statistical Analysis of Cardiac Diffusion Tensors	55
3.4.1 Introduction to DT-MRI Processing	55
3.4.2 Log-Euclidean Mean and Covariance	60
3.4.3 A New Analysis of the Diffusion Tensor Covariance Matrix .	60
3.5 Conclusion	63
4 A CANINE CARDIAC DT-MRI ATLAS	65
4.1 Introduction	65
4.2 Canine DT-MRI Atlas and Intra-Species Variability	67
4.2.1 Data Acquisition	67

4.2.2	Pre-Processing Data	67
4.2.3	Statistical Analysis	68
4.2.4	Reorientation Strategies and Inter-Subject Variability	75
4.3	Atlas Comparison with Other Models	76
4.3.1	Inter-Species Comparison with Human Data	76
4.3.2	Comparison with Synthetic Models	80
4.4	Conclusion	84
 PART III - COMPARISON OF CARDIAC FUNCTION AND ANATOMY FROM 4D CT		87
5	SPATIO-TEMPORAL REGISTRATION OF TIME-SERIES OF IMAGES	89
5.1	Introduction	89
5.2	General Setting	91
5.2.1	Temporal Transformation as Physiological States Mapping	92
5.2.2	Spatial Transformation as Trajectory Mapping	94
5.3	From 4D Registration to Multichannel 3D Registration	96
5.4	Spatial 4D Registration with Diffeomorphic Demons	98
5.4.1	Standard 3D Diffeomorphic Demons	99
5.4.2	Multichannel 3D Diffeomorphic Demons	100
5.5	Conclusion	101
6	REGISTRATION OF 4D CARDIAC CT SEQUENCES: EVALUATION AND APPLICATION	103
6.1	Introduction	103
6.2	An Evaluation Study on Intersubject Registration	104
6.2.1	A General Computation Time Study	106
6.2.2	Registration of Electromechanically Simulated Sequences	107
6.2.3	Intersubject Registration of Real Sequences	114
6.3	Application to the Analysis of Ventricular Remodeling after Therapy	120
6.3.1	Data	122
6.3.2	Strain Analysis from Motion Tracking	122
6.3.3	<i>Remodeling Strain</i> Analysis from 4D Registration	129
6.4	Conclusion	131
 PART IV - CONCLUSION		133
7	CONCLUSION AND PERSPECTIVES	135
7.1	Synthesis of Contributions	136
7.1.1	A Statistical Atlas of Cardiac Fibre Architecture	136
7.1.2	Registration of 4D Time-Series of Images	137
7.2	Discussion and Perspectives	138
7.2.1	Improvement of the Atlas of Cardiac Fibre Architecture	138

7.2.2	Towards <i>in vivo</i> Imaging of Cardiac Fibre architecture	139
7.2.3	Improvement of 4D Registration Framework	140
7.2.4	Towards a Statistical Atlas of Cardiac Anatomy and Function	141
7.3	Publications	141
A	Affine Transformation of a Plane	145
B	Covariance Matrix Projections	147
C	Atlas and Synthetic Models in AHA Zones	149
D	Maximum Step Length	165
	BIBLIOGRAPHY	167

PART I

INTRODUCTION

CHAPTER 1

INTRODUCTION

Contents

1.1 Importance of Cardiovascular Diseases	3
1.2 Towards a Better Understanding of the Heart	5
1.3 Overview and Contributions	5

The research work presented in this thesis was done in the Asclepios Team at INRIA and in collaboration with Siemens that funded this PhD. This close collaboration was realized by sharing knowledge, computational tools, and data through a couple of stays (for a total of about 9 months) in the Interventional Imaging Group of the Imaging and Visualization Department at Siemens Corporate Research (Princeton, NJ, USA). This research work was also done in the context of CardioSense3D ¹, a 4-year Large Initiative Action launched in 2005 and funded by the French national research center INRIA which focused on the electromechanical modeling of the heart.

The main purpose of this thesis was to compare cardiac anatomy and function with the computational analysis of medical images. The first research project focused on a specific aspect of cardiac anatomy, the cardiac fibre architecture, that has an important role in the electrical and mechanical function of the heart. This project lead to a collaboration with the National Institute of Health (NIH) and Johns Hopkins University (JHU) through the person of Professor Elliot McVeigh for provision of *ex vivo* DT-MRI data of canine and human hearts. The second research project focused on the joint comparison of cardiac anatomy and function with the analysis of 4D cardiac CT sequences provided by Dr Harold Litt, a clinical research collaborator of Siemens Corporate Research from the Hospital of University of Pennsylvania.

1.1 Importance of Cardiovascular Diseases

Cardiovascular diseases are a large group of pathologies of the heart and blood vessels including hypertension, coronary heart disease, cerebrovascular disease, peripheral vascular disease, rheumatic heart disease, congenital heart disease, heart failure,

¹more details at <http://www-sop.inria.fr/CardioSense3D>

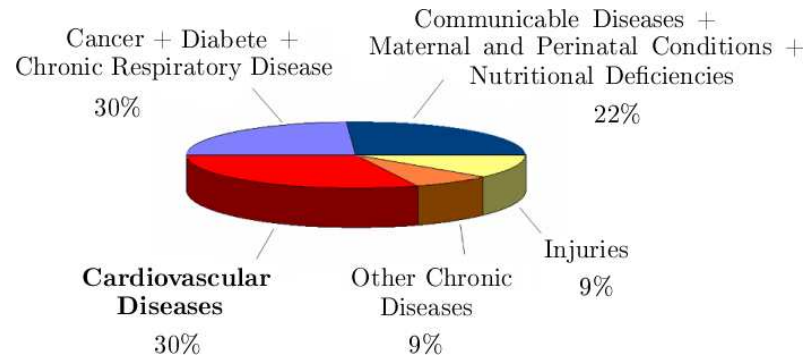


Figure 1.1: Cardiovascular diseases are the largest cause of death over the world in 2002 (from “The world health report 2004 - changing history” of World Health Organization).

and cardiomyopathies. The most frequent cardiovascular causes of death are heart attacks due to coronary heart diseases and strokes due to cerebrovascular diseases.

Cardiovascular diseases are the largest cause of death over the world and are projected to remain so. Nearly 17 million people died from cardiovascular disease in 2002, representing 30% of all deaths (see Figure 1.1). If current trends continue, World Health Organization estimates that more than 20 million people will die from cardiovascular diseases by 2020, representing 31.5% of all deaths. In developed countries such as Europe, mortality due to cardiovascular diseases is even higher representing nearly 48% of all deaths with over 4.3 million deaths per year. Cardiovascular diseases are not only a cause of mortality, but also a cause of morbidity (diseased state, disability, or poor health) that is more difficult to measure. The main measure of the burden of diseases is the Disability Adjusted Life Year (DALY) combining years of life lost due to premature death and years of healthy life lost due to disability. In Europe, 23% of all DALYs are due to cardiovascular diseases and only 10% over the world. For example, the American Heart Association (AHA) estimated in 2004 that about 60 million people in the United States (nearly 23% of the population) have a form of cardiovascular disease.

The high incidence of cardiovascular diseases is a major financial burden. For instance, in European Union (EU), the cost of cardiovascular diseases for the health-care system was just under 110 billion euros in 2006. This accounts for 10% of the total health expenditure in the EU. And the overall cost for the EU economy is estimated to 192 billion euros a year.

Due to the social and economical impacts of cardiovascular diseases, their prevention (prophylaxis), detection and identification (diagnosis), prediction of evolution, and therapy are important issues in developed countries.

1.2 Towards a Better Understanding of the Heart

Not only at macroscopic level with shape but also at microscopic level with fibre structure, the cardiac anatomy has an important role in the electromechanical behavior of the heart, and thus in cardiac function. For instance, an alteration of cardiac anatomy due to pathologies or therapy, called remodeling, affects cardiac function. Conversely, an alteration of cardiac function can initiate a remodeling process to restore it. Studying both cardiac anatomy and function is essential for a better understanding of cardiovascular system and diseases.

Including a wide range of different modalities, cardiovascular imaging non-invasively provides information about cardiac anatomy and function whose analysis relies on more and more elaborated image processing tools. This analysis is not only useful for a better general understanding of the heart, from which can be built physiological [Hunter 2003, Ayache 2004, Sachse 2004, Smith 2004] and pathophysiological models [Sermesant 2005, Reumann 2009], but also for clinical applications, such as diagnosis or guidance of therapies when planning (use of pre-operative data), monitoring (fusion of pre- and per-operative data) and assessing (comparison of pre- and post-operative data) interventions.

Moreover, the fusion of comprehensive generic models and patient-specific cardiac imaging can provide powerful quantitative predictive tools for clinicians to improve diagnosis, prediction, and therapy of cardiovascular diseases, such as in radiofrequency ablation (RFA) and cardiac resynchronization therapy (CRT). In RFA, cardiac tissue is burnt to correct pathological electrical pathways in the heart. An electrophysiology (EP) study measures the cardiac electrical potentials interpreted by the cardiologist to locate the ablation zones. This interpretation requiring significant training depends on the cardiologist experience. In CRT, a pacemaker is implanted to the heart to correct the asynchronous ventricular contraction. The choice of the number, positions and delays between electrodes makes this intervention so difficult that shows no improvement in 30% of them. A personalized electromechanical model of the heart can help to predict results of both therapies and thus to customize and optimize them [Sermesant 2005, Sermesant 2008, Reumann 2007, Plank 2008, Romero 2008, Reumann 2008].

1.3 Overview and Contributions

The research work presented in this thesis deals with the comparison of cardiac anatomy and function by proposing novel medical image analysis tools. An overview of the thesis follows with the main contributions highlighted in bold characters.

Chapter 2 “*From Microstructure to Function of the Heart*” describes the cardiovascular system and cardiac imaging techniques that give access to information about the heart at the different scales of microstructure, anatomy and function.

An analysis of the cardiac anatomy, more specifically the cardiac fibre architecture, is presented in the next two chapters composing the part II of the thesis, called “COMPARISON OF CARDIAC FIBRE ARCHITECTURE FROM DT-MRI”.

Chapter 3 “*Statistical Analysis of Cardiac DT-MRI*” describes a **computational framework to build a statistical atlas of cardiac fibre architecture from diffusion tensor MRI**. This framework is based on a groupwise registration of cardiac DT-MRIs whose reorientation is necessary when warping the space to a reference geometry. **Insights on differences between the most common reorientation strategies of cardiac diffusion tensors** are detailed. A complete analysis of the statistical atlas of DT-MRI as cardiac fibre architecture variability is proposed with a **novel analysis of the covariance matrix of diffusion tensors decomposed into eigenvalues and eigenvectors variabilities**.

Chapter 4 “*A Canine Cardiac DT-MRI Atlas*” presents the results of the construction of a statistical atlas of cardiac fibre architecture from nine canine *ex vivo* cardiac DT-MRIs. This atlas is the first **average description of the full cardiac fibre architecture built from a population of hearts and associated to its intra-species variability**. Thanks to the rare access to a single human heart acquisition of DT-MRI, we performed a first **quantitative inter-species comparison between the canine atlas and a human heart** confirming inter-species consistency of fibre orientations and discrepancies of laminar sheet orientations. We also **compared the atlas to synthetic models of cardiac fibre architecture** showing locally oversimplified descriptions of cardiac fibre orientations.

An analysis of cardiac anatomy and function with 4D time-series of images is presented in the next two chapters composing part III of the thesis, called “COMPARISON OF CARDIAC FUNCTION AND ANATOMY FROM 4D CT”.

Chapter 5 “*Spatio-Temporal Registration of Time-Series of Images*” presents a **general setting for the spatio-temporal registration of 4D time-series of images** decoupled into temporal and spatial registration. The temporal registration aims at mapping corresponding physiological events. The spatial registration aims at mapping trajectories of homologous physical points. This trajectory mapping yields **the definition of specific constraints, called the trajectory constraints (TC)**, that simplify the 4D spatial registration problem into a multichannel 3D registration problem. To solve the multichannel 3D registration problem, we propose a **new extended version of 3D Diffeomorphic Demons (DD) to vector-valued images, called Multichannel Diffeomorphic Demons (MDD)**.

Chapter 6 “*Registration of 4D Cardiac CT Sequences: Evaluation and Application*” presents **an evaluation of the proposed 4D registration method under trajectory constraints (TC) with Multichannel Diffeomorphic Demons (MDD)**. This evaluation is performed by comparing the proposed method to other standard methods in the context of inter-subject non-linear registration of 4D cardiac CT sequences with real patient data and **synthetic data simulated from a physiologically realistic electromechanical model**. Results show that the trajectory constraints act as a temporal regularization consistent with motion whereas the multichannel registration acts as a spatial regularization. **As an example of new possible clinical application of 4D spatio-temporal registration, we measure the effects of remodeling after radiofrequency ablation (RFA) in atrial fibrillation (AF) by comparing cardiac anatomy and function with the analysis of inter-sequence spatial transformations over time between pre- and post-operative 4D CT sequences.**

Chapter 7 “*Conclusion and Perspectives*” summarizes the contributions and results followed by the perspectives of the research work presented in this thesis.

FROM MICROSTRUCTURE TO FUNCTION OF THE HEART

Contents

2.1 At the Heart of the Cardiovascular System	9
2.1.1 Cardiac Anatomy	11
2.1.2 Cardiac Myofibres	14
2.1.3 Cardiac Fibre Architecture	15
2.1.4 Cardiac Function	17
2.2 Cardiac Imaging	20
2.2.1 4D Computed Tomography (CT)	22
2.2.2 Diffusion Tensor Magnetic Resonance Imaging (DT-MRI) . .	25

2.1 At the Heart of the Cardiovascular System

The cardiovascular system is composed of the heart, blood, and the blood vessels (divided into veins that carry blood to the heart at low pressure and arteries that carry away blood from the heart at high pressure). The cardiovascular system ensures the circulation of blood throughout the body to maintain homeostasis delivering oxygen and nutrients to the cells and removing wastes. The circulation of blood in the cardiovascular system can be divided into several steps as follows (see Figure 2.1):

1. deoxygenated blood is pumped from the heart into the lungs through pulmonary arteries;
2. in the lungs, the blood is reoxygenated;
3. oxygenated blood is carried back to the heart through the pulmonary veins;
4. oxygenated blood is then pumped from the heart to the many organs and tissues of the body through aorta and arteries;
5. in the tissues, the arteries narrow to capillaries where blood is deoxygenated;
6. the capillaries widen into the veins, which carry the deoxygenated blood back to the heart.

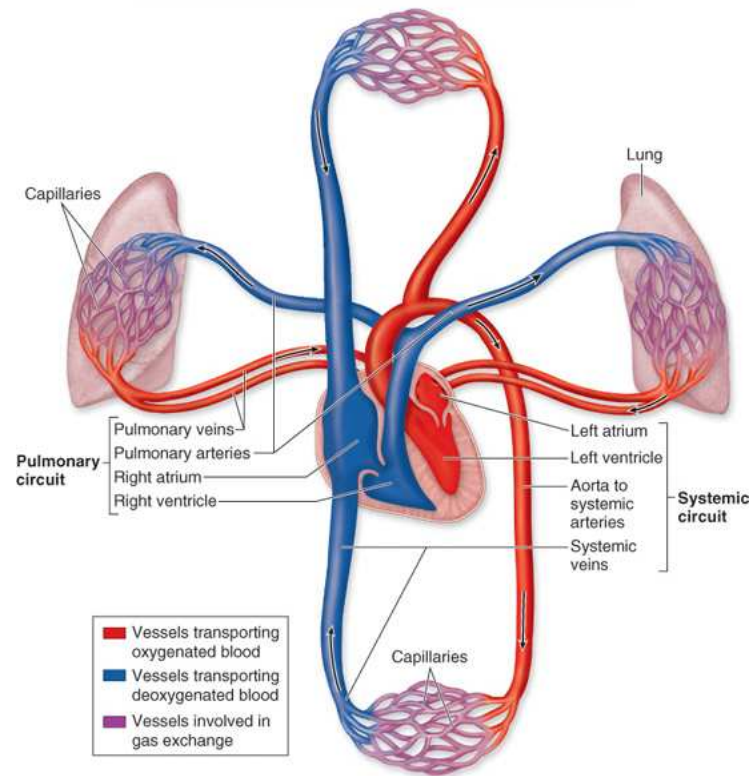


Figure 2.1: Schematic diagram of the blood flow throughout the cardiovascular system. The blood flow can be followed by the arrows on the diagram. Oxygenated blood is in red, while deoxygenated is in blue (from <http://academic.kellogg.edu/>).

The heart has the key active role of pumping the blood to make it flow in the cardiovascular system. In this chapter, we describe how the cardiac function is achieved at different levels of observation with different phenomenologies (mechanical, electrical, chemical). At the anatomical level (see Section 2.1.1), the heart is a muscular organ acting as a mechanical pump that distributes the blood in the body through the vascular network. Cardiac mechanics is achieved by the contraction of cardiac muscle fibres. This contraction is involuntary activated by an electrical impulse triggered by cells of the cardiac conduction system. The rate of triggering is regulated by the autonomic nervous system. This electrical impulse propagates in the heart first through the conduction system and then through the rest of the cardiac muscles. The propagation of the electrical impulse and the mechanical contraction are mainly along cardiac muscle fibres. Thus their spatial organization and orientation have an impact on the cardiac function (see Section 2.1.3). At the cellular level (see Section 2.1.2), cardiac muscle fibres consist of highly aligned cardiomyocytes containing myofibrils oriented parallel to the fibre axis. When the membrane potential of cardiomyocytes is modified, an ionic exchange occurs to command the contraction of the cells.

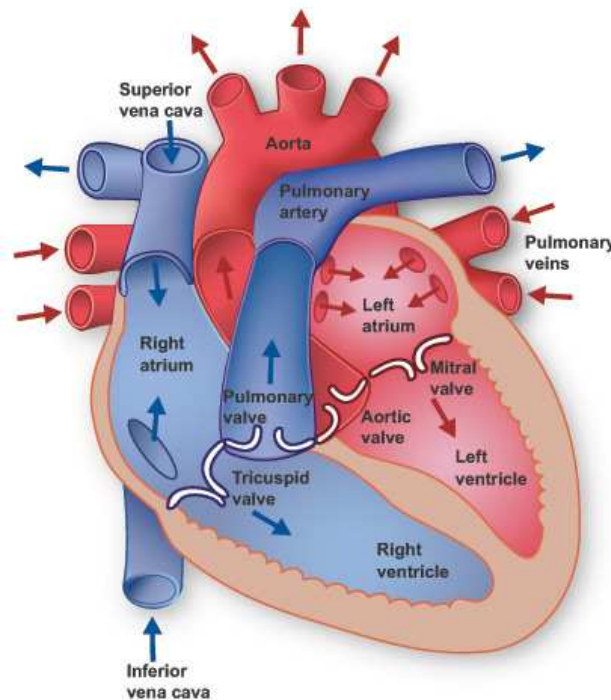


Figure 2.2: Anatomy of the heart and blood flow that can be followed by the arrows on the diagram, oxygenated blood in red and deoxygenated in blue (from <http://www.texasheart.org/>).

2.1.1 Cardiac Anatomy

The heart is a muscular cone-shaped organ about the size of a clenched fist of the same person. It is located in the upper body (chest area) between the lungs. The basic anatomy of the heart (illustrated in Figure 2.2) may be described as follows:

The Cardiac Chambers The heart is divided into right and left sections separated by the interventricular septum. The right section pumps the deoxygenated blood and the left section pumps the oxygenated blood. Each of these right and left sections is also divided into upper and lower chambers known as atria (one is called an atrium) and ventricles, respectively. The four main chambers of the heart are therefore:

- the *right atrium* (RA), pumps blood into the right ventricle;
- the *right ventricle* (RV), pumps blood into the pulmonary artery;
- the *left atrium* (LA), pumps blood into the left ventricle;
- the *left ventricle* (LV), pumps blood into the aorta.

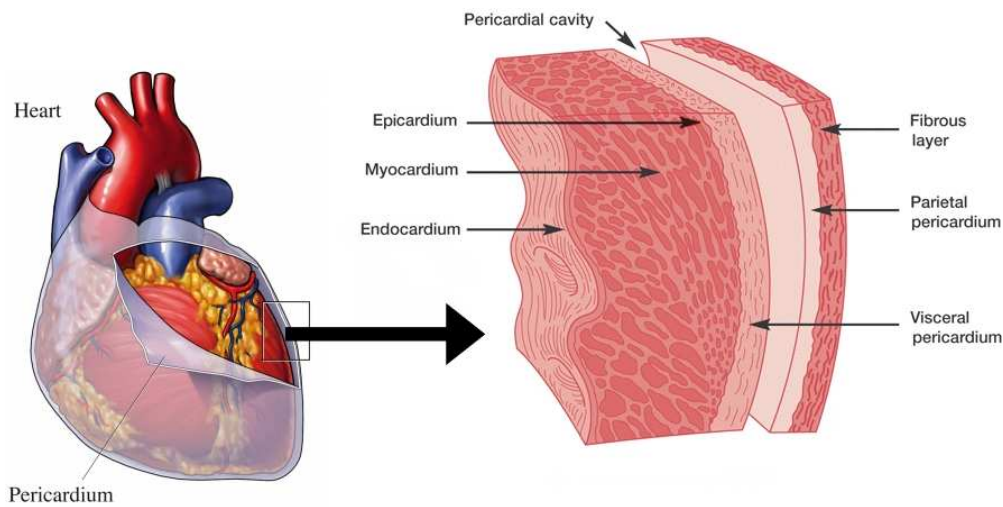


Figure 2.3: Layers of the myocardium (adapted from <http://catalog.nucleusinc.com> and <http://www.ncbi.nlm.nih.gov/>).

The Cardiac Valves To ensure the blood to circulate always in the same direction, the heart includes a series of valves (see Figure 2.2):

- the *tricuspid valve* separates the right atrium from the right ventricle;
- the *pulmonary valve* separates the right ventricle from the pulmonary artery;
- the *mitral valve* (also known as the bicuspid valve) separates the left atrium from the left ventricle;
- the *aortic valve* separates the right ventricle from the aorta.

The pulmonary and aortic valves passively open and close with pressure difference between the ventricles and the arteries. The tricuspid and mitral valves are actively controlled by papillary muscles to avoid backflow of blood in atria when blood pressure increases in the contracting ventricles.

The Cardiac Layers The heart has three layers of tissue (see Figure 2.3):

- the *endocardium*, the inner layer of the heart wall tissue that make a barrier between blood and cardiac muscle, and whose cells are similar to the endothelial cells in blood vessels;
- the *myocardium*, the middle layer of the heart wall composed of cardiac muscle;
- the *epicardium*, the outer layer of the heart wall composed of connective tissues.

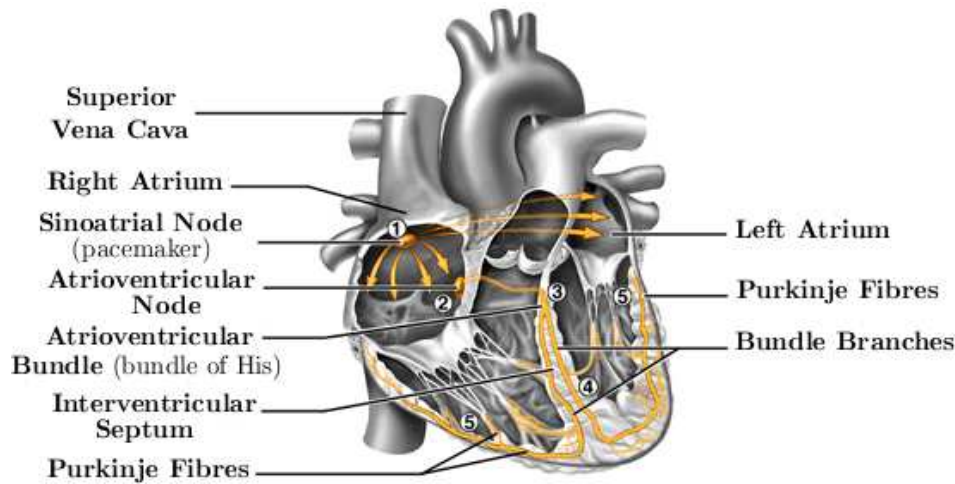


Figure 2.4: Heart cut away showing the cardiac conduction system.

Moreover, the heart is surrounded by a double-walled sac known as the *pericardium* (see Figure 2.3). The pericardium consists of two parts: a strong external layer composed of tough fibrous tissue, called the *fibrous pericardium*, and an internal double-layered sac, called the *serous pericardium*. Protecting the heart against sudden overfilling, the fibrous pericardium surrounds the roots of the great vessels and is attached by ligaments to the spinal column, the diaphragm, and other parts of the body. The two layers of serous pericardium are the *parietal pericardium* and the *visceral pericardium*. The parietal pericardium is fused to the internal surface of the fibrous pericardium. The visceral pericardium is reflected onto the heart where it forms the epicardium. The potential space between the parietal and visceral layers of the serous pericardium is called the pericardial cavity. This cavity contains a thin film of lubricant fluid, called the *pericardial fluid*, that enables the heart to move and beat in a frictionless environment.

The Cardiac Conduction System Electrical impulses in the heart originate in specialized cardiac muscle cells, known as autorhythmic cells. These self-excitable cells are able to generate an action potential without external stimulation by nerve cells. Solely the rate of self-excitability is regulated by the autonomous nervous system depending on needs of the body. The autorhythmic cells serve as a pacemaker to initiate the cardiac cycle and provide a conduction system to coordinate the contraction of muscle cells throughout the heart. The cardiac conduction system can be divided into five parts enumerated in the direction of propagation of the electrical impulse (see Figure 2.4):

1. the *sino-atrial node* (SA), located in the upper wall of the right atrium, initiates the cardiac cycle by generating an electrical impulse that spreads through both atria;

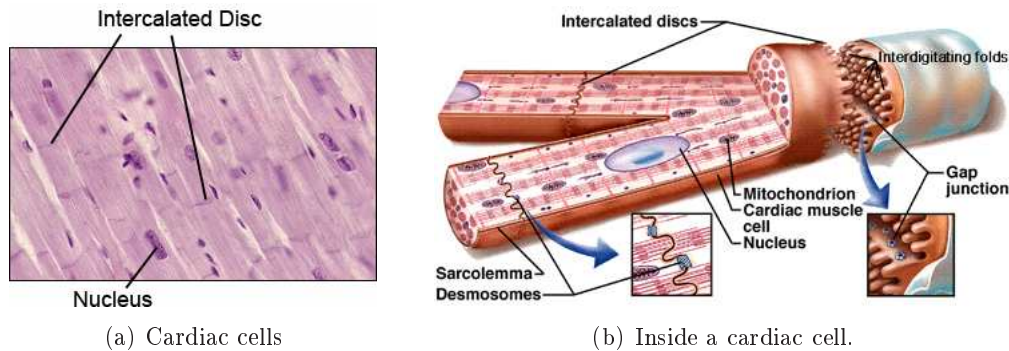


Figure 2.5: Cardiac cells.

2. the *atrio-ventricular node* (AV), located near the lower region of the interatrial septum, receives the electrical impulse generated by the SA node. A slight delay of the electrical transmission occurs here, allowing the atria to fully contract before the electrical impulse propagates into the ventricles;
3. the *bundle of His*, receives the action potential from the AV node and transmits the electrical impulse to the ventricles by way of the right and left bundle branches;
4. the *left* and *right bundle branches*, propagates the electrical impulse in two different parts of the heart, the left and right ventricles;
5. the *Purkinje fibres*, conduct the action potential from the interventricular septum, down to the apex, and then upward through the ventricles.

The electrical function of the heart can be observed with the electrocardiogram (ECG), which gives a global electrical state of the heart (see Figure 2.8). The three main features of the ECG are the following:

1. *P wave*, indicating that the atria are electrically stimulated to pump blood into the ventricles.
2. *QRS complex*, indicating that the ventricles are electrically stimulated to pump blood out.
3. *T wave*, indicating the recovery period of the ventricles.

2.1.2 Cardiac Myofibres

Cardiomyocytes (or cardiac myocytes) are the major component of cardiac muscle representing about 70% of its volume. Cardiomyocytes are faintly striated, branching, mononucleated cells about 10-20 μm wide and 80-100 μm long (see Figure 2.5). Adjacent cardiomyocytes are connected at their ends through the intercalated disks.

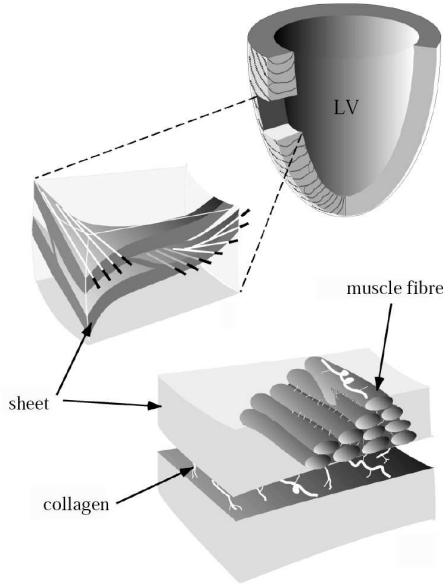
These intercalated disks connect adjacent cells structurally with desmosomes and electrically with gap junctions (see Figure 2.5). This connectivity of cardiomyocytes helps to coordinate the muscle contraction and create the cardiac function. The rest of cardiac muscle is composed of a dense vascular network and connective tissues. Microcirculation in cardiac muscle is carried out by capillaries following the long axis of the cardiomyocytes and by other blood vessels lying between myofibres. The connective tissue, mainly collagen, binds the cardiomyocytes and the vascular network with the interconnection between cardiomyocytes, the connection between cardiomyocytes and capillaries, and the connection between bundles of cardiomyocytes, called myofibres.

Cardiomyocyte contraction can be triggered either chemically or electrically. Chemically, the release of activating neurotransmitters from the sympathetic nervous system regulates the entry of extra-cellular calcium into the cell. Since the ionic channels are also voltage sensitive, they open and close in response to a change in the voltage difference across the membrane. Thus, contraction is also triggered electrically by cellular transmembrane potential.

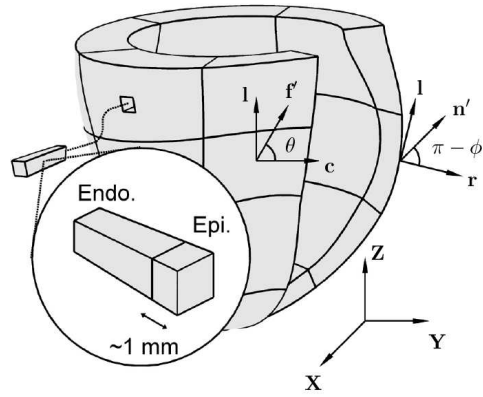
2.1.3 Cardiac Fibre Architecture

As mentioned previously, by propagating the electrical stimulus and contracting, the cardiomyocytes create the cardiac function. At a larger scale, this function is also realized by the spatial arrangement of cardiomyocytes. First, they are arranged into distinct layers, known as laminar sheets [LeGrice 1995a], of about four cells thick separated by extracellular collagen network (see Figure 2.6). The cardiomyocytes are tightly coupled within the same laminar sheet, but sparsely coupled between adjacent laminar sheets. This structure makes the cardiac muscle an orthotropic tissue. The electrical propagation and mechanical contraction are mainly along the fibre axis, whereas they are constrained in the normal direction of the laminar sheets. Second, due to this anisotropy, the spatial variation of the fibre and laminar sheet orientations in the myocardium has also an important role in the realization of the cardiac function [Rijcken 1999, Costa 1999, Costa 2001, Arts 2001, Hooks 2007]. Fibre orientation has been shown to be designed for maximum homogeneity of strain along fibres during ejection [Rijcken 1999]. And laminar sheets have been shown to explain systolic wall thickening with relative sliding of laminar sheets [LeGrice 1995b] and to coincide with planes of maximum systolic shear [Arts 2001]. The electrical properties have also been shown to be influenced by laminar sheets [Hooks 2002, Hooks 2007] but also by the presence of collagen in the cleavage planes between laminar sheets [Pope 2008].

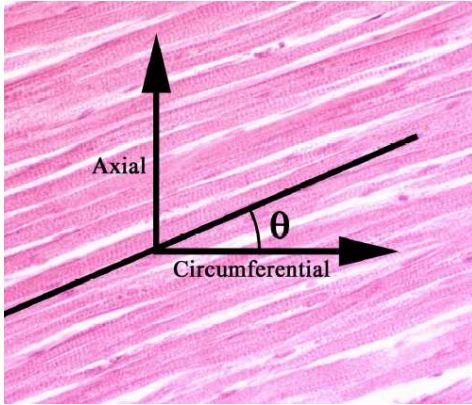
The cardiac fibre architecture, determined by the fibre and laminar sheet orientations, can be measured by several methods: studies of histological slices [Streeter 1979, LeGrice 1995a], optical mapping studies using the diffraction of polarized light [Jouk 1995], or diffusion tensor magnetic resonance imaging (DT-MRI) [McCulloch 1998, Hsu 2001], that have been shown to be related to fibre [Scollan 1998, Hsu 1998, Holmes 2000] and laminar sheet [Tseng 2003,



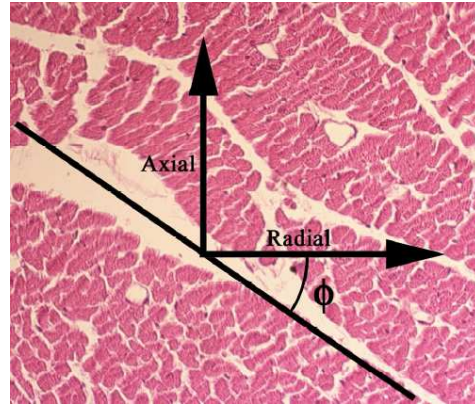
(a) Schematic view of cardiac fibre architecture (from [LeGrice 2001]).



(b) Prolate coordinate system to describe fibre and laminar sheet orientations (adapted from [Helm 2005a]).



(c) Histological section showing fibre orientation described with helix angle θ (from [Helm 2005a]).



(d) Histological section showing laminar sheet orientation described with intersection angle ϕ (from [Helm 2005a]).

Figure 2.6: Cardiac Fibre Architecture

[Helm 2005c] orientations. Histological studies are laborious methods that are by definition limited to a 2D projection of the fibre architecture that requires a reconstruction in 3D prone to errors. Optical mapping only measures the out-of-plane component of orientations also requiring a reconstruction in 3D. On the contrary to other methods, DT-MRI is a non-destructive way to observe the cardiac fibre architecture and moreover provides the orientations directly in 3D. Recent work [Dierckx 2009] also proposed to image the cardiac fibre architecture with Q-ball imaging that could help to study the intravoxel presence of several structures of fibres and laminar sheets in the myocardium.

The first quantitative studies of cardiac fibre architecture reconstructed in 3D were performed with histological slices. The 2D nature of histological slice constrained to measure projection of fibre directions describing the cardiac fibre architecture with angles in the prolate coordinate system [Nielsen 1991]. Due to the circular symmetry of cardiac fibre architecture, mainly two angles were necessary to describe the most relevant spatial variation of fibre and laminar sheet orientations: the helix (or elevation or inclination) angle θ for fibre orientation and the intersection angle ϕ for laminar sheet orientation. These angles are defined in the prolate coordinate system $(\mathbf{r}, \mathbf{c}, \mathbf{l})$ where \mathbf{r} is the radial direction normal to the surface of the heart, \mathbf{c} is the circumferential direction tangential to the surface of the heart, and \mathbf{l} is the longitudinal or axial direction tangential to the surface of the heart (see Figure 2.6). The fibre direction \mathbf{f} is described with the helix (or elevation or inclination) angle θ between the projection \mathbf{f}' of \mathbf{f} in the tangent plane (defined by \mathbf{l} and \mathbf{c}) and \mathbf{c} . And the direction normal to the laminar sheet \mathbf{n} is described with the intersection angle ϕ between the projection \mathbf{n}' of \mathbf{n} in the radial plane (defined by \mathbf{l} and \mathbf{r}) and \mathbf{r} .

All studies confirmed a gradual transmural variation of the helix angle from epicardium to endocardium with opposite extremal values and a full circumferential fibre orientation at the mid wall. The transmural variation of intersection angle has been shown to be more complex with the presence of two different populations of laminar sheets [Helm 2005c] that both coincide with planes of maximum systolic shear [Arts 2001].

At a macroscopic scale, a new concept of cardiac anatomy and function was proposed by Torrent-Guasp in 1972 and firstly published in 1980 [Torrent-Guasp 1980, Torrent-Guasp 2005, Kocica 2006]. He observed that the ventricular myocardium could be seen as a continuous muscular band that folds to form the ventricular cavities (see Figure 2.7). But this theory of a helical ventricular myocardial band is still controversial [von Segesser 2005].

2.1.4 Cardiac Function

Since the heart has a periodic motion, the description of the cardiac function can be limited to one cardiac cycle. The cardiac cycle is divided into two general categories: *systole* and *diastole*. The systole includes events associated with ventricular contraction and ejection, and the diastole includes the rest of the cardiac cycle,

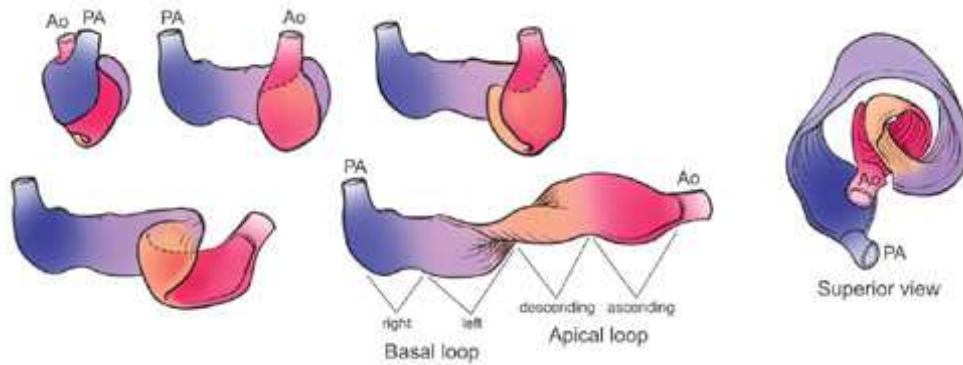


Figure 2.7: Torrent-Guasp Band [Torrent-Guasp 1980] (figure from The Cardiothoracic Surgery Network - <http://www.ctsnet.org/>).

ventricular relaxation and filling. Usually, the cardiac cycle is described from end of diastole (ED) of the previous cycle to the end of diastole of the current cycle. The cardiac cycle is further divided into seven phases:

1. the *atrial systole*: It refers to the contraction of the atrial muscle. As the atria contract, the pressures within the atrial chambers increase, this drives blood from the atria, across the open atrio-ventricular valves, and into the ventricles. This phase starts when the P wave occurs on the ECG.
2. the *isovolumetric contraction*: This phase includes the contraction of the ventricle with all valves closed. The pressure in the ventricle increases. It is during this phase that the first heart sound is heard when the atrio-ventricular valves close. This phase starts when the R wave occurs in the ECG.
3. the *rapid ejection*: When the intraventricular pressures exceed the pressures within the aorta and pulmonary artery, the aortic and pulmonary valves open and blood is ejected out of the ventricles. While blood is ejected and ventricular volumes decrease, the atria continue to fill with blood from their respective venous inflow tracts. The opening of healthy valves is silent.
4. the *reduced ejection*: During this phase ventricular pressure falls slightly below outflow tract pressure; however, outward flow still occurs owing to kinetic energy of the blood that helps to propel the blood into the aorta and pulmonary artery. Atrial pressures gradually rise during this phase owing to continued venous return into the atrial chamber. This phase is characterized by the end of the T wave on the ECG.
5. the *isovolumetric relaxation*: In this phase the ventricles relax, the intraventricular pressure decreases. When this occurs, a pressure gradient reversal causes the aortic and pulmonary valves to abruptly close, causing the second heart sound.

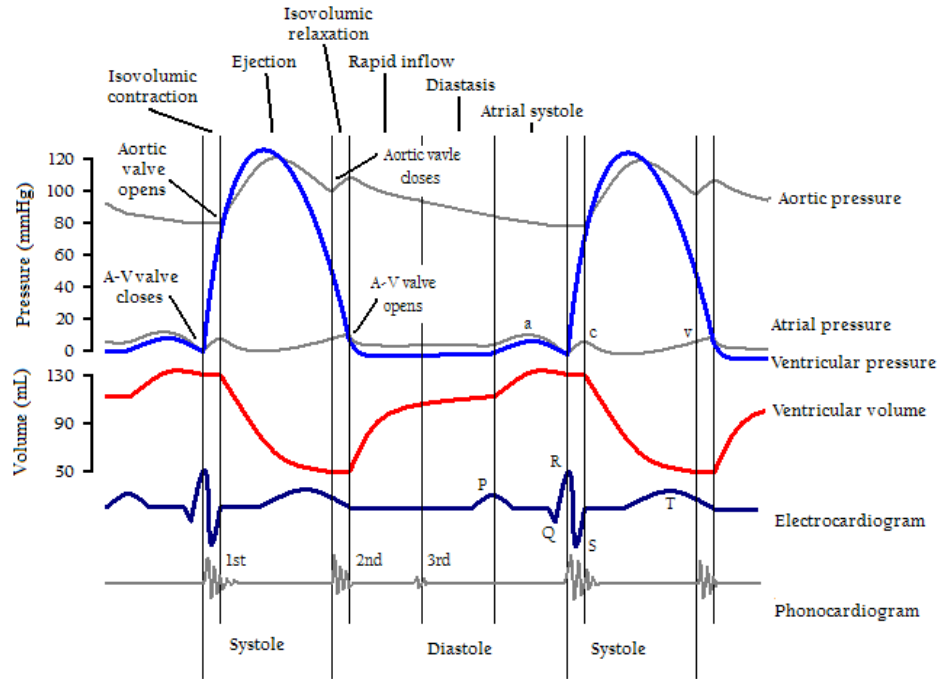


Figure 2.8: Wiggers Diagram [Richardson 1998] - It shows different parameters of the cardiac function during a cardiac cycle (from http://en.wikipedia.org/wiki/Cardiac_cycle).

6. the *rapid inflow*: When the ventricular pressures fall below atrial pressures, the atrio-ventricular valves open and ventricular filling begins. The ventricles briefly continue to relax, which causes intraventricular pressures to continue to fall despite on-going ventricular filling. Filling is very rapid because the atria are maximally filled just prior to atrio-ventricular valve opening. Once the valves open, the elevated atrial pressures coupled with the low resistance of the opened atrio-ventricular valves results in rapid, passive filling of the ventricle.
7. the *diastasis*: This reduced filling phase is the period during diastole when passive ventricular filling is nearing completion. Increased intraventricular pressure reduces the pressure gradient across the atrio-ventricular valves so that the rate of filling declines, even though atrial pressures continue to increase slightly as venous blood continues to flow into the atria. Aortic pressure and pulmonary arterial pressure continue to fall during this period as blood flows into the systemic and pulmonary circulations.

These phases can be detected by the temporal evolution of different parameters such as: the ECG, sound of the heartbeat, volume curves, and pressure curves. The Figure 2.8 summarizes the evolution of these parameters over a cardiac cycle. The most common and simple parameters used to assess the cardiac function are the left ventricular (LVEF) and right ventricular (RVEF) ejection fractions. They represent

the fraction of blood pumped out of a ventricle with each heart beat.

2.2 Cardiac Imaging

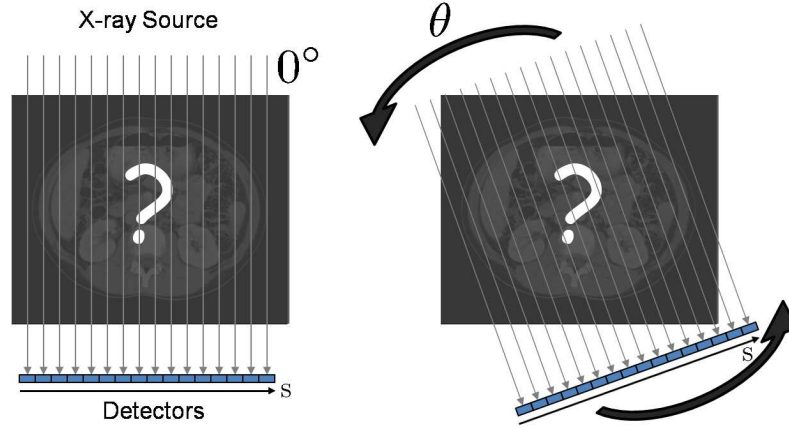
Imaging techniques make possible to visualize anatomical structures and morphological anomalies of the heart. Due to the inherent nature of cardiac function, the temporal visualization of cardiac anatomy allows a better assessment of cardiac motion and mechanical function. Beyond cardiac anatomy and motion, metabolic function of the heart can also be observed with molecular imaging techniques. We briefly present here the most common imaging techniques that allow to observe cardiac structure, anatomy, and function based on different physical principles.

- ***Echography*** (US) measures the gradient of acoustic impedance at the interface of tissues with the intensity of reflected acoustic waves. It has the advantage to non-invasively image in real-time and has been recently extended from time-series acquisitions of 2D images to 3D volumes. Echocardiography is used for assessment of shape, thickness and motion of the cardiac walls and of the heart valves. Measuring frequency shifts between emitted and reflected acoustic signal, *Echo-Doppler Imaging* can also provide an additional motion information displayed as a color overlay on the standard echography sequences. Typically, positive Doppler shift signals corresponding to flow towards the transducer are displayed at the red end of the spectrum and flow away from the transducer at the blue end. It is mostly used to study blood flow characterized by high velocities with low amplitude. It is also used to measure myocardial wall motion characterized by low velocities with high amplitude. In this case, we talk more specifically about *Tissue Doppler Imaging* (TDI). Combined with contrast agent (microbubbles of gas) with different acoustic properties from that of tissues, *Echography* can enhance both normal grey-scale and flow-mediated Doppler signals. It can also be used as molecular imaging method by targeting specific molecules with labeled microbubbles.
- ***Computed Tomography*** (CT) measures the density of tissues with the intensity attenuation of X-Rays passing through the patient. The improvement of technology enabled the acquisition of time-series of 3D volumes (dynamic 4D CT). Contrast agent can be used to enhance the contrast between blood and cardiac tissues. Cardiac CT is especially useful in evaluating the myocardium, coronary arteries, pulmonary veins, thoracic aorta, pericardium, and cardiac masses, such as thrombus of the left atrial appendage.
- ***Nuclear Imaging*** (SPECT and PET) uses low doses of radioisotopes (the marker) linked to compounds (the tracer) usually involved in a metabolic process. Nuclear imaging is restricted to functional and perfusion information and cannot be used for assessment of cardiac and coronary artery morphology. *Single photon emission computed tomography* (SPECT) uses tracers which emit gamma rays with an energy between 50 and 500 keV. Individual

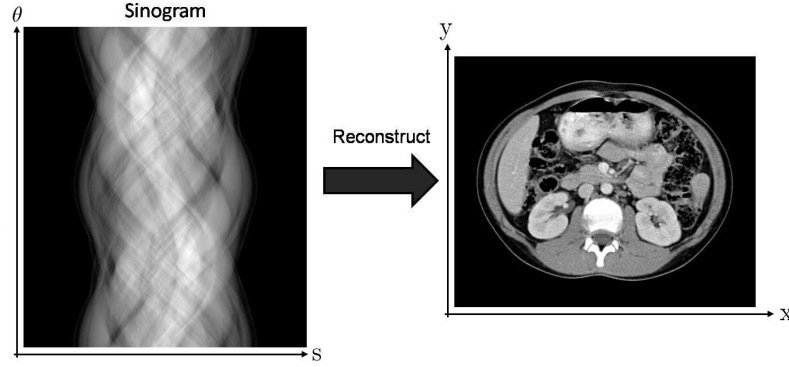
photons are detected using either a rotating gamma camera or special purpose multi-detector devices. All detectors used for single photon imaging require some form of gamma ray collimation and, hence, suffer basic limitations to spatial resolution and, more particularly, sensitivity. SPECT is used to detect areas of normal and reduced perfusion in the myocardium. *Positron emission tomography* (PET) uses radioactive tracers labeled with radioisotopes emitting positrons during their radioactive decay. The subsequent positron annihilation within a millimeter of the emission point leads to the production of two back-to-back 511 keV gamma rays detected with a positron camera surrounding the patient. PET can be used to measure myocardial perfusion or to identify areas of normal and reduced metabolism in order to separate viable and necrotic myocardium, for instance after a heart attack.

- **Magnetic Resonance Imaging** (MRI) measures magnetic material properties of tissues (mostly water and fat) due to different relaxation times and density of ^1H proton spins after magnetic excitation. Standard MRI has shown applications in the diagnosis of cardiac morphology but also in the assessment of cardiac function, myocardial perfusion and myocardial viability by means of dynamic and functional imaging. *Cine Magnetic Resonance Imaging* (Cine-MRI) acquires time-series of 2D slices during a cardiac cycle. *Tagged Magnetic Resonance Imaging* (Tagged-MRI) is an extension of Cine-MRI, which consists in tattooing the myocardium with lines or grids using selective spatial presaturation pulses (SPAMM - Spatial Modulation of Magnetization). Analysis of the tattooed images calls for techniques like HARP (Harmonic Phase MRI) that quickly and automatically extract the deformations consecutive to cardiac motion. *Velocity-Encoded Cine-Magnetic Resonance Imaging* (VEC-MRI), another extension of Cine-MRI based on the principle that moving protons change phase in proportion to their velocity, can measure a through plane blood velocities and flows. *Diffusion Weighted Magnetic Resonance Imaging* (DW-MRI) measures the diffusion of water molecules in tissues with the attenuation of the magnetic signal after successive dephasing and rephasing in different directions (gradient directions). It is used mainly in stroke diagnosis to detect an ischemic cytotoxic edema, to date the stroke event and to distinguish between acute and subacute strokes. This diffusion imaging technique has been also used to measure the directional diffusion of water molecules related to the tissue structure, such as with *Diffusion Tensor Magnetic Resonance Imaging* (DT-MRI). *Magnetic Resonance Spectroscopy* (MRS) measures the relaxation of other nuclei than ^1H . For instance, ^{31}P -MR spectroscopy allows the study of cardiac high-energy phosphate metabolites ATP and phosphocreatine. The phosphocreatine/ATP ratio is considered an index of the energetic state of the heart.

Among these many imaging techniques, we will focus more particularly on diffusion tensor magnetic resonance imaging (DT-MRI) and dynamic computed tomog-



(a) Acquisition of projections in the reference direction 0° and after a rotation θ of the X-ray source.



(b) Reconstruction of the slice from its sinogram.

Figure 2.9: (a) Acquisition and (b) reconstruction of a CT slice (adapted from <http://scien.stanford.edu/>).

raphy (4D CT) acquisition techniques to have a better understanding of the research work presented in this thesis.

2.2.1 4D Computed Tomography (CT)

Computed tomography (CT) is an imaging technique using X-rays [Prokop 2003, Ohnesorge 2003, Halpern 2008]. The basic principle of X-ray imaging can be described as follows. A source generates X-rays. The X-rays pass through the body that attenuates their intensity according to the tissue density. The more dense is the tissue, the more attenuated is the X-ray. The transmitted X-rays are measured by the flux of photon hitting a detector. The flux ϕ of transmitted photons is given by the Beer-Lambert law:

$$\phi(M) = \phi_0 e^{-\int_{L(M)} \mu(x) dx} \quad (2.1)$$

where

- ϕ_0 is the flux of emitted photons,
- M is the position on the detector where the flux of photons is measured,
- $L(M)$ is the straight line from the source to the detector position M ,
- $\mu(x)$ is the tissue density at the position x .

The output of the CT scan is an intensity I_H given in Hounsfield Units (HU) defined by the relative tissue density μ compared to water density μ_0 :

$$I_H = \frac{\mu - \mu_0}{\mu_0} 1000$$

On the contrary to traditional radiography that only shows superimposition of structures in a 2D image, a CT scan provides a 3D volume of tissue density. Different geometries of CT scanners exist (see Figure 2.10) but the fundamental principle of slice image acquisition is to rotate the source of X-rays around the patient to measure the attenuation on detectors in every direction (see Figure 2.9). The recorded signals form a sinogram from which can be reconstructed 2D/3D images by solving an inverse problem with filtered backprojection, iterative or analytic reconstruction methods. The reconstruction method mainly depends on the type of source (line, fan or cone beam collimation), the geometry of the CT scanner and the acquisition process.

The first generation of scanners creates finely collimated X-ray beam and uses a single pair of planar source-detector moving in a translate-rotate mode. The second generation creates a narrow fan beam ($\sim 10^\circ$) and uses multiple pairs of source-detectors moving in a translate-rotate mode. The third generation uses a single source of X-ray cone beam and multiple detectors that jointly rotate around the patient. The fourth generation of CT scanners has a full static ring of detectors and only the X-ray cone beam source rotates around the patient.

Two acquisition processes exist. First, the axial (or sequential) CT is a “step-and-shoot” acquisition process where each 2D slice is reconstructed independently to finally form a 3D volume (see Figure 2.11). The table, on which the patient lies, is translated at each step to select a slice. Then the source rotates around the patient to acquire the image projection in every directions. Second, in helical (or spiral) CT, the patient continuously translates while the source rotates around him. In the reference frame of the patient, the trajectory of the source is a helix as shown in Figure 2.11. The 3D volume is then reconstructed with 2D slices interpolated from the signal acquired. The slices can be defined *a posteriori* at any position as opposed to axial CT, in which the slices are defined by the acquisition process itself. Hence, a helical CT acquisition is closer to a real 3D scan than axial CT that is only a succession of contiguous 2D scans. Helical CT has the advantage to provide a faster volume coverage speed combined with a lower dose irradiation.

The technological breakthrough of multi-slice CT (MSCT) using multi-detector systems extended 2D slice to 3D volume reconstruction. Indeed, the image projection of all detectors are used simultaneously to solve the reconstruction problem directly in 3D. But since detectors do not form a closed surface, MSCT has to deal with truncated data and thus use specific 3D reconstruction algorithms. The

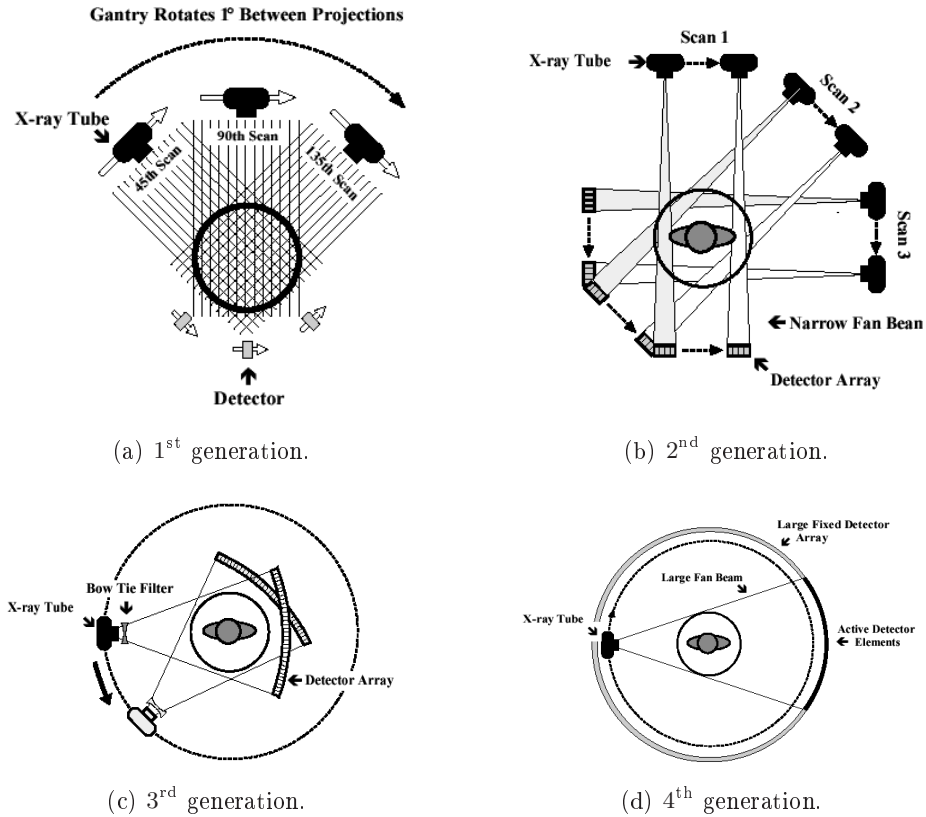


Figure 2.10: Four generations of CT scanner geometries (from http://en.wikibooks.org/wiki/Basic_Physics_of_Nuclear_Medicine/X-Ray_CT_in_Nuclear_Medicine).

combination of multi-slice and helical CT highly improved the acquisition speed and limited dose irradiation opening doors to new applications such as sequence acquisitions for lung and heart.

To cope with the lung motion, an acquisition of the heart must be performed during breathhold. In static 3D cardiac imaging, the CT acquisition is synchronized with the peak of the ECG R-wave. This peak is commonly used to define the end of diastole (ED) where the least amount of cardiac motion occurs. Axial scanning is a prospective ECG-triggered scanning, in which the instant of acquisition is predefined. Helical scanning is a retrospective ECG-gated scanning, in which the acquisition is performed during the whole cardiac cycle while simultaneously recording the ECG. The necessary projection data are selected only during the reconstruction process with the help of the ECG.

When acquiring dynamic 4D CT, the reference time-point is the ED detected with the peak of the ECG R-wave. The temporal positions at which the acquisition is performed are defined by either the percentage of the RR-interval covering the whole cardiac cycle or the absolute time distance relatively to the R-wave (positive

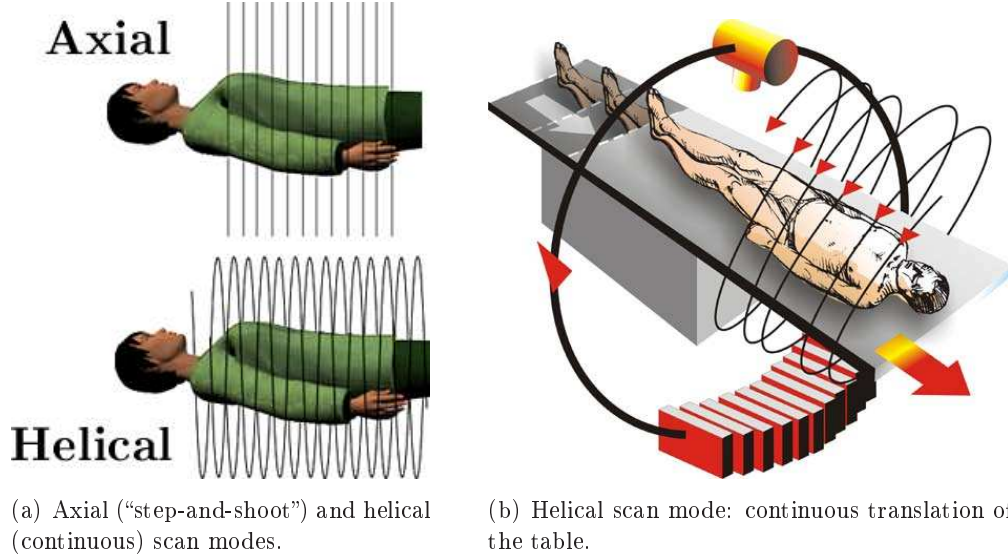


Figure 2.11: Two different scan modes for CT acquisitions (adapted from <http://imaging.cancer.gov/>).

values mean after the R-wave and negative values mean before). When acquiring cardiac 4D CT data, the speed of rotation of the source limits the temporal resolution of the sequence. To improve the temporal resolution, a different section of the full rotation is completed at the same time of several cardiac cycles. The drawback is a higher radiation dose and blurring due to non-periodicity of the heart. Dual source scanners were also proposed to acquire twice faster a full rotation. Similarly to temporal resolution, when the field of view is limited by the size of the detectors, the full heart can be acquired translating the table over multiple cardiac cycles. Over the last years, the size of the detectors has increased rapidly up to 320 slices with 160 mm coverage allowing a lower dose imaging of a sequence in a single heart-beat.

2.2.2 Diffusion Tensor Magnetic Resonance Imaging (DT-MRI)

We present the principle of nuclear magnetic resonance that is used to acquire magnetic resonance images [Hashemi 2004, Lardo 2004]. Based on this acquisition technique, diffusion weighted magnetic resonance has been developed to measure the average diffusion of water molecules in the tissue or a more complex model of diffusion with directional information [Mori 2007].

Nuclear Magnetic Resonance Protons (hydrogen nuclei ^1H), widely present in many biological tissues, have intrinsic angular momentum \mathbf{I} , called nuclear spin, and an associated magnetic momentum $\mu = \gamma\mathbf{I}$ where γ is the gyromagnetic ratio. Without external magnetic field, the momenta of protons are randomly oriented and hence create a null net magnetization (or macroscopic magnetization) \mathbf{M} (see

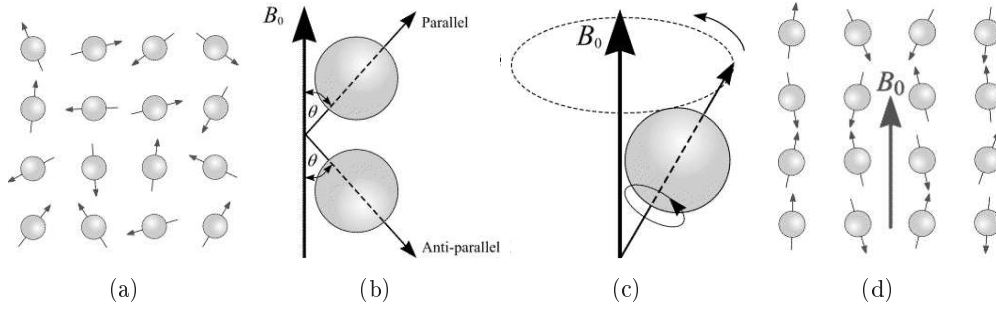


Figure 2.12: Nuclear Magnetic Resonance - (a) No external magnetic field. (b) Parallel and anti-parallel states within external magnetic field \mathbf{B}_0 . (c) Precession about the axis of the magnetic field \mathbf{B}_0 . (d) Within external magnetic field \mathbf{B}_0 (adapted from <http://www.easymeasure.co.uk/>).

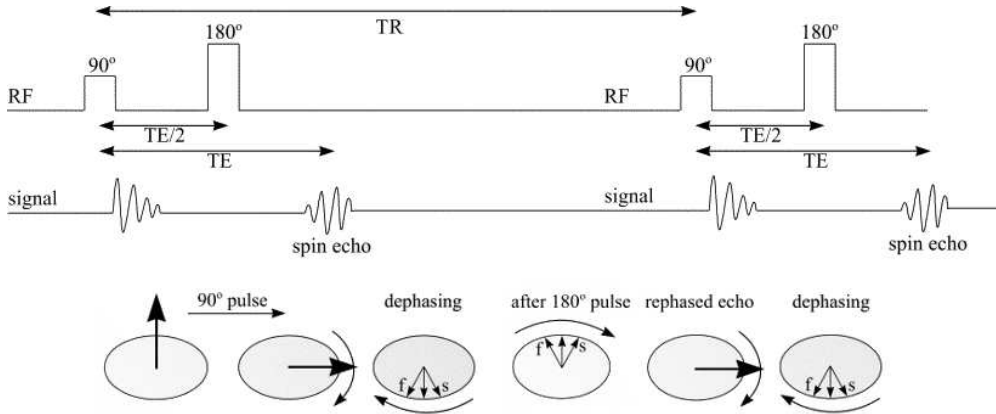


Figure 2.13: MRI pulse sequence and evolution of the magnetic momentum M during the TE (adapted from <http://www.easymeasure.co.uk/>).

Figure 2.12(a)). Within an external magnetic field \mathbf{B}_0 , nuclear spins align with the external field (parallel) or against the field (anti-parallel) (see Figure 2.12(b)) and precess about the axis of the magnetic field \mathbf{B}_0 with Larmor frequency $\omega_0 = \gamma B_0$ (see Figure 2.12(c)). The magnetic momentum vector of spinning protons can be decomposed into two orthogonal components: a longitudinal component along \mathbf{B}_0 , and a transverse component, orthogonal to \mathbf{B}_0 . Since the orientations of spins are more parallel with low energy state than anti-parallel with high energy state, the longitudinal net magnetization \mathbf{M}_l has the same orientation as \mathbf{B}_0 . Moreover since there is no phase coherence between spins, the transverse net magnetization \mathbf{M}_t is null (see Figure 2.12(d)).

When a radiofrequency (RF) pulse \mathbf{B}_1 lying in the plane perpendicular to \mathbf{B}_0 at the Larmor frequency $\omega_0 = \gamma B_0$, the nuclear spins are in resonance with the RF pulse and absorb its energy to align with \mathbf{B}_1 . This absorption of energy, called

excitation, modifies the energy level and spin phases. During excitation, the longitudinal magnetization decreases due to the alignment of spins with \mathbf{B}_1 whereas the transverse magnetization increases due to the spins getting into phase coherence. The return of the nucleus to its state of equilibrium with an emission of electromagnetic energy is called *relaxation*. The recovery of the net magnetization is due to two different phenomena: a longitudinal relaxation due to the realignment of spins with the external magnetic field B_0 and a transverse relaxation due to the loss of phase coherence. These two relaxations follow an exponential law with different recovery rates characterized by tissue-specific time constant T_1 and T_2 . The time constant T_1 corresponds to the time for longitudinal magnetization to return to 63% of its final value whereas the time constant T_2 corresponds to the time for transverse magnetization to decrease by 63% of its original value. T_2 , which is unrelated to magnetic field strength, is always shorter than T_1 , which is longer at higher magnetic field strength.

Magnetic Resonance Imaging With the acquisition of the emitted electromagnetic signal during relaxation, MRI scanners can measure magnetic properties of tissues that depend on the proton density ρ and the relaxation times T_1 and T_2 . For MRI acquisition, many pulse sequences exist but we limit here the description to the spin echo (SE) sequence, the most common pulse sequence. The electromagnetic signal is measured at echo time (TE) after excitation by two successive pulses (see Figure 2.13). A first 90° RF pulse at time 0 causes a rotation of the longitudinal magnetization into the transverse plane and the dephasing of the transverse magnetization starts. A second 180° RF pulse at time TE/2 causes a rephasing of the spins to recover transverse magnetization, producing a spin echo at the acquisition time TE. Then, the sequence of pulses is repeated at the repetition time TR.

The signal measured by MRI scanners is the transverse net magnetization strength M_t . In a spin echo pulse sequence, it satisfies the following equation:

$$M_t = M_0(\rho) (1 - e^{-\frac{TR}{T_1}}) e^{-\frac{TE}{T_2}}$$

By modifying the length of pulse sequence parameters TR and TE, one can select the most influent magnetic tissue property (proton density ρ , relaxation times T_1 or T_2) on the measured magnetization strength M_t . The choice of the echo time (TE) and the repetition time (TR) to obtain Proton Density-weighted, T_1 -weighted or T_2 -weighted images is presented in Figure 2.14.

Image	TR	TE	Measured Signal
PD-weighted	long	short	$M_t \simeq M_0(\rho)$
T_1 -weighted	short	short	$M_t \simeq M_0(\rho) (1 - e^{-\frac{TR}{T_1}})$
T_2 -weighted	long	long	$M_t \simeq M_0(\rho) e^{-\frac{TE}{T_2}}$

Figure 2.14: Choice of the pulse sequence parameters TR and TE to image different tissue contrasts.

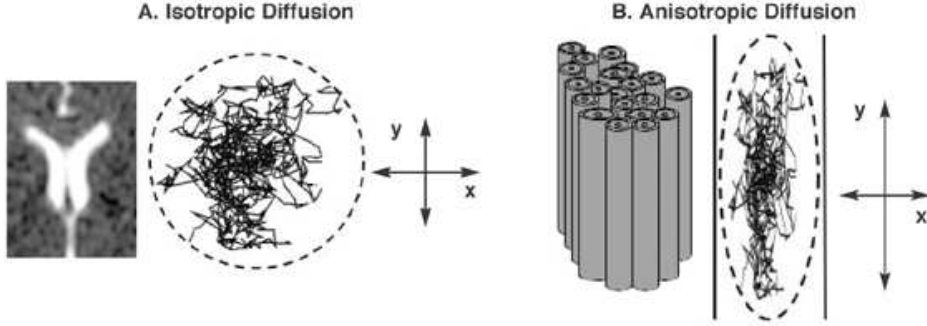


Figure 2.15: Influence of microstructure on diffusion properties. Diffusion is called isotropic when water molecules are free to move in every directions. Diffusion is called anisotropic when water molecules have constrained directions of propagation (from [Rosenbloom 2003]).

The spatial position is encoded by applying different magnetic gradient fields (G_x , G_y and G_z) for each spatial direction (respectively x, y and z). First, a slice selection (SS) gradient G_z perpendicular to the desired slice plane is added to the external magnetic field such that $\mathbf{B}_0 = \mathbf{B}_0 + z \mathbf{G}_z$ during the excitation by RF pulses. Thus, the Larmor frequency depends on the slice position along \mathbf{G}_z . When a RF pulse is applied at the resonance frequency of a given slice, only the protons in this slice are excited. The second step of spatial localization is called phase-encoding (PE). A magnetic gradient field \mathbf{G}_y is applied briefly after the first RF pulse in a direction perpendicular to \mathbf{G}_z . As the change in frequency is very brief, when the gradient is switched off, it causes a change in phase that is proportional to the magnetic field amplitude and thus to the position in the y direction. The last step of spatial localization is frequency-encoding (FE). A magnetic gradient field \mathbf{G}_x is applied during data acquisition in the direction perpendicular to \mathbf{G}_z and \mathbf{G}_y . Thus, the Larmor frequency of nuclear spins varies in the direction of the frequency-encoding gradient. The MR signal is a mix of signals with all these frequencies (encoding in the frequency-encoding direction) and phase shifts (encoding in the phase-encoding direction) that give access to the image slice in the frequency domain. The image slice is reconstructed in the spatial domain using a 2D inverse Fourier transform.

Diffusion Tensor Magnetic Resonance Imaging Diffusion magnetic resonance imaging [LeBihan 1985, Bassar 1994, Mori 2007] measures the mobility of the water molecules inside a voxel due to their Brownian motion [Einstein 1956] constrained by the tissue structure (see Figure 2.15). The diffusion of water molecules is measured with a T_2 -weighted sequence including two additional diffusion gradient fields \mathbf{G}_{diff} . The first gradient pulse is applied for a short time δ and introduces a phase shift that is dependent on the strength of the gradient at the position of the spin. Before applying the second gradient pulse after a diffusion time Δ , the 180° RF pulse reverse the phase shift. Protons staying at the same position along

the gradient direction recover their original phase. Protons moving to a different position from their original position are rephased with a different field strength and do not recover their original phase. This final phase shift due to motion results in a reduction of the measured signal. This reduction due to the application of the diffusion gradient pulse can be related to the amount of diffusion that is occurring through the following Stejskal-Tanner formula:

$$S = S_0 e^{-\gamma^2 G^2 \delta^2 (\Delta - \frac{\delta}{3}) D} = S_0 e^{-bD} \quad (2.2)$$

where

- S_0 is the T_2 -weighted signal intensity without the gradient pulses,
- S is the signal with the gradient pulse,
- γ is the gyromagnetic ratio,
- G is the strength of the diffusion gradient,
- δ is the duration of the gradient pulse,
- Δ is the diffusion time between the two gradient pulses,
- D is the tissue-specific diffusion constant.

To determine the reference signal S_0 from which is measured the signal loss due to diffusion, a baseline image b_0 is acquired without gradient pulse, which corresponds to a T_2 -weighted image. Then acquiring diffusion weighted images with different directions and strength of the magnetic diffusion gradient \mathbf{G}_{diff} and comparing them to the baseline image b_0 , an average diffusion value called apparent diffusion coefficient (ADC) can be estimated with a least square approximation of the parameter D in Equation 2.2.

Instead of estimating an average diffusion value over all directions, a directional model of diffusion D where the b-value is a vector can be estimated. A simple and common diffusion model is the diffusion tensor model that needs at least six gradient directions to be estimated. The resulting image is called diffusion tensor magnetic resonance image (DT-MRI). In this way, the tissue structure surrounding water molecules can be characterized. This description of tissue structure is particularly useful in the heart that has a highly anisotropic structure with fibres and laminar sheets. But to obtain high resolution images, diffusion imaging is limited to *ex vivo* acquisitions. *In vivo* acquisition of high resolution DT-MRI is still a challenging research topic in progress. Due to the acquisition of several diffusion weighted images with different magnetic diffusion gradients, the main issue is the temporal resolution that is too low to cope with cardiac motion. But still some studies have shown the interest of low resolution acquisitions for clinical applications.

PART II

COMPARISON OF CARDIAC FIBRE ARCHITECTURE FROM DT-MRI

CHAPTER 3

STATISTICAL ANALYSIS OF CARDIAC DT-MRI

Contents

3.1	Introduction	33
3.2	Atlas Building	38
3.2.1	Introduction to Atlas Building	38
3.2.2	Pairwise Registration	41
3.2.3	Groupwise Registration	44
3.3	Transformation of Cardiac Diffusion Tensors	45
3.3.1	Finite Strain (FS)	47
3.3.2	Preservation of the Principal Direction (PPD)	49
3.3.3	Comparison of the Reorientation Strategies	51
3.4	Statistical Analysis of Cardiac Diffusion Tensors	55
3.4.1	Introduction to DT-MRI Processing	55
3.4.2	Log-Euclidean Mean and Covariance	60
3.4.3	A New Analysis of the Diffusion Tensor Covariance Matrix	60
3.5	Conclusion	63

3.1 Introduction

The recent emergence of diffusion MRI [LeBihan 1985], and in particular diffusion tensor MRI [Basser 1994], has opened novel applications by imaging the structure of tissues, in particular its anisotropy. Diffusion MRI consists in measuring, in a specific direction of space, the motion of water molecules. This motion is better known as the *Brownian motion* formalized as the average squared distance of displacement per unit of time [Einstein 1956]. From the acquisition of diffusion values in different directions of space, we can compute an average diffusion value, called the apparent diffusion coefficient (ADC). A more complex description of diffusion can be inferred from these acquisitions by using a directional model of diffusion in the tissue. Different models were proposed: 2nd order diffusion tensor model [Basser 1994], bi-tensor model [Alexander 2001a, Tuch 2002], CHARMED

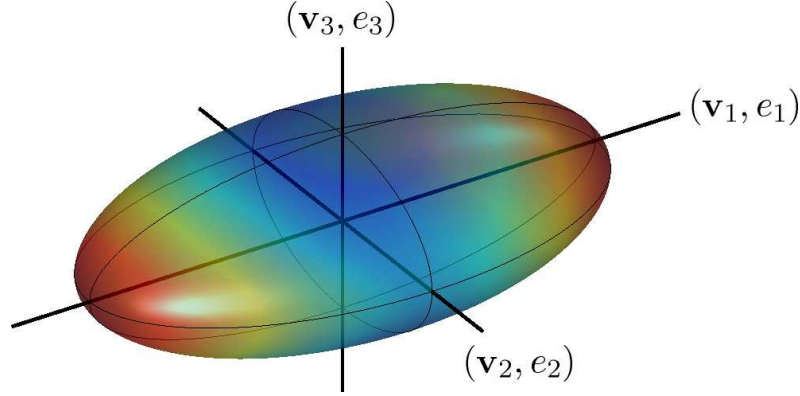


Figure 3.1: Visualization of a diffusion tensor as an ellipsoid. The eigenvectors \mathbf{v}_1 , \mathbf{v}_2 , and \mathbf{v}_3 give the direction of the main axis of the ellipsoid. The eigenvalues e_1 , e_2 , and e_3 give the radii of the ellipsoid. The colors from blue to red show the directional distribution of increasing diffusion values.

[Assaf 2005], Q-Ball [Tuch 2004], orientation density function [Tournier 2004], or even higher order tensors [Barmpoutis 2007].

The most commonly used model of diffusion is the 2nd order diffusion tensor model (or diffusion tensor), which uses a Gaussian directional distribution of diffusion values. Mathematically, a diffusion tensor is represented by a symmetric positive definite matrix whose eigenvectors and corresponding eigenvalues give the main directions of diffusion and corresponding diffusion values, respectively. The eigen decomposition of a diffusion tensor D gives:

$$D = V E V^T = e_1 \mathbf{v}_1 \mathbf{v}_1^T + e_2 \mathbf{v}_2 \mathbf{v}_2^T + e_3 \mathbf{v}_3 \mathbf{v}_3^T$$

where V is the orthogonal matrix of eigenvectors and E is the diagonal matrix of eigenvalues:

$$V = \begin{pmatrix} | & | & | \\ \mathbf{v}_1 & \mathbf{v}_2 & \mathbf{v}_3 \\ | & | & | \end{pmatrix} \quad \text{and} \quad E = \begin{pmatrix} e_1 & 0 & 0 \\ 0 & e_2 & 0 \\ 0 & 0 & e_3 \end{pmatrix}$$

When sorted in decreasing order, the eigenvalues e_1 , e_2 , and e_3 are called the primary, secondary, and tertiary eigenvalues, respectively. These eigenvalues are strictly positive since they are homogeneous to a squared distance per unit of time. By extension, their corresponding eigenvectors \mathbf{v}_1 , \mathbf{v}_2 , and \mathbf{v}_3 are called the primary, secondary, and tertiary eigenvectors, respectively. It is commonly visualized with a 3D ellipsoid whose axes directions are the eigenvectors and whose radii are the eigenvalues (see Figure 3.1).

By measuring the directional differences of diffusion, the anisotropy of the underlying tissue can be observed. In the case of cardiac DT-MRI, the primary eigenvector is related to the cardiac muscle fibre direction [Scollan 1998, Hsu 1998,

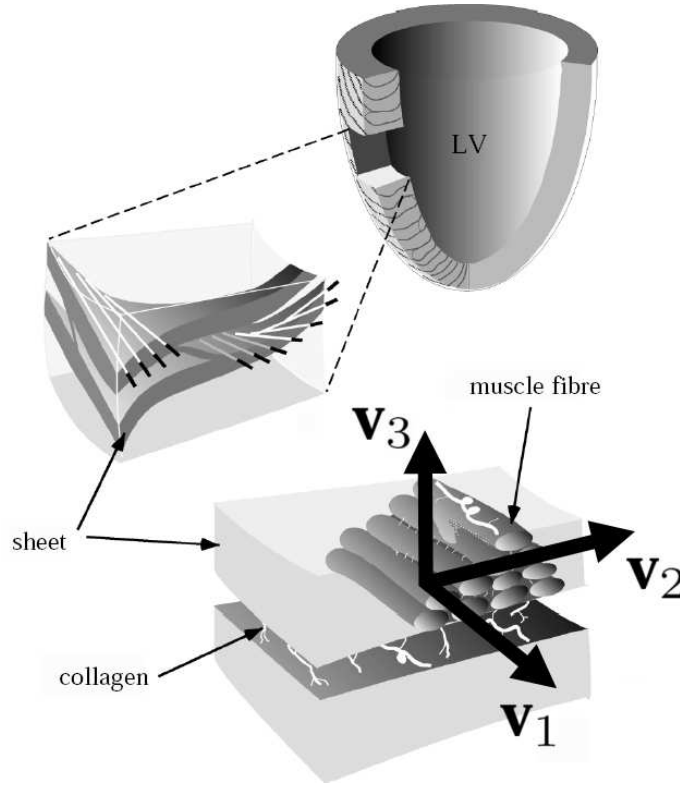


Figure 3.2: Cardiac fibre structure and eigenvectors of diffusion tensor (adapted from LeGrice *et al.* [LeGrice 1995a]). The cardiac fibre structure constrains the diffusion of water molecules in the tissue. The primary eigenvector \mathbf{v}_1 of a diffusion tensor D is along the fibre direction. The secondary eigenvector \mathbf{v}_2 is orthogonal to the fibre direction lying in the laminar sheet plane. The tertiary eigenvector \mathbf{v}_3 is normal to the laminar sheet plane.

[Holmes 2000] and the tertiary eigenvector to the normal direction of the laminar sheet plane [Tseng 2003, Helm 2005c] (see Figure 3.2).

In this chapter, we propose a unified computational framework to build an atlas of the cardiac fibre architecture that is learned statistically from a population of DT-MRI. Our approach differs from other cardiac studies in computing statistics directly on the diffusion tensors instead of using angles [Helm 2005a, Gilbert 2007] or vectors [Sundar 2006, Garcia-Barnes 2009]. This approach has the advantage to work directly on entities that contain the complete description of fibre structure. However, since diffusion tensors are symmetric positive definite matrices that do not lie on a vector space, standard Euclidean multivariate statistics are not consistent with the positivity constraint on the eigenvalues. Riemannian geometry, based on either affine-invariant [Moakher 2005, Batchelor 2005, Pennec 2006, Lenglet 2006, Fletcher 2007] or Log-Euclidean [Arsigny 2006] metrics, gives a general and consistent computational framework. Statistics on diffusion tensors have already been used to build brain atlases. But none of them defined a complete and consistent

framework with the most recent advances on diffusion tensor processing. Jones *et al.* [Jones 2002] computed first-order statistics with a Euclidean metric. Their second-order statistics were limited to features of the diffusion tensor (the dyadic tensor [Basser 2000] formed from the primary eigenvector). Second-order statistics on the whole diffusion tensor were computed for model-based diffusion tensor tractography [Masutani 2006] in the brain but only with a Euclidean metric. A population study of brain diffusion tensors used statistics with the Log-Euclidean metric but was limited to their averaging [Goodlett 2009].

Unlike previous works on statistical analysis of DT-MRI, the proposed computational framework is both complete and consistent in terms of the following three aspects. First, we use a Riemannian metric to be consistent with the positivity constraint on the eigenvalues. Second, we compute the average and covariance matrix of the whole diffusion tensors. Third, we employ new tools to extract the variabilities of the eigenvectors and eigenvalues from the covariance matrix that are better suited for studying the variability of the cardiac fibre and laminar sheet orientations.

The workflow to compute statistics on cardiac DT-MRI can be divided into three parts (see Figure 3.3):

- *Registration of anatomical MRI (Section 3.2).* To compare different hearts, we first need to find an inter-subject mapping for normalizing their geometries. This mapping is obtained from a groupwise registration of anatomical MRI. To ensure the accuracy of the atlas we build, matching corresponding anatomical structures is necessary. Thus, we propose to include interactive guidance of pairwise registrations [Azar 2006] in a standard workflow for atlas building [Guimond 2000].
- *Transformation of DT-MRI (Section 3.3).* Once a mapping between the hearts is known, an important issue is to transform the diffusion tensors properly. These tensors contain a directional information of diffusion linked to the reference frame of the image. When warping an image, this reference frame is modified. Thus, the diffusion tensors have to be transformed according to the modification of the reference frame. Different transformation strategies have been proposed [Alexander 2001b]. We compare these strategies on synthetic data to characterize their impacts on diffusion tensors and give insights on how to determine the most suited transformation strategy.
- *Complete and consistent statistics on diffusion tensors (Section 3.4).* This is realized by computing average diffusion tensors and their corresponding covariance matrices in the Log-Euclidean framework. The difficulty is to interpret directly the covariance matrix of diffusion tensors, especially in terms of cardiac fibre architecture. Thus, we propose new efficient tools to extract from this covariance matrix the variability of the eigenvectors and eigenvalues.

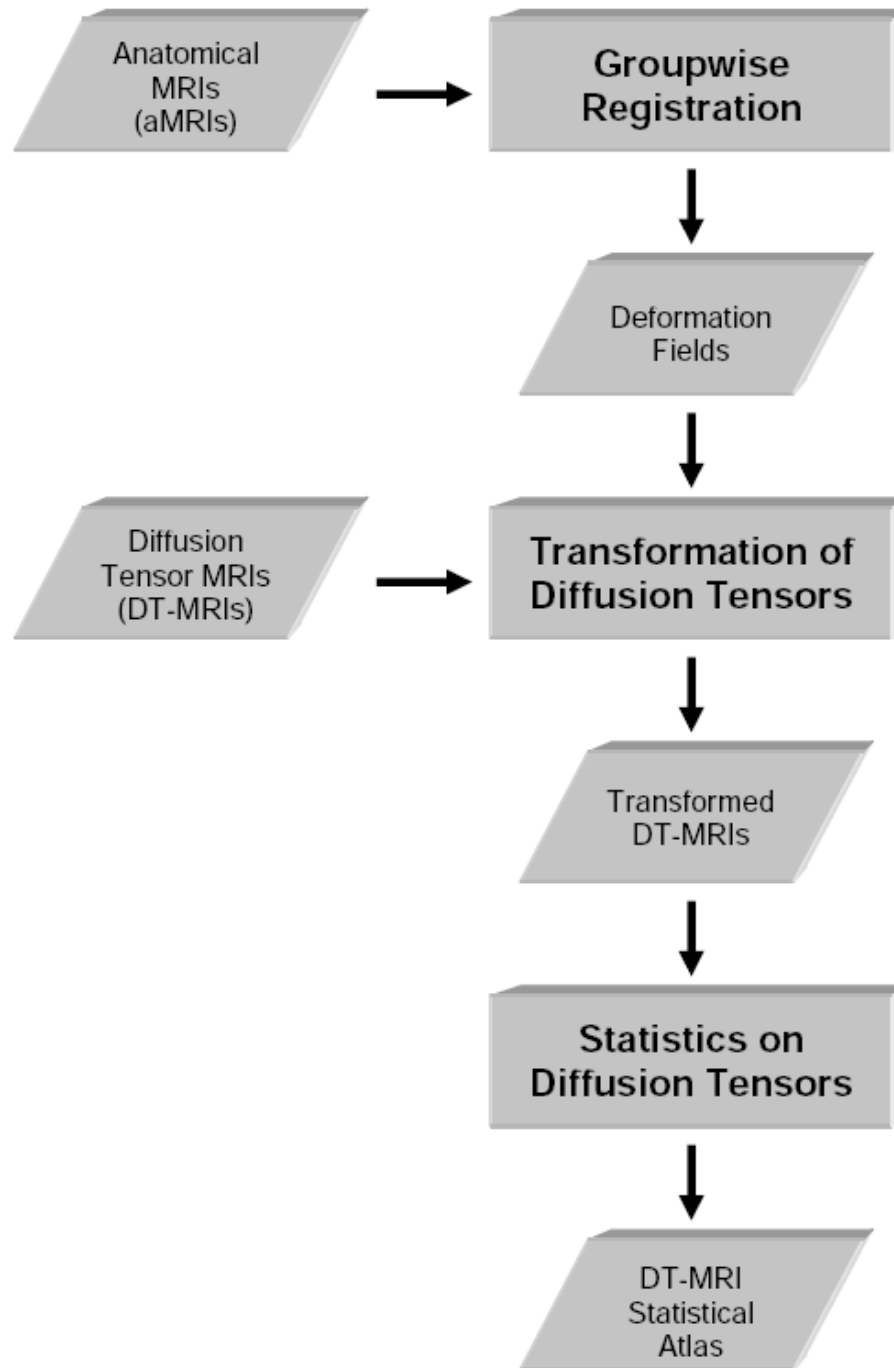


Figure 3.3: Overall workflow of the proposed framework to build a DT-MRI atlas that is compared to human and synthetic data.

3.2 Atlas Building

The choice of information used for the spatial normalization of cardiac geometries is fundamental. We can use either the DT-MRI that holds fibre architecture information or the baseline T2 (unweighted) MRI used for DT-MRI estimation that only holds anatomical information. Registering the geometries based on the DT-MRIs [Ruiz-Alzola 2002, Rohde 2003, Park 2003, Zhang 2006, Cao 2006, Van Hecke 2007, Chiang 2008, Yeo 2009] implies a minimization of the differences between diffusion tensors. In this case, we make the assumption that there are similarities between cardiac DT-MRIs. Actually, it is exactly what we want to evaluate in the following statistical analysis. To avoid introducing a bias, we prefer to register only anatomical information with the baseline T2 (unweighted) MRIs. These anatomical MRIs have the advantage to be acquired in the same geometry as the DT-MRIs, image distortion induced by magnetic field eddy-current being already corrected for DT-MRI estimation [Mansfield 1977, Jezzard 1998, Rohde 2004, Finsterbusch 2009]. Thus, the deformation fields used to transform the anatomical MRIs can be directly used to transform the DT-MRIs to the same geometry.

To register the anatomical MRI to a common coordinate system, we propose here a standard workflow for atlas building. First, we give an overview of existing atlas building strategies. Then, we present a pairwise registration algorithm allowing interactive guidance that ensures the quality of the inter-subject mapping. Finally, we describe the alternate groupwise registration of the anatomical MRI based on pairwise registration steps.

3.2.1 Introduction to Atlas Building

To study intra- and inter-population variabilities, the construction of an atlas is useful to map all 3D images to the same common reference frame. In this way, local parameters can be compared at corresponding anatomical positions. Furthermore, the transformations matching all images to the atlas image can be used to study shape variabilities.

The choice of the common reference frame (or template image I_{atlas}) is important since the arbitrary choice of an image in the dataset as a template would introduce a bias. In [Park 2005], they propose to choose the template image as the image in the dataset that minimizes the distance with all other images. Other methods [Guimond 2000, Marsland 2004, Bhatia 2004, Beg 2004, Joshi 2004, Avants 2004, Marsland 2004, Zollei 2005, Bossa 2007] proposed to build an unbiased atlas from a set of images by defining the template image as an average representation of geometries and intensities of all images. A “template free” approach was also proposed in [Studholme 2004] where intensity values of transformed images are not averaged in the common reference frame. The transformed images are stored in a vector-valued image used for registration. This vector-valued image can actually be seen as a more complex template than an image with average intensities.

Intuitively, the unbiased atlas building problem has been defined as follows.

Given a set of N images $\{I_i\}_{i=1,\dots,N}$, we want to estimate the atlas image I_{atlas} and the set of transformations $\{T_i\}_{i=1,\dots,N}$ mapping the set of images $\{I_i\}_{i=1,\dots,N}$ to the atlas image I_{atlas} such that:

$$I_{\text{atlas}} = \frac{1}{N} \sum_{i=1}^N I_i \circ T_i \quad (3.1)$$

In this unbiased approach, the estimation of the atlas image I_{atlas} and the estimation of the transformations T_i are mutually dependent problems. The transformations T_i are needed to compute the atlas image I_{atlas} . And the average template I_{atlas} is needed to estimate the transformations T_i by registering each image I_i to I_{atlas} . Actually, the atlas building can also be formulated as a more general problem of alternate minimization of an energy functional:

$$(I_{\text{atlas}}, T_1, \dots, T_N) = \underset{(\tilde{I}_{\text{atlas}}, \tilde{T}_1, \dots, \tilde{T}_N)}{\operatorname{argmin}} \left(\sum_{i=1}^N \left(\operatorname{Sim}(\tilde{I}_{\text{atlas}}, I_i \circ \tilde{T}_i) + \operatorname{Reg}(\tilde{T}_i) \right) + \operatorname{Reg}_{\text{set}}(\tilde{T}_1, \dots, \tilde{T}_N) \right) \quad (3.2)$$

where

- Sim is a similarity measure between two images,
- Reg is a spatial regularization term for a given transformation,
- $\operatorname{Reg}_{\text{set}}$ is a regularization term for a set of transformations.

The alternate minimization has two main steps. First, the atlas image I_{atlas} is estimated with fixed transformations T_i . It has been shown in [Joshi 2004] that the intuitive definition of the atlas is actually the solution that minimizes Equation 3.2 for fixed transformations T_i when using the sum of squared differences (SSD) as the similarity measure. Second, the transformations T_i are estimated with I_{atlas} fixed by registering each image I_i to I_{atlas} . Furthermore, the transformations T_i are usually constrained such that they equally contribute to the geometry of the atlas image. These constraints can be included to the regularization term $\operatorname{Reg}_{\text{set}}$ by coupling transformations. For instance, in [Bhatia 2004] the sum of the displacement vector fields \mathbf{T}_i are constrained to be null. In the remainder, we differentiate displacement vector fields from deformation fields (or transformations) with bold characters. To simplify the problem, this coupling is usually included as an additional step after estimating independently each transformation T_i . These transformations are corrected with the inverse of the average transformation T_{mean}^{-1} to center the geometry of the template image among the set of images $\{I_i\}_{i=1,\dots,N}$ as follows:

$$I_{\text{atlas}} = \frac{1}{N} \sum_{i=1}^N I_i \circ T_i \circ T_{\text{mean}}^{-1} \quad (3.3)$$

In [Guimond 2000], the average transformation is computed with the arithmetic mean of the displacement vector fields \mathbf{T}_i , whereas it is computed on the curved

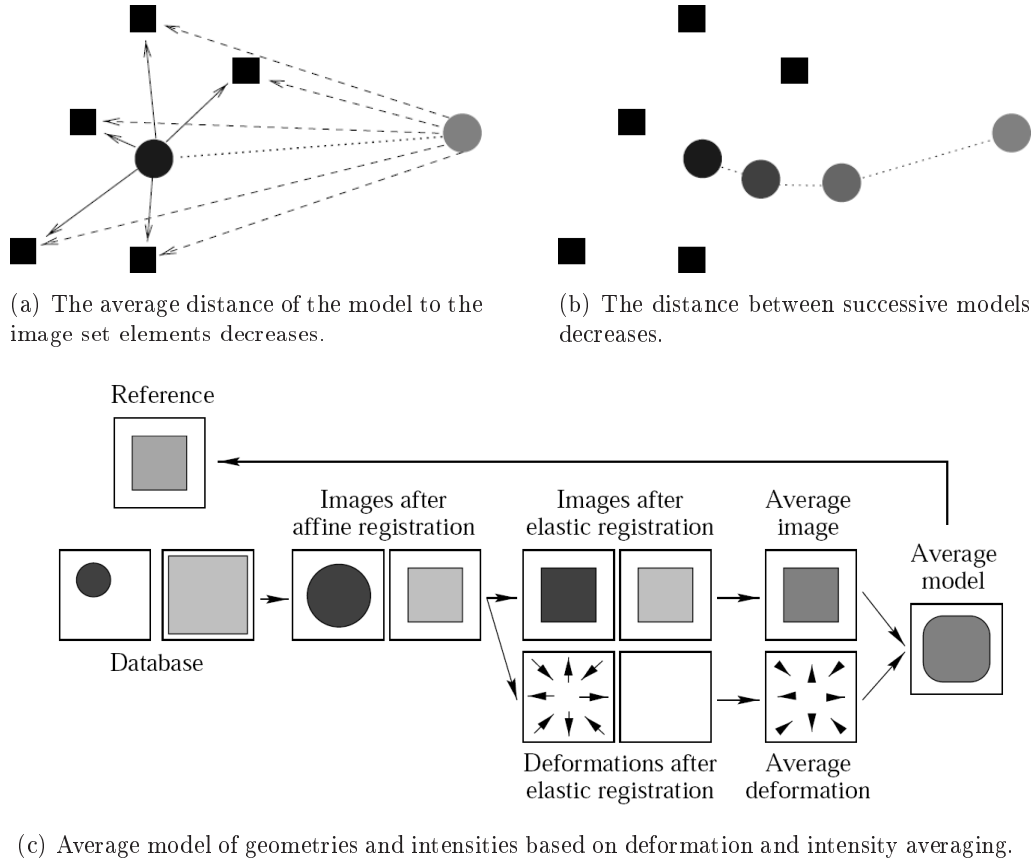


Figure 3.4: Average model construction method (from [Guimond 2000]).

space of diffeomorphisms using velocity vector fields in [Beg 2004, Avants 2004, Marsland 2004, Bossa 2007] to ensure the resulting transformation to be invertible. The general spirit of these methods are summarized with the average model construction [Guimond 2000] described in Figure 3.4.

The direction of registration between an image and the template (formulated in the similarity term) is also important. We presented here the *backward* scheme for atlas building, which estimates the atlas by registering each image to the common template reference frame. This scheme is the most widely used method for its lower computational complexity. But recently the *forward* scheme, which estimates the atlas by registering the template to each image, has been shown to provide a well-posed method for atlas building [Allasonnière 2007, Ma 2008, Durrleman 2009]. Indeed, this forward scheme considers images as noisy transformations of a noise-free template. In the backward scheme, images and their noise are transformed to the template image. Thus, the nature of noise is modified between the two schemes.

3.2.2 Pairwise Registration

The mapping of cardiac geometries is challenging due to large differences in alignment and scales of the data. Thus, there is a need for a robust affine registration before using any non-linear algorithm. In [Beg 2004], they proposed a landmark- and image intensity-based large deformation diffeomorphic metric mapping (LDDMM) method for non-linear registration of cardiac anatomies using MRI. But the landmarks are only used to initialize the non-linear registration.

We propose here to use pre-defined landmarks to constrain the initial affine transformation but also to interactively define landmarks to guide and correct the following non-linear registration.

3.2.2.1 Constrained Affine Registration

An affine transformation is performed interactively to control its quality and to get an appropriate initialization for the non-linear registration. An affine transformation can be defined by four landmarks. The difficulty to find four repeatable landmarks to best normalize the geometry of the hearts limited us to use only three landmarks and add constraints on the affine transformation. The three interactively located landmarks used to determine the constrained affine transformation S are: the left ventricular apex (A_{LV}) and the two right ventriculo-septal junctions (corner points C_1 and C_2) in the valve plane orthogonal to the long axis of the heart (see Figure 3.5). The long axis of the hearts are considered aligned due to the acquisition process of *ex vivo* data. In a more general case, an additional step aligning the long axis of the hearts should be performed.

We use these landmarks to define a composition of transformations $S = S_z \circ S_{xy} \circ R_{\theta_z} \circ T_r$ (see Figure 3.5), which aligns the hearts and normalizes their heights and radius:

- the translation T_r to match the centroids G and G' of the two pairs of corner points,
- the rotation R_{θ_z} around the direction of the long axis of the heart to match the directions given by the two pairs of corner points (C_1, C_2) and (C'_1, C'_2) ,
- the scaling S_{xy} to match the length of the line segments defined by the two pairs of corner points (C_1, C_2) and (C'_1, C'_2) ,
- the scaling S_z along the axis of the heart to match the heights h and h' from the plane containing the LV endocardial apex to the valve plane.

3.2.2.2 Interactive Non-Linear Registration

For non-linear registration, we used an hybrid intensity and landmark-based registration algorithm [Azar 2006] that is well suited for fast interactive corrections. The interactive guidance by a selection of pairs of landmarks is useful to control

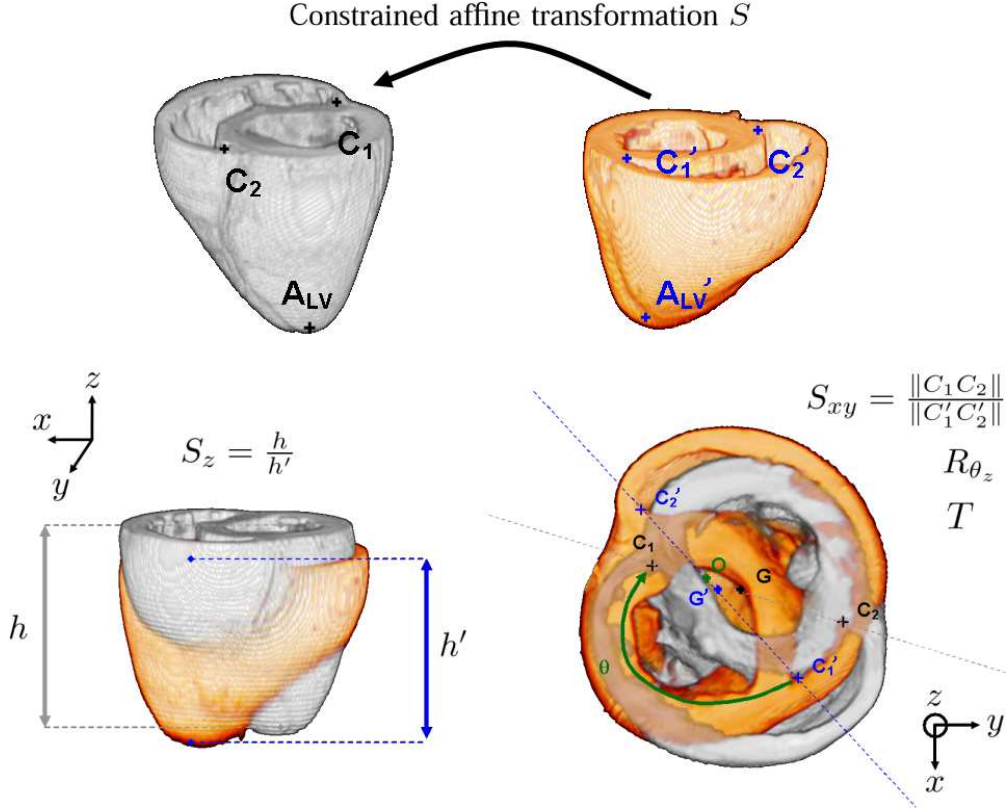


Figure 3.5: The pairwise registration is initialized with a constrained affine transformation S based on the matching of three interactively located landmarks: the left ventricular apex (A_{LV}) and the two corners of the right ventricle in the valve plane (C_1 and C_2). This transformation is defined as a composition of a translation T_r , a rotation R_{θ_z} , a radial scaling S_{xy} and a long axis scaling S_z . The atria are not shown here for a better visualization of the landmarks.

the registration, to avoid matching different structures and to improve the convergence. The advantage of this hybrid algorithm is to easily combine any intensity and landmark-based registration algorithms. This hybrid registration problem is formulated with the energy functional proposed in [Cachier 2001]:

$$E(Q_1, Q_2, T) = E_{\text{sim}}(I, J, Q_1) + \sigma \|Q_1 - T\|^2 + \sigma \gamma \|Q_2 - T\|^2 + \sigma \nu E_{\text{reg}}(T) \quad (3.4)$$

where

- Q_1 is the dense intensity-based deformation,
- Q_2 is the dense landmark-based deformation,
- T is the final dense intensity and landmark-based deformation,
- σ is a parameter that bounds the spatial uncertainty on the correspondences transformation Q_1 and Q_2 ,
- ν is a parameter that quantifies the amount of the regularization,
- γ is a trade-off coefficient between intensity matching and landmark matching.

An iterative dual energy minimization of equation 3.4 is performed by determining alternately the transformation Q_1 matching the intensities between images and the displacement field Q_2 matching corresponding landmarks and by combining these two displacement fields to provide the final displacement field T as follows:

1. Minimize with respect to Q_1 :

$$E(Q_1) = E_{\text{sim}}(I, J, Q_1) + \sigma \|Q_1 - T_N\|^2$$

2. Minimize with respect to Q_2 via iterative closest point (ICP) algorithm which gives new matches between set of landmarks S_I and S_J that most closely fits T_N :

$$E_{\text{feature}}(S_I, S_J, Q_2, T_N)$$

3. Minimize with respect to T_{N+1} to find an optimal and smooth transformation that fits Q_1 and Q_2 :

$$E(T_{N+1}) = \sigma \|Q_1 - T_{N+1}\|^2 + \sigma \gamma \|Q_2 - T_{N+1}\|^2 + \sigma \nu E_{\text{reg}}(T_{N+1})$$

This approach similar to the one proposed in [Cachier 2001] has been shown to yield to the following displacement field \mathbf{T} that is a weighted-average of the two regularized displacement fields \mathbf{Q}_1 and \mathbf{Q}_2 :

$$\mathbf{T}(x) = (1 - \lambda(x)) K_1 \star \mathbf{Q}_1(x) + \lambda(x) K_2 \star \mathbf{Q}_2(x)$$

where

- x is the voxel position in the reference space,
- \mathbf{T} is the displacement field of the transformation T with $T = \text{Id} + \mathbf{T}$,
- K_1 and K_2 are regularization kernels for each displacement field \mathbf{Q}_1 and \mathbf{Q}_2 ,
- $\lambda(x) \in [0, 1]$ is a confidence map across the image defining the trust in the displacement field \mathbf{Q}_1 versus \mathbf{Q}_2 . This confidence map is a mixture of 3D normalized Gaussian centered on each landmark in the reference space and whose variance depends on its distance to the corresponding landmark.

Thin-plate splines [Bookstein 1989] are used to extrapolate the sparse matching of landmarks to a dense displacement field \mathbf{Q}_2 . The intensity-based displacement field \mathbf{Q}_1 determined at step 1 of the minimization using a diffeomorphic registration algorithm [Hermosillo 2002] based on the mutual information. The weighted-average of a thin-plate spline transformation Q_1 and a diffeomorphic transformation Q_2 is not guaranteed to be diffeomorphic. The invertibility of the transformations is necessary for the groupwise registration scheme proposed in the following. But since displacement fields are previously regularized and weighted with the confidence map λ , as long as interactive corrections are not too large the resulting transformation T should be invertible.

The hybrid intensity and landmark-based registration is mainly used to correct errors of purely intensity-based registration. When large deformations occur, which

means large distance between corresponding landmarks, the confidence map λ of the landmark matching is too large and might influence areas where landmark correspondences are not significant. Thus, in practice, it is preferable to first minimize the distance between corresponding landmarks by performing a purely intensity-based non-linear registration of cardiac anatomies including atria and ventricles. Then when using the hybrid registration, about ten landmarks were used to correct the registration. These landmarks were mostly located where the initial purely intensity-based non-linear registration is not perfect: in the area of the atria where structures are more complex and where the constrained affine registration is not sufficient for matching of corresponding structures.

Finally, the pairwise registration results in a transformation T that is the composition of a constrained affine transformation S with a non-linear transformation.

3.2.3 Groupwise Registration

As mentioned previously, groupwise registration is not trivial since the average template image and its mapping with the subject images are interrelated. We choose the method of Guimond *et al.* [Guimond 2000] to which the interactive pairwise registration method presented previously can be easily included. We alternately build an average template image and register the subjects images to it. We first register the set of images $\{I_i\}_{i=1,\dots,N}$ to the current reference image I_{mean}^n at the step n using the pairwise registration described previously (the initial reference image I_{mean}^0 is chosen within the dataset). The resulting transformations T_i^n registering the initial images I_i to the current reference image I_{mean}^n are averaged with an arithmetic mean. In our case, the average transformations have been shown to be smooth enough and small enough to be computationally invertible. A least squares approximation of the inverse of the average transformation T_{mean}^n is computed [Cachier 2002] and applied to the current reference image I_{mean}^n which then gets closer to a barycentric geometry of the dataset (see Figure 3.6). The intensities are averaged in this new average geometry. Therefore, through the transformations T_i^n , the original geometry and intensities of each heart are taken into account in the new average heart I_{mean}^{n+1} .

One iteration can be summarized with the equation as follows:

$$I_{\text{mean}}^{n+1}(x) = \frac{1}{N} \sum_{i=1}^N I_i \circ T_i^n \circ [T_{\text{mean}}^n]^{-1}(x)$$

where

- x is the voxel position,
- I_i is the anatomical MRI of the image i ,
- I_{mean}^n is the current average anatomical MRI at the step n ,
- T_i^n is the transformation matching the current average geometry I_{mean}^n to I_i ,
- $T_{\text{mean}}^n = \frac{1}{N} \sum_{i=1}^N T_i^n$ is the average transformation at the step n .

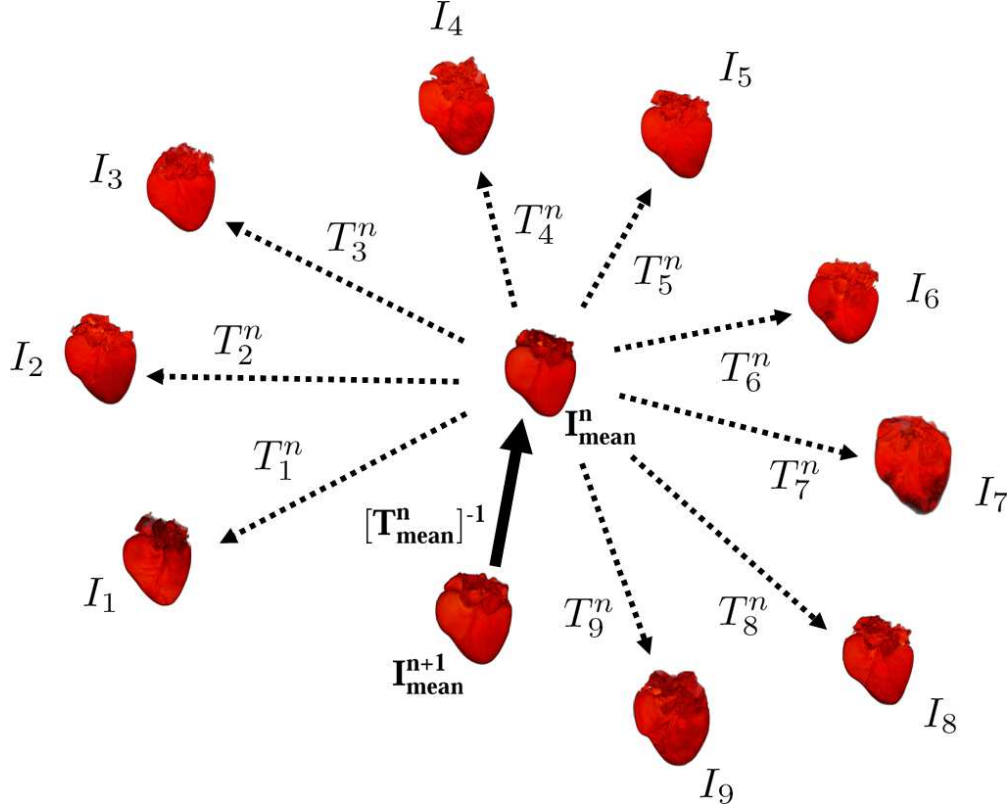


Figure 3.6: The groupwise registration of the anatomical MRI $\{I_i\}_{i=1,\dots,9}$ is adapted from the algorithm proposed by Guimond *et al.* [Guimond 2000]. This algorithm is based on an alternate registration process using the resulting average geometry I_{mean}^{n+1} as a reference for the next step. The transformations $\{T_i^n\}_{i=1,\dots,9}$ at the step n are a composition of a constrained affine transformation and a non-linear transformation as described in Section 3.2.2.

These steps are repeated using the new average heart I_{mean}^{n+1} as the reference geometry until it converges. In practice, a couple of iterations (three in our case) are sufficient to get a stable geometry. The atlas building strategy is summarized in the following Table 3.1.

Finally, the outputs of this process are an average geometry of cardiac anatomical MRI and a dense deformation field for each heart of the dataset. Then, these deformation fields can be used to transform the DT-MRI.

3.3 Transformation of Cardiac Diffusion Tensors

Since we use the unweighted image of the DT-MRI acquisition as the anatomical MRI, the DT-MRI and the anatomical MRI have the same reference frame. Furthermore image distortion induced by magnetic field eddy-current are already corrected for DT-MRI estimation. Thus, we can directly apply to the DT-MRI the deformation fields computed with anatomical MRI as detailed previously. The trans-

Table 3.1: Atlas Building Algorithm. (from [Guimond 2000])

-
- (A) Choose randomly an image I_k in the dataset as the initial atlas image I_{mean}^0
- (B) Iterate until convergence $n \leftarrow n + 1$:
- (1) Affine registration of each image I_i to the current atlas image I_{mean}^n providing affine transformation A_i^n
 - (2) Non-Linear Registration of each image I_i to the current atlas image I_{mean}^n initialized with A_i^n providing transformation T_i^n
 - (3) Average transformations providing $T_{\text{mean}}^n = \frac{1}{N} \sum_{i=1}^N T_i^n$
 - (4) Invert the average transformation T_{mean}^n
 - (5) Update the atlas image $I_{\text{mean}}^{n+1} = \frac{1}{N} \left(\sum_{i=1}^N I_i \circ T_i^n \circ [T_{\text{mean}}^n]^{-1} \right)$
-

formation of DT-MRI is more complex than anatomical MRI. A diffusion tensor is a covariance matrix (symmetric definite positive matrix) modeling the directional distribution of diffusion rates of water molecules. This directional information is linked to the local reference frame that is modified during the transformation. To describe this distribution in the new local reference frame, a transformation of the diffusion tensor is necessary.

We first consider a linear transformation A applied to the diffusion tensor field D to be transformed into the diffusion tensor field D' . A basic way to transform diffusion tensors would be to directly use the inverse of the affine transformation A to correct the directional distribution of a diffusion tensor at the voxel position x :

$$D'(x) = A^{-1} D(A(x)) A^{-1 \top}$$

Note that the transformation used to modify the diffusion tensors is the inverse of the transformation used to resample the diffusion tensor field.

This basic strategy directly transforms the symmetric definite positive matrix modeling the directional distribution of diffusion rates without considering the underlying microstructure from which results diffusion properties. The eigenvalues and eigenvectors of the diffusion tensor can be modified inconsistently with the underlying microstructure. The order of the eigenvalues and corresponding eigenvectors can be swapped such that we loose the link between the order of eigenvalues and the underlying microstructure. For instance, this would occur with non-uniform scaling.

To avoid this effect, we first make the assumption that the diffusion rates (eigenvalues) in each specific directions (eigenvectors) of the fibre structure only depend

on material properties of the underlying microstructure. In other words, we can consider that these material properties are intensive properties at our scale of observation. Warping the space does not modify the eigenvalues of the diffusion tensor and consequently their order. Thus, the original diffusion tensor and the transformed diffusion tensor have the same eigenvalues. Given two diffusion tensors with the same eigenvalues, a rotation matching the orthonormal basis of eigenvectors is sufficient to transform a diffusion tensor into the other one. In this way, the transformation of diffusion tensors can be decomposed into two steps: the resampling and the reorientation. The transformation of a diffusion tensor D into the diffusion tensor D' can be formulated as follows:

$$D'(x) = A \star D(A(x)) = R D(A(x)) R^\top$$

where

- A is the affine transformation used to resample the diffusion tensor field,
- the operator \star is the reorientation action of a linear transformation on a diffusion tensor (note that the reorientation is driven by the inverse of the resampling transformation),
- R is the rotation matrix used to reorient the diffusion tensor.

This formulation can easily be extended to any non-linear transformations T with the local linear approximation of the first derivative of its inverse ∇T^{-1} used as the linear transformation A for reorientation [Alexander 2001b].

The remaining difficulty is to define the rotation R used to reorient the diffusion tensor. Different methods have been proposed to reorient diffusion tensors. Thorough experiments are difficult to set up to validate the choice of the reorientation strategy. In our opinion, the experiments proposed in the literature [Alexander 2001b, Van Hecke 2007] are not satisfying and do not really take into account the nature of the transformation between two subjects. Thus, we propose here to compare the reorientation strategies to understand their fundamental differences and to justify their use given the registration context.

First, we describe the two commonly used reorientation strategies: the *Finite Strain* (FS) and the *Preservation of the Principal Direction* (PPD) proposed by Alexander *et al.* [Alexander 2001b]. Second, we point out their fundamental differences on a typical case of synthetic diffusion tensor field transformed by affine transformations.

3.3.1 Finite Strain (FS)

The FS consists in using the rotation component of the linear transformation to reorient the diffusion tensor. The polar decomposition of an affine transformation A can be written as follows: $A = RU$ where R is the rotation component and U a deformation component. Actually, the rotation component is the least squares approximation of the affine transformation by a rotation and has a closed-form

solution [Malvern 1969]:

$$R = (AA^\top)^{-\frac{1}{2}}A$$

In the case of the FS, the reorientation action of an affine transformation on a diffusion tensor D (whose operator is \star) is defined as follows:

$$A \star D = R_{\text{FS}}(A) D R_{\text{FS}}^\top(A)$$

where $R_{\text{FS}}(A)$ is the rotation component of the affine transformation A .

Since the reorientation of a diffusion tensor with the FS only depends on the affine transformation A , we can infer interesting properties. For instance, we propose to compare the action of the transformation on the diffusion tensor field (whose operator is \star) and the action of the transformation on the gradient of diffusion tensors (whose operator is \bullet) in the case of a global affine transformation.

Let us consider x the voxel coordinates in the original space and D the original diffusion tensor field. Respectively $x' = Ax$ and D' are their transformed values. We use here the minimal representation $\text{vec}(D)$ of a diffusion tensor $D = (D_{ij})_{i,j=1,2,3}$ to take into account the multiplicity of its off-diagonal elements [Pennec 2006]:

$$\text{vec}(D) = (D_{11} \quad \sqrt{2}D_{12} \quad D_{22} \quad \sqrt{2}D_{31} \quad \sqrt{2}D_{32} \quad D_{33})^\top \quad (3.5)$$

Thus, the standard Euclidean norm of this vector representation is equal to the standard Euclidean norm of the diffusion tensor.

The gradient $\nabla_{x'}$ in the reference frame of transformed image can be formulated as follows:

$$\nabla_{x'} \text{vec} (D'_{\text{FS}}(x')) = \nabla_{x'} \text{vec} (A \star D(A^{-1}x'))$$

$$\nabla_{x'} \text{vec} (D'_{\text{FS}}(x')) = \nabla_{x'} \text{vec} (R_{\text{FS}}(A) D(A^{-1}x') R_{\text{FS}}^\top(A))$$

As R_{FS} only depends on A that is constant over the space, we can use:

$$\nabla_{x'} = \nabla_{Ax} = A^{-1} \bullet \nabla_x$$

to derive:

$$\nabla_{x'} \text{vec} (D'_{\text{FS}}(x')) = A^{-1} \bullet \nabla_x \text{vec} (R_{\text{FS}}(A) D(x) R_{\text{FS}}^\top(A))$$

And finally:

$$A \bullet \nabla_{x'} \text{vec} (D'_{\text{FS}}(x')) = \nabla_x \text{vec} (A \star D(x))$$

The gradient of a transformed diffusion tensor field is equal to the transformed gradient of the original diffusion tensor field. Since the action of the transformation is consistent with the gradient on diffusion tensors, we expect to preserve geometric features. And more precisely we expect to preserve angular differences between neighboring eigenvectors. Thus, we can characterize the affine transformation of a diffusion tensor field with FS as a “conformal transformation” of diffusion tensor fields.

3.3.2 Preservation of the Principal Direction (PPD)

The basic idea of the PPD reorientation strategy is to come back to the underlying microstructure described by the diffusion tensor. In the case of cardiac diffusion tensors, it has been shown [Scollan 1998, Hsu 1998, Tseng 2003, Helm 2005c, Helm 2005b] that the eigenvectors are linked to the fibre and laminar sheet orientations. The primary eigenvector \mathbf{v}_1 is aligned with the fibre direction as is the tertiary eigenvector \mathbf{v}_3 with the normal direction to the laminar sheet (see Figure 3.2). Once we have a model of the underlying microstructure, we transform it through the local affine transformation. Then, from this transformed microstructure we build the transformed diffusion tensor according to the relationship between the eigenvectors and the underlying microstructure [Alexander 2001b]. Since the correlation between eigenvectors and underlying microstructure might be subject to acquisition noise, Xu *et al.* [Xu 2003] proposed an extension of the PPD where the fiber structure is statistically estimated from the voxel neighborhood.

An affine transformation can be described by a composition of basic transformations: translation, rotation, scaling and shearing. Translations and uniform scalings do not modify the orientation of the fibre structure, and the transformation of the fibre structure through rotations is obvious. Non-uniform scalings and shearings are the most problematic basic transformations to apply to the fibre structure since the amount of deformation depends on the original structure. An illustration of this dependency is shown in Figure 3.7 with the action of pure shearing on an elementary structure of cardiac fibres. The direct transformation of the original eigenvectors \mathbf{v}_i leads to the vectors $A\mathbf{v}_i$ and the final transformation deduced from the deformation of the fibre structure leads to the vector \mathbf{v}'_i .

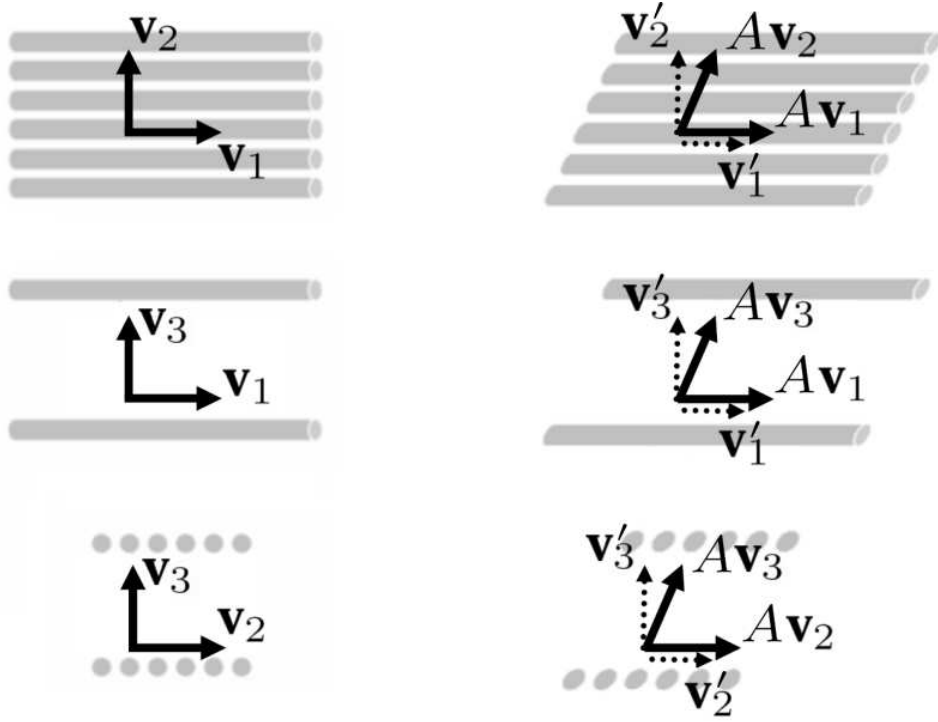
Locally, fibres are considered as a line and the affine transformation of a line is a line. Thus, the new primary eigenvector \mathbf{v}'_1 pointing in the direction of the deformed fibres is the normalized direct transformation of the primary eigenvector \mathbf{v}_1 pointing in the direction of the original fibres:

$$\mathbf{v}'_1 = \frac{A\mathbf{v}_1}{\|A\mathbf{v}_1\|}$$

Laminar sheets are considered locally plane and the image of a plane through an affine transformation is a plane. It means that these laminar sheets are locally stable approximating locally the non-linear transformation with an affine transformation. Thus, the laminar sheet is spanned by \mathbf{v}_1 and \mathbf{v}_2 and its image by $A\mathbf{v}_1$ and $A\mathbf{v}_2$. The secondary eigenvector \mathbf{v}'_2 lies in the laminar sheet plane and is orthogonal to the fibre direction by definition:

$$\mathbf{v}'_2 = \frac{A\mathbf{v}_2 - \left((A\mathbf{v}_2)^\top \mathbf{v}'_1 \right) \mathbf{v}'_1}{\|A\mathbf{v}_2 - \left((A\mathbf{v}_2)^\top \mathbf{v}'_1 \right) \mathbf{v}'_1\|}$$

The tertiary eigenvector \mathbf{v}_3 is aligned locally with the normal vector of the laminar sheet plane. The normal vector of the image of a plane through an affine transfor-



(a) Elementary cardiac fibre structure with corresponding eigenvectors \mathbf{v}_i of diffusion tensor.

(b) Elementary cardiac fibre structure and eigenvectors \mathbf{v}_i mechanically deformed with shearing transformation A .

Figure 3.7: Mechanical deformation of an elementary cardiac fibre structure (fibres and laminar sheet planes). Column (a) shows the original cardiac fibre structure and corresponding eigenvectors \mathbf{v}_i . Column (b) shows the deformed cardiac fibre structure and corresponding eigenvectors \mathbf{v}'_i (dashed arrows). The \mathbf{v}'_i correspond to the reorientation of the \mathbf{v}_i with PPD. $A\mathbf{v}_i$ are the eigenvectors directly deformed with the transformation A .

mation is given by the following expression (more details in the Appendix A):

$$\mathbf{v}'_3 = \frac{(A^{-1})^\top \mathbf{v}_3}{\|(A^{-1})^\top \mathbf{v}_3\|}$$

One can easily show that this last formulation of \mathbf{v}'_3 leads to the same result as the one proposed in [Alexander 2001b] where they build \mathbf{v}'_3 from \mathbf{v}'_1 and \mathbf{v}'_2 to obtain an orthonormal frame: $\mathbf{v}'_3 = \mathbf{v}'_1 \times \mathbf{v}'_2$. This new formulation has the advantage to be independent of the computation of the other eigenvectors and to point out the contravariant influence of the affine transformation on the tertiary eigenvector.

The three transformed eigenvectors form an orthonormal frame. Thus, the diffusion tensor is reoriented as follows:

$$A \star D = R_{\text{PPD}}(A, D) D R_{\text{PPD}}^\top(A, D)$$

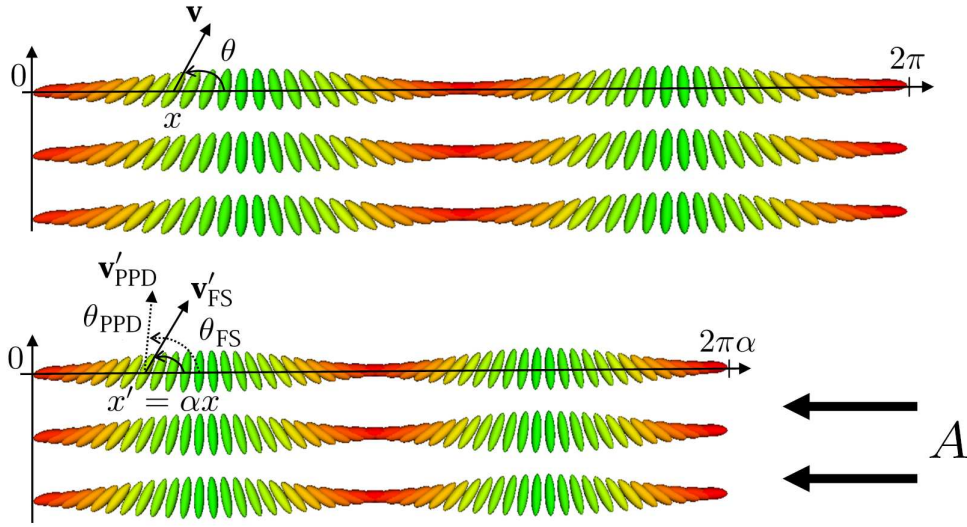


Figure 3.8: Synthetic diffusion tensor field with a sinusoidal variation of the orientation θ of the primary eigenvector \mathbf{v} along the direction of the x coordinates. The diffusion tensors are colored in red when the primary eigenvector is oriented along the direction of the x coordinates and in green along the direction of the y coordinates. As an illustration of the differences between the action of the FS and PPD reorientation strategies, a basic non-uniform scaling A (in this figure a compression $\alpha < 1$ along the x coordinates) is applied to the diffusion tensor field.

where $R_{\text{PPD}}(A, D) = V'^{\top} V$ is the rotation mapping the original eigenvectors $\{\mathbf{v}_i\}_{i=1,2,3}$ on the transformed eigenvectors $\{\mathbf{v}'_i\}_{i=1,2,3}$ respectively described by the matrices $V = [\mathbf{v}_1, \mathbf{v}_2, \mathbf{v}_3]$ and $V' = [\mathbf{v}'_1, \mathbf{v}'_2, \mathbf{v}'_3]$.

Since the PPD relies on the mechanical deformation of the underlying microstructure, it is by definition a mechanical transformation of cardiac fibre architecture that for instance occurs when the heart is deformed during the cardiac cycle.

3.3.3 Comparison of the Reorientation Strategies

Setting up a thorough experiment to validate the choice of a reorientation strategy is not trivial. Some proposed to deform a synthetic diffusion tensor field with a known deformation field [Alexander 2001b, Van Hecke 2007]. The problem in their experiment is that they rely on the deformation of the underlying structure to obtain their ground truth deformed diffusion tensor fields. Thus, they implicitly choose the case where the transformation is really a mechanical deformation. And the better results they obtain using the PPD is obvious. They also extended their experiment to real data comparing the quality of the transformation of brain DT-MRI using either the FS or the PPD. In [Alexander 2001b], results with PPD and FS were similar. But since their local affine transformations are close to a rotation, it is

normal to obtain similar results that cannot really help to conclude. Furthermore, registration is an ill-posed problem and the solution of the problem might not be unique. There might exist a different deformation field, which is a valid solution of the registration problem, that is better suited for each reorientation strategy. In [Van Hecke 2007], they investigate the registration of diffusion tensor fields with different reorientation strategy. In this way, the resulting deformation fields are optimized for each reorientation strategy. But the problem we have here is slightly different. We do not want to use diffusion tensor information in the registration process to avoid introducing a bias. So given a transformation known to register cardiac anatomies, we want to determine which reorientation strategy would be the most appropriate.

Since we believe that there is not a unique best reorientation strategy in every situation, we propose here an experimental comparison of the two reorientation strategies to better understand their fundamental differences. Without proper experiments on non-linear transformations of two different subjects, we illustrate these differences with a global affine transformation applied on synthetic data.

3.3.3.1 Affine Transformation of Synthetic Data

We have shown that the rotation computed with PPD depends on the original orientation of diffusion tensors whereas the rotation computed with the FS does not. The difference between the rotations of the two strategies exist when the local affine transformation has shearing and non-uniform scaling components. To better understand the effect of these differences, we compare the transformation of a simple synthetic diffusion tensor field transformed with a non uniform-scaling (similar results can be obtained with shearing) when using the FS and the PPD (see Figure 3.8). To simplify the calculations and to clarify the example, we only consider the primary eigenvector of the diffusion tensors in 2D. One can easily extend this study in 3D on all the eigenvectors. Let us consider the following profile of the primary eigenvector orientations that only depends on the coordinate $x \in [0, 2\pi]$:

$$\mathbf{v}(x) = \begin{pmatrix} \cos(x) \\ \sin(x) \end{pmatrix}$$

We apply the following non-uniform scaling to the vector field:

$$A = \begin{pmatrix} \alpha & 0 \\ 0 & 1 \end{pmatrix}$$

Let $\mathbf{v}'_{\text{FS}}(x') = R_{\text{FS}}(A)\mathbf{v}(x)$ be the transformed vector by the FS and let $\mathbf{v}'_{\text{PPD}}(x') = R_{\text{PPD}}(A, \mathbf{v})\mathbf{v}(x)$ be the transformed vector by the PPD with $x' = \alpha x \in [0, 2\pi\alpha]$:

$$\mathbf{v}'_{\text{FS}}(x') = \mathbf{v}\left(\frac{x'}{\alpha}\right)$$

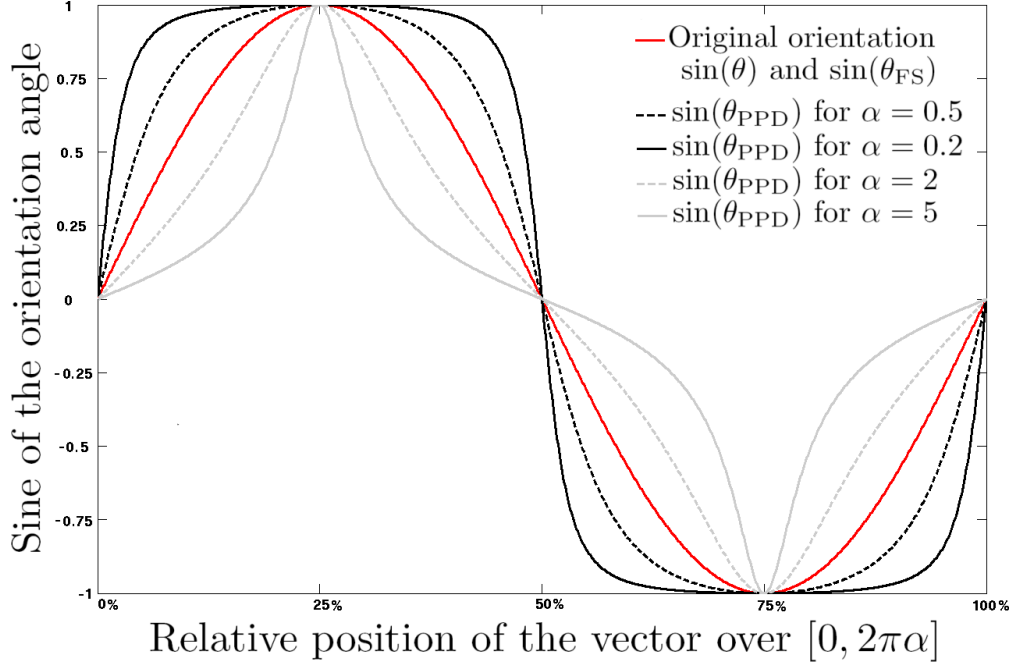


Figure 3.9: Illustration of the difference between the action of the FS and PPD reorientation strategies: sine of the orientation angles θ_{PPD} and θ_{FS} of the vector field after a non-uniform scaling transformation. The orientation angle θ is the angle between the primary eigenvector and the direction of the x coordinates as described in Figure 3.8. The original orientation is described by the red curve.

$$\mathbf{v}'_{PPD}(x') = \frac{A\mathbf{v}(\frac{x'}{\alpha})}{\|A\mathbf{v}(\frac{x'}{\alpha})\|} = \begin{pmatrix} \frac{\alpha \cos(\frac{x'}{\alpha})}{\sqrt{\alpha^2 \cos^2(\frac{x'}{\alpha}) + \sin^2(\frac{x'}{\alpha})}} \\ \frac{\sin(\frac{x'}{\alpha})}{\sqrt{\alpha^2 \cos^2(\frac{x'}{\alpha}) + \sin^2(\frac{x'}{\alpha})}} \end{pmatrix}$$

Since the polar decomposition of a non-uniform scaling does not contain any rotation component, the orientation of the vectors is not modified using the FS reorientation strategy: $R_{FS} = \text{Id}$. Thus, only a resampling of the diffusion tensor field is performed.

Results are shown in Figure 3.9. We observe that the profile of vector orientation along the direction of the x coordinates is modified in the case of the PPD strategy whereas this profile is only resampled in the case of the FS strategy. The difference between these two strategies is enhanced with the importance of the compression ($\alpha < 1$) and stretching ($\alpha > 1$). This example illustrates the mechanical effect with the PPD and the preservation of the gradient with the FS.

3.3.3.2 Choice of the Reorientation Strategy

Both reorientation strategies seem valid but each one in a different context. If we consider that there is a mechanical transformation due to the registration process

(for instance, the registration of the same heart at a different time of its cycle), we would prefer the PPD. On the other hand, if we want to preserve geometric features of the diffusion tensor field (for instance, in the case of a resampling of the heart), we would prefer the FS. We propose to rely on the three following arguments to decide which reorientation strategy is better suited for our inter-subject statistical study.

First, the FS preserves the geometric features of the diffusion tensor fields. Thus, using the FS, we can directly compare these features, especially the transmural variation of the fibre orientation which is known to be a common feature between hearts.

Second, the FS does not depend on the extraction of the eigenvectors whereas the PPD relies on a strong correlation between the eigenvectors and the underlying fibre structure. An error in the extraction of this structure (for instance, due to noise in the DT-MRI acquisition) could be propagated to the transformation of diffusion tensors and thus to the computed statistics. Thus, the interpretation of these statistics should take into account these errors on the transformation of diffusion tensors.

Third, the FS is consistent with the Log-Euclidean metric used to compute statistics that should not depend on the reference geometry. Indeed, if the reference geometry is modified, all registered diffusion tensors in a voxel of this reference geometry are transformed with respect to the same rotation. Since the Log-Euclidean metric is rotation invariant, the statistics computed in two different reference geometries are equivalent. On the contrary, since the PPD reorientation depends on the original diffusion tensor, each of the registered diffusion tensors in a given voxel are transformed with respect to a different rotation. Thus, one can easily show that statistics computed with the Log-Euclidean metric would not be equivalent in two different reference geometries.

Consequently, we think that one should prefer the FS reorientation strategy in the context of inter-subject cardiac DT-MRI registration for statistical analysis to preserve geometric features. On the other hand, since the PPD reorientation strategy is based on a mechanical deformation of the underlying microstructure, it is probably better suited to the mechanical deformations occurring when the heart is in motion.

In our study, we transform diffusion tensor fields into the same geometry to compare their statistical variability among a population. Thus, it is important to understand the meaning of the diffusion tensor fields transformation to be able to give a proper interpretation of the resulting statistics. We decided to rely on theoretical assumptions to choose the reorientation strategy. In practice, it might happen that a reorientation strategy better explains the inter-subject variability. A reorientation strategy might better model the inter-subject variability and thus might help to understand the origin of this variability. In the following chapter, we will use real data to compare the two reorientation strategies and check if a reorientation strategy provides better insights on the inter-subject variability. In other words, does a reorientation strategy better explain how the cardiac fibres are

remodeled when anatomy changes?

3.4 Statistical Analysis of Cardiac Diffusion Tensors

Once the DT-MRI are transformed into the same coordinate system, a statistical analysis of a population of diffusion tensors can be performed at each voxel. We propose to compute the first- and second-order statistics on diffusion tensors from which can be extracted relevant information about the average cardiac fibre architecture and its variability.

First, we introduce some concepts about diffusion tensor processing and especially the necessity to define a proper metric on the diffusion tensor space. The Log-Euclidean framework has been chosen to compute our statistics thanks to its fast and simple computation [Arsigny 2006].

Second, we present novel tools to extract eigenvectors and eigenvalues variability from the covariance matrix of diffusion tensors. Indeed the geometric and physical interpretation of the 6×6 covariance matrix is not straightforward. We show that the projection of this covariance matrix onto proper directions can give eigenvalues and eigenvectors variability. These tools extend previous work [Basser 2000] that computes statistics on eigenvectors after extracting them from each diffusion tensor.

3.4.1 Introduction to DT-MRI Processing

The space of diffusion tensors, also known as the space of symmetric positive definite matrices Sym_3^{+*} , is not a vector space for the common algebraic operators. For instance, this space is not stable with the scalar multiplication. The multiplication of a diffusion tensor by a negative scalar value is no more a diffusion tensor. Unfortunately, for some image processing algorithms, such as solving Partial Differential Equations (PDE) or computing statistics, this vector space structure is necessary to avoid going out of the diffusion tensor space. Thus the extension of image processing for scalar images to diffusion tensor images is not straightforward.

To overcome this absence of vector space structure, Riemannian frameworks have been developed for diffusion tensor processing [Moakher 2005, Batchelor 2005, Lenglet 2006, Pennec 2006, Arsigny 2006, Fletcher 2007, Kindlmann 2007b, Verma 2007]. Basically, the diffusion tensor space has been replaced by a regular and complete manifold endowed with a Riemannian metric. The Riemannian metric provides a theoretically grounded framework for generalizing standard image processing tools [Pennec 2006] to the diffusion tensors manifold, and more specifically for generalizing statistics [Pennec 1999] in which we are interested in this section.

3.4.1.1 Distance between Diffusion Tensors

We present here the most common distances used for diffusion tensor processing with their advantages and limitations. Figure 3.10 illustrates the differences in

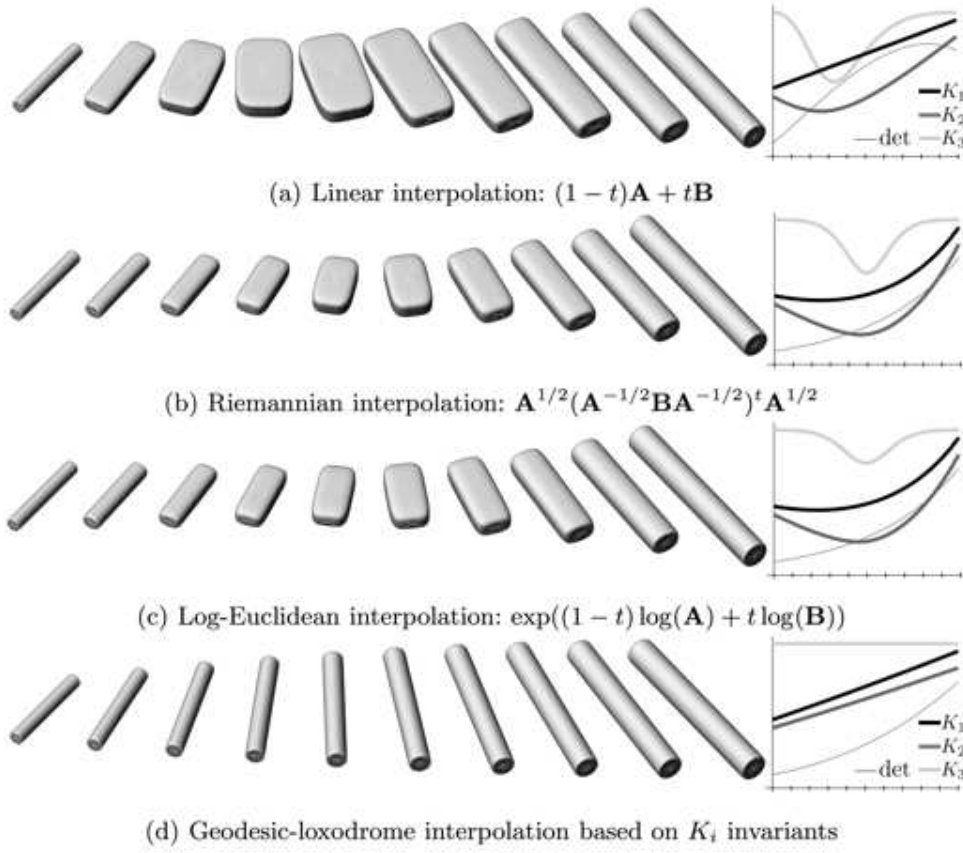


Figure 3.10: Linear interpolation of two diffusion tensors \mathbf{A} and \mathbf{B} using different frameworks (from [Kindlmann 2007b]). Plots show the determinant (\det), the trace (K_1), eigenvalue standard deviation (K_2), and the mode (K_3).

interpolation results with some of these distances.

Euclidean Distance The standard Euclidean distance between two diffusion tensors D_1 and D_2 is defined as follows:

$$\text{dist}(D_1, D_2) = \|D_1 - D_2\| = \sqrt{\text{Tr}((D_1 - D_2)(D_1 - D_2)^\top)}$$

As mentioned previously, the Euclidean framework for diffusion tensor processing has limitations when linear combination of diffusion tensors is necessary (solving PDE or compute statistics).

Cholesky Decomposition The Cholesky decomposition states that any symmetric positive-definite matrix can be written as a product of matrices $D = LL^\top$ where L is a lower triangular matrix. In this framework [Wang 2004], diffusion tensors are processed through their corresponding lower triangular matrices

that form a vector space. However, this framework does not overcome all limitations of the Euclidean calculus where diffusion tensors with null eigenvalues are still at a finite distance to any diffusion tensors.

J-Divergence The dissimilarity between two diffusion tensors can be defined with the J-divergence of the corresponding Gaussian distributions [Wang 2005]:

$$\text{dist}(D_1, D_2) = \frac{1}{2} \sqrt{\text{Tr}(D_1^{-1} D_2 + D_2^{-1} D_1) - 6}$$

It is a symmetrized version of the Kullback-Leibler divergence between distributions. The J-divergence gives an affine-invariant dissimilarity measure between tensors whose Fréchet mean has a closed form solution. But since the triangular inequality might not be verified, it cannot define a distance and thus it cannot provide a complete framework to perform diffusion tensor processing such as interpolation or gradient descent.

Affine-Invariant Riemannian Distance A geodesic distance has been defined with a Riemannian metric that has the property to be invariant to affine transformation of symmetric positive definite matrices [Moakher 2005, Batchelor 2005, Lenglet 2006, Pennec 2006, Fletcher 2007]. This property can be formulated such that $\text{dist}(D_1, D_2) = \text{dist}(A \star D_1, A \star D_2)$ where $A \star D = ADA^\top$ and leads to the definition of the affine-invariant distance:

$$\text{dist}(D_1, D_2) = \|\log(D_1^{-\frac{1}{2}} D_2 D_1^{-\frac{1}{2}})\| = \sqrt{\text{Tr}\left(\log\left(D_1^{-\frac{1}{2}} D_2 D_1^{-\frac{1}{2}}\right)^2\right)}$$

This Riemannian metric provides a valid framework for the diffusion tensor processing, and especially for computing statistics [Pennec 2006]. The completeness of the diffusion tensor manifold endowed with the Riemannian metric ensures its boundaries to be at an infinite distance of any diffusion tensor. But the Fréchet mean does not have a closed form solution and thus relies on a minimization process.

The affine-invariant property of this metric is derived from the action of an affine transformation defined as $A \star D = ADA^\top$. This action of an affine transformation on diffusion tensors has been shown in Section 3.3 not to take into account the transformation of the underlying microstructure that defines the diffusion properties. Thus, this invariance property might not be the most suited one for diffusion tensors.

Log-Euclidean Distance The Log-Euclidean framework [Arsigny 2006] relies on the fact that the matrix exponential and logarithm are two diffeomorphisms between the space of symmetric positive definite matrices and the space of symmetric matrices. The logarithms of diffusion tensors are processed in the

vector space of symmetric matrices and mapped back to the space of symmetric positive definite matrices with the exponential. From this framework can be derived the Log-Euclidean metric that is the classic Euclidean metric on the logarithm of diffusion tensors:

$$\text{dist}(D_1, D_2) = \|\log(D_1) - \log(D_2)\|$$

The Log-Euclidean framework gives a vector space structure to diffusion tensors with new algebraic operators where boundaries of diffusion tensor manifold are always at an infinite distance to any diffusion tensor. This framework also provides a closed form solution to the Fréchet mean and the property to be similarity-invariant. Moreover, results have been shown to be very similar to affine-invariant metric with simpler and faster computation.

Geodesic-Loxodromes In [Kindlmann 2007b] has been proposed a new class of interpolation paths for tensors, which explicitly preserve clinically important tensor attributes (such as mean diffusivity or fractional anisotropy) while using basic differential geometry to interpolate tensor orientation. Path integrals of tangents of geodesic-loxodromes generate a distance measure between diffusion tensors. But it is uncertain whether geodesic-loxodromes are geodesics on some six-dimensional Riemannian manifold embedded in Sym_3 .

Isomaps A manifold learning technique, called Isomap, is used to capture the underlying manifold topology of the data [Verma 2007]. A geodesic distance between diffusion tensors can be defined specifically to the manifold topology of the data.

3.4.1.2 Statistics on Diffusion Tensors

Different approaches were proposed to compute statistics on diffusion tensors. Statistics can be computed on features extracted from the diffusion tensors (for instance eigenvalues or eigenvectors) or directly on the diffusion tensor itself taken as a whole. Computing statistics on scalar values extracted from a diffusion tensor (eigenvalues, fractional anisotropy, or others detailed in [Basser 1996]) has the advantage to rely on standard statistical tools.

Using features of higher dimension such as eigenvectors might be more convenient for the interpretation of results. The sign ambiguity of the eigenvectors is a problem when computing statistics in the linear Euclidean space of vectors. To raise this ambiguity, Basser and Pajevic [Basser 2000] proposed to compute statistics on the second-order dyadic tensor $\mathbf{v}_i \mathbf{v}_i^\top$ of the primary eigenvector \mathbf{v}_i . The scatter matrix S is defined as the average dyadic tensor of a population of N eigenvectors \mathbf{v}^k :

$$S = \frac{1}{N} \sum_{k=1}^N \mathbf{v}^k \mathbf{v}^{k\top} \quad (3.6)$$

The eigenvalues s_1 , s_2 , and s_3 of the scatter matrix S describe the distribution of vectors in spherical coordinates. The eigenvectors \mathbf{s}_1 , \mathbf{s}_2 , and \mathbf{s}_3 describe the orientations of this distribution. The principal eigenvector \mathbf{s}_1 of the scatter matrix corresponds to the average eigenvector $\bar{\mathbf{v}}$ and the associated principal eigenvalue s_1 quantifies the coherence around this average orientation. This eigenvalue s_1 can be related to the variance $\sigma^2 = 1 - s_1$ that is the squared radius of the cone of uncertainty around a vector having a unit length. From this eigenvalue, Basser and Pajevic [Basser 2000] defined the dispersion measure $\sqrt{\frac{1 - s_1}{2s_1}}$. This dispersion measure has also been used to define the dyadic coherence κ [Jones 2002]:

$$\kappa = 1 - \sqrt{\frac{1 - s_1}{2s_1}}$$

This statistical analysis of dyadic tensors is well-suited in brain DT-MRI applications where mainly the primary eigenvector has meaningful information. For instance, the scatter matrix has been used to study background noise of diffusion tensor field [Basser 2000], to study the fibre orientation dispersion in a population of brain [Jones 2002], to evaluate directional fibre organization and the interhemispheric symmetry of the brain [Wu 2004], and to perform a statistical test to know whether two groups of subjects have the same mean direction [Schwartzman 2005].

Statistics can also be computed directly on the whole diffusion tensor without extracting any feature. For instance, a brain DT-MRI atlas was built in [Jones 2002] by computing the mean, median and mode of diffusion tensors. The normalized scatter measure \bar{S}_2 describing a global dispersion of diffusion tensors is also computed:

$$\bar{S}_2^2 = \frac{\frac{1}{N-1} \sum_{i=1}^N \|D_i - \bar{D}\|^2}{\|\bar{D}\|^2}$$

where

- D_i are the diffusion tensors of the population,
- $\bar{D} = \frac{1}{N} \sum_{i=1}^N D_i$ is the Euclidean average diffusion tensor.

But statistics are computed with a Euclidean metric that does not take into account the structure of the diffusion tensor manifold. Furthermore, the dispersion of fibre orientation is computed from the average of the dyadic tensors whereas the atlas is built from the average diffusion tensor. The statistical analysis of fibre orientation and the statistical analysis of diffusion tensors are not consistent. First and second-order statistics that compute an average diffusion tensor and a covariance matrix of diffusion tensors with a proper metric would provide a more valid and consistent framework. But still second-order statistics are limited to a scalar value describing the global dispersion of diffusion tensors or a scalar value describing the global dispersion of the first eigenvector orientation. More detailed description of

the high dimensional diffusion tensor dispersion would be particularly well-suited for cardiac DT-MRI whose all eigenvectors are necessary to study the cardiac fibre architecture. The methodology presented with the dyadic tensors could have been used to quantify each eigenvector variability independently as performed with the primary eigenvector in brain DT-MRI. But this would not take into account the fact that eigenvectors are linked by forming an orthonormal basis. We propose in the following to refine this description of dispersion based on the analysis of the covariance matrix of diffusion tensors.

3.4.2 Log-Euclidean Mean and Covariance

Owing to its simplicity and its low computational time, we chose the Log-Euclidean framework [Arsigny 2006] to compute statistics on the diffusion tensor manifold. For clarity of the notations in the remainder, we call D_i the diffusion tensor fields transformed to the average atlas geometry and interpolated with the Log-Euclidean metric. The mean \bar{D}_{\log} of the transformed diffusion tensor fields D_i and its corresponding unbiased covariance matrix field Σ [Pennec 2006] in the Log-Euclidean space are computed at each voxel x of the average geometry:

$$\bar{D}_{\log}(x) = \exp \left(\frac{1}{N} \sum_{i=1}^N \log(D_i(x)) \right)$$

$$\Sigma(x) = \frac{1}{N-1} \sum_{i=1}^N \text{vec}(\Delta D_i(x)) \text{vec}(\Delta D_i(x))^{\top}$$

where

- N is the size of the dataset,
- $\text{vec}(\Delta D_i)$ is the minimal representation of $\Delta D_i = \log(D_i) - \log(\bar{D}_{\log})$ as previously defined by Equation 3.5 in Section 3.3.

Thus, the standard Euclidean norm of this vector representation is equal to the standard Euclidean norm of the diffusion tensor.

3.4.3 A New Analysis of the Diffusion Tensor Covariance Matrix

We define the norm of the covariance matrix Σ as $\sqrt{\text{Tr}(\Sigma)}$ which is actually the square root of the unbiased mean square distance of the samples to the mean diffusion tensor:

$$\text{Tr}(\Sigma) = \frac{1}{N-1} \sum_{i=1}^N \|\Delta D_i\|^2 = \frac{1}{N-1} \sum_{i=1}^N \text{vec}(\Delta D_i)^{\top} \text{vec}(\Delta D_i)$$

Since the covariance matrix is formulated in the Log-Euclidean space, its norm is homogeneous to a ratio quantifying the relative variability of the whole diffusion tensor. This can be related to the normalized scatter measure \bar{S}_2 computed in the Euclidean space:

$$\overline{S}_2^2 = \frac{\frac{1}{N-1} \sum_{i=1}^N \|D_i - \overline{D}\|^2}{\|\overline{D}\|^2}$$

We are interested in further details about the origin of the variability of the whole diffusion tensor within the population. We propose here new efficient tools to extract the variability of the eigenvalues and eigenvectors around their mean from the covariance matrix of diffusion tensors. The basic idea is to project the covariance matrix onto the directions given by an appropriate orthonormal basis $\{W_i\}_{i=1,\dots,6}$ of the tangent space of the diffusion tensors manifold at the mean diffusion tensor (see Appendix B for more details):

$$\begin{aligned} W_1 &= \mathbf{v}_1 \mathbf{v}_1^\top & W_4 &= \frac{1}{\sqrt{2}}(\mathbf{v}_3 \mathbf{v}_2^\top + \mathbf{v}_2 \mathbf{v}_3^\top) \\ W_2 &= \mathbf{v}_2 \mathbf{v}_2^\top & W_5 &= \frac{1}{\sqrt{2}}(\mathbf{v}_1 \mathbf{v}_3^\top + \mathbf{v}_3 \mathbf{v}_1^\top) \\ W_3 &= \mathbf{v}_3 \mathbf{v}_3^\top & W_6 &= \frac{1}{\sqrt{2}}(\mathbf{v}_2 \mathbf{v}_1^\top + \mathbf{v}_1 \mathbf{v}_2^\top) \end{aligned}$$

where the \mathbf{v}_i are the sorted eigenvectors of the mean diffusion tensor.

This orthonormal basis, used here for the statistical analysis of a population of diffusion tensors, has also been used for the decomposition of the spatial gradient of a diffusion tensor field [Kindlmann 2007a]. They also proposed other decompositions to extract the gradient of other diffusion tensor features based on eigenvalues (such as the trace, the determinant or the fractional anisotropy). These decompositions could also be applied to the covariance matrix of diffusion tensors in order to get the population variability of these features. Since mainly eigenvectors variability is important to study cardiac fibre architecture, we will not develop it here.

3.4.3.1 Eigenvalues Variability

Let us consider d_i the eigenvalues of \overline{D}_{\log} and $\lambda_i = \log(d_i)$ the eigenvalues of \overline{D}_{\log} in the log-space. We call $\delta\lambda_i$ the deviation of the eigenvalues λ_i about their mean in the log-space. Their variances $E(\delta\lambda_i^2)$ can be formulated as the projection of the covariance matrix onto the directions of the $\{W_i\}_{i=1,2,3}$ (see Appendix B):

$$E(\delta\lambda_i^2) = \mathbf{vec}(W_i)^\top \Sigma \mathbf{vec}(W_i)$$

Since $\delta d_i = d_i \delta\lambda_i$ at the first order, these variances can easily be linked to the relative variability of eigenvalues in the Euclidean space:

$$E(\delta\lambda_i^2) = \frac{E(\delta d_i^2)}{d_i^2}$$

The absolute variance of the eigenvalues in the Euclidean space can also be directly derived from the covariance matrix Σ :

$$E(\delta d_i^2) = d_i^2 E(\delta\lambda_i^2) = d_i^2 \mathbf{vec}(W_i)^\top \Sigma \mathbf{vec}(W_i)$$

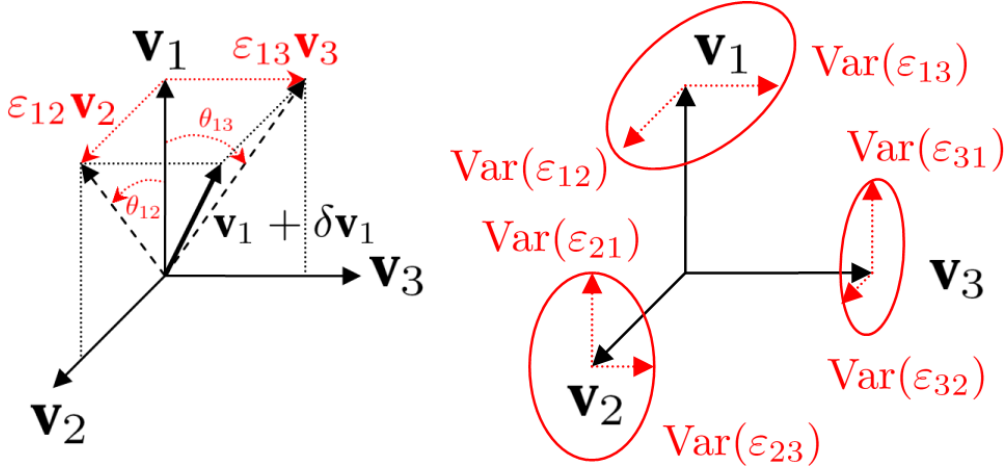


Figure 3.11: [Left] Increment $\delta\mathbf{v}_1$ of the primary eigenvector about its average \mathbf{v}_1 . [Right] Orientation variability of the eigenvectors described by an ellipsoidal cone of uncertainty.

3.4.3.2 Eigenvectors Variability

Let us consider ε_{ij} the coordinates of the deviation $\delta\mathbf{v}_i$ of the eigenvectors \mathbf{v}_i in the frame of the mean eigenvectors. These coordinates correspond to the tangent $\tan(\theta_{ij})$ of the angle between the mean eigenvector \mathbf{v}_i and the deviated eigenvector in the direction of \mathbf{v}_j (see Figure 3.11). Furthermore, it can be shown that $\varepsilon_{ij} = -\varepsilon_{ji}$. The projections of the covariance matrix Σ onto the $\{W_i\}_{i=4,5,6}$ are the rotation variability of the coupled orthonormal vectors $(\mathbf{v}_2, \mathbf{v}_3)$, $(\mathbf{v}_3, \mathbf{v}_1)$ and $(\mathbf{v}_1, \mathbf{v}_2)$ respectively around \mathbf{v}_1 , \mathbf{v}_2 and \mathbf{v}_3 (see Appendix B for more details):

$$\begin{aligned} E(\varepsilon_{23}^2) &= \frac{1}{2(\lambda_2 - \lambda_3)^2} \mathbf{vec}(W_4)^\top \Sigma \mathbf{vec}(W_4) \\ E(\varepsilon_{13}^2) &= \frac{1}{2(\lambda_1 - \lambda_3)^2} \mathbf{vec}(W_5)^\top \Sigma \mathbf{vec}(W_5) \\ E(\varepsilon_{12}^2) &= \frac{1}{2(\lambda_1 - \lambda_2)^2} \mathbf{vec}(W_6)^\top \Sigma \mathbf{vec}(W_6) \end{aligned}$$

The advantage of this formulation compared to previous works [Basser 2000, Jones 2002, Wu 2004, Schwartzman 2005] where they study independently each eigenvector \mathbf{v}_i through their corresponding dyadic tensor $\mathbf{v}_i\mathbf{v}_i^\top$, is to get the eigenvectors variability knowing that they are coupled to form an orthonormal frame. It means that when an eigenvector is changing, the others are following this change such that they still form an orthonormal basis.

These orientation variances are dependent on the distance between the eigenvalues. When two eigenvalues are close to each other, the associated eigenvectors are not well defined. Thus, high variances on eigenvectors may correspond to two different situations: either a high variability of well defined eigenvectors, or a situation where eigenvectors are not well defined. On the contrary, low variances have a unique interpretation: the eigenvectors are well defined and their variability is low.

This dependence on the definition of the eigenvectors is not specific to our methodology since the one developed by [Basser 2000] needs also to extract the eigenvectors to build their corresponding dyadic tensors. The main difference between the two approaches lies in the order of the computation of statistics. The dyadic tensor approach first extract the eigenvectors before computing their statistics whereas in our method the tensor statistics are first computed before extracting the eigenvectors. Thus, in our framework, we can preserve the coupling between eigenvectors when computing statistics.

From those three variances $E(\varepsilon_{ij}^2)$, we can describe the variability of each eigenvector with an ellipsoidal cone of uncertainty around that eigenvector (see Figure 3.11). This is in contrast to the dyadic coherence κ used in brain population analysis [Jones 2002] to assess the orientation dispersion around an average eigenvector $\bar{\mathbf{v}}_i$ with a circular cone of uncertainty. A complete analysis of the scatter matrix could also lead to a more complex cone of uncertainty but would still not take into account the orthonormality between eigenvectors.

3.5 Conclusion

In this chapter, we presented a framework for the construction and analysis of diffusion tensors atlas. First, we presented how to perform a groupwise registration of cardiac anatomies with interactive guidance. Second, we gave insights on the fundamental differences between *Finite Strain* (FS) and *Preservation of the Principal Direction* (PPD) reorientation strategies. The FS is more suited for preserving geometric features of diffusion tensor fields, whereas the PPD is more suited when the deformation field correspond to a mechanical deformation. Third, we proposed novel complete and consistent tools for the statistical analysis of a population of diffusion tensors. These tools are consistent by using Riemannian metric on the diffusion tensors manifold and complete by computing the covariance matrix of the whole diffusion tensors that can be decomposed into eigenvalues and eigenvectors variability. In this way, we proposed a new description of the eigenvectors variability. Instead of measuring the variability of each eigenvector independently, we measure the variability of pairs of eigenvectors which takes into account the orthonormality between eigenvectors. We obtain an anisotropic description of their variability that is particularly well-suited for the statistical analysis of cardiac fibre architecture.

CHAPTER 4

A CANINE CARDIAC DT-MRI ATLAS

Contents

4.1	Introduction	65
4.2	Canine DT-MRI Atlas and Intra-Species Variability	67
4.2.1	Data Acquisition	67
4.2.2	Pre-Processing Data	67
4.2.3	Statistical Analysis	68
4.2.4	Reorientation Strategies and Inter-Subject Variability	75
4.3	Atlas Comparison with Other Models	76
4.3.1	Inter-Species Comparison with Human Data	76
4.3.2	Comparison with Synthetic Models	80
4.4	Conclusion	84

4.1 Introduction

As presented in Chapter 2, the cardiac fibre architecture, a complex arrangement of myofibres [Streeter 1979] bounded to each other to form laminar sheets [LeGrice 1995a], plays an essential role in defining the electrical and mechanical behavior of the heart [Rijcken 1999, Costa 1999, Costa 2001, Arts 2001, Hooks 2007]. Mathematical modeling of the cardiac fibre architecture and its variability is important to better understand physiological principles and to construct computational models of the heart [LeGrice 2001, Nash 2001, Hunter 2003, Ayache 2004, Sachse 2004, Smith 2004, Sermesant 2006a]. However, the *in vivo* imaging of the cardiac fibre architecture at high resolution is still considered to be infeasible in the near term because of heart motion and limitations in current imaging techniques [Reese 1995, Tseng 1999, Dou 2002, Dou 2003, Gamper 2007]. But still some studies have shown the interest of low resolution acquisitions for clinical applications [Wu 2006, Wu 2009]. Therefore, modeling of the cardiac fibre architecture and its variability on *ex vivo* data is particularly important. For instance, the fibre architecture model can be used to simulate the electrical and mechanical functions of the heart for planning patient-specific therapies [Sermesant 2006b, Sermesant 2008,

Moireau 2008, Reumann 2007, Plank 2008, Romero 2008, Reumann 2008] as opposed to experiments on electrical parameter estimation with *ex vivo* hearts where acquisition of DT-MRI is available [Pop 2008, Relan 2009].

Until recently, the modeling of the cardiac fibre architecture mostly came from studies of gross dissections and histological slices [Streeter 1979, Nielsen 1991]. They revealed the common features between species such as the transmural variation of the fibre and laminar sheet orientations parametrized by the inclination angle (also known as elevation angle) and the intersection angle [LeGrice 1995a]. However, the definition of these angles was limited by the 2D nature of histological slices, whose accurate reconstruction in 3D is not straightforward [Pitiot 2006]. Measurements of fibre architecture have been eased by the use of diffusion tensor magnetic resonance imaging (DT-MRI) [Basser 1994, Hsu 2001]. Indeed, a correlation between the cardiac fibre structure and diffusion tensors has been demonstrated: the primary eigenvector of the diffusion tensor is locally aligned with the fibre direction [Scollan 1998, Hsu 1998, Holmes 2000] as is the tertiary eigenvector with the laminar sheet normal [Tseng 2003, Helm 2005c]. Thus, DT-MRI provides directly a 3D description of the fibre architecture in a shorter time but at a lower resolution compared to histological studies. In the past years several authors have performed studies on the variability of fibre [Geerts 2002, Helm 2005a, Sundar 2006] and laminar sheet [Helm 2005c, Helm 2005b, Geerts 2002, Helm 2005a, Gilbert 2007] orientations using DT-MRI. They have been so far limited to features extracted from diffusion tensors such as scalar values (for instance, inclination and intersection angles [Helm 2005c, Helm 2005b, Gilbert 2007]) or vector values (primary eigenvector [Sundar 2006, Garcia-Barnes 2009] only describing the fibre orientation). From these studies, different models of the cardiac fibre architecture were proposed and used for electromechanical simulations: a synthetic model based on general observations of the common features in mammalian hearts [LeGrice 1997], a model based on the 3D reconstruction of the fibre orientation of a canine heart from histological studies [Nielsen 1991], and a single DT-MRI acquisition of an *ex vivo* canine heart [McCulloch 1998]. These models are either too generic and simplified or too specific to accurately describe the detailed anatomy and its inter-subject variability. To improve these models, a framework to build very high resolution 3D models of the cardiac fibre architecture from histological studies has been proposed [Plank 2009].

We propose here a new approach that differs from previous studies on two points: a population of cardiac DT-MRI is used to compute a statistical model and statistics are directly computed on diffusion tensors that contain the whole fibre structure information. The following preliminary studies try to bridge the gap between statistical models, synthetic models and patient-specific models. First, we use the framework described in Chapter 3 to build a statistical atlas of cardiac fibre architecture from a small database of nine canine *ex vivo* DT-MRI acquisitions. An average cardiac DT-MRI¹ and its corresponding covariance matrix are computed to provide an average cardiac fibre architecture and its variability within a popu-

¹<http://www-sop.inria.fr/asclepios/data/heart>

lation. They show the good inter-species stability of fibre orientation as opposed to the variability of laminar sheet orientation. Second, we proceed to an inter-species comparison between the canine hearts and a human heart whose *ex vivo* DT-MRI acquisition at high resolution is rare. Moreover, since *in vivo* acquisition of high resolution cardiac DT-MRI is made difficult by heart motion, it provides a preliminary evaluation of the relevance to use a canine heart model for clinical applications. Finally, we compare this atlas with a synthetic model of mammalian hearts [LeGrice 2001, Sermesant 2006a] to evaluate the relevance of the simplifications made when building an analytical description of the fibre orientation.

4.2 Canine DT-MRI Atlas and Intra-Species Variability

4.2.1 Data Acquisition

We used a DT-MRI dataset of *ex vivo* fixed normal hearts (9 canine from beagle dogs and 1 human) acquired by the Center of Cardiovascular Bioinformatics and Modeling (CCBM) at the Johns Hopkins University [Helm 2005a] and available on the internet². Each heart was placed in an acrylic container filled with Fomblin, a perfluoropolyether (Ausimon, Thorofare, NJ). Fomblin has a low dielectric effect and minimal MR signal thereby increasing contrast and eliminating unwanted susceptibility artifacts near the boundaries of the heart. The long axis of the hearts were aligned with the z-axis of the scanner. A 3D fast spin echo (FSE) MRI sequence is used to acquire diffusion weighted images (DWI) in the short-axis plane with a 3D fast spin echo (FSE) MRI sequence with a 4-element knee phased array coil on a 1.5 T GE CV/i MRI Scanner (GE, Medical System, Wausheka, WI) using a gradient system (from 14 to 28 gradients) with 40 mT/m maximum gradient amplitude and a 150 T/m/s slew rate. The acquisition resolution of the images are around $0.3 \times 0.3 \times 0.9 \text{ mm}^3$ per voxel. The temperature during acquisition was different from one heart to another in a range from 18 to 25°C. The sequence description and acquisition process are more detailed in [Helm 2005a].

4.2.2 Pre-Processing Data

We first extract the heart from background noise by thresholding the Log-Euclidean norm of the diffusion tensors. The histogram of the trace of the diffusion tensors shows that there is an important dispersion which is not necessarily due to an intrinsic variability between hearts (see Figure 4.1). For instance, the temperature of acquisition can be different. We perform a global normalization of the mean value of the diffusion tensors norm to minimize the influence of this dispersion. Thus, the inter-subject statistical analysis of the eigenvalues will mostly provide an information about the dispersion of the diffusion rates variability over the space. But to obtain realistic averaged diffusion rates in the atlas, we scale the average of

²http://gforge.icm.jhu.edu/gf/project/dtmri_data_sets/

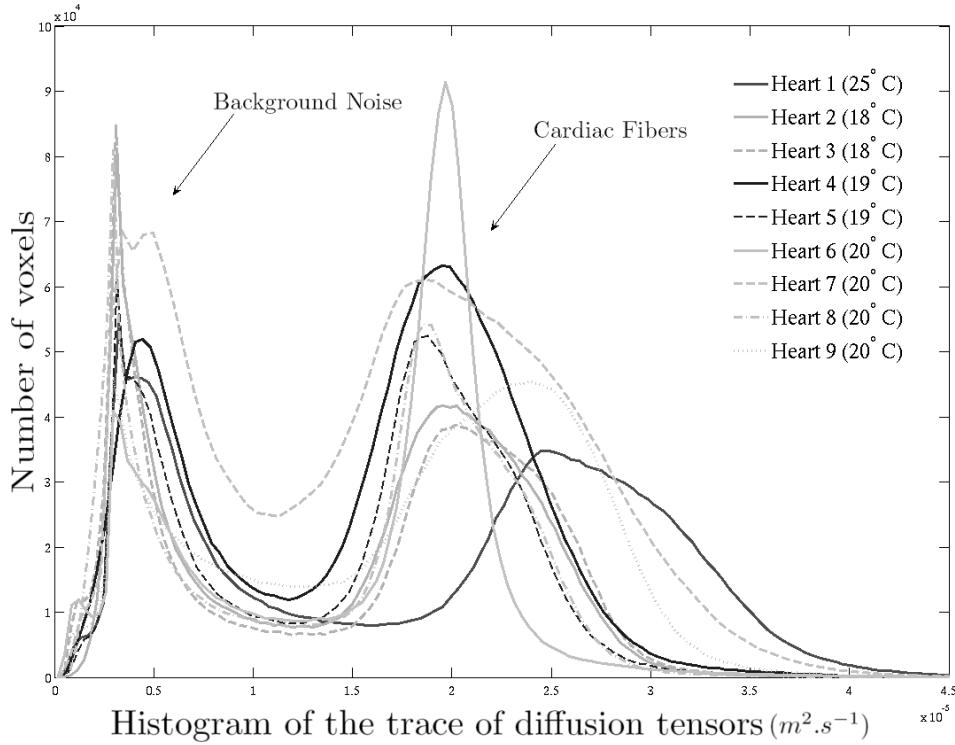


Figure 4.1: Histograms of the trace of the diffusion tensors in each heart acquired at different temperatures. The DT-MRI are normalized to better capture the intrinsic variability between hearts.

normalized DT-MRI with the Log-Euclidean mean (which is the geometric mean in a one dimension space) of all the normalization factors.

4.2.3 Statistical Analysis

We applied the framework presented in Chapter 3 to the dataset of nine canine hearts presented previously. We obtain an average geometry (see Figure 4.2) and a cardiac DT-MRI atlas \bar{D}_{\log} whose smoothness is suited for fibre tracking (see Figure 4.3). The covariance matrix of diffusion tensors Σ is computed at each voxel of the DT-MRI atlas. In Figure 4.4, we can observe its norm $\sqrt{\text{Tr}(\Sigma)}$ that measures the population variability of the whole diffusion tensor with a single scalar value. It shows a global stability of the compact myocardium and several variable regions, such as the RV and LV endocardial apices where the fiber structure is probably less organized. Some other variabilities at the surface of the heart are also probably due to acquisition artifacts (partial volume effect) and registration errors. The histogram of the norm of the covariance matrix (see Figure 4.5) shows an average variability of the whole diffusion tensor of around 10%.

In order to have a better interpretation of this covariance matrix and to understand the origin of the variabilities, we project it onto the orthonormal basis

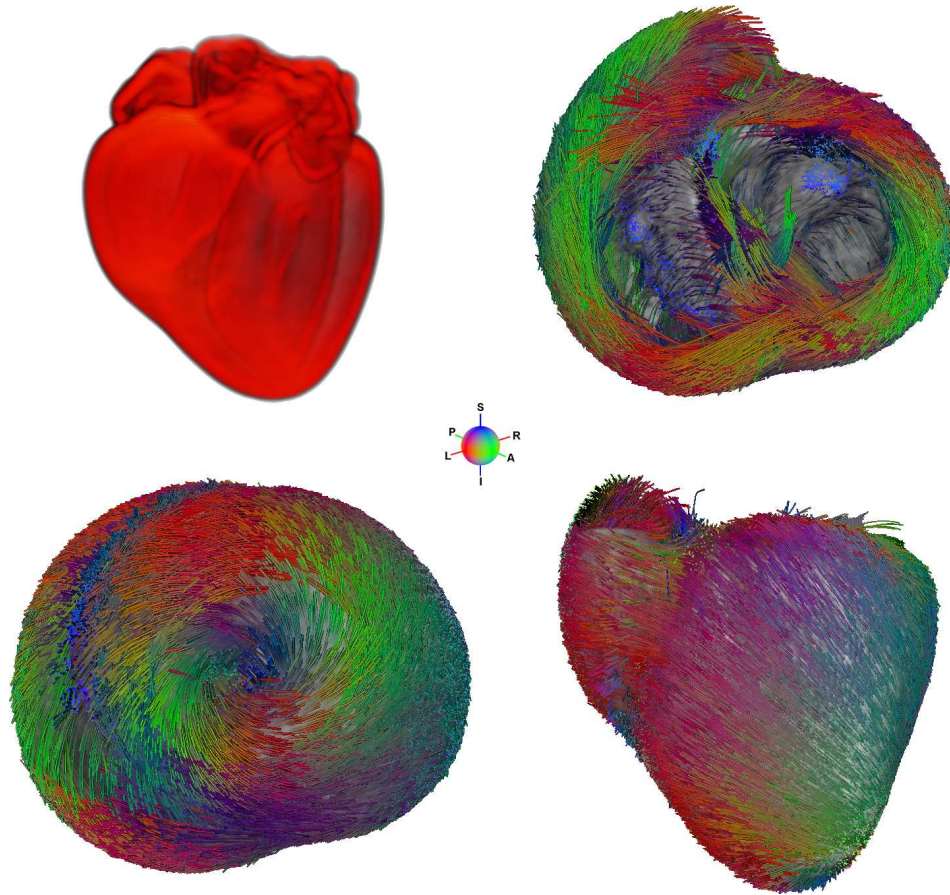
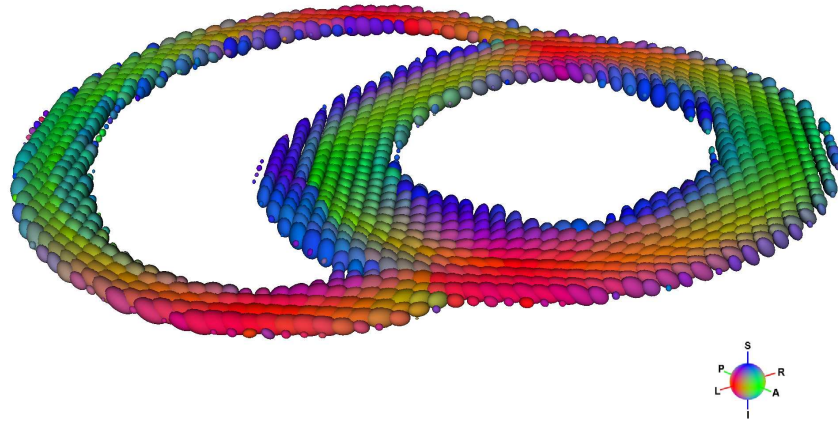
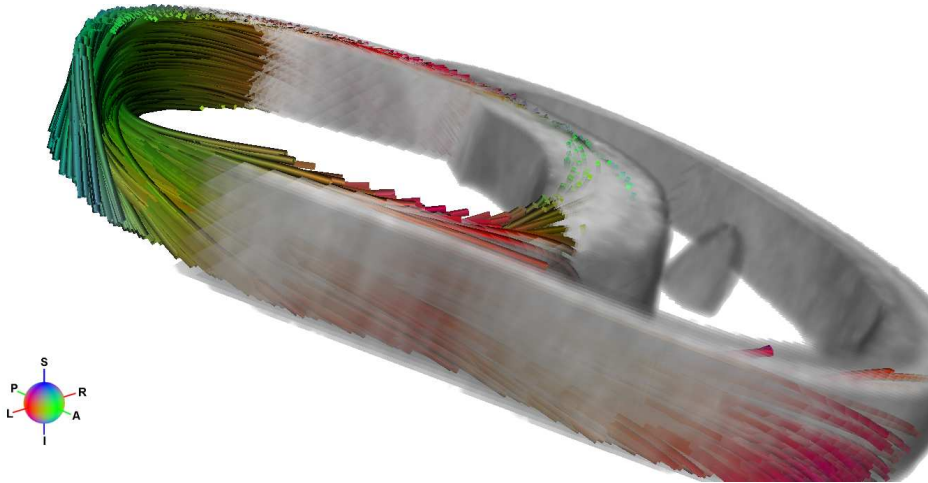


Figure 4.2: [*Upper Left*] Average geometry from the anatomical MRI. [*Others*] Top (*Upper Right*), side (*Lower Right*) and bottom (*Lower Left*) views of fiber tracking computed on the average DT-MRI. The colors describe the orientation of the primary eigenvector according to the color sphere (visualization and tensor processing were performed with MedINRIA available at <http://www-sop.inria.fr/asclepios/software/MedINRIA/>). Atlas data are available on the internet at <http://www-sop.inria.fr/asclepios/data/heart>.



(a) Smooth DT-MRI Atlas



(b) Fibre tracking showing transmurial variation of fibre orientation.

Figure 4.3: Short-axis views of atlas.

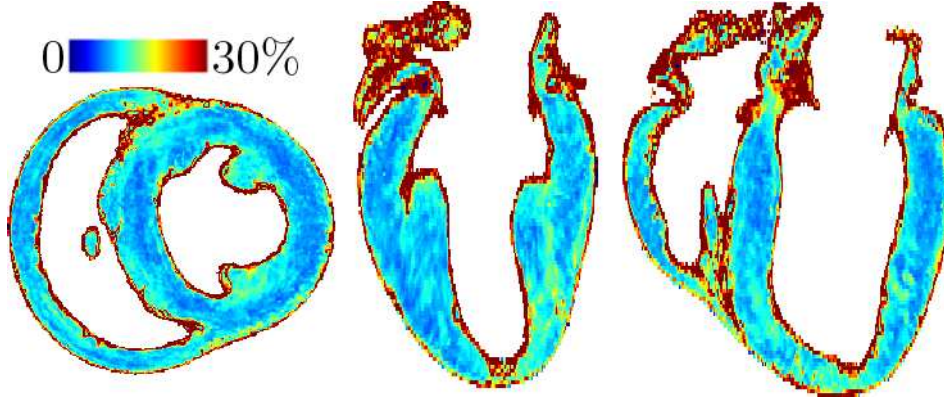


Figure 4.4: Global variability $\sqrt{\text{Tr}(\Sigma)}$ (homogeneous to a ratio and expressed as a percentage) of the whole tensor in three different orthogonal views: a short axis view and 2 long axis views.

$\{W_i\}_{i=1,\dots,6}$ of the tangent space at the mean diffusion tensor. In Figure 4.6, we can observe the spatial distribution of the variability of the eigenvalues. The percentages of variability of the 1st, 2nd and 3rd eigenvalues are mostly lower than 10% in the compact myocardium (see Figure 4.5). The variabilities of the diffusion rates are homogeneous over the heart and stable over the population.

Extracting the variability of the eigenvectors orientation is important to evaluate the variability of the myocardial fiber architecture. As shown in Figures 4.5 and 4.7, the mode of the standard deviations are 7.9 and 7.7 degrees for the two rotations around the secondary and tertiary eigenvectors in the planes containing the primary eigenvector. These two values are to be related to the dispersion of the fiber orientation that appears to be consistent within the population.

The orientation of the laminar sheets described by the rotation of the plane $\text{Span}(\mathbf{v}_2, \mathbf{v}_3)$ around \mathbf{v}_1 shows a much higher mode of the standard deviation with 22.7 degrees. Mostly located in the sub-epicardium and sub-endocardium of the left ventricle, these high variabilities of the laminar sheet orientations could be due to the presence of two populations of symmetric laminar sheets in the same heart [Helm 2005a]. The existence of these two populations was explained as the optimal configurations of the fibers to maximize the systolic shear [Arts 2001]. Second, since the secondary and tertiary eigenvalues are closer one to each other than to the primary eigenvalue, we can expect to have a low confidence in their definition. But a low confidence in their definition reveals either the absence of laminar sheet structure or the presence of crossing laminar sheets in the voxel. Beside these high variabilities in the sub-epicardium and sub-endocardium, the laminar sheet orientations are still globally less consistent within the population than the fiber orientation.

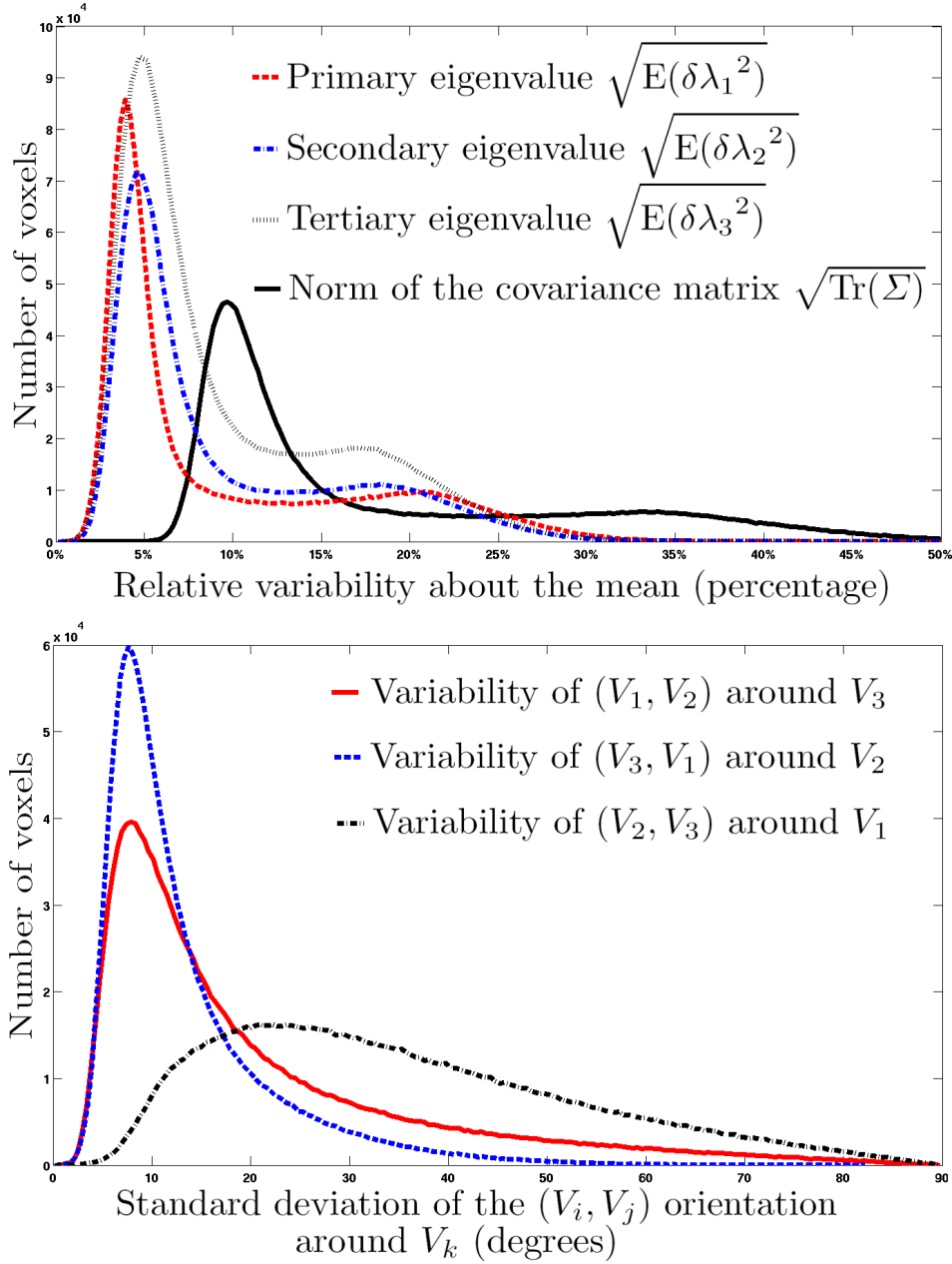


Figure 4.5: [First Row] Histograms of the global variability $\sqrt{\text{Tr}(\Sigma)}$ of the whole diffusion tensor (homogeneous to a ratio and expressed as a percentage) and the variability of the primary, secondary and tertiary eigenvalues in the Log-Euclidean space $\{\sqrt{E(\delta\lambda_i^2)}\}_{i=1,2,3}$ which are also the relative variability of the eigenvalues in the Euclidean space. [Second Row] Histograms of the standard deviations of the (V_1, V_2) frame orientation around V_3 , the (V_3, V_1) frame orientation around V_2 and the (V_2, V_3) frame orientation around V_1 eigenvectors (angles in degrees).

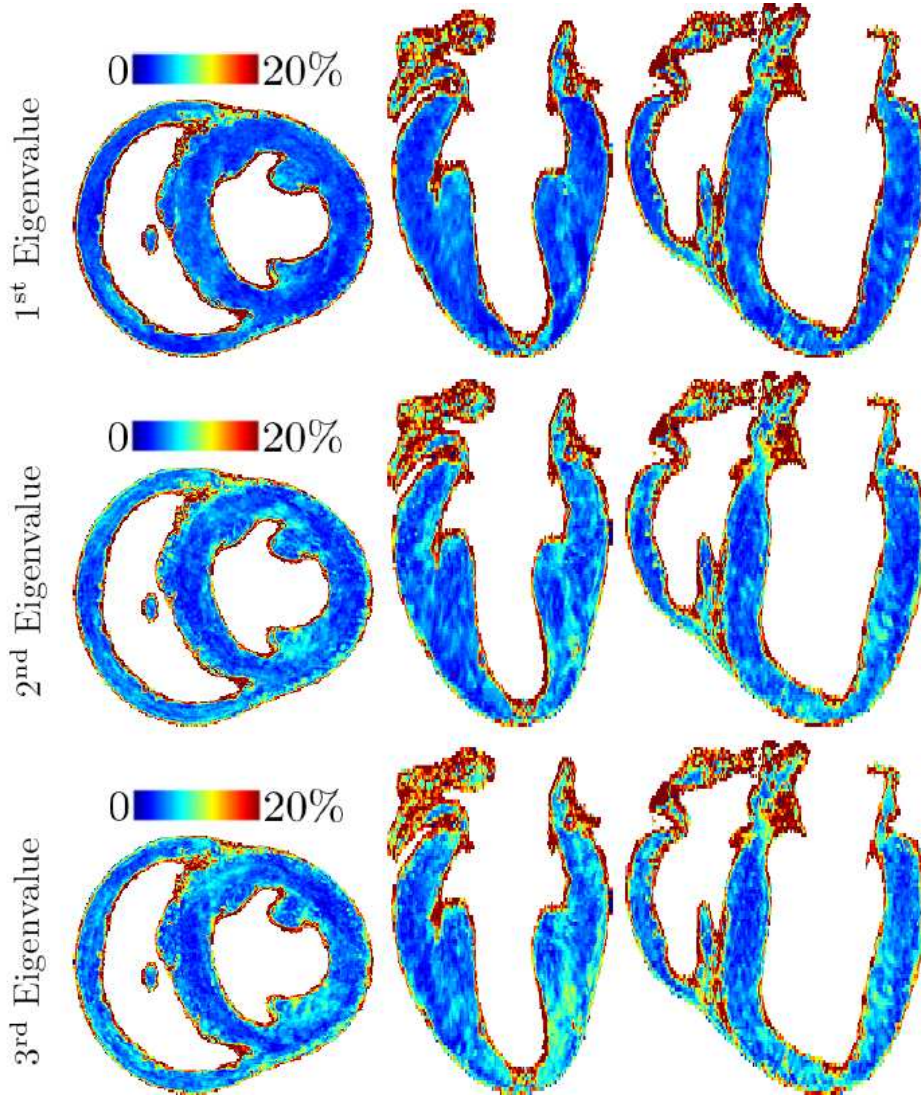


Figure 4.6: Relative variabilities of the primary, secondary and tertiary eigenvalues $\{\sqrt{E(\delta\lambda_i^2)}\}_{i=1,2,3}$ about their respective mean. These variabilities are shown in three different orthogonal views: a short axis view and 2 long axis views.

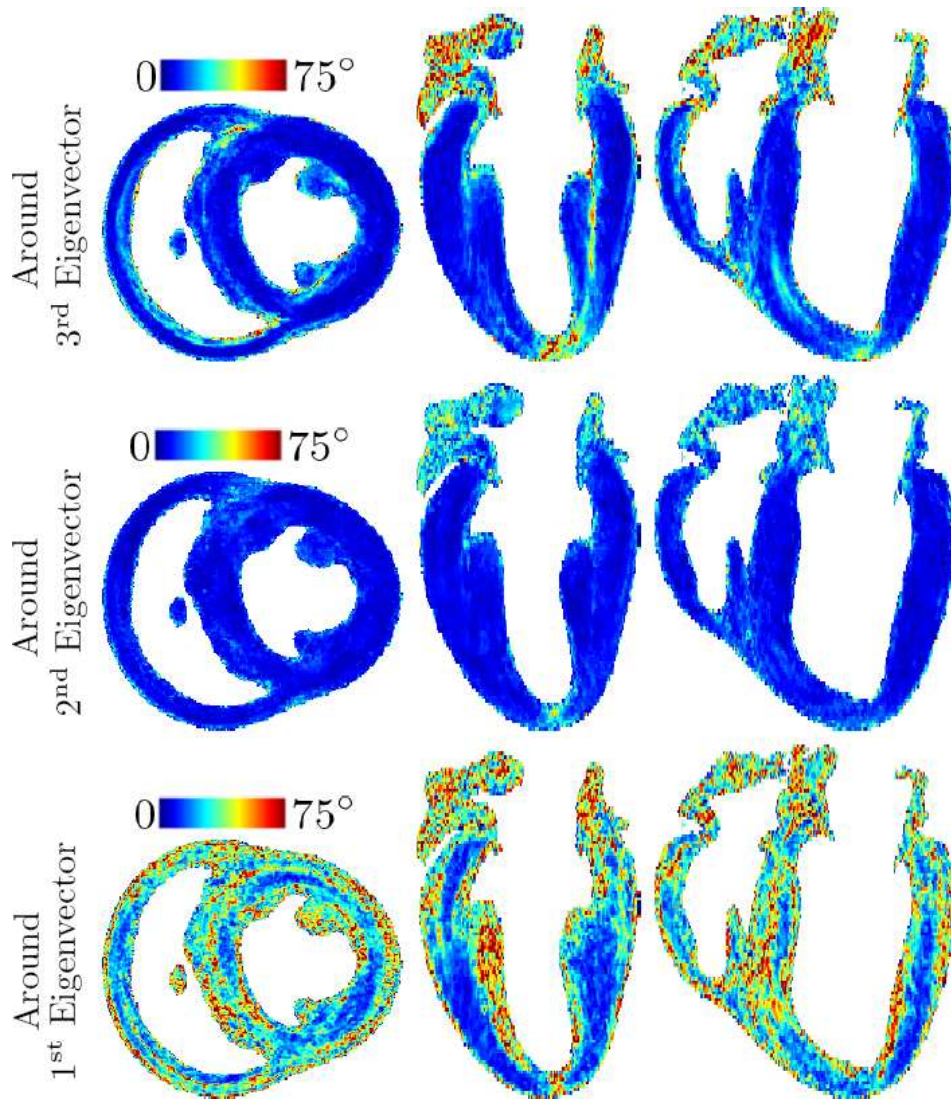


Figure 4.7: Standard deviation of the (V_1, V_2) frame orientation around V_3 , the (V_3, V_1) frame orientation around V_2 and the (V_2, V_3) frame orientation around V_1 eigenvectors (angles in degrees). These variabilities are shown in three different orthogonal views: a short axis view and 2 long axis views.

4.2.4 Reorientation Strategies and Inter-Subject Variability

Since no convincing experimental studies with non-linear transformation of real data has been proposed so far in the literature to compare reorientation strategies [Alexander 2001b, Van Hecke 2007], we propose to compare the effects of reorientation strategies on inter-subject variability with real data and limit the conclusion of this study to which one better models and explains the inter-subject “remodeling” of a given population (as opposed to intra-subject remodeling that occurs when organization of cardiac fibres changes to optimize the cardiac function after infarcts or interventions for instance).

As explained previously, we chose the Finite Strain (FS) reorientation strategy over the Preservation of the Principal Direction (PPD) to transform the DT-MRI essentially to be sure to compare their geometric features at the same mechanical state. Actually, we can also use the differences between reorientation strategies to try to explain the inter-subject variability. A reorientation strategy might be the right one to transform diffusion tensors. But another one might minimize the inter-subject variability and thus explain the inter-subject “remodeling” due to geometry change.

Let’s model the difference between the transformed diffusion tensor D of the target image and the corresponding diffusion tensor D' of the reference image:

$$D' = R D R^\top + \varepsilon_{\text{var}}$$

where

- D' is the diffusion tensor of the reference image,
- D is the diffusion tensor of the target image,
- $R D R^\top$ is the transformed diffusion tensor of target image,
- ε_{var} is the measured inter-subject variability.

If a given reorientation strategy minimizes the measured variability ε_{var} , it means that the reorientation strategy better models the inter-subject variability. The nature of the reorientation strategy (mechanical transformation or transformation preserving geometric features) can thus explain fibre architecture reorientation when geometry changes, which can be called inter-subject “remodeling”. The basic experiment proceeds as follows. First, we register the whole cardiac dataset to a given heart. This reference heart is not transformed to minimize the influence of the reorientation strategy in the following comparisons. After registering a heart to the geometry of the reference heart, we compare the eigenvectors of the transformed DT-MRI with those of the reference image. Since both reorientation strategies preserve the eigenvalues, the difference between them only relies on the orientation of the transformed eigenvectors. The inter-subject variability ε_{var} is measured with the basic angular differences between the eigenvectors of the reference diffusion tensor and the transformed ones obtained from both of the reorientation strategies. Gathering the comparisons of 16 registrations using 2 reference hearts, 7.2% of all the registered voxels are better registered with the FS than with the PPD. The average

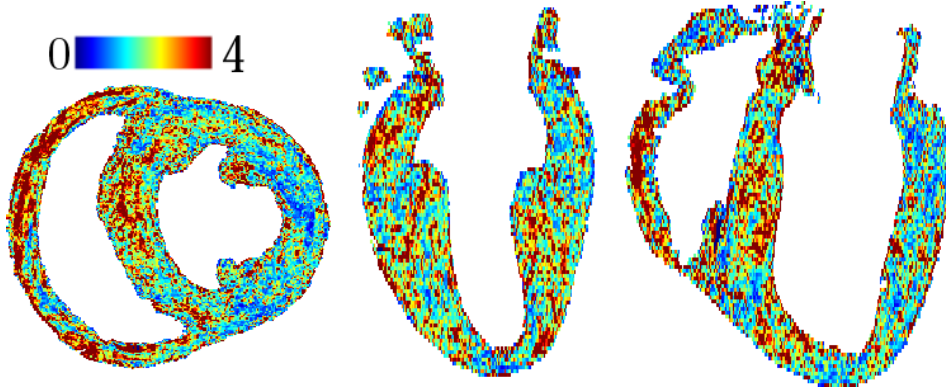


Figure 4.8: Mahalanobis distance of diffusion tensors between the canine atlas and a human heart.

angular difference of the eigenvectors is 0.3 degrees over all the voxels. These differences on real data are not significant enough to rely on the reorientation strategy to explain all the inter-subject variabilities. Probably, the inter-subject variability of cardiac fibre architecture is not only due to cardiac geometry but probably also to other physiological parameters.

4.3 Atlas Comparison with Other Models

4.3.1 Inter-Species Comparison with Human Data

In vivo acquisition of cardiac DT-MRI has been recently made possible for research purpose [Reese 1995, Tseng 1999, Dou 2002, Dou 2003] and preliminary clinical applications [Wu 2006, Wu 2009], but only at low resolution. Furthermore, normal hearts are usually preferred to be transplanted rather than used for research purpose. Thus, *ex vivo* acquisitions of cardiac DT-MRI are rare but nevertheless recent work on cardiac diffusion tensor regularization was performed on *ex vivo* human hearts [Frindel 2009b, Bao 2009].

Since studies of cardiac fiber architecture are mainly based on dissections and *ex vivo* DT-MRI acquisitions of other mammals, comparing the statistical canine atlas with human data gives the opportunity to provide preliminary results on the relevance of using prior knowledge from canine data in clinical applications. Only one human heart is available in the JHU database³, and even if it is a high quality acquisition, the quality of the heart itself is not as good as the canine ones due to its planned use for clinical applications. It limits the conclusion of this study but since it is rare to have access to human data at high resolution, it is a first step towards a more exhaustive inter-species comparison of the cardiac fiber architecture.

We register the human data on the statistical atlas with the same steps as described in Sections 3.2 and 3.3 to be consistent with the atlas building framework.

³http://gforge.icm.jhu.edu/gf/project/dtmri_data_sets/

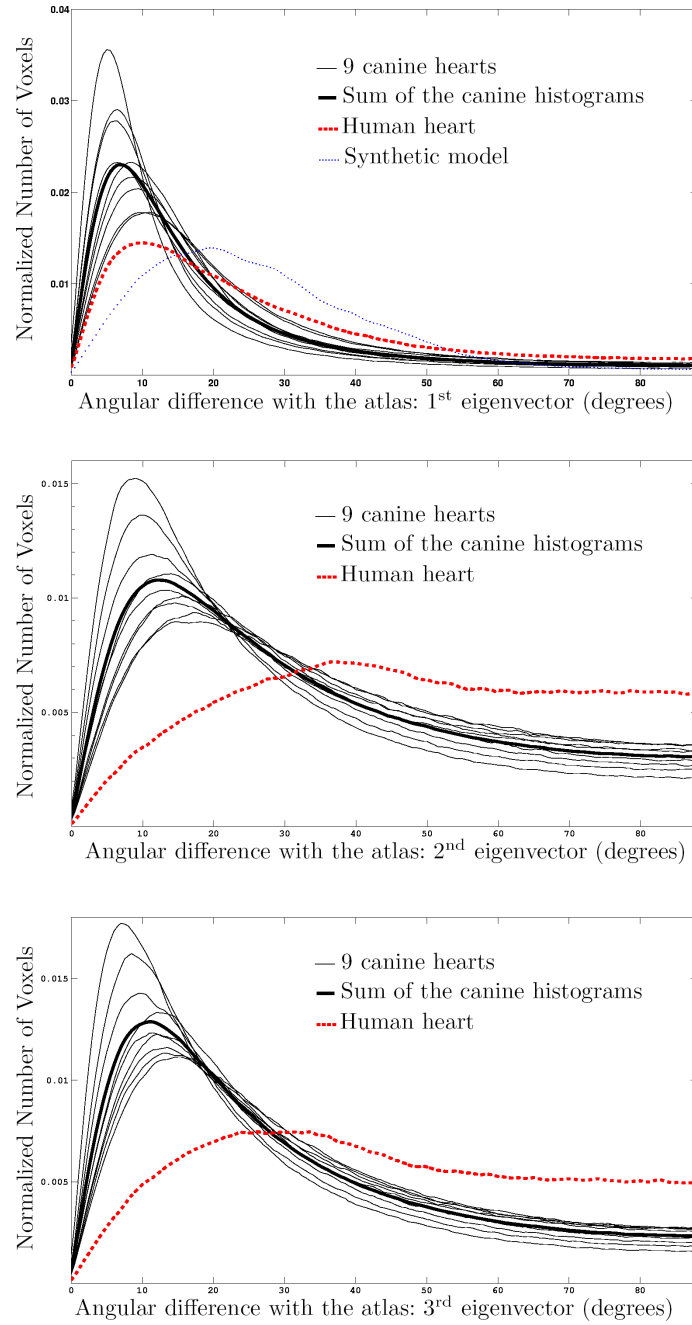


Figure 4.9: Normalized histograms of the absolute angular difference (degrees) of the primary, secondary and tertiary eigenvectors between the atlas and respectively the canine hearts, the human heart and the synthetic model (only describing fibre orientation).

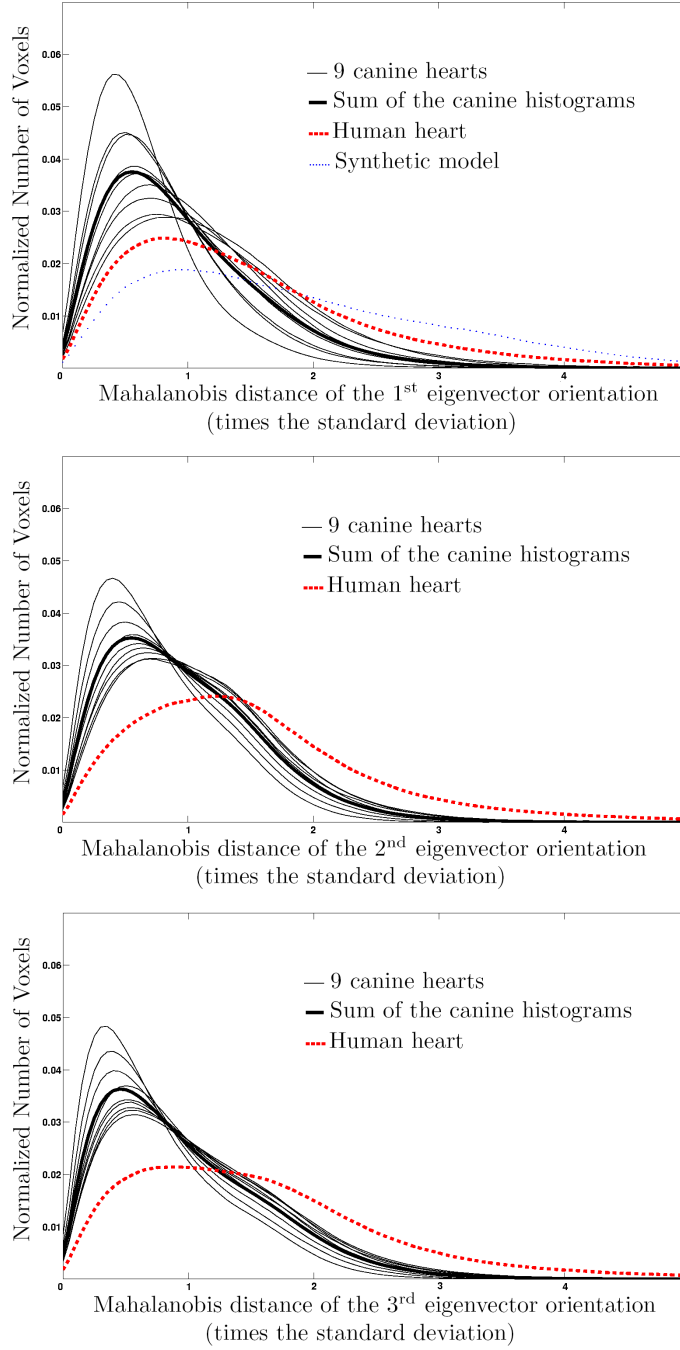


Figure 4.10: Mahalanobis distance of the angular difference (times the standard deviation) of the primary, secondary and tertiary eigenvectors between the atlas and respectively the canine hearts, the human heart and the synthetic model (only describing fibre orientation).

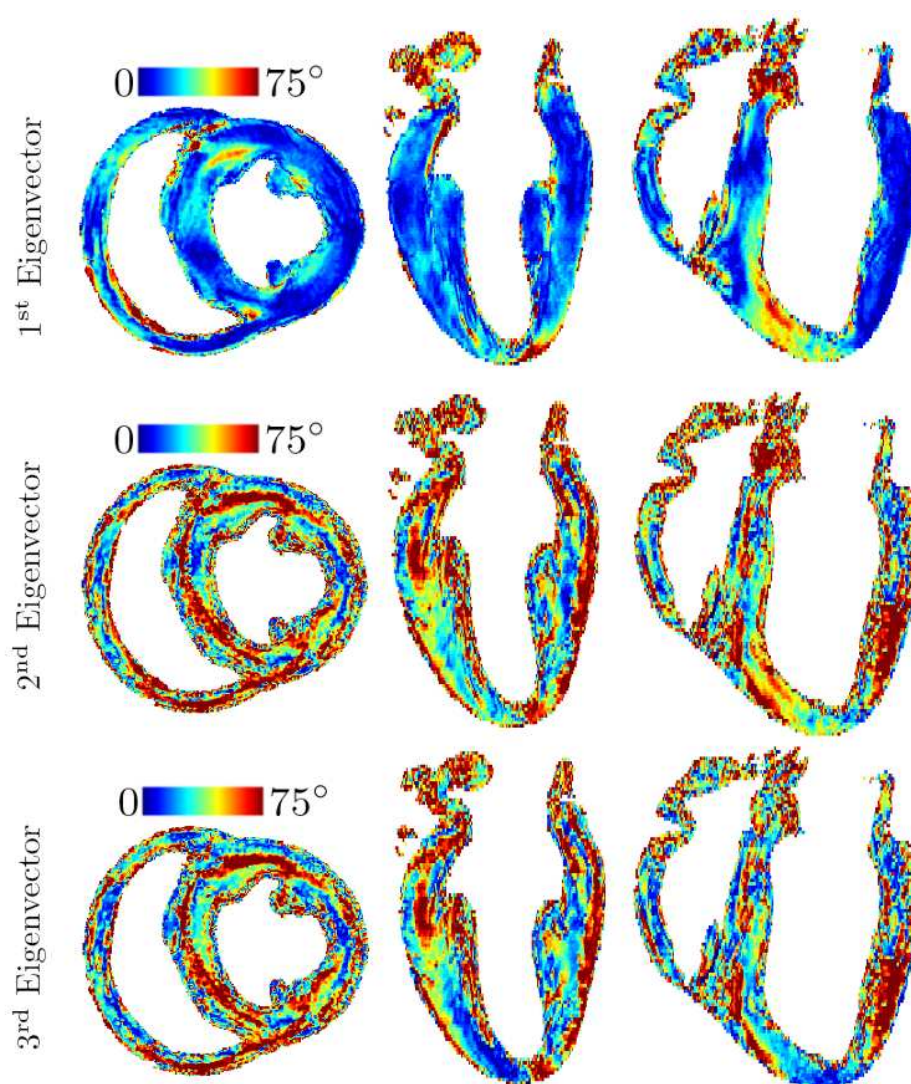


Figure 4.11: Angular difference of the primary, secondary and tertiary eigenvectors between the canine atlas and a human heart.

Eigenvector/Heart	Canine Hearts	Human Heart	Synthetic Model
Primary	6.9° - 0.58	10.1° - 0.81	19.6° - 0.95
Secondary	11.6° - 0.57	36.2° - 1.15	-
Tertiary	11.4° - 0.46	29.1° - 1.09	-

Table 4.1: Distribution modes of the angular differences between the eigenvectors (degrees) and of their corresponding Mahalanobis distances (times the standard deviation).

Then, we perform a statistical comparison at each voxel. First, we compute the normalized Mahalanobis distance μ between diffusion tensors [Pennec 2006]:

$$\mu_{(\bar{D}_{\log}, D_{\text{human}})}^2 = \frac{1}{6} \text{vec}(\Delta D)^\top \Sigma^{-1} \text{vec}(\Delta D)$$

where

$$\Delta D = \log(D_{\text{human}}) - \log(\bar{D}_{\log}).$$

The mode of the normalized Mahalanobis distance is 1.49 whereas it is lower than 1 for canine hearts of the dataset. To have a better understanding of the origin of this difference, we compare the human heart and the synthetic model with the canine hearts using directly the orientation of the eigenvectors (see Figures 4.9 and 4.10) and not pairs of eigenvectors that are not available for the synthetic model. The mode of the angular differences of the primary, secondary and tertiary eigenvectors are respectively 10.1, 36.2 and 29.1 degrees. To compare these differences with the variability of the canine population, we compute the Mahalanobis distance of these orientation parameters that are respectively 0.81, 1.15 and 1.09 times the standard deviation (see Table 4.1). These results confirm that the fiber orientations between human and canine hearts are more consistent than the laminar sheet orientations.

4.3.2 Comparison with Synthetic Models

Synthetic models of the cardiac fiber architecture, formulated by analytical laws, are usually built from common features observed on mammalian hearts [Streeter 1979, LeGrice 1995a] and formulated by analytical laws [Nielsen 1991, LeGrice 1997] where the transmural variation of the helix angle from endocardium to epicardium is linear. The synthetic model proposed in [Sermesant 2006a] describes the fiber orientations in a bi-ellipsoidal template geometry of the ventricles where the helix angle is going from -90° to $+90^\circ$ (see Figure 4.13). The registration of the bi-ellipsoidal geometry to the atlas geometry is necessary to compare the fibre orientations. This model can also be directly constructed in a given cardiac geometry to obtain the cardiac fibre orientation based on the same analytical laws [Nielsen 1991, LeGrice 1997]. In this case, a distance map between endocardium and epicardium is computed directly in the atlas geometry (see Figure 4.13). The distance map is computed from the distance maps d_{EPI} to epicardium, d_{LV} to left ventricular endocardium, and d_{RV} to right ventricular endocardium.

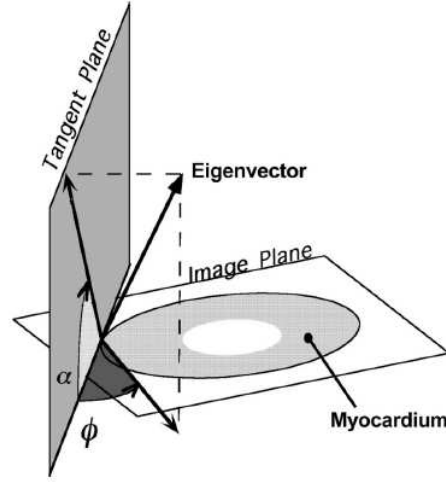


Figure 4.12: Prolate coordinate system in the heart: helix or elevation angle α and transverse angle ϕ .

$$d = \frac{d_{\text{in}}}{d_{\text{in}} + d_{\text{out}}}$$

where depending on the localization in the left ventricle, right ventricle, or septum

- d_{in} is either d_{LV} or d_{RV} ,
- d_{out} is either d_{RV} or d_{EPI} .

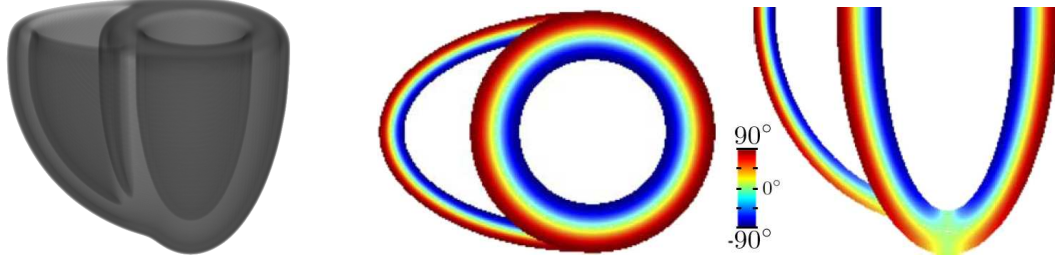
This distance map is first used to define a prolate coordinate system with radial \mathbf{r} , circumferential \mathbf{c} , and longitudinal \mathbf{l} vectors (see Figure 4.12). The radial vector \mathbf{r} follows the gradient direction of the distance map. \mathbf{l} is computed as the normal vector orthogonal to \mathbf{r} in the plane spanned by \mathbf{r} and the long axis direction of the left ventricle. The circumferential vector \mathbf{c} is then defined such that \mathbf{r} , \mathbf{c} , and \mathbf{l} form an orthonormal basis. Second, the helix angle α is obtained with the distance value d as follows:

$$\alpha(d) = (1 - d) \alpha_{\text{endo}} + d \alpha_{\text{epi}}$$

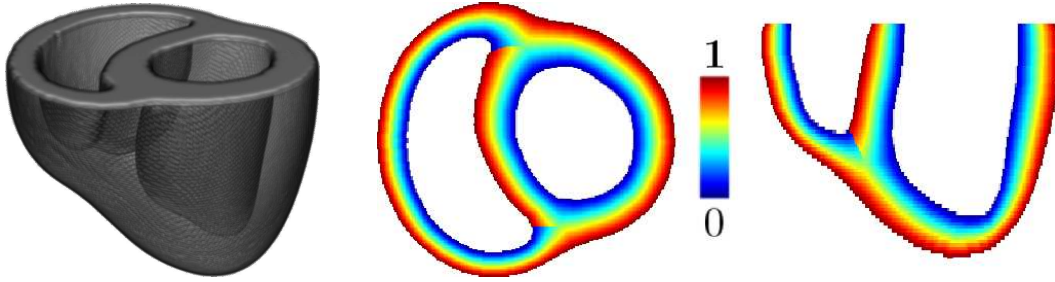
where

- α_{endo} is the helix angle at the endocardium,
- α_{epi} is the helix angle at the epicardium.

Synthetic models of fibre orientations are built with both strategies and compared to the fibre orientation of the DT-MRI atlas. First, we non-linearly register the bi-ellipsoidal synthetic geometry to the atlas geometry using the same method as presented in Section 3.2 [Peyrat 2007b]. Since this synthetic description is simply a vector field of the fiber orientation, we only use the primary eigenvector of the statistical atlas. We compare the histograms of the angular difference and its Mahalanobis distance between the fiber orientations of the synthetic model and the



(a) Synthetic 3D bi-ellipsoidal shape and fiber orientation parameterized with its helix angle.



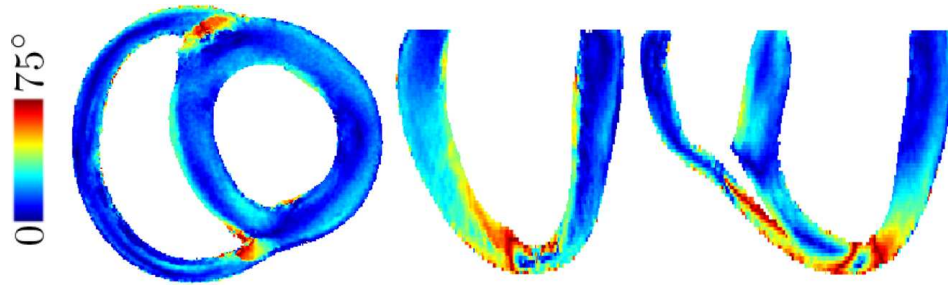
(b) Bi-ventricular shape of the atlas and distance map used to define the helix angle from epicardium to endocardium.

Figure 4.13: Synthetic models of cardiac fibre orientations.

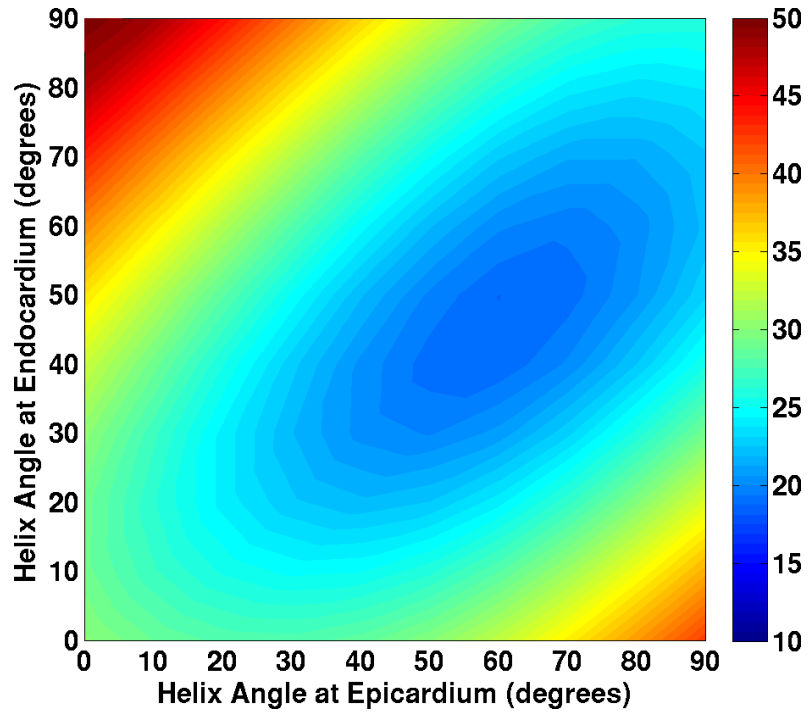
atlas. In Table 4.1 and Figures 4.9 and 4.10, we observe that the distribution modes of the synthetic model (19.6 degrees and 0.95 times the standard deviation) are higher than the distribution modes of the canine hearts (6.9 degrees and 0.58 times the standard deviation). The synthetic model is farther to the population of canine hearts than the human heart. The ellipsoidal geometry and the fiber orientations of the synthetic model are probably not accurate enough to catch all their subtle variations. For instance, in the short axis view the discontinuity at the crossing of the two ventricular walls is not realistic. Moreover, the synthetic description reaches its limits at the right ventricular and left ventricular apices where the modeling probably needs different analytical laws from the compact myocardium.

We also compare the atlas to synthetic models directly built in the atlas geometry with different absolute values of helix angles at endocardium and epicardium from 0° to 90° . Figure 4.14(b) shows that the best fit to the atlas corresponds to the endocardial helix value of $+45^\circ$ and the epicardial helix value of -60° . More local comparisons in each American Heart Association (AHA) zones are detailed in Appendix C. Same conclusions than with the bi-ellipsoidal model can be done based on the spatial distribution of the differences where the ventriculo-septal junctions and the apices are following different analytical laws.

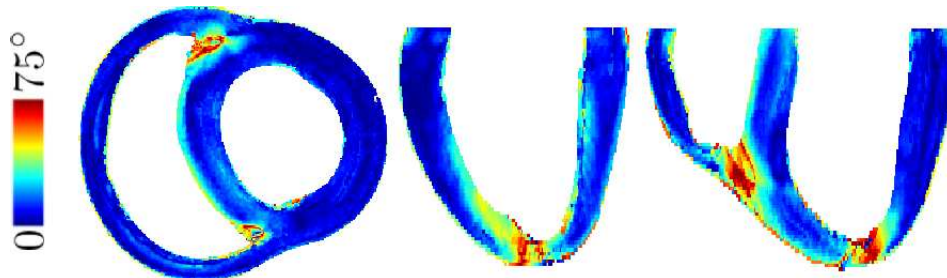
We can also compare the atlas to synthetic models extracting the helix and transverse angles of the atlas fibre orientation. Results in Figure 4.15 show the distribution of angles with respect to the transmural distance from endocardium



(a) Angular difference between the canine atlas and the bi-ellipsoidal synthetic model.



(b) Comparison of fibre direction between atlas and synthetic models constructed in atlas geometry and parametrized with different helix angles at epicardium and endocardium. The color represents the average angular difference. The best fit of atlas fibre direction is obtained with helix angle from $+45^\circ$ at endocardium to -60° at epicardium.



(c) Angular difference between the canine atlas and the synthetic model directly computed in the atlas geometry with helix angle from $+45^\circ$ at endocardium to -60° at epicardium.

Figure 4.14: Angular difference between the canine atlas and the synthetic models.

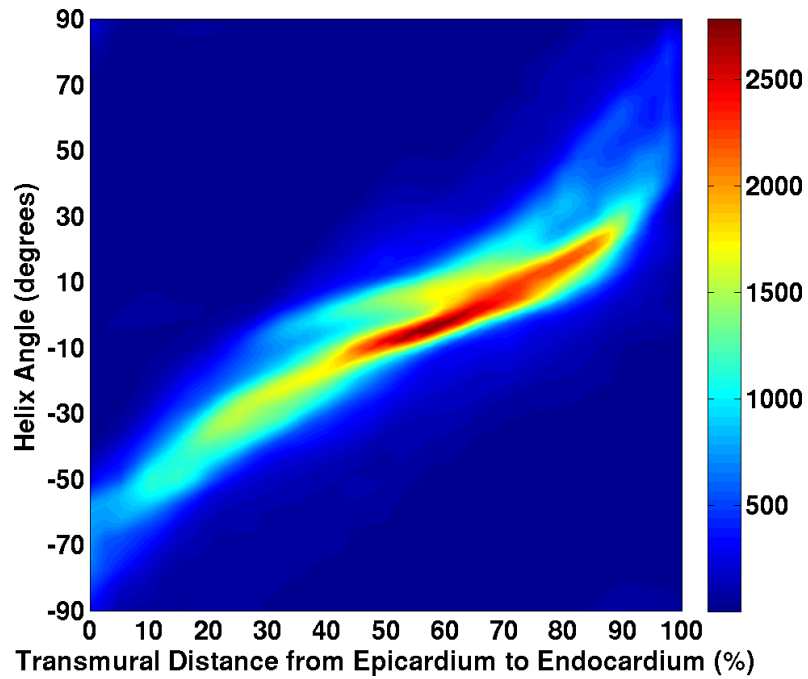
to epicardium. Linear and cubic regressions of these distributions in Figure 4.16 show that the linear model of transmural variation of helix angle is sufficient and consistent with extreme values of helix angles obtained from Figure 4.14(b). But as shown in Appendix C, the linear model of transmural variation of helix angle might not be valid in several AHA zones. Actually, in some regions such as the apex, no model of transmural variation of fibre orientation is really apparent. More generally, the distribution of fibre orientation is more consistent in the left ventricle than in the right ventricle, and at the base than at the apex.

4.4 Conclusion

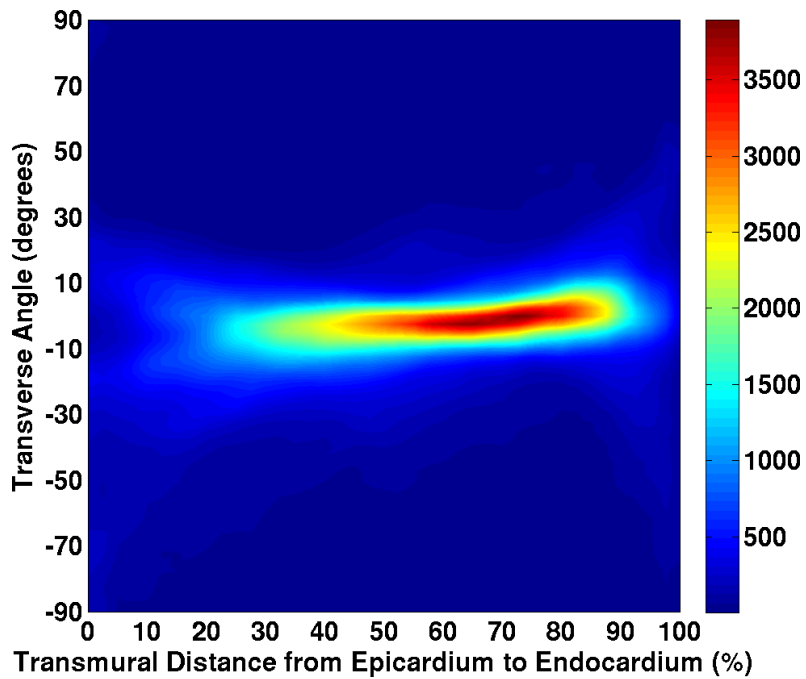
We believe that this statistical atlas⁴ will lead to a better understanding of the cardiac fibre architecture. For instance, the application of this framework to nine canine hearts confirms the already established stronger intra-species stability of fiber orientations than laminar sheet orientations [Helm 2005a, Gilbert 2007]. As preliminary results of an inter-species comparison between a human heart and the statistical atlas of canine hearts, we observe the good inter-species stability of the fiber orientations. Of course, the access to a larger database will provide more reliable inter- and intra-species statistics. A better understanding of the inter-species differences would help for instance to extend experimental results from one species to another. Building and comparing statistical atlases of normal and pathological hearts could also help in a better quantification of the pathology, for instance in the remodeling process.

Moreover, such a statistical atlas offers a valuable prior knowledge in the context of electromechanical modeling of the heart. The information about the laminar sheets is particularly relevant since it has been shown to influence significantly the cardiac motion [Arts 2001, Usyk 2000], in particular the wall thickening and the apico-basal torsion [Costa 2001]. As initiated in [Geerts 2003], a precise study of the impact of the cardiac fibre architecture on the electromechanical simulations would make it possible to design the best fibre model for simulation-based clinical applications.

⁴<http://www-sop.inria.fr/asclepios/data/heart>

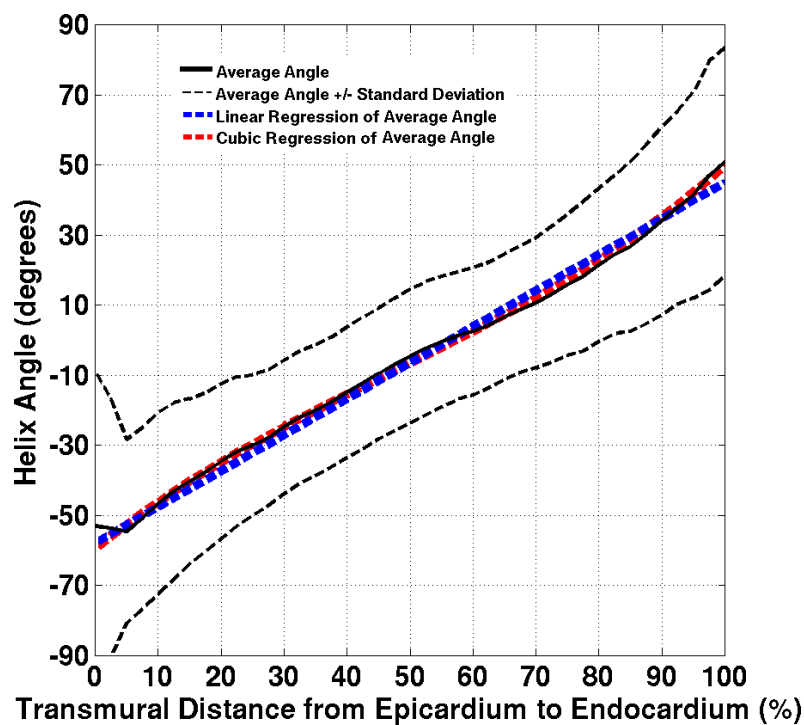


(a) Joint histogram of helix angle and normalized transmural distance from epicardium to endocardium in atlas (color represents the number of voxels)

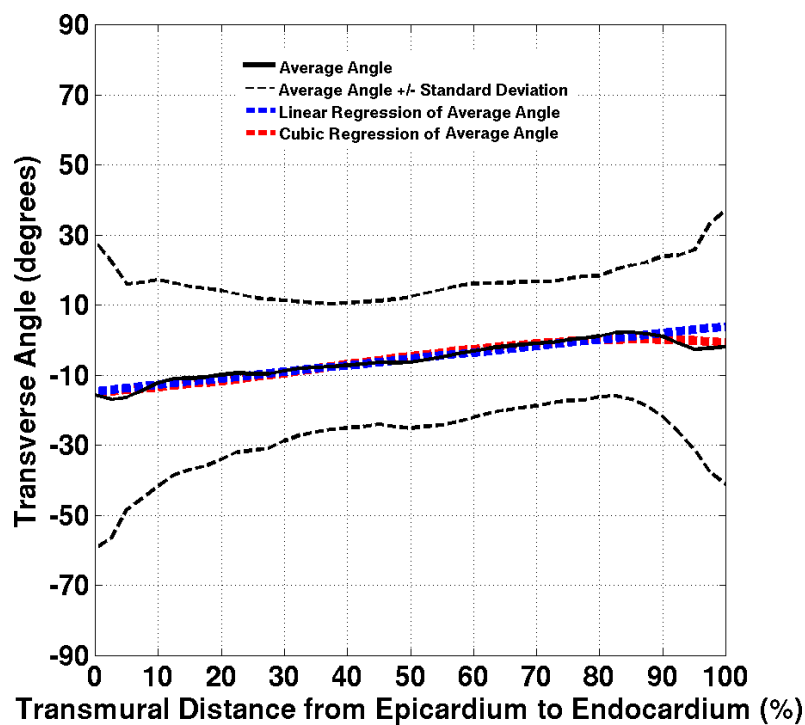


(b) Joint histogram of transverse angle and normalized transmural distance from epicardium to endocardium in atlas (color represents the number of voxels)

Figure 4.15: Joint histogram of helix (a) or transverse (b) angles with the relative transmural distance from epicardium to endocardium in the atlas.



(a) Helix Angle



(b) Transverse Angle

Figure 4.16: Average helix (a) and transverse (b) angles (in continuous black lines) at given relative transmural distance from epicardium to endocardium in the whole heart obtained from joint histograms in Figure 4.15 and its corresponding envelop at a distance of one standard deviation (dashed black lines). Linear and cubic regression are also shown (respectively in dashed blue and red lines).

PART III

COMPARISON OF CARDIAC FUNCTION AND ANATOMY FROM 4D CT

SPATIO-TEMPORAL REGISTRATION OF TIME-SERIES OF IMAGES

Contents

5.1	Introduction	89
5.2	General Setting	91
5.2.1	Temporal Transformation as Physiological States Mapping	92
5.2.2	Spatial Transformation as Trajectory Mapping	94
5.3	From 4D Registration to Multichannel 3D Registration	96
5.4	Spatial 4D Registration with Diffeomorphic Demons	98
5.4.1	Standard 3D Diffeomorphic Demons	99
5.4.2	Multichannel 3D Diffeomorphic Demons	100
5.5	Conclusion	101

5.1 Introduction

During the last decade, the improvement of medical imaging technologies extended 3D image acquisitions to 4D sequence acquisitions such as cine MRI, tagged MRI, 4D CT or 4D ultrasound. They give access to additional information important for studying the motion of organs (such as heart and lung) or for real-time control during image-guided surgical procedures. Since the temporal dimension cannot be considered as an additional spatial dimension, the extension of 3D image processing tools to 4D spatio-temporal data is not straightforward. Thus, the development of specific algorithms for spatio-temporal data is necessary such as temporal interpolation [Ehrhardt 2006], segmentation [Angelini 2001, Bosch 2002, Lorenzo-Valdés 2004, Montagnat 2005, Fritscher 2005, Lelieveldt 2006, Uzumcu 2006, Kohlberger 2006, Cousty 2007, Casero 2008], statistical analysis of cardiac shape and dynamics [Perperidis 2005a, Hoogendoorn 2009], motion tracking [Prince 1992, Park 1996, Declerck 1998, Osman 1999, Huang 1999, McEachen 2000, Chandrashekar 2004, Ledesma-Carbayo 2005, Clarysse 2005, Delhay 2006, Sundar 2009, Bistoquet 2007, Sarrut 2007, De Craene 2009], image-to-sequence registration [Roche 2001, Pennec 2005], temporal

alignment [Singh 2007, Perperidis 2005b], and spatio-temporal registration [Caspi 2002, Huang 2005, Zhang 2007, Perperidis 2005b, Lopez 2008a, Lopez 2008b, Schreibmann 2008]. Most of the spatio-temporal registration algorithms deal with the registration of sequences of the same patient acquired with different imaging modalities. Recently, research has addressed the more complex inter-subject spatio-temporal registration of sequences. Some 3D image registration applications were extended to 4D sequences, such as registration-based segmentation [Lopez 2008a, Lopez 2008b] or atlas construction [Perperidis 2005a]. Furthermore, it opens doors to applications specific to spatio-temporal data, for instance by comparing the temporal evolution of local parameters of homologous anatomical points (such as strain or depolarization/repolarization times) or by analyzing the temporal change of inter-sequence transformations over a cardiac cycle to better understand the link between anatomical and functional differences.

Caspi and Irani [Caspi 2002] were among the first to propose a framework for sequence-to-sequence alignment using spatio-temporal transformations. Since their algorithm was designed for the registration of different camera views of the same dynamic scene, they constrained the spatio-temporal transformation to a 1D temporal linear transformation to cope with the different acquisition rates of the cameras and to a 3D affine transformation constant over time to cope with the different camera views. They showed that folding spatial and temporal information into a single alignment framework outperforms a purely image-to-image alignment of corresponding frames.

Sundar *et al.* [Sundar 2009] proposed to embed cardiac motion tracking into a 4D registration framework. The original sequence is registered to a static sequence built from the image at a reference time-point. All 3D transformations from a given time-point to the reference time-point are determined simultaneously with spatio-temporal smoothness constraints. Compared to the independent 3D registration of each time-point to the reference time-point, this method showed more robust results. But since this framework was limited to motion estimation in a single sequence, issues specific to the comparison of different sequences, like temporal misalignment and large inter-sequence deformations, were not addressed.

Perperidis *et al.* [Perperidis 2005b] proposed to register two cardiac MR sequences of different patients with spatio-temporal free-form deformation models based on B-Splines. The registration algorithm optimizes either the spatial and temporal transformation models simultaneously or optimizes the temporal transformation before optimizing the spatial transformation. The temporal transformation is a 1D B-Spline transformation that corrects temporal misalignment caused by length differences of the cardiac cycles and by kinetic differences of cardiac phases. The spatial transformation is a single 3D B-Spline transformation that corrects spatial misalignment at all corresponding time-points caused by global anatomical differences. Since the same inter-subject spatial transformation is used over time, residual anatomical differences occur between corresponding time-points. These differences are used to build a probabilistic MR cardiac atlas representing the anatomy and function of a healthy heart.

To catch those residual differences and to fully map corresponding images at each time-point, a time-dependent spatial transformation is necessary. When registering 4D lung CT sequences of the same patient for image-guided radiotherapy, Schreibmann *et al.* [Schreibmann 2008] determined a spatial 3D B-Spline transformation independently at selected time-points. For inter-subject registration of cardiac cine MRIs where the anatomies and motion patterns can have high discrepancies between patients, Lopez *et al.* [Lopez 2008a, Lopez 2008b] extended this solution by including image information from neighboring time-points (called bridging points). They computed a 3D B-Spline transformation at each time-point with an energy functional matching simultaneously the normalized mutual information of three pairs of images: the pair of images at the current time-point and two pairs of images at the neighboring time-points transformed to the geometry of the current time-point with intrasubject motion transformations. Their results show an improvement of the registration accuracy by comparing endocardial and atrial segmentations. But in both methods, the 3D B-Spline transformations are computed independently at each time-point. Thus they are not necessarily consistent with motion occurring in each sequence by matching the same physical points at different time-points. This constraint is important when comparing the temporal evolution of local parameters of homologous anatomical points.

In this chapter, we present a general framework in which the resulting inter-sequence spatial transformations verify the constraints to map the same physical points over time, called the *trajectory constraints*. In this framework, the 4D spatio-temporal registration is decoupled into a 4D temporal registration, defined as mapping physiological states, and a 4D spatial registration, defined as mapping trajectories of physical points. A temporal registration is performed using global cardiac physiological state parameters. After this global temporal alignment, the 4D spatial registration is performed. Our contribution focuses more specifically on the improvement of this 4D spatial registration step by including the trajectory constraints. A motion tracking is performed with the *Diffeomorphic Demons* (DD) algorithm [Vercauteren 2009] to determine the dense trajectories of points in both sequences. Then, these dense trajectories are used to constrain temporally the inter-sequence spatial transformations. By including the trajectory constraints, we show that the 4D spatial registration can be formulated as a *multichannel registration* of 3D images at a reference time point combined with inversions and compositions of transformations. The multichannel registration problem is solved by using the *Multichannel Diffeomorphic Demons* (MDD), a novel extension of the DD algorithm to vector-valued data that is presented at the end of this chapter.

5.2 General Setting

We describe here the general setting for the spatio-temporal registration of 4D sequences that estimates two different types of transformations: a temporal transformation and a spatial transformation. First, we introduce the temporal transforma-

tion as a physiological state mapping. Second, we present the 4D spatial registration as a trajectory mapping from which we derive a discrete formulation of the trajectory constraints that should be verified.

Let's consider the reference sequence I and the target sequence I' whose acquisition space-time are respectively $\Omega \times \tau \subset \mathbb{R}^3 \times \mathbb{R}$ and $\Omega' \times \tau' \subset \mathbb{R}^3 \times \mathbb{R}$:

$$\begin{aligned} I : \Omega \times \tau &\longrightarrow \mathbb{R} & I' : \Omega' \times \tau' &\longrightarrow \mathbb{R} \\ (x, t) &\longmapsto I(x, t) = i & (x', t') &\longmapsto I'(x', t') = i' \end{aligned}$$

When registering the target sequence I' to the reference sequence I , the spatio-temporal transformation S that maps a spatio-temporal position (x, t) of I to the corresponding spatio-temporal position (x', t') of I' must be found:

$$\begin{aligned} S : \Omega \times \tau &\longrightarrow \Omega' \times \tau' \\ (x, t) &\longmapsto S(x, t) = (x', t') \end{aligned}$$

The spatio-temporal transformation S can be formulated as the combination of a spatial transformation S_{space} and a temporal transformation S_{time} as follows:

$$S(x, t) = (S_{\text{space}}(x, t), S_{\text{time}}(x, t))$$

In the following, we give more details about the two types of transformations. First, we present the temporal transformation as a mapping of corresponding physiological states. Second, we present the spatial transformation as a mapping of corresponding trajectories of physical points.

5.2.1 Temporal Transformation as Physiological States Mapping

The temporal transformation S_{time} is defined as follows:

$$\begin{aligned} S_{\text{time}} : \Omega \times \tau &\longrightarrow \tau' \\ (x, t) &\longmapsto S_{\text{time}}(x, t) = t' \end{aligned}$$

The idea behind the temporal transformation is to match an event occurring at the time-point t and the spatial position x in the reference sequence to a similar event occurring at the corresponding time-point t' in the target sequence. In medical imaging, corresponding time-points can be defined as time-points at which physiological states are the same, for instance the end of diastole/systole for a given cardiac ventricle or the beginning of a respiration cycle for a lung. Thus the temporal transformation is highly dependent on which physiological parameters we want to compare. In previous works, the temporal transformation S_{time} was determined by matching a parameter describing a global physiological state of the heart such as a specific event of the ECG (e.g. P, Q, R, S, and T peaks), volume extrema of the left ventricle, the average cross-correlation coefficient between frame intensities [Larson 2004, Perperidis 2005b] or the path of a specific anatomical point [Singh 2007]. Since these global parameters are the same for every position

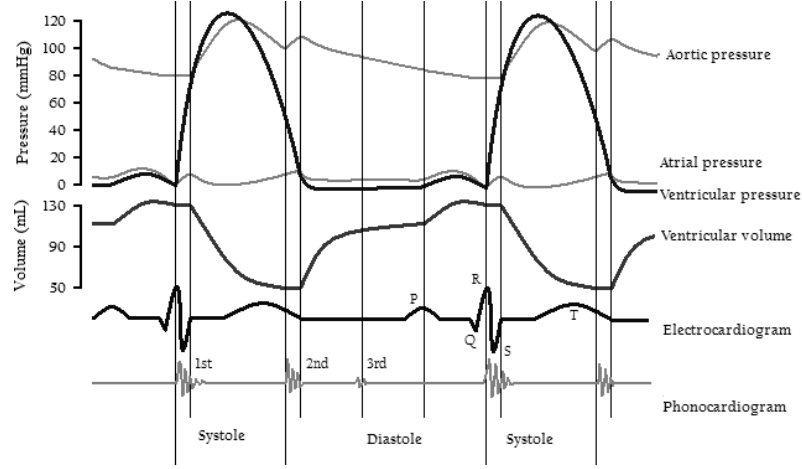


Figure 5.1: Wiggers Diagram [Richardson 1998] - This diagram shows different physiological parameters with the same timeline of a cardiac cycle: pressure and volume curves, ECG, and phonocardiogram (figure adapted from Wikipedia - http://en.wikipedia.org/wiki/Cardiac_cycle). These physiological parameters can be used to detect different physiological events occurring in a cardiac cycle such as diastole, systole, or valves opening and closing.

at a given time-point, the resulting temporal transformation is independent of the spatial position x and thus a function of time only. Actually the temporal transformation can be space dependent when two structures have different physiological patterns. For instance the periods of the cardiac and respiration cycles are different and the temporal transformation of a sequence imaging heart and lungs should be different for each organ. It could also happen with different areas of a single organ. For instance we might want to temporally register independently the left and right cardiac ventricles in pathological cases such as a left bundle branch block (LBBB) where the activation of the left ventricle is delayed, which results in the left ventricle contracting later than the right ventricle. We could also imagine to temporally register events that are locally defined such as depolarization/repolarization or maximum contraction that are spatially dependent. Obviously the temporal transformation can become very complex when comparing local physiological events. The complexity of the temporal transformation and the choice of the features used for temporal registration should be governed by the desired application.

As mentioned previously, the temporal transformation is determined by the registration of some signals or quantities that may not be intensity-based (see Figure 5.1) whereas the spatial registration is intensity-based. Thus, when using different data, the temporal transformation S_{time} can be determined independently from the spatial transformation S_{space} . The temporal transformation can even be applied after the spatial transformation as long as structures are not appearing and/or disappearing during the sequences and as long as images at each time-point in the reference sequence has an image at the same time point in the target sequence to be compared

to. This happens when the same structures are present during the whole sequence and when the acquisition time intervals τ and τ' exactly overlap, which is the case after global linear temporal registration. This linear transformation is often implicitly performed in the acquisition process such as in 4D cardiac CT sequences that are gated from the end of diastole (ED) of a cardiac cycle to the ED of the next cycle.

For instance, in the following experiments of Chapter 6 where 4D cardiac CT sequences are registered, we first define the global physiological state with the ECG (as a percentage of R-R interval) temporally aligned with a linear transformation. In practice, this linear transformation is implicitly performed in the ECG-gated acquisition process of 4D cardiac CT where each frame correspond to a percentage of the R-R interval. Then, a non-linear temporal transformation refines the linear transformation by matching global mechanical state defined with blood volume curves. In this way, the following inter-sequence spatial registration between corresponding frames are performed at corresponding mechanical states and thus with similar geometries.

When the temporal transformation is known, sequences can be temporally re-sampled. Due to the nature of the temporal dimension, one should note that the temporal interpolation cannot be performed only as an intensity-based linear interpolation of images without coping with the motion occurring in the sequence. Temporal interpolation should rely on a motion-based interpolation of images as proposed by Ehrhardt *et al.* [Ehrhardt 2006]. Thus motion tracking, computed as described in the following Section ??, is necessary for the temporal resampling of sequences.

5.2.2 Spatial Transformation as Trajectory Mapping

The spatial transformation S_{space} is defined as follows:

$$\begin{aligned} S_{\text{space}} : \quad \Omega \times \tau &\longrightarrow \Omega' \\ (x, t) &\longmapsto S_{\text{space}}(x, t) = x' \end{aligned}$$

To be physically meaningful when determining the time-dependent spatial transformation S_{space} , the same physical points should be mapped at different time points in both sequences. In other words, if we define the position of a physical point X over time as the trajectory ϕ_X :

$$\begin{aligned} \phi_X : \quad \tau &\longrightarrow \Omega \\ t &\longmapsto \phi_X(t) = x \end{aligned}$$

we can formulate the problem as finding the transformation S_{space} such that the trajectory ϕ_X of a physical point X in the reference sequence maps the trajectory $\phi_{X'}$ of its corresponding physical point X' in the target sequence:

$$S_{\text{space}}(\phi_X(\cdot), \cdot) = \phi_{X'}(\cdot) \quad (5.1)$$

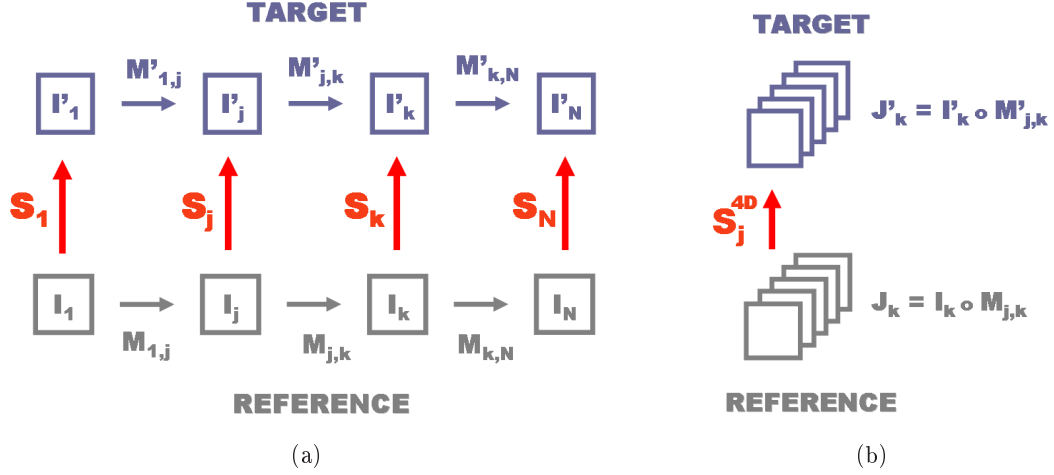


Figure 5.2: (a) Discretization of the 4D spatial registration with the spatial transformations S_j between the sequences and the motion transformations $M_{j,k}$ and $M'_{j,k}$ between frames at times t_j and t_k (note that the arrows show the direction of the resampling deformation fields used to transform the target image to the reference image) - (b) Under the trajectory constraints, the 4D registration can be parametrized by a single reference spatial transformation S_j^{4D} and thus formulated as a multichannel 3D registration problem. Frames I_k and I'_k of the two sequences are transformed through the motion transformations $M_{j,k}$ and $M'_{j,k}$ to the reference geometry of images I_j and I'_j . The transformations S_k^{4D} are then reconstructed from S_j^{4D} to satisfy the trajectory constraint: $S_k^{4D} = M'_{j,k} \circ S_j^{4D} \circ M_{j,k}^{-1}$.

With this formulation we can easily understand why matching corresponding trajectories is independent from matching corresponding time-points as mentioned in the previous section. Indeed a temporal transformation does not modify the nature of a trajectory but does solely modify the speed of a physical point along its trajectory. It simply means that a temporal transformation does not modify the anatomical position of a physical point but does only modify its physiological state over time. Our goal here is to perform a robust intensity-based image matching of corresponding anatomical points independently of occurring physiological events.

The temporal discretization of the 4D spatial registration is illustrated in Figure 5.2 (note that we call transformations the resampling transformations used to deform the target image to the reference image, the arrows show the direction of the resampling deformation fields used to find the corresponding point of the reference image in the target image). The inter-sequence transformations S_j map the reference volume I_j to the target volume I'_j at time t_j knowing the trajectories of points given by the intrasequence motion transformations $M_{j,j+1}$ and $M'_{j,j+1}$ between the times t_j and t_{j+1} respectively in the reference and target sequences. In the discrete world, Equation 5.1 is equivalent to stating that if a point position x in image I_j maps a point position x' in I'_j by the inter-sequence transformation S_j then the remaining inter-sequence transformations S_{j+1} should map the displaced point

position $M_{j,j+1}(x)$ to the displaced point position $M'_{j,j+1}(x')$. This translates into a set of constraints, called the trajectory constraints, that link the inter-sequence transformations S_j and S_k with the motion transformations $M_{j,k}$ (from I_j to I_k) and $M'_{j,k}$ (from I'_j to I'_k) :

$$S_k \circ M_{j,k} = M'_{j,k} \circ S_j \quad (5.2)$$

In the sequel, we formulate the 4D spatial registration as the minimization of a functional including those trajectory constraints and considering the motion tracking as a known parameter previously computed independently in each sequence.

5.3 From 4D Registration to Multichannel 3D Registration

When determining the inter-sequence transformation S_j , the standard approach is to minimize the image similarity measure between the pair of images (I_j, I'_j) :

$$S_j^{3D} = \underset{S}{\operatorname{argmin}} \left(\int_{\omega \in \Omega_j} \operatorname{Sim}(I_j(\omega), I'_j \circ S(\omega)) d\omega \right) \quad (5.3)$$

We call this inter-sequence transformation S_j^{3D} the solution to the 3D registration problem that only involves one pair of images (I_j, I'_j) .

When determining the set of inter-sequence transformations $(S_j^{4D})_{j=1,\dots,N}$ for the 4D spatial registration, we want to simultaneously minimize the image similarity measure between all pairs of images (I_j, I'_j) :

$$(S_1^{4D}, \dots, S_N^{4D}) = \underset{(S_1, \dots, S_N)}{\operatorname{argmin}} \left(\sum_{k=1}^N \int_{\omega \in \Omega_k} \operatorname{Sim}(I_k(\omega), I'_k \circ S_k(\omega)) d\omega \right) \quad (5.4)$$

If each transformation S_j^{4D} is considered independent from the others, the solution is similar to finding each transformation S_j^{3D} . Actually to ensure that the transformations $(S_j^{4D})_{j=1,\dots,N}$ map the same physical point over time, the trajectory constraints of Equation 5.2 should be verified. Thus a strong link exists between all inter-sequence transformations that cannot be considered independent anymore. The trajectory constraints can be reformulated as $S_k^{4D} = M'_{j,k} \circ S_j^{4D} \circ M_{j,k}^{-1}$ that may be interpreted as follows: to satisfy the trajectory constraints, the transformation $M'_{j,k} \circ S_j^{4D} \circ M_{j,k}^{-1}$ should map image I_k into image I'_k .

Motion tracking is performed with an updated Lagrangian scheme with Gaussian regularization. Basically, the intrasequence motion transformations $M_{j,k}$ and $M'_{j,k}$ are iteratively computed by initializing the registration of frame t_k to reference frame t_j in each sequence with the motion transformations $M_{j,k-1}$ and $M'_{j,k-1}$ obtained at the previous step. Since motion tracking is necessary to temporally resample the sequences when using motion-based interpolation, motion tracking is actually performed with the original sequences before temporal resampling. Then motion tracking is also temporally resampled according to the temporal transformation in order to be consistent with the temporally resampled sequence.

In the remainder, we consider the motion transformations $M_{j,k}$ and $M'_{j,k}$ as fixed when determining the inter-sequence transformation S_j^{4D} . Indeed, motion tracking is intrinsically independent from any inter-sequence registration. Motion transformations are estimated independently and then used to improve the estimation of the inter-sequence transformations. This assumption makes sense when considering that the motion transformations are much easier to estimate than inter-sequence transformations. Indeed, inter-sequence transformations have larger deformations than motion transformations (especially in sequences with high temporal resolution). Furthermore, they are less constrained than cardiac motion, since cardiac motion follows the law of biomechanics that can be included as an *a priori* knowledge, for instance elasticity or nearincompressibility of cardiac tissue [Bistoquet 2007, Mansi 2009]. In this way, physically meaningful constraints on the estimation of the intrasequence motion transformations would be indirectly included to the estimation of inter-sequence anatomical transformations through the trajectory constraints.

Applying the trajectory constraints to the set of variables $(S_j)_{j=1,\dots,N}$ in the minimization process, any transformation S_k can be parametrized with a single transformation S_j at a reference time-point t_j and the motion transformations $M'_{j,k}$ and $M_{j,k}$. The number of unknown variables is highly decreased by determining only the chosen reference transformation S_j^{4D} that minimizes the following modified functional of Equation 5.4 :

$$S_j^{4D} = \underset{S}{\operatorname{argmin}} \left(\int_{\omega \in \Omega_j} \operatorname{Sim}(I_j(\omega), I'_j \circ S(\omega)) d\omega + \sum_{k \neq j} \int_{\omega \in \Omega_k} \operatorname{Sim}(I_k(\omega), I'_k \circ M'_{j,k} \circ S \circ M_{j,k}^{-1}(\omega)) d\omega \right)$$

Applying the appropriate change of variable $\omega = M_{j,k}(\nu)$ for each term of the functional, the 4D spatial registration can be formulated as the minimization of similarity criterion between several pairs of images (see Figure 5.2):

$$S_j^{4D} = \underset{S}{\operatorname{argmin}} \left(\int_{\omega \in \Omega_j} \operatorname{Sim}(I_j(\omega), I'_j \circ S(\omega)) d\omega + \sum_{k \neq j} \int_{\nu \in \Gamma_j} \operatorname{Sim}(J_{j,k}(\nu), J'_{j,k} \circ S(\nu)) |\operatorname{Jac}(M_{j,k})(\nu)| d\nu \right)$$

where $J_{j,k} = I_j \circ M_{j,k}$ and $J'_{j,k} = I'_j \circ M'_{j,k}$ are respectively the images at frame k transformed into the geometry of the image at frame j in the reference and target sequences, $\Gamma_j \in \Omega_j$ is part of image I_j , and $\operatorname{Jac}(M_{j,k})$ is the Jacobian of transformation $M_{j,k}$.

In other words, the inter-sequence transformation S_j^{4D} must optimize the sum of similarity criteria between the pair of images (I_j, I'_j) and all pairs of images $(J_{j,k}, J'_{j,k})$. Note also that the terms $\operatorname{Jac}(M_{j,k})$ deriving from the change of variables take into account volume change of voxels when transforming I_k into $J_{j,k}$. This term acts as a voxel-wise weight map in each similarity criterion to ensure the equivalence of the energy functional formulated in the original and warped spaces. Once S_j^{4D}

is estimated, the other transformations S_k^{4D} can be computed from S_j^{4D} with the trajectory constraints: $S_k^{4D} = M'_{j,k} \circ S_j^{4D} \circ M_{j,k}^{-1}$.

Finally, we have shown that including the trajectory constraints in the estimation of the inter-sequence transformation S_j^{4D} translates the 4D spatial registration problem into a single 3D multichannel registration problem associated with pairs of images (I_k, I'_k) transformed respectively in the reference space of the images I_j and I'_j .

The 4D spatio-temporal registration framework can be summarized as follows:

4D Spatio-Temporal Registration Algorithm

- (1) Temporal alignment w.r.t. global physiological parameters.
 - (2) Compute motion tracking $M_{j,k}$ and $M'_{j,k}$ registering each frame t_k to the reference frame t_j .
 - (3) Resample motion tracking $M'_{j,k}$ and target sequence I' with motion-based interpolation.
 - (4) Transform each frame of I and I' to the reference frame with the motion tracking $M_{j,k}$ and $M'_{j,k}$.
 - (5) Compute S_j^{4D} in the reference frame using 3D multichannel registration algorithm (cf. 5.4.2).
 - (6) Compute S_k^{4D} in other frames using the trajectory constraints : $S_k^{4D} = M'_{j,k} \circ S_j^{4D} \circ M_{j,k}^{-1}$.
-

5.4 Spatial 4D Registration with Diffeomorphic Demons

In this section, we present a novel extension of the *Diffeomorphic Demons* (DD) [Vercauteren 2009] to multichannel data (or vector-valued data), called the *Multichannel Diffeomorphic Demons* (MDD). We have chosen to extend the DD algorithm but this choice is not exclusive. Other registration algorithms could also be extended to multichannel data. Due to the trajectory constraints, the space of resulting transformations should be stable by composition and inversion which is the case with the DD. Mainly the speed of DD algorithm is a significant advantage when considering to process large 4D datasets in a reasonable amount of time. Recently, it has been shown in a thorough comparison of registration algorithms for brain applications [Klein 2009] that DD was one of the fastest diffeomorphic registration algorithm [Hermosillo 2002, Beg 2005, Ashburner 2007, Hernandez 2007, Marsland 2007, Avants 2008].

We begin with the presentation of the diffeomorphic extension [Vercauteren 2009] of Thirion's Demons registration algorithm [Thirion 1998]

for 3D images that is used to determine the motion transformations $M_{j,k}$ and $M'_{j,k}$. Then we present a novel extension of Demons algorithm to vector-valued images that is used to determine the reference shape transformation S_j^{4D} of the 4D registration framework.

5.4.1 Standard 3D Diffeomorphic Demons

The original Demons registration algorithm [Thirion 1998] is based on optical flow. But it has been shown that introducing a hidden variable, called the correspondences, the Demons can be formulated as a well-posed energy minimization with an alternate optimization scheme [Cachier 2003]. When registering the target 3D image I' to the reference 3D image I , the update transformation u of the current transformation S is first determined by minimizing the correspondences energy E^{corr} (see Equation 5.5) to obtain the correspondences transformation $c = S \circ u$. Second, the correspondences transformation c is regularized to obtain the new transformation S . The correspondences energy E^{corr} is formulated as follows:

$$E^{\text{corr}}(\mathbf{u}) = \frac{1}{2|\Omega|} \int_{\omega \in \Omega} \left\| \begin{bmatrix} I(\omega) - I' \circ S(\omega) \\ \mathbf{0} \end{bmatrix} + \begin{bmatrix} \mathbf{G}^T(\omega) \\ \sigma(\omega)/\sigma_c \text{Id} \end{bmatrix} \mathbf{u}(\omega) \right\|^2 d\omega \quad (5.5)$$

where Ω is the overlap between I and $I' \circ S$, ω is the voxel position, $\mathbf{G}(\omega) = \frac{1}{2}(\nabla I(\omega) + \nabla I' \circ S(\omega))$ is the spatial gradient of intensity whose formulation comes from a linearization of the ESM scheme detailed in [Vercauteren 2009], $\sigma(\omega) = |I(\omega) - I' \circ S(\omega)|$ is the local estimation of the image noise, and σ_c is a fixed parameter that bounds the spatial uncertainty on the correspondences transformation. Note that the transformation u , which outputs a position, and its corresponding deformation field \mathbf{u} are differentiated by bold characters. The link between them can be formulated as follows: $u = \text{Id} + \mathbf{u}$ where Id is the identity transformation.

A closed form solution of the minimization of the correspondences energy is given by the update vector field \mathbf{u} :

$$\mathbf{u} = -\frac{I - I' \circ S}{\mathbf{G}^T \mathbf{G} + \sigma^2/\sigma_c^2} \mathbf{G} \quad (5.6)$$

To constrain the update transformation to be diffeomorphic, the minimization of the functional is performed directly in the one-parameter subgroup of diffeomorphisms with stationary speed vector fields. Vercauteren *et al.* [Vercauteren 2009] showed that at a first order approximation this is equivalent to using the standard Demons algorithm and taking the exponential of the update transformation u . In this way, the update vector field \mathbf{u} is the speed vector field parametrizing the update diffeomorphic transformation $v = \exp(u)$.

The algorithm can be summarized as follows :

3D Diffeomorphic Demons Registration Algorithm

(from [Vercauteren 2009])

- (A) Choose an initial spatial transformation S .
 - (B) Iterate until convergence:
 - (1) Given S , compute the update vector field \mathbf{u} with Equation 5.6.
 - (2) If a fluid-like regularization is used (typically a Gaussian kernel),
let $\mathbf{u} \leftarrow K_{\text{fluid}} \star \mathbf{u}$.
 - (3) Fast computation of the exponential $\exp(u)$:
 - (a) Choose n such that $\|2^{-n}\mathbf{u}\|$ is close enough to 0, e.g.
 $\max\|2^{-n}\mathbf{u}(p)\| \leq 0.5$ voxel.
 - (b) Perform an explicit first order integration: $\mathbf{v}(p) \leftarrow 2^{-n}\mathbf{u}(p)$
for all pixels p .
 - (c) Do n (not 2^n !) recursive squarings of $v = \text{Id} + \mathbf{v} : v \leftarrow v \circ v$.
 - (4) Let $S \leftarrow S \circ v$.
 - (5) If a diffusion-like regularization is used (typically a Gaussian kernel), let $\mathbf{S} \leftarrow K_{\text{diff}} \star \mathbf{S}$.
-

5.4.2 Multichannel 3D Diffeomorphic Demons

Multichannel non-linear registration algorithms were mostly developed for the registration of DT-MRI [Ruiz-Alzola 2002, Rohde 2003, Park 2003, Zhang 2006, Cao 2006, Van Hecke 2007, Chiang 2008, Yeo 2009]. They were recently applied to the simultaneous fusion of multiple modalities [Avants 2007] and to the construction of multichannel atlas with different modalities [Rohlfing 2008]. Among those registration algorithms, an extension of the Demons algorithm to multichannel data has been proposed for DT-MRI registration based on transformation invariant tensor characteristics [Park 2003]. Basically, the authors average the update vector field computed independently for each channel. But in this approach, the real coupling between the channels is lost and approximated by averaging the update vector fields. Yeo *et al.* [Yeo 2009] preserved this coupling by extending the Demons algorithm to vector-valued images and also including the finite-strain differential to take into account the reorientation of diffusion tensors [Alexander 2001b]. In our case, we deal with data that do not need any reorientation, but we include a voxel-wise confidence map to each channel. Thus, we can formulate the multichannel Demons correspondences energy as follows :

$$E^{\text{corr}}(\mathbf{u}) = \sum_{j=1}^N \left(\frac{1}{2|\Omega_j|} \int_{\omega \in \Omega_j} \left\| \begin{bmatrix} I_j(\omega) - I_j' \circ S(\omega) \\ \mathbf{0} \end{bmatrix} + \begin{bmatrix} \mathbf{G}_j^T(\omega) \\ \sigma_j(\omega)/\sigma_c \text{Id} \end{bmatrix} \mathbf{u}(\omega) \right\|^2 \alpha_j(\omega) d\omega \right)$$

where N is the number of channels, Ω_j is the overlap between I_j and I'_j , $\mathbf{G}_j = \frac{1}{2}(\nabla I_j(\omega) + \nabla I'_j \circ S(\omega))$ is the spatial gradient of intensity in channel j whose formulation comes from a linearization of the ESM scheme detailed in [Vercauteren 2009], σ_j is the local noise estimation in channel j , and $\alpha_j > 0$ the voxel-wise weight map for the channel j .

Its minimization gives the following equation to solve at each voxel :

$$\sum_{j=1}^N \alpha_j (\mathbf{G}_j \mathbf{G}_j^T + \sigma_j^2 / \sigma_c^2 \text{Id}) \mathbf{u} = - \sum_{j=1}^N \alpha_j (I_j - I'_j \circ S) \mathbf{G}_j$$

Considering the eigen decomposition $\sum_{i=1}^3 \lambda_i^2 \mathbf{e}_i \mathbf{e}_i^T$ of the 3×3 symmetric positive matrix $D = \sum_{j=1}^N \alpha_j \mathbf{G}_j \mathbf{G}_j^T$, the update vector field becomes :

$$\mathbf{u} = \sum_{i=1}^3 \frac{P_i}{\lambda_i^2 + \sigma^2 / \sigma_c^2} \mathbf{e}_i \quad (5.7)$$

where $P_i = - \left(\sum_{j=1}^N \alpha_j (I_j - I'_j \circ S) \mathbf{G}_j^T \right) \mathbf{e}_i$ and $\sigma^2 = \sum_{j=1}^N \alpha_j \sigma_j^2$, and σ_c is a parameter that constrains the maximum step length such that the update vector field verifies $\|\mathbf{u}\| \leq \sigma_c \sqrt{d}/2$ (d the number of spatial dimensions in the image). The coupling between channels relies on the eigen decomposition of the sum D of the dyadic tensors $\alpha_j \mathbf{G}_j \mathbf{G}_j^T$. This formulation should improve the speed and accuracy of the convergence compared to previous multichannel approach with Demons algorithm [Park 2003], especially in the case of non-aligned gradient vectors.

The *Multichannel Diffeomorphic Demons* (MDD) algorithm is similar to the *Diffeomorphic Demons* (DD) algorithm except that at step (B)(1) the update vector field should be computed with Equation 5.7 instead of Equation 5.6.

5.5 Conclusion

In this chapter, we introduced a general setting of spatio-temporal registration of 4D time-series of images. In this setting, the registration can be decomposed into temporal and spatial transformations. The temporal transformation corrects the misalignment of physiological events defined by physiological state parameters chosen depending on the desired application. The spatial transformation aims to map the same corresponding physical points over time, or in other words to map corresponding trajectories of points. This can be translated into constraints on the inter-sequence spatial transformations and the intrasequence motion transformations previously determined independently in each sequence. We called these constraints the trajectory constraints.

We showed that under these constraints the 4D spatial registration of two sequences can be formulated as a multichannel 3D registration at a reference time point. In this way, the problem is highly simplified by determining a single spatial transformation mapping two sequences and by using the trajectory constraints to

reconstruct the other transformations with the help of the intrasequence motion transformations.

We also proposed a rigorous extension of the 3D *Diffeomorphic Demons* to vector-valued images, called *Multichannel Diffeomorphic Demons*. This extension has been used to perform the multichannel 3D registration, a simplified version of 4D spatial registration taking into account the trajectory constraints.

REGISTRATION OF 4D CARDIAC CT SEQUENCES: EVALUATION AND APPLICATION

Contents

6.1	Introduction	103
6.2	An Evaluation Study on Intersubject Registration	104
6.2.1	A General Computation Time Study	106
6.2.2	Registration of Electromechanically Simulated Sequences	107
6.2.3	Intersubject Registration of Real Sequences	114
6.3	Application to the Analysis of Ventricular Remodeling after Therapy	120
6.3.1	Data	122
6.3.2	Strain Analysis from Motion Tracking	122
6.3.3	<i>Remodeling Strain</i> Analysis from 4D Registration	129
6.4	Conclusion	131

6.1 Introduction

The framework presented in Chapter 5 is applied to the inter-subject registration of 4D cardiac CT sequences for evaluation. We compare it to other standard methods with real patient data and synthetic data simulated from a physiologically realistic electromechanical cardiac model [Serresant 2006a]. Then a prospective example of application is presented with the spatio-temporal registration of 4D cardiac CT sequences of the same patient before and after radiofrequency ablation (RFA) in case of atrial fibrillation (AF). The inter-sequence spatial transformations over a cardiac cycle allow to analyze and quantify the regression of left ventricular hypertrophy and its impact on the cardiac function.

6.2 An Evaluation Study on Intersubject Registration

In order to evaluate the advantages of the proposed registration method based on the multichannel 3D registration with trajectory constraints, we compare it to other methods based on the 3D registration of scalar-valued images with or without the trajectory constraints. When trajectory constraints are considered, the reference frame is set as the ED frame that is the first frame of the 4D cardiac CT sequences. To use these trajectory constraints as mentioned in section 5.2.2, motion tracking is previously performed in each sequence with an updated Lagrangian scheme where the registration of the current frame k to the reference frame 1 is initialized with the registration result of the previous frame $k - 1$ to the reference frame 1. We used the DD algorithm [Vercauteren 2009] described in Section 5.4.1 for pairwise registration with the following parameters in both synthetic and real data experiments: diffusion-like regularization $\sigma_{\text{diff}} = 1$, maximum update field length bounded with $\sigma_c = 1$, and 30 iterations (stopped if the similarity measure increases) at each of the 3 levels of multiscaling (size of each dimension divided by 2 at each level). The resulting motion transformations $M_{1,k}$ and $M'_{1,k}$ are considered as fixed during the estimation of the inter-sequence transformations S_k . The inversion of motion transformations is also necessary when using trajectory constraints. This inversion is performed by minimizing a functional as described in [Cachier 2002].

The different methods we use to register sequences are the following:

- **3D direct**: each inter-sequence transformation S_k is computed independently from the others.
- **3D sequential**: the computation of the inter-sequence transformation S_k is initialized with the transformation $M'_{k,k-1} \circ S_{k-1} \circ M_{k,k-1}^{-1}$ using the previously computed transformation corrected with the motion tracking to satisfy the trajectory constraints.
- **3D + TC**: solely the inter-sequence transformation S_1 in the ED frame is computed independently from the others that are then reconstructed from S_1 and the motion tracking in both sequences to satisfy the trajectory constraints (TC).
- **3D average + TC**: solely the inter-sequence transformation S_1 is computed using the average grey-level image of all the frames registered to the reference ED frame with the motion tracking. The inter-sequence transformations S_k at other time-points are then reconstructed from S_1 and the motion tracking to satisfy the trajectory constraints (TC).
- **3D MC + TC**: solely the inter-sequence transformation S_1 is computed using the multichannel (MC) registration of vector-valued image whose components are all the frames registered to the reference ED frame. The inter-sequence transformations S_k at other time-points are then reconstructed from S_1 and the motion tracking to satisfy the trajectory constraints (TC). This method

corresponds to the 4D spatial registration algorithm presented in Section 5.2.2 in which the multichannel registration is performed with the MDD detailed in Section 5.4.2.

These methods can be divided into three groups. First, the group of registration methods that perform a 3D scalar-valued image registration at each time point. We call this group the “3D” methods (*3D direct* and *3D sequential*). Second, the group of registration methods that perform a 3D scalar-valued image registration at a reference time-point and that reconstruct the other inter-sequence transformations using the trajectory constraints. We call this group the “3D + TC” methods (*3D + TC* and *3D average + TC*). And the last group uses the 3D multichannel registration method at a reference time-point and reconstructs the other inter-sequence transformations using the trajectory constraints. We call this group the “3D MC + TC” method (*3D MC + TC*). The comparison between the “3D” methods and the two other groups of methods, “3D + TC” and “3D MC + TC” methods, will show the advantage of registering a single reference time-point and using the trajectory constraints to reconstruct the other inter-sequence transformations. And the comparison between the “3D + TC” methods group and the “3D MC + TC” methods will show the advantage of using a multichannel registration when registering the reference time-point.

When estimating the inter-sequence transformation S_k with either scalar-valued (DD) or vector-valued (MDD) registration algorithms, the following parameters are used in both synthetic and real data experiments: fluid-like regularization $\sigma_{\text{fluid}} = 0.5$, diffusion-like regularization $\sigma_{\text{diff}} = 0.5$, maximum update field length bounded with $\sigma_c = 1$, and 100 iterations (stopped if the similarity measure increases) at each of the 3 levels of multiscaling (size of each dimension divided by 2 at each level).

Since registration is an ill-posed problem, solely checking the intensity matching between the reference image and the transformed target image to compare the different methods is not sufficient. Different mappings can lead to the same similarity measure. Thus we might perfectly match the intensities without recovering the expected deformation field. The best accuracy measurement of a registration algorithm would be to compare the estimated deformation field to the expected deformation field (e.g., gold standard). Generally these ground truth transformations are not available [Mäkelä 2002] which makes difficult the validation of registration algorithms, especially in the case of inter-subject registration. Thus validation of registration algorithms is often limited to partial ground truth information such as segmentations. To overcome the lack of full ground truth information in patient data, we compare the registration methods with synthetic cardiac sequences simulated from a physiologically realistic electromechanical cardiac model [Serresant 2006a] in which the ground truth inter-sequence and intrasequence transformations are known. With real 4D cardiac CT sequences, we compare the registration methods using semi-automatic segmentations of the LV/RV endocardium and epicardium since the underlying ground truth transformations are unknown. We start with a computation time comparison between the *Diffeomorphic Demons* (DD) and the

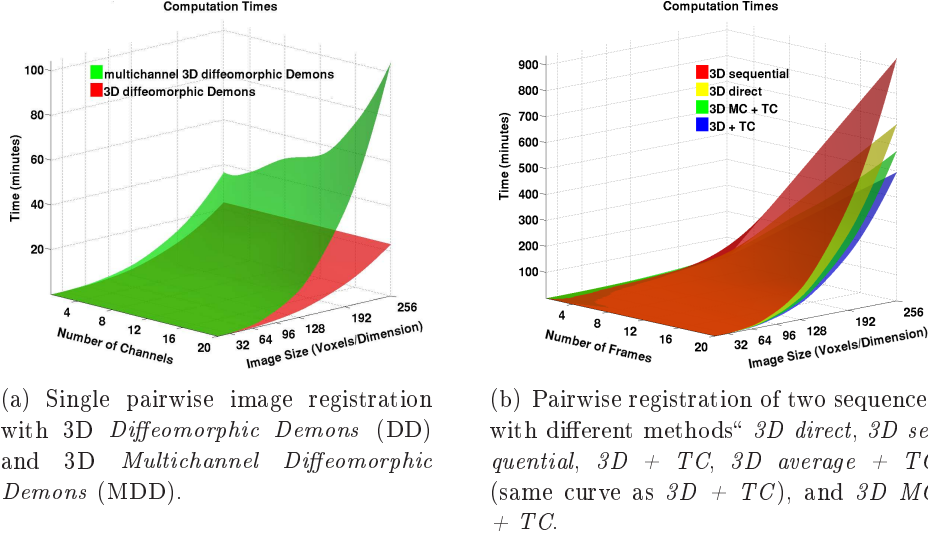


Figure 6.1: Computation time of different registration algorithms with respect to the number of channels (a) or frames (b), and the size of the images (same size in every dimension X, Y, and Z). The same number of iterations has been performed for each method (30 iterations at each of the 3 levels of multiscaling). The experiments are performed on a PC with Intel Core 2 Duo @ 2.26GHz processor. - (a) A general comparison between the pairwise registration of scalar-valued images and the pairwise registration of vector-valued images is shown. By definition, the scalar-valued image registration does not depend on the number of channels. The vector-valued image registration is more time consuming when the number of channels and the size of the image increase significantly. - (b) Comparison between the different methods used to register sequences: *3D direct*, *3D sequential*, *3D + TC* (whose curve is similar as *3D average + TC*), and *3D MC + TC*. The differences between methods increases significantly when the number of frames in the sequence and the size of the images increase.

Multichannel Diffeomorphic Demons (MDD) to register images, and between the methods previously presented to register sequences.

6.2.1 A General Computation Time Study

Computation time is an important issue when dealing with large data as 4D cardiac CT sequences. First, we compare the computation time of the core scalar-valued DD and the vector-valued MDD registration algorithms. Figure 6.1 shows that MDD is more time consuming than DD especially when the number of channels and the image size increase significantly. Note that when only one channel is considered, the computation times between the two algorithms are different. Indeed, the MDD is coded with a vectorial data structure that is more complex to handle.

Second, we compare the computation time when registering two sequences with the different methods. In these computation times are included the time to compute the motion tracking in the target sequence used for temporal transformation with

motion-based interpolation (all methods), the time to compute the motion tracking in the reference sequence, compose and invert deformation fields when using trajectory constraints (methods with TC and *3D sequential*), the time to compute the inter-sequence transformations (all methods). Since *3D + TC* and *3D average + TC* have very similar computation times, we only show in Figure 6.1 the computation time of *3D + TC*. The results clearly show when estimating the inter-sequence transformation at every frame takes longer, even if using only 3D scalar-valued registrations that is faster than 3D vector-valued registrations. More registrations are necessary when using the trajectory constraints (additional motion tracking computed in the reference sequence). But since the motion tracking converges faster than inter-subject registration (smaller and smoother deformations), the use of trajectory constraints keeps having lower computation times. The *3D sequential* is the most time consuming since trajectory constraints are used and inter-sequence transformations are estimated at each frame. The *3D MC + TC* method is not the fastest one but has reasonable computation times compared to the fastest *3D + TC* method. The counterpart of the reasonable computation time of the *3D MC + TC* method that solves globally the 4D registration is the memory requirements. Compared to other registration methods that are scalar-valued, the *3D MC + TC* method has memory requirements multiplied by about the number of channels. For instance, in experiments with real data ($174 \times 134 \times 174$ voxels and 20 frames) detailed in the following, a vector-valued registration requires up to about 11 Gb RAM (which can be handled on regular 64 bits PC), whereas a scalar-valued registration requires only up to about 500 Mb RAM.

6.2.2 Registration of Electromechanically Simulated Sequences

6.2.2.1 Construction of Electromechanically Simulated Sequences

Previous works [Segars 2008, Haddad 2007] already proposed methods to build synthetic 4D cardiac sequences. But these methods do not provide a framework directly applicable to the evaluation of 4D registration in which we need the joint construction of two sequences where both intrasequence and inter-sequence transformations are fully known. Thus to simulate physiologically realistic and fully controlled time-series of cardiac images, we built two cardiac sequences using an electromechanical model of the heart [Sermesant 2006a] from a single 4D CT frame as described in Figure 6.2.

We start from an initial frame at ED of a real cardiac CT sequence with $190 \times 150 \times 190$ voxels at a resolution of $1.0 \times 1.0 \times 1.0$ mm³. A segmentation of the myocardium is used as an input for electromechanical simulations of a full cardiac cycle lasting 0.8 seconds. The output of the simulation is a deformation field in the myocardium extrapolated outside the myocardium with an iterative diffusion process. Basically, we perform successive Gaussian smoothing of the deformation field ($\sigma = 1, 50$ iterations) where at each iteration the deformation field in the myocardium is reset to the simulated one and the deformation field farther than

15 mm of the myocardium is reset to be null. Thus, the initial grey-level image at ED can be physiologically deformed to create a sequence over a whole cardiac cycle with a temporal sampling of 20 frames. In the resulting sequence, the ground truth intrasequence motion transformations are known. In order to build a second sequence whose inter-sequence transformations with the first one are known, we register the initial frame of the first sequence to the anatomy of another real patient. Then, the resulting deformation field is used to transform the initial frame of the first patient and create another cardiac anatomy. Based on this new cardiac anatomy, we simulate another sequence using different parameters chosen such that both sequences have the same cardiac cycle length with corresponding ED and ES physiological time-points. Thus, the two sequences are by construction temporally aligned according to the global physiological events defined for temporal alignment in Section 5.2.1. In this way, we can directly focus on the 4D spatial registration we want to evaluate. Finally, we obtain two electromechanically simulated sequences of 20 frames whose inter-sequence anatomical and intrasequence motion transformations are fully known. We also created a noisy version of these simulated sequences adding Gaussian noise with different signal-to-noise ratio (SNR ranging from 18 to 54) at each frame.

6.2.2.2 Results

As mentioned previously, since the solution of the registration is not unique (aperture problem), we decided not to use the similarity measure (SSD) as a registration accuracy measure. For the same intensity matching, different transformations are possible. In our experiments, we even noticed that a better matching of the intensities did not necessarily imply a better estimation of the expected ground truth transformation (up to a certain extent). We used two measures to compare the registration algorithms: the distance to the ground truth transformations and the deviation from the trajectory constraints. Both measures are computed solely in a region of interest which is the myocardium.

The distance to the ground truth transformations, which measures the accuracy of the registration at each time-point, is presented in Figures 6.3 and 6.4. The comparison of average motion tracking errors (0.48 mm for a standard deviation of 0.47 mm) and average inter-sequence registration errors when using trajectory constraints (from 1.79 mm to 2.80 mm with a standard deviation of 0.97 mm at the lowest) confirms the assumption that motion tracking is more accurately estimated than inter-sequence transformations and thus can help for the improvement of inter-sequence registration. The basic *3D direct* registration is not a good strategy with the lowest and most variable registration accuracy over time. The *3D sequential* registration is an improved version of the *3D direct* registration where the inter-sequence transformations are linked to their temporal neighbors by using the result of the previous time-point registration with motion correction to initialize the registration. The *3D sequential* registration performs the best in terms of registration accuracy after a transient period where *3D MC + TC* registration performs better.

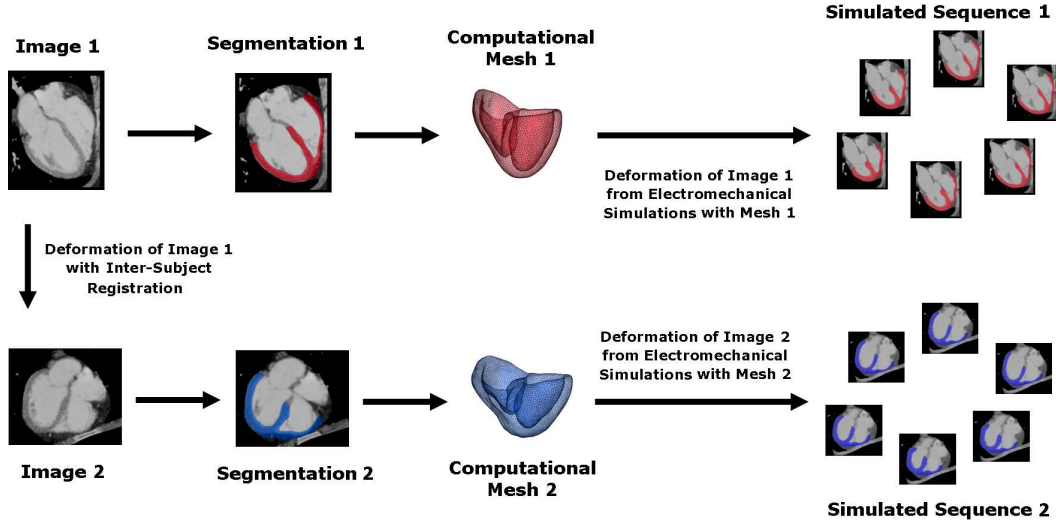


Figure 6.2: Construction of simulated sequences using a physiologically realistic electromechanical model of the heart [Sermesant 2006a]. The ED frame (Image 1) from the 4D cardiac CT sequence of a given patient is segmented (Segmentation 1) to obtain a mesh of the myocardium (Computational Mesh 1). This mesh is used for electromechanical simulations and for creation of a synthetic but physiologically realistic motion of the heart where the deformation fields between each frame are known. Based on these deformation fields, the reference image (Image 1) is deformed to create a sequence of images (Simulated Sequence 1). Next the reference ED frame is transformed into the ED frame of another patient (Image 2) with a known deformation field that was computed to best match the anatomy of the two patients. From this image of another anatomy at ED (Image 2), we can apply the same process as previously with Image 1 to build another sequence of images (Simulated Sequence 2). In the end, we obtain two electromechanically simulated sequences whose intrasequence physiological motion transformations and inter-sequence anatomical transformations are known. These ground truth transformations can be used to assess the accuracy of different registration methods.

Actually, $3D\ MC + TC$ registration is more accurate than other methods performing a single registration at a reference time-point (in our case the ED frame) and reconstructing the spatial transformations at other time-points using the trajectory constraints ($3D + TC$ and $3D\ average + TC$). It shows the advantage of using information from the whole sequence and the advantage of combining this information in a multichannel framework. For instance, the lower registration accuracy of the $3D\ average + TC$ registration shows that the multichannel registration is a good strategy to combine the information from the whole sequence. Averaging the images instead of keeping the original multichannel values yields a blurring of the original information and a loss of structural information. On the other hand the multichannel registration preserves the original intensity values of each frame in a vector. Only the update vector field as formulated in Equation 5.7 is combining the information from all channels without modifying the original information used for

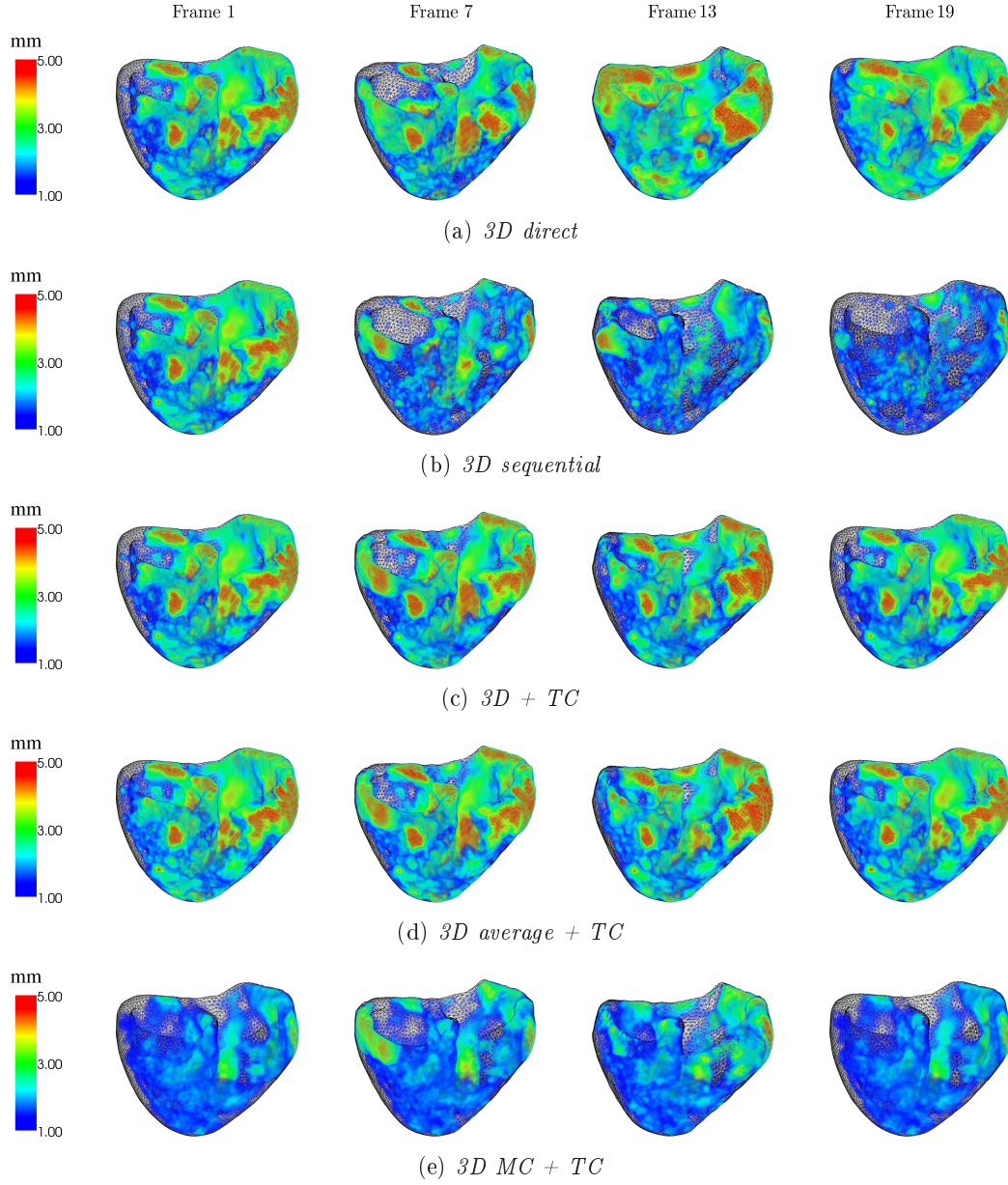


Figure 6.3: Registration Accuracy with Electromechanically Simulated Sequences - Spatial distribution of differences between the estimated inter-sequence anatomical transformation S_j and the ground truth transformations in the myocardium of simulated sequences at different time-points (frames 1, 7, 13 and 19).

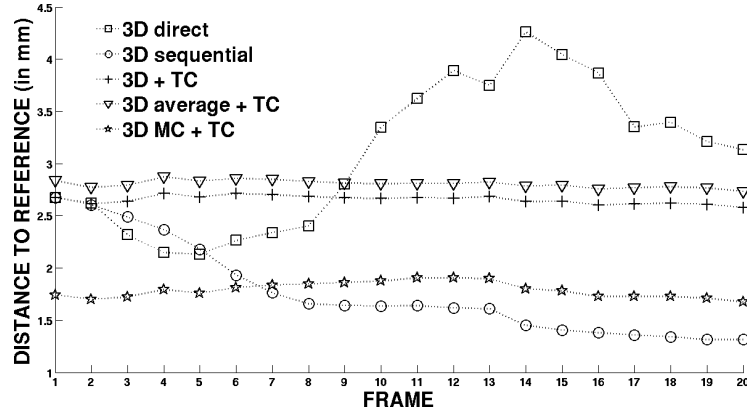


Figure 6.4: Registration Accuracy with Electromechanically Simulated Sequences - Difference between the computed inter-sequence anatomical transformations S_j and the ground truth transformations over time in the myocardium.

the registration. Furthermore, the registration methods using the trajectory constraints (“3D + TC” and “3D MC + TC” groups) have more consistent registration accuracy over time than methods of the “3D” group. Trajectory constraints act as a temporal regularization of inter-sequence transformations. The good results of the *3D MC + TC* registration show that taking into account the information from the whole sequences even in a single 3D registration at a given time-point helps to improve the registration accuracy.

The deviation to the trajectory constraints measures the consistency between the inter-sequence anatomical transformations and the intrasequence motion transformations. This measure of consistency is computed as described in Figure 6.5. We perform a pairwise comparison of all the transformations $T_j = M_{1,j}'^{-1} \circ S_j \circ M_{1,j}$ matching the initial reference frames of the two sequences and obtained through different pathways. This measure is complementary to the registration accuracy and different from the registration consistency in loops presented in [Roche 2001, Pennec 2005]. A better estimation of the inter-sequence transformations does not necessarily mean that the deviations to the trajectory constraints get lower, since these deviations are computed with an estimation of the apparent motion, and not the ground truth motion we are not supposed to have access to. In Figure 6.6, results show that trajectory constraints are not properly satisfied when computing independently the inter-sequence transformations at each time-point (“3D” group). In the “3D + TC” and “3D MC + TC” groups, the deviation to trajectory constraints is very low. It was expected since by construction these methods satisfy the trajectory constraints. Actually these errors we observe correspond to residual errors due to composition and inversion of transformations in the reconstruction process. It is important to see that these errors are very low compared to the deviations observed in the “3D” group. It shows that these higher deviations are not due to computational errors when determining the transformations

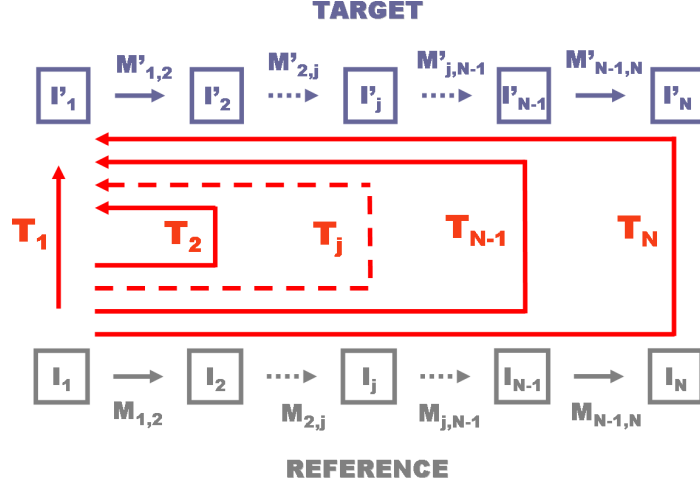


Figure 6.5: Deviation from Trajectory Constraints - The deviation from trajectory constraints is measured by computing the distance between the transformations $T_j = M'^{-1}_{1,j} \circ S_j \circ M_{1,j}$ that should be the same if they satisfy the trajectory constraints. For electromechanically simulated data, we compute it in the whole myocardium. For real data since the accuracy of the registration is restricted to the LV/RV endocardial and epicardial surfaces, we also limit the measure of the deviation to trajectory constraints on these surfaces.

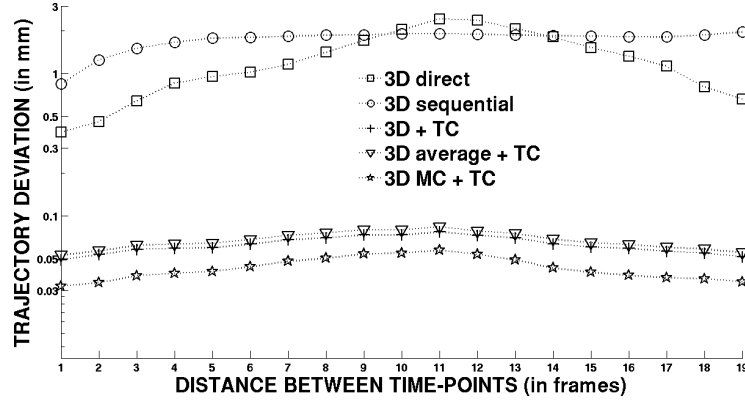


Figure 6.6: Trajectory Constraints with Electromechanically Simulated Sequences - The deviation from the trajectory constraints in the myocardium is computed by measuring the distance between the transformations T_j corresponding to a given pathway using the inter-sequence transformation S_j as described in Figure 6.5. A log-scale is used for a better visualization of the methods that by construction satisfy the trajectory constraints ($3D + TC$, $3D \text{ average} + TC$, and $3D \text{ MC} + TC$). The other methods are significantly less consistent with the motion tracking.

T_j but are mostly due to low consistency between inter-sequence and intrasequence transformations.

We also measure the smoothness of the inter-sequence transformation with the

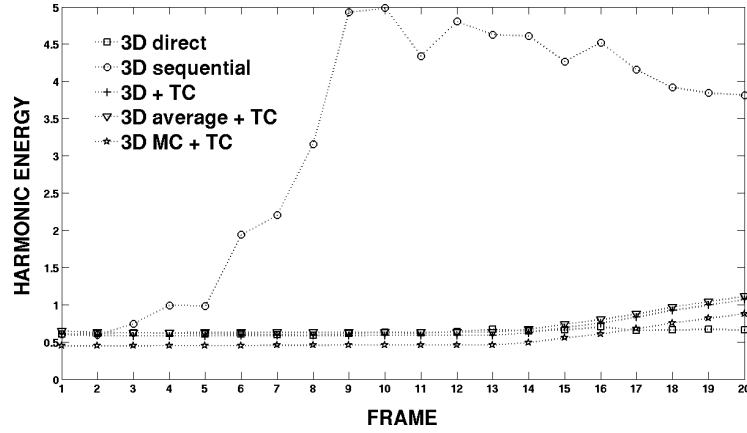


Figure 6.7: Harmonic Energy with Electromechanically Simulated Sequences - The harmonic energy quantifies the amount deformation in the transformation. The *3D MC + TC* registration gives a much smoother deformation field at the initial reference frame where the multichannel registration is computed.

Method	μ Diff.	σ Diff.	Dev. TC	HE
<i>3D direct</i>	3.08 mm	1.90 mm	1.27 mm	1.48
<i>3D sequential</i>	1.78 mm	1.33 mm	1.76 mm	7.49
<i>3D + TC</i>	2.65 mm	1.93 mm	0.06 mm	1.58
<i>3D average + TC</i>	2.80 mm	1.92 mm	0.07 mm	1.68
<i>3D MC + TC</i>	1.79 mm	0.97 mm	0.04 mm	1.25

Figure 6.8: Results summary of the registration of electromechanically simulated sequences with mean difference to ground truth transformation (μ Diff.), standard deviation of difference to ground truth transformation (σ Diff.), deviation from trajectory constraints (Dev. TC), and harmonic energy (HE).

harmonic energy of their corresponding deformation fields (the average norm of the Jacobian). As shown in Figure 6.7, the harmonic energy are almost the same for every method except the *3D sequential* whose smoothness decreases when registration accuracy increases. Thus the *3D MC + TC* seems to be a good compromise between registration accuracy and smoothness of the resulting deformation field.

Figure 6.8 summarizes the performances of each registration method in terms of registration accuracy, deviation to trajectory constraints, and harmonic energy. Similar results were obtained with noisy simulated sequences except that the registration with every method was not as accurate as with noise-free simulated sequences. All these results support the thesis that the *3D MC + TC* registration is the best compromise between accuracy, spatial smoothness, and temporal consistency with motion tracking. But even if these results are obtained with physiologically realistic simulated sequences, the different registration methods still need to be evaluated on experiments with real patient data as in the following.

6.2.3 Intersubject Registration of Real Sequences

6.2.3.1 Data and Processing

In the following experiments, we used 4D cardiac CT sequences acquired with contrast agent at a spatial resolution of about $0.825 \times 0.825 \times 1.00 \text{ mm}^3$ with $256 \times 256 \times 231$ voxels on 5 different patients with pulmonary stenosis. We are grateful of Dr Harold Litt from the Hospital of University of Pennsylvania for provision of 4D CT datasets. Since the field of view (FOV) of each acquisition is different, the sequences were cropped to get similar structures in the surrounding area of the heart. The images are then resampled at a spatial resolution of $1.00 \times 1.00 \times 1.00 \text{ mm}^3$ with $174 \times 134 \times 174$ voxels. The temporal acquisition is synchronized to the ECG from ED over a cardiac cycle with 20 frames. At this temporal resolution, each frame correspond to an acquisition after 5% of R-R time interval (interval between two consecutive R peaks of the ECG).

Since sequences were acquired with contrast agent, we can easily differentiate the blood pool that has higher intensity values than the myocardium. Unfortunately the SSD similarity criterion for registration is meaningless in the blood pool where the intensity values are highly variable in space and time. Since these artifacts can mislead the registration, we first decrease the range of intensity values of the blood pool by linearly transforming the part of the image histogram (basically the intensities higher than a given threshold). Furthermore there might also be inter-sequence differences in the intensity histogram (for instance a sequence of our dataset had obviously higher intensity values for the myocardium). To avoid a mismatch of corresponding structures using the SSD similarity criterion, we perform a matching of the intensity histogram (*HistogramMatchingImageFilter* from ITK Software Library [Ibanez 2003]) between each corresponding frames of the reference and target sequences. The histogram matching is only performed for inter-sequence registration and not when performing the motion tracking between frames of the same sequence whose intensity histogram are stable over time.

Given the standardized acquisition process of 4D cardiac CT sequences, the global linear temporal registration between different sequences to match the R-R interval is intrinsically performed. The nonlinear part of the temporal transformation is based on blood volume curves (basically obtained with an intensity threshold followed by a main connected component extraction and a closing) that defines a global mechanical state of the heart. Figure 6.9 shows the normalized volume curves of each sequence before and after alignment. The temporal transformation is obtained with a Piecewise Cubic Hermite Interpolating Polynomial (PCHIP) matching specific points of the curves: the first and last frames that corresponds to the linear matching of the R-R interval, the null first derivative of the curve that corresponds to ES, and two null second derivatives of the curves. The resulting transformations have been compared to transformations obtained from ground truth segmentations used in the following to measure the accuracy of 4D registration. Results showed that the error on the temporal transformation was significantly below the temporal resolution of 1 frame: an average of 0.26 frame, a standard deviation of 0.19 frame,

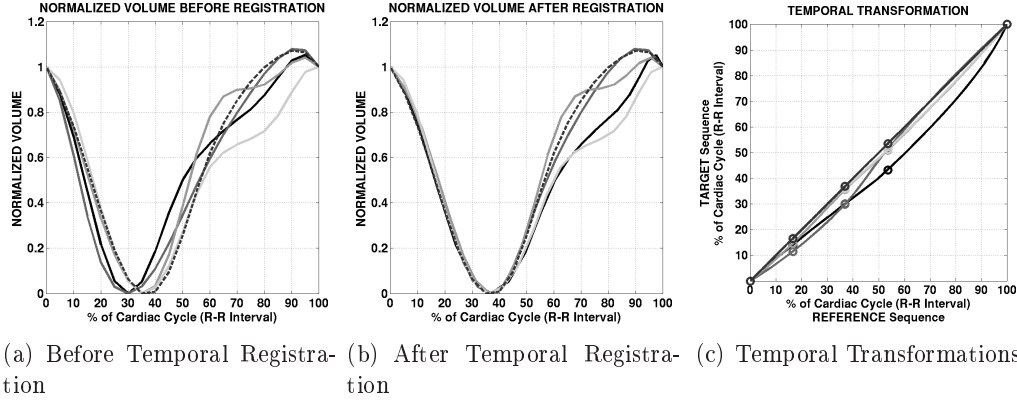


Figure 6.9: Normalized blood volume curves (a) before and (b) after temporal registration in each sequence. The dashed black curve is the reference sequence. The continuous curves are the target sequences. The temporal transformations are shown in figure (c).

and a maximum error of 0.59 frame. It shows that the basic segmentation we proposed is sufficient for the estimation of the temporal transformation. The result of the temporal alignment is shown in Figure 6.9. Once the temporal transformation is known, the target sequence is temporally resampled using a motion-based interpolation [Ehrhardt 2006], as well as its corresponding intrasequence motion transformations.

For 4D spatial registration, we first choose the reference frame as the ED frame (first initial frame in each sequence that correspond to the acquisition at the R peak of the ECG). This reference frame is used to perform motion tracking with an updated Lagrangian scheme that provides a temporal causality : estimation of the motion transformations $M_{1,k}$ registering a given frame at a time-point t_k to the reference frame at the reference time-point t_1 with an initial transformation set as the motion transformation $M_{1,k-1}$. Then a reference sequence is chosen among the dataset on which the other ones are registered using the methods presented at the beginning of this Chapter 6. The inter-sequence registrations are initialized with an affine transformation determined by matching the blood volumes previously determined for temporal alignment.

6.2.3.2 Results

Since we do not have access to the ground truth transformations, we rely on a partial ground truth information, the segmentations of the myocardium with a semi-automatic delineation of the LV/RV endocardium and epicardium. Thanks to the image quality and the high contrast of intensities between the myocardium and the blood pool, the endocardium is easily identified in the sequences. We performed a supervised segmentation of the endocardium in the reference frame (ED) using a single connected-component surface isovalue that has been interactively restricted to be below the valve plane and visually checked. On the other hand, the epicardium is

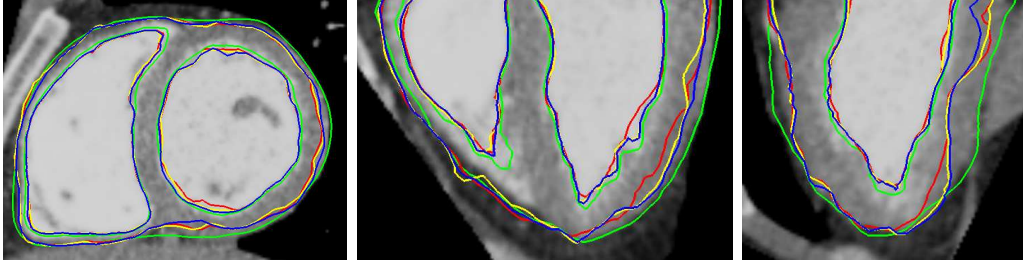


Figure 6.10: Registration Accuracy with Real Sequences - We illustrate the accuracy of the registration by showing the transformed LV/RV endocardial and epicardial surfaces with the transformation fields computed with different methods. We only show one method for each group for a better visualization of the differences. The color codes are: *3D direct* in red, *3D + TC* in yellow, *3D MC + TC* in blue, and the ground truth in green. The differences are not apparent everywhere but the *3D MC + TC* provides an overall better registration. Lower registration accuracy appears in areas where structures have high curvature for the endocardium and in areas where there is a low intensity gradient between the heart and neighboring organs for epicardium.

difficult to define solely in terms of intensity features due to the low intensity gradient between the heart and neighboring organs in some areas. The segmentation of the epicardium is performed interactively by manually adding landmarks that lie on the epicardial surface interpolated with radial basis functions. These segmentations in the reference frame are then propagated over the whole sequence with motion transformations.

To measure the accuracy of the registration, we first compute in each frame a symmetric distance between the reference surface transformed with S_j and the target surface. The symmetric distance between two surfaces Σ and Σ' is defined as follows:

$$d(\Sigma, \Sigma') = \frac{1}{|\Sigma|} \int_{v \in \Sigma} \min_{v' \in \Sigma'} d(v, v') dp$$

where v and v' are vertices respectively on surfaces Σ and Σ' .

Results show that the *3D MC + TC* registration performs better than others (see Figures 6.10, 6.11, and 6.16) with an improvement of about 11% compared to the second best method and about 17% compared to the *3D direct* method. For every methods, registration accuracy is locally lower in areas where structures are more complex and where there is low intensity gradient between neighboring organs for the epicardium. For instance, the RV apex is a narrow region where the complex structures of trabeculae that are highly variable between patients make the registration more difficult. The *3D sequential* registration does not perform as well with real data as with electromechanically simulated data but still improves the *3D direct* method. It probably shows some limitations of simulated data which are not as complex as real data. For instance, both simulated sequences were built from the same reference intensity image making the registration task easier. For real data, we observe that the group of “3D” methods are clearly not as good as

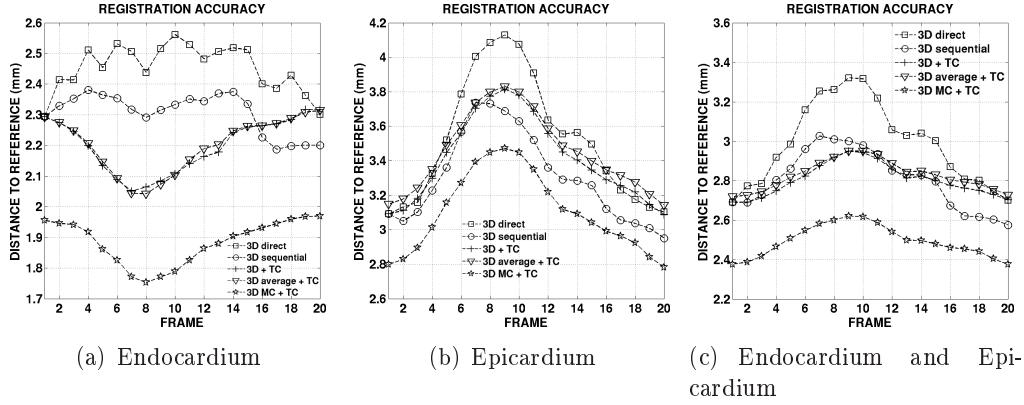


Figure 6.11: Registration Accuracy with Real Sequences - We measure the accuracy of the registration by computing a symmetric distance between the reference and transformed LV/RV endocardial and epicardial surface meshes. These values are an average value over all the patients. The *3D sequential* method improves the *3D direct* method but it does not perform as well as observed in electromechanically simulated sequences. Using the motion tracking with the trajectory constraints clearly improves the accuracy of the registration compared to inter-sequence transformations computed at each frame. The *3D MC + TC* method shows better results than other methods. It illustrates the advantage of using a multichannel registration in the reference frame over a single channel registration with original images or averaged images.

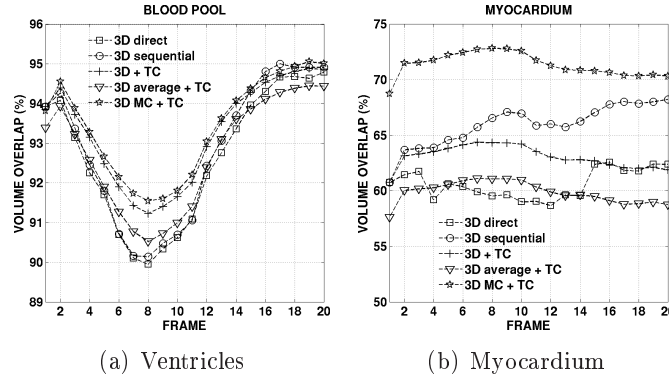


Figure 6.12: Registration Accuracy with Real Sequences - We measure the accuracy of the registration by computing the volume overlap of the ventricles and myocardium between the reference sequence and the transformed target sequence. These values are an average value over all the patients. The improvement of the volume overlap of the ventricles is low by using *3D TC + MC* method. And the volume overlap of the myocardium is significantly improved.

the others. It shows the limitations of the 3D pairwise registration of scalar-valued images for large inter-subject deformations, especially when getting closer to the ES frame. When using the information from the motion tracking, which is easier to

obtain with more accuracy than inter-subject anatomical registration, the registration is more consistent over time. The use of the trajectory constraints acts as a temporal regularization of the inter-sequence transformations with a stronger and more realistic *a priori* regularization between inter-sequence transformations than a basic smoothing that could not handle high motion speed and acceleration between frames. We also computed the volume overlap of the ventricles and the myocardium between the reference and transformed target sequences [Perperidis 2005b] to evaluate the registration accuracy as shown in Figure 6.12. The myocardium volume overlap is improved when using motion tracking information and even more when multichannel registration is used. Considering the better registration of the endocardium and the volume occupied by the ventricles compared to the myocardium, it is normal to obtain much higher volume overlap of the ventricles than myocardium.

As described in Figure 6.5, the deviation to trajectory constraints is measured comparing the reference endocardial surface deformed with the transformations $T_j = M_{1,j}'^{-1} \circ S_j \circ M_{1,j}$. The transformation T_j corresponds to the pathway from ED of the reference sequence to ED of the target sequence using the inter-sequence transformation S_j . When trajectory constraints are satisfied, all transformations T_j should be the same and thus all transformed endocardial surfaces should match. The deviation to trajectory constraints quantifies the consistency between motion and inter-sequence transformations. The use of trajectory constraints in the registration process clearly shows the improvement compared to methods computing independently the inter-sequence transformations at each frame (see Figures 6.13 and 6.14). In this way, the trajectory constraints act as a temporal regularization of the inter-sequence transformations. This advantage is particularly significant in areas of high curvature of the structures (e.g. the right ventricular apex). As mentioned previously, this high curvature can explain the locally lower registration accuracy but mostly the temporal change of this curvature due to cardiac motion can explain the discrepancies of registration accuracy over time.

To measure the quality of the registration, we also compared the spatial smoothness of the resulting deformation fields. To quantify the smoothness of the resulting deformation field, we compute at each time-point their harmonic energy. The lowest is the harmonic energy, the smoothest is the deformation field and the more likely it is to be a realistic solution. As shown in Figure 6.15, the *3D MC + TC* method provides the smoothest transformations. Combining the information coming from different time-points directly on the update vector field as formulated in Equation 5.7 provides intrinsically a smoother deformation field. On the contrary, when using trajectory constraints with 3D scalar-valued registration (“3D +TC” group), the resulting deformation fields are sharper than “3D” group of methods.

In terms of computation times, different methods have pretty similar computation times except for the *3D sequential* method that is slower than others (see Figure 6.16). In addition to temporal alignment (mostly motion tracking in target sequence) and spatial registration (scalar-valued or vector-valued), computation times also take into account the time for motion tracking in reference sequence, inversion and reconstruction of inter-sequence transformations with trajectory con-

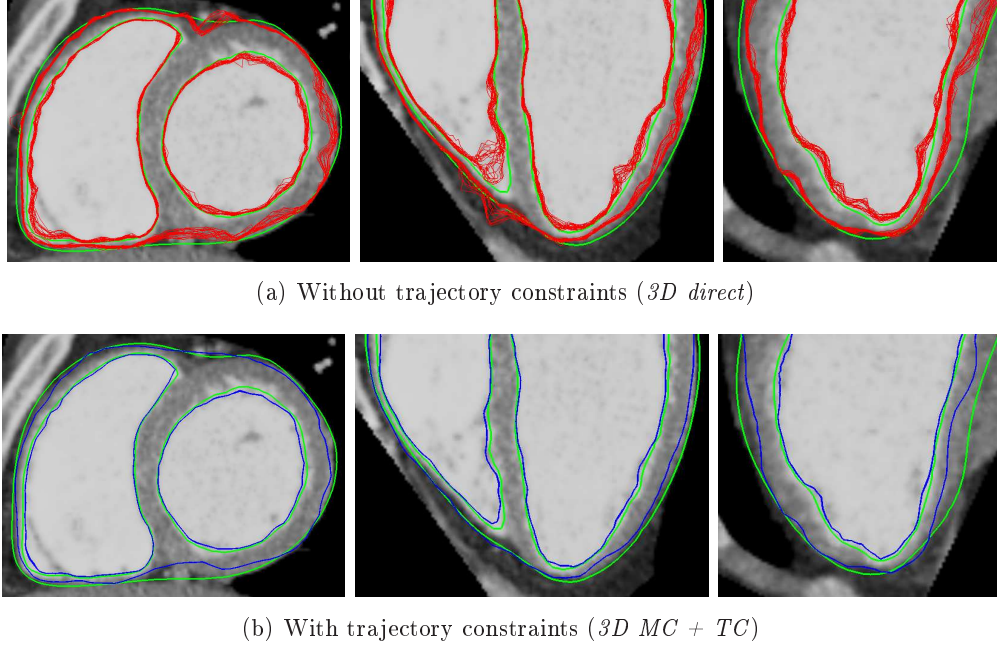


Figure 6.13: Trajectory Constraints with Real Sequences - We illustrate the deviation from the trajectory constraints with the transformation of the LV/RV endocardial and epicardial surfaces through different pathways in case of *3D direct* registration (first row in red) and in case of *3D MC + TC* registration (second row in blue). The ground truth segmentations are shown in green. When trajectory constraints are satisfied all the transformed contours should perfectly overlay to form a single contour. When the trajectory constraints are not used in the registration process (first row), it is obvious that the transformed contours have high discrepancies showing that the inter-sequence transformations are not consistent with the motion tracking. On the other hand, when trajectory constraints are used in the registration process (second row), we barely see the differences between transformed contours. The trajectory constraints are satisfied by construction as expected in theory. But it also shows that in practice numerical errors from composition and inversions of transformations are not significant. Showing the ground truth contour in green, we can visualize at the same time the quality of the registration. When trajectory constraints are not used, high discrepancies in quality of registration show that the quality of registration is not consistent over time.

straints when necessary. The advantage of using the trajectory constraints is that motion tracking is already available for the reference sequence if willing to compare motion between the two sequences.

Finally, results with real data also support the thesis that the *3D MC + TC* method is a good compromise between registration accuracy, temporal consistency with motion tracking, spatial smoothness, and computation time.

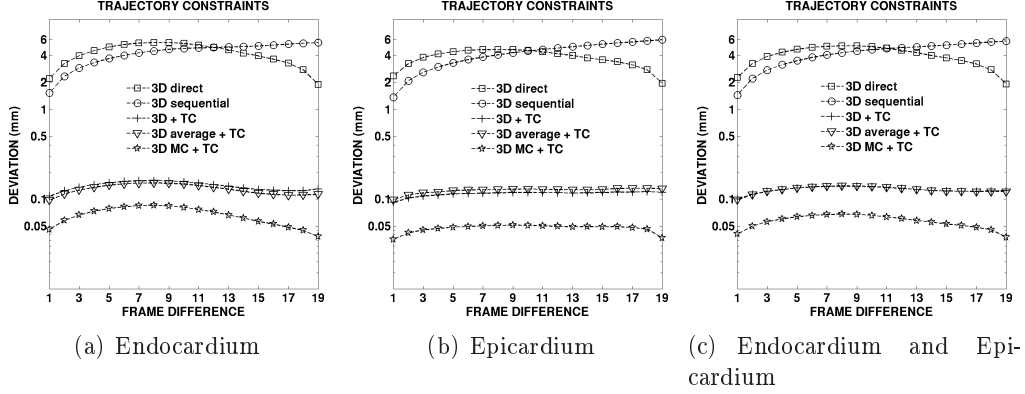


Figure 6.14: Trajectory Constraints with Real Sequences - The deviation from the trajectory constraints is computed with a distance between transformed segmentations through different pathways as shown in Figure 6.5. We compare all the transformed segmentations to each other. We plot this deviation with respect to the distance in frames between the two inter-sequence transformations used by a given pathway. A log-scale is used for a better visualization of the methods that by construction satisfy the trajectory constraints ($3D + TC$, $3D average + TC$, and $3D MC + TC$). The other methods are less consistent with the motion tracking as also shown in Figure 6.13 with the transformed segmentations.

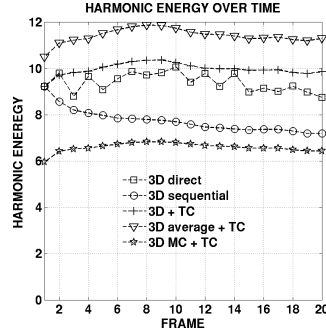


Figure 6.15: Harmonic Energy with Real Sequences - The harmonic energy quantifies the amount of deformation in the transformation. A method that gives similar accuracy results with a smoother transformation are more likely to be realistic. The $3D MC + TC$ registration provides the smoothest transformation. Whereas the $3D + TC$ and $3D average + TC$ do not improve and even increase the harmonic energy compared to $3D direct$ or $3D sequential$ methods.

6.3 Application to the Analysis of Ventricular Remodeling after Therapy

In this section, we present an example of potential clinical application where 4D spatio-temporal registration could help in analyzing the remodeling process of the heart after therapy. Pre- and post-operative sequences are compared in case of atrial

Method	μ Dist.	σ Dist.	VO	Dev. TC	HE	Time
<i>3D direct</i>	2.99 mm	2.07 mm	60.6 %	3.82 mm	9.4	56 min
<i>3D sequential</i>	2.80 mm	1.87 mm	65.9 %	4.07 mm	7.7	86 min
<i>3D + TC</i>	2.80 mm	1.91 mm	63.1 %	0.12 mm	10.0	47 min
<i>3D average + TC</i>	2.83 mm	1.94 mm	59.9 %	0.12 mm	11.4	49 min
<i>3D MC + TC</i>	2.49 mm	1.69 mm	71.3 %	0.05 mm	6.6	59 min

(a) Endocardium + Epicardium

Method	μ Dist.	σ Dist.	Dev. TC
<i>3D direct</i>	2.45 mm	1.79 mm	4.03 mm
<i>3D sequential</i>	2.31 mm	1.57 mm	4.12 mm
<i>3D + TC</i>	2.20 mm	1.55 mm	0.13 mm
<i>3D average + TC</i>	2.20 mm	1.56 mm	0.12 mm
<i>3D MC + TC</i>	1.88 mm	1.33 mm	0.06 mm

(b) Endocardium

Method	μ Dist.	σ Dist.	Dev. TC
<i>3D direct</i>	3.52 mm	2.36 mm	3.60 mm
<i>3D sequential</i>	3.30 mm	2.16 mm	4.02 mm
<i>3D + TC</i>	3.41 mm	2.27 mm	0.11 mm
<i>3D average + TC</i>	3.46 mm	2.34 mm	0.12 mm
<i>3D MC + TC</i>	3.10 mm	2.08 mm	0.04 mm

(c) Epicardium

Figure 6.16: Results summary of the registration of real sequences where μ Dist. is the mean distance to reference segmentation, σ Dist. is the standard deviation of the distance to reference segmentation, VO is the volume overlap of the myocardium, Dev. TC is the deviation from trajectory constraints, and HE is the harmonic energy. Computation times were performed with a PC with an AMD Opteron 246 @ 2GHz processor with 12Gb RAM. In these computation times are taken into account the time to perform the inter-sequence registration, to compute motion tracking, to align temporally the sequences, and to reconstruct of transformations with trajectory constraints when necessary.

fibrillation (AF) before radiofrequency ablation (RFA) and 3 months after. AF is the most common sustained cardiac arrhythmia where electrical impulses from sinoatrial nodes are overwhelmed by disorganized electrical impulses coming from the atria and pulmonary veins. The conduction of irregular impulses to the ventricles affects the rhythm of ventricular contraction and thus the cardiac mechanical function. It leads to hypertension, left atrial enlargement, and left ventricular hypertrophy. In case of hypertrophy, the contraction is faster and more powerful to cope with increase of pressure but it has a limited range of motion with a difficulty to relax properly. RFA is a common intervention for AF where the correction of the electrical activity in the left atrium is related to the regression of left ventricular hypertrophy [Mattioli 2005].

We first perform a strain analysis in both sequences before and after therapy

to compare cardiac function. Unfortunately, this comparison of cardiac function is not sufficient to explain the whole remodeling process and more specifically the anatomical remodeling process. Thus, we propose to use the 4D spatio-temporal registration framework to analyze the regression of left ventricular hypertrophy after therapy and its impact on cardiac function.

6.3.1 Data

We used two 4D cardiac CT sequences acquired with contrast agent at different spatial and temporal resolutions. The pre-operative sequence is acquired at a spatial resolution of $0.51 \times 0.51 \times 1.00 \text{ mm}^3$ with $512 \times 512 \times 249$ voxels and a temporal resolution of 10 frames for a cardiac cycle. The post-operative sequence is acquired at a spatial resolution of $0.88 \times 0.88 \times 1.00 \text{ mm}^3$ with $256 \times 256 \times 182$ voxels and a temporal resolution of 20 frames for a cardiac cycle. Both sequences are resampled at a spatial resolution of $1.00 \times 1.00 \times 1.00 \text{ mm}^3$ with $226 \times 226 \times 182$ voxels and a temporal resolution of 10 frames for a cardiac cycle. We are grateful of Dr Harold Litt from the Hospital of University of Pennsylvania for provision of these datasets.

6.3.2 Strain Analysis from Motion Tracking

The alteration of cardiac function is not always apparent with common global cardiac function indices, such as left ventricular ejection fraction (LVEF). For instance, LVEF of pre- and post-operative sequences are similar: 59.7% before and 61.1% after therapy. A more detailed analysis of cardiac function is necessary. Cardiac function can also be measured more locally with the strain derived from motion tracking in the myocardium.

We performed a motion tracking in each sequence using physically-constrained diffeomorphic Demons to ensure elasticity and nearincompressibility of myocardial tissue as described in [Mansi 2009]. These physical constraints have shown to provide more realistic strain values [Bistoquet 2008, Mansi 2009]. The elasticity is introduced by extending the Gaussian smoothing of the regularization step of the Demons algorithm to an elastic smoothing [Cachier 2004]. The myocardium near-incompressibility is ensured by constraining the deformations to be divergence free. To achieve it, each iteration of the Demons algorithm ends with an additional step of divergence free projection [Simard 1988] of the resulting deformation field in the myocardium. The motion tracking is computed in an updated Lagrangian scheme by determining the motion transformations M_j registering the current frame j to the reference frame at ED where the motion transformation M_{j-1} of previous step is used as an initialization. Once we know the motion transformations M_j , the Lagrangian finite strain tensor E is computed from the motion transformation $M_j = \text{Id} + \mathbf{M}_j$:

$$E_j = 1/2 (\nabla \mathbf{M}_j + \nabla \mathbf{M}_j^\top + \nabla \mathbf{M}_j^\top \nabla \mathbf{M}_j)$$

The projection of this strain tensor in the prolate coordinate system provides at each frame the radial, circumferential and longitudinal strains (respectively E_j^{rad} ,

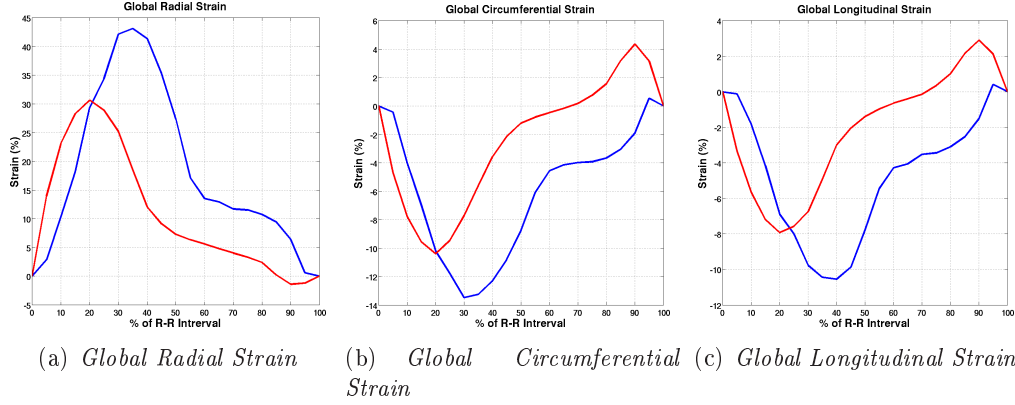


Figure 6.17: Global (a) radial, (b) circumferential and (c) longitudinal strains over a cardiac cycle (R-R interval) in LV myocardium of pre- and post-operative sequences (respectively red and blue curves).

E_j^{circ} and E_j^{long}) that are common clinical parameters used to evaluate cardiac function [Moore 2000].

Once strain values are computed in each sequence, they can be compared using different correspondence models from global to local. In absence of point-to-point correspondences between sequences, the cardiac function can be compared either globally by averaging strain values in the whole heart or locally by averaging strain values in each AHA zone (see Appendix C for definition of AHA zones).

6.3.2.1 Global Strain Comparison - Whole Heart

In this case, no correspondence are used between the two sequences. Thus, we average the radial, circumferential and longitudinal strains over the myocardium at each frame over the whole myocardium. In this way, we have access to global measures of cardiac function over time in each sequence as shown in Figure 6.17 with strain and in Figure 6.18 with strain rate.

Two major differences can be observed. First, the peak amplitudes of radial, circumferential and longitudinal strains are lower in the pre-operative sequence than in the post-operative sequences. To measure the relative change of strain between pre- and post-operative sequences, we compute the percentage of maximum strain difference relatively to the maximum strain value before intervention:

$$\Delta E = 100 \times \frac{E_{\max}^{\text{post}} - E_{\max}^{\text{pre}}}{E_{\max}^{\text{pre}}}$$

After intervention, the peak amplitudes are improved by 40.7% for radial strain, 29.7% for circumferential strain and 33.1% for longitudinal strain. Second, these peaks occur earlier in the pre-operative sequence ($\sim 20\%$ of R-R interval) than in the post-operative sequence ($\sim 35\%$ of R-R interval). When comparing the myocardium strain rate curves, the rates of contraction have similar behavior and

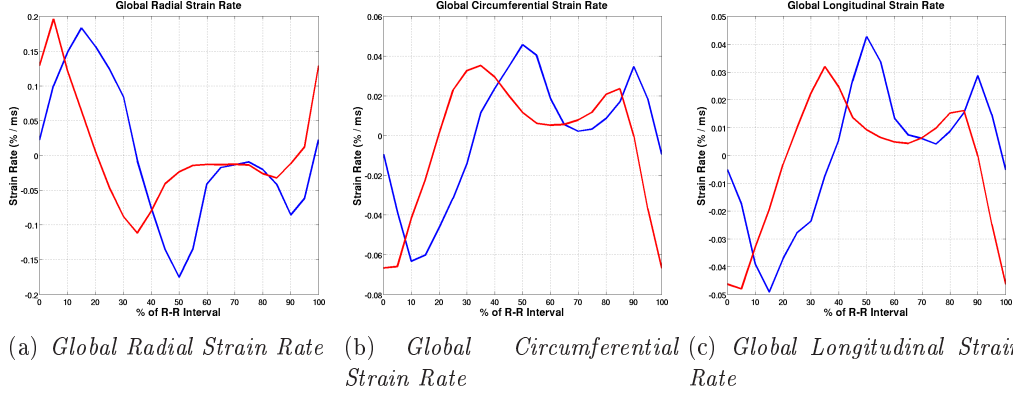


Figure 6.18: Global (a) radial, (b) circumferential and (c) longitudinal strain rates over a cardiac cycle (R-R interval) in LV myocardium of pre- and post-operative sequences (respectively red and blue curves).

maximum amplitude whereas the rate of relaxation have similar behavior but a bit lower maximum amplitude. It shows that the cardiac tissue mechanical properties do not really change after intervention. Mostly the times of contraction and relaxation are different between sequences. After RFA, the contraction lasts longer with similar strain rate which shows an improvement of the cardiac function.

6.3.2.2 Local Strain Comparison - AHA Zones

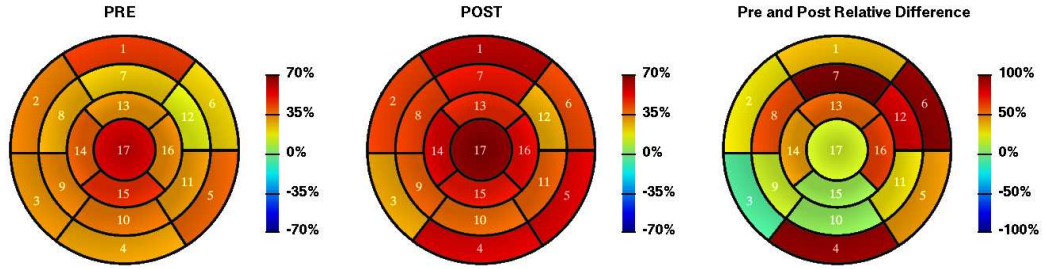
The AHA zones defined by the American Heart Association (described in Appendix C) are standardized zones of the myocardium longitudinally separated with basal, mid and apical zones and circumferentially separated with anterior, septal, inferior and lateral zones. In this way, quantities averaged in AHA zones can easily be compared in corresponding zones of different cardiac geometries. Radial, circumferential and longitudinal strains are averaged in each AHA zones and at each frame of pre- and post-operative sequences as shown with a bull's eye view in Figure 6.19 and as detailed in Figures 6.20, 6.21, 6.22, 6.23, 6.24, 6.25.

To measure the strain modification between pre- and post-operative sequences, we first compute the percentage of maximum strain difference relatively to the global average maximum strain value over the myocardium:

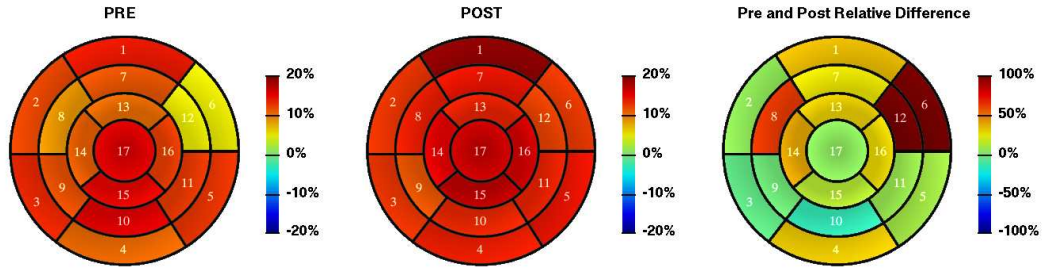
$$\Delta E = 100 \times \frac{E_{\max}^{\text{post}} - E_{\max}^{\text{pre}}}{E_{\text{mean}}^{\text{pre}}}$$

and show it with a bull's eye view in Figure 6.19. This local analysis of strain gives the opportunity to identify areas where strain change is the most significant. For instance, we observe from the strain comparison in corresponding AHA zones that the strain improvement mostly occurs in anterior and antero-lateral zones.

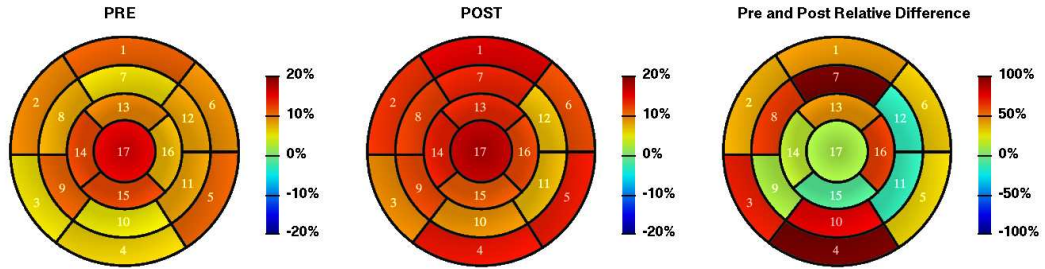
Then we measure the asynchrony of maximum strain value in each sequence with the difference between the time of maximum strain in an AHA zone and the



(a) Maximum Radial Strain (%) in Pre- and Post-Operative Sequences



(b) Maximum Circumferential Strain (%) in Pre- and Post-Operative Sequences



(c) Maximum Longitudinal Strain (%) in Pre- and Post-Operative Sequences

Figure 6.19: Bulls eye view of extremal (a) radial, (b) circumferential and (c) longitudinal strains in AHA zones of pre- and post-operative sequences.

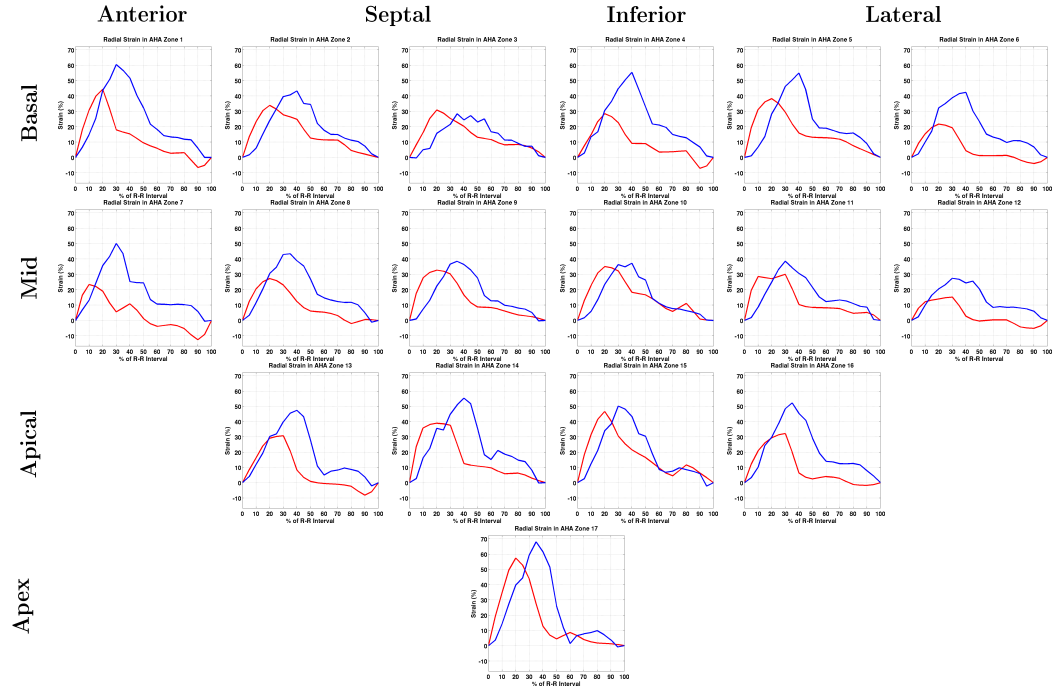


Figure 6.20: Radial strain over a cardiac cycle (R-R interval) in AHA zones of pre- and post-operative sequences (respectively red and blue curves).

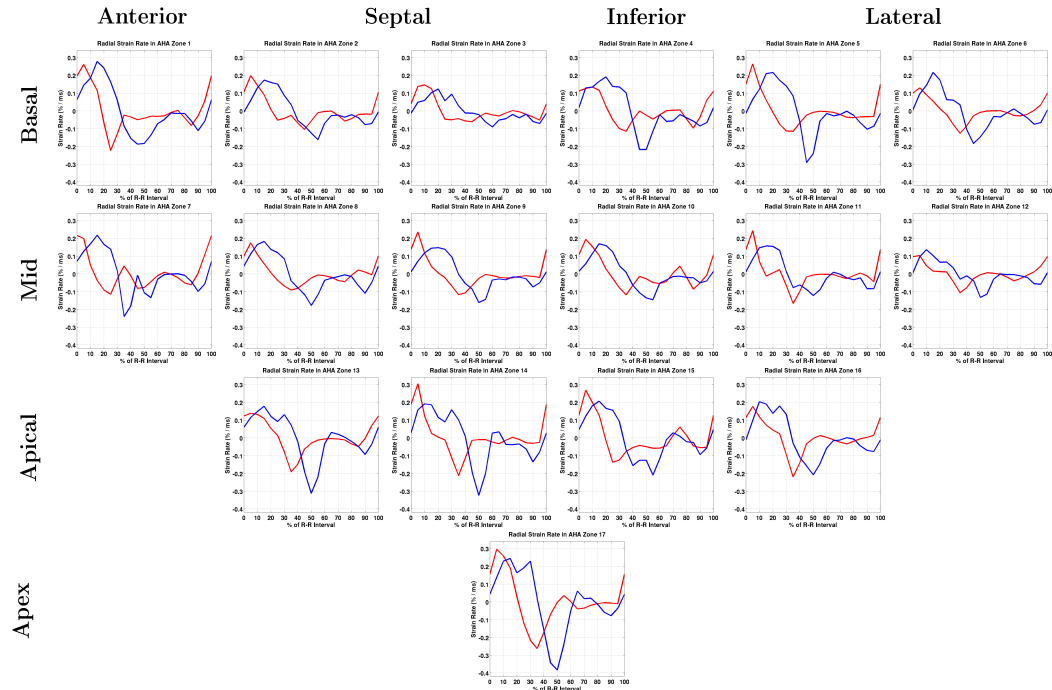


Figure 6.21: Radial strain rate over a cardiac cycle (R-R interval) in AHA zones of pre- and post-operative sequences (respectively red and blue curves).

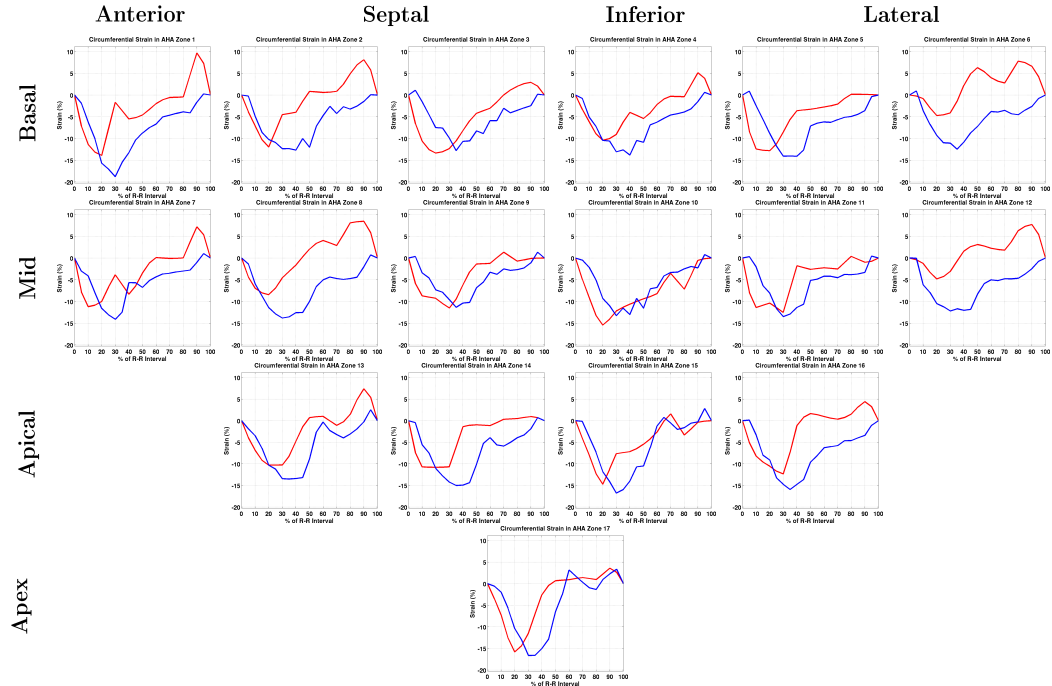


Figure 6.22: Circumferential strain over a cardiac cycle (R-R interval) in AHA zones of pre- and post-operative sequences (respectively red and blue curves).

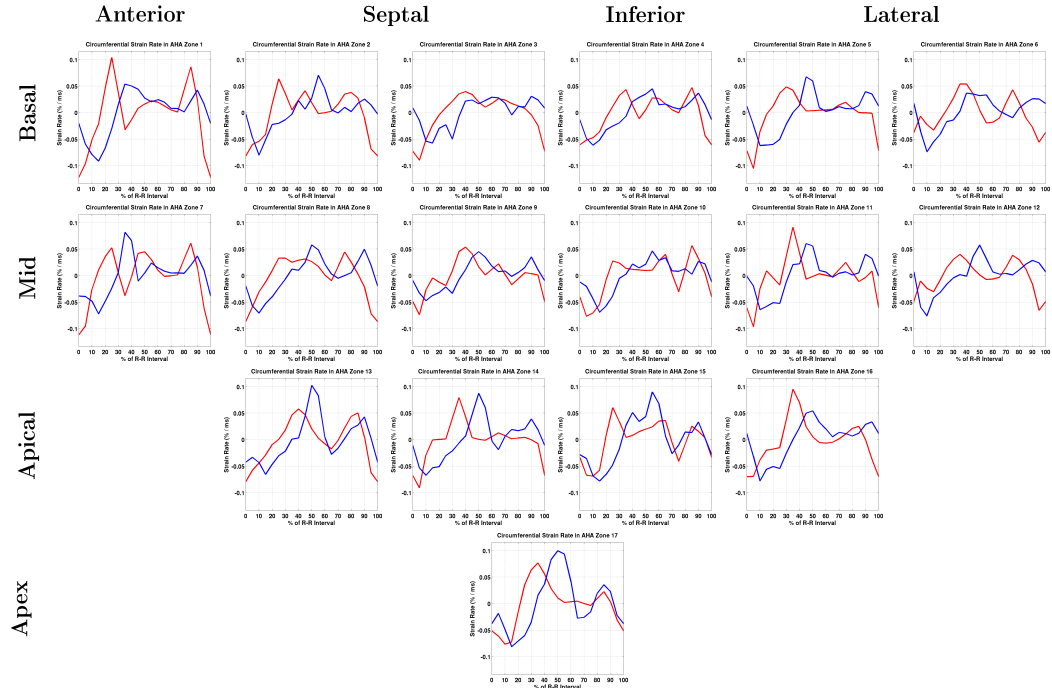


Figure 6.23: Circumferential strain rate over a cardiac cycle (R-R interval) in AHA zones of pre- and post-operative sequences (respectively red and blue curves).

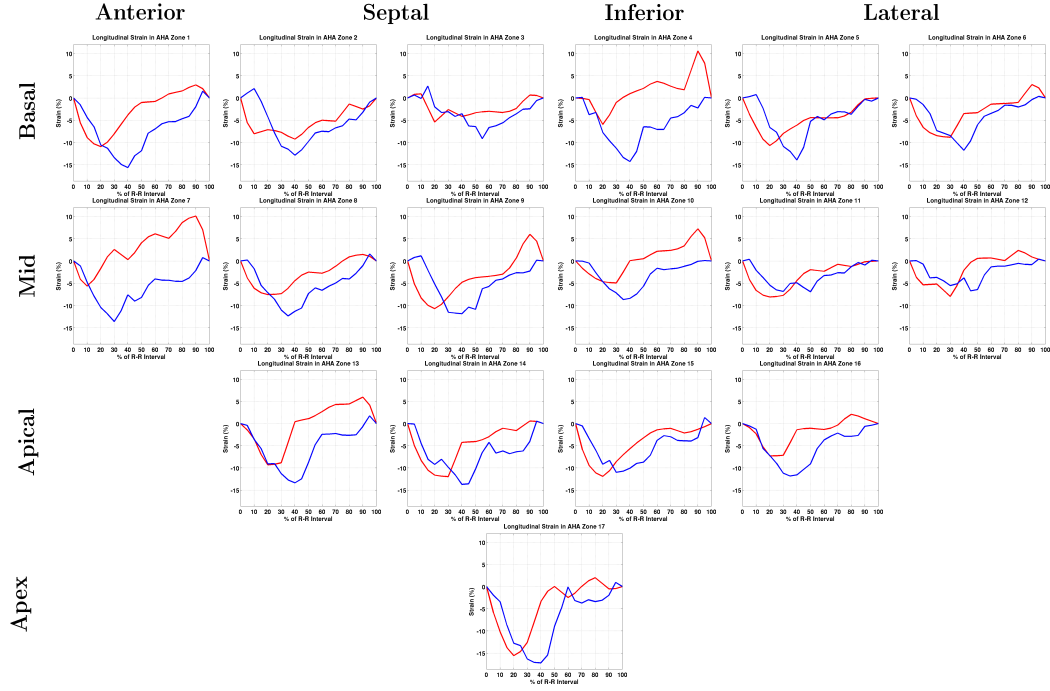


Figure 6.24: Longitudinal strain over a cardiac cycle (R-R interval) in AHA zones of pre- and post-operative sequences (respectively red and blue curves).

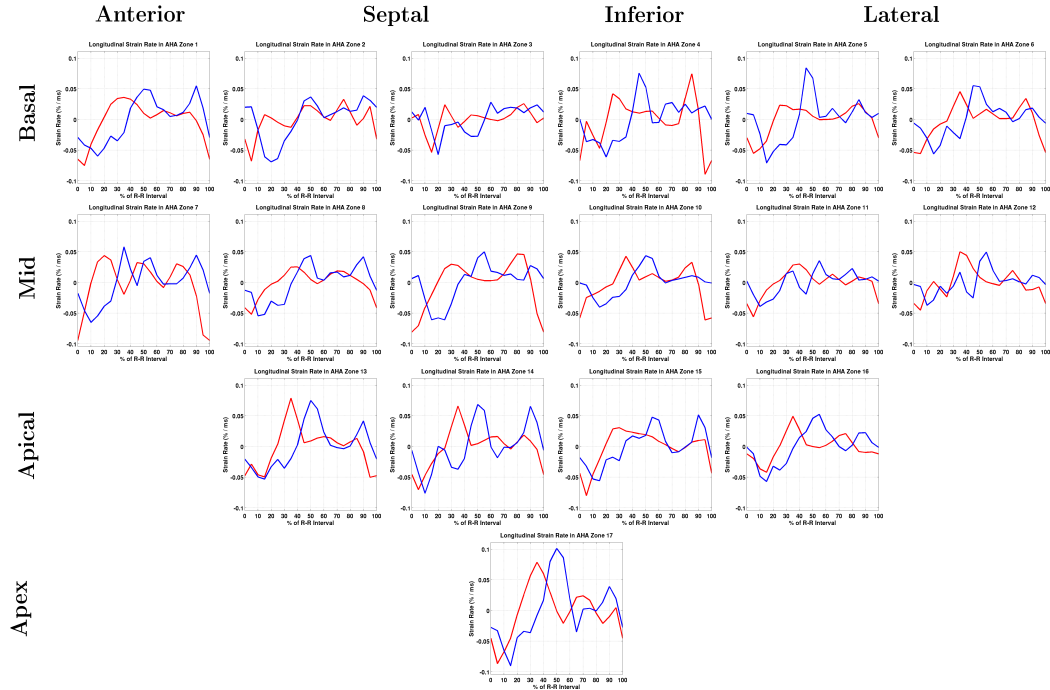


Figure 6.25: Longitudinal strain rate over a cardiac cycle (R-R interval) in AHA zones of pre- and post-operative sequences (respectively red and blue curves).

time of maximum global strain in the whole myocardium. We show in Figure 6.26 these time differences in a bulls eye view for radial, circumferential and longitudinal strains. Due to the low and different temporal resolutions between sequences, these values should be interpreted carefully knowing their limitation. But still we can observe an improvement of synchrony in areas where maximum strain is improved.

6.3.3 Remodeling Strain Analysis from 4D Registration

As shown in the previous strain analysis from motion tracking, the cardiac function is improved. But this improvement is difficult to interpret in terms of anatomical remodeling. To bridge the gap between anatomical and functional remodeling, we propose a new comparison of cardiac anatomy and function based on 4D spatio-temporal registration complementary to standard comparison of strain computed from motion tracking.

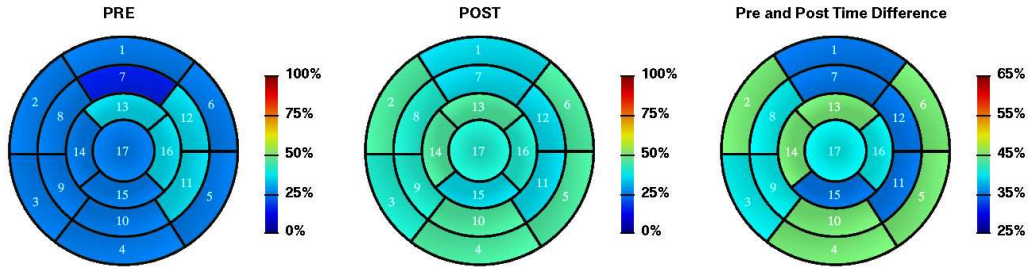
The pre-operative sequence is spatio-temporally registered to the post-operative sequence under trajectory constraints with MDD as described in Section 6.2. We obtain an inter-sequence transformation at each frame of the cardiac cycle that matches cardiac anatomies at corresponding physiological states (defined according to the ECG and the blood volume curves). These inter-sequence transformations between pre- and post-operative sequences can be used to better analyze the impact of anatomical remodeling on the LV function that cannot be observed with a direct comparison of cardiac function measurements.

The post-operative sequence is spatiotemporally registered to the pre-operative sequence under trajectory constraints with MDD. First of all, the temporal transformation (computed from the ECG and the blood volume curves) shows a lengthening of the systolic phase from 20% of R-R interval before therapy to a more standard value of 35% after therapy (see Figure 6.27). Then we estimate the intersequence transformation at each frame of the cardiac cycle that matches cardiac anatomies at corresponding physiological states. As one of the possible measurement of the impact of anatomical remodeling on the LV function, we propose to analyze these transformations between pre- and post-operative sequences. We introduce here the new concept of *remodeling strain* defined as the Lagrangian finite strain tensor R_k is computed from the intersequence transformations $S_k = \text{Id} + \mathbf{S}_k$ at frame k :

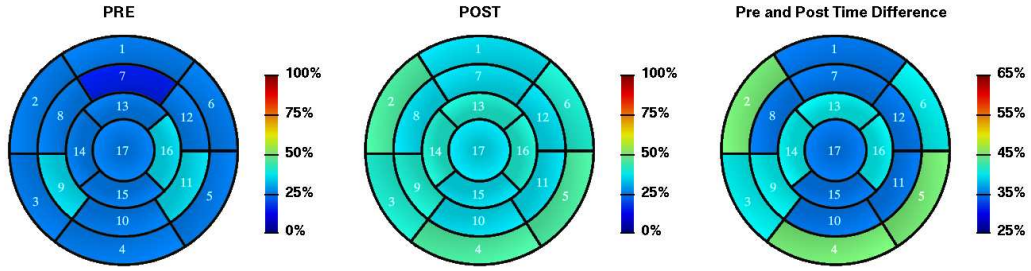
$$R_k = 1/2 (\nabla \mathbf{S}_k + \nabla \mathbf{S}_k^\top + \nabla \mathbf{S}_k^\top \nabla \mathbf{S}_k)$$

The projection of this strain tensor in the prolate coordinate system provides the radial, circumferential and longitudinal remodeling strains (respectively R_k^{rad} , R_k^{circ} and R_k^{long}) at each frame. The radial remodeling strain can be interpreted as intersequence wall thickness change that for instance occurs in case of hypertrophy. Negative radial remodeling strain means a decrease of wall thickness.

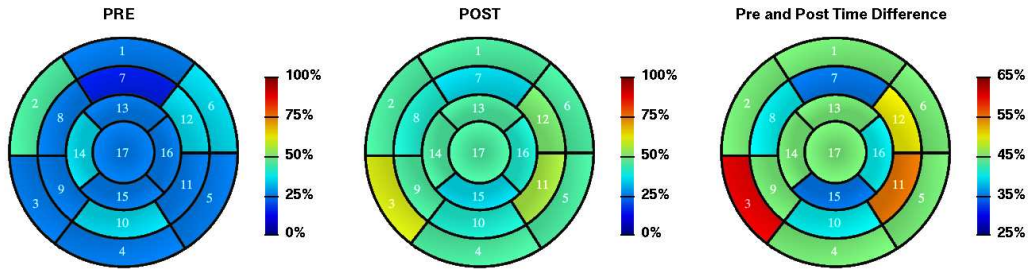
As shown in Figure 6.27, the average radial remodeling strain between pre- and post-operative sequences is about -12% showing the anatomical remodeling effect of RFA with a global regression of hypertrophy. The temporal variation of radial remodeling strain over the cardiac cycle shows that intersequence wall



(a) Time of Maximum Radial Strain (% of R-R Interval) in Pre- and Post-Operative Sequences



(b) Time of Maximum Circumferential Strain (% of R-R Interval) in Pre- and Post-Operative Sequences



(c) Time of Maximum Longitudinal Strain (% of R-R Interval) in Pre- and Post-Operative Sequences

Figure 6.26: Bulls eye view of time of extremal (a) radial, (b) circumferential and (c) longitudinal strains in AHA zones of pre- and post-operative sequences.

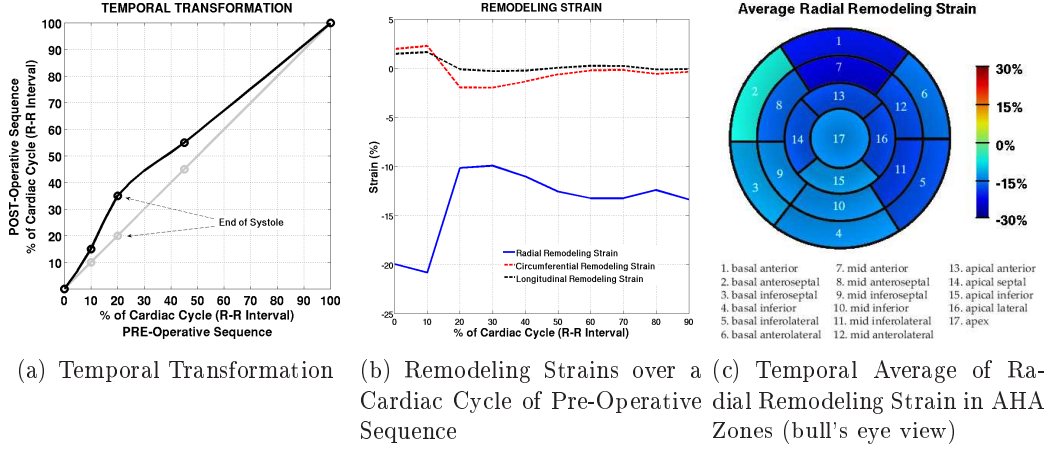


Figure 6.27: (a) Temporal transformation between pre- and post-operative sequences showing a modification of cardiac dynamic with a lengthening of systolic phase after therapy. - (b) Remodeling strains in radial, circumferential, and longitudinal directions of the prolate coordinate system over a cardiac cycle with temporal alignment of the sequences. Negative strain values mean that contraction occurs after therapy (for instance wall thickness decreases after intervention when radial strain is negative). - (c) Temporal average of radial remodeling strain in AHA zones showing regional wall thickness differences due to hypertrophy of left ventricular myocardium.

thickness change is more important at ED than at ES. This higher radial remodeling strain at ED (about -20%) can be explained by the combination of two phenomena: the regression of hypertrophy (anatomical remodeling) and the improvement of the relaxation stage during diastole (functional remodeling). A bull's eye view of the average regional radial strain in each AHA zone presented in Figure 6.27 shows a higher regression of left ventricular hypertrophy in the anterior and lateral zones.

This example shows the potential of 4D spatio-temporal registration to analyze the impact of therapy on cardiac anatomy and function by giving access to the inter-sequence transformations over time. Further studies on remodeling strains with larger databases would help to better understand the anatomical and functional impact of remodeling processes.

6.4 Conclusion

The spatio-temporal registration of different 4D sequences (or any time-series images such as longitudinal studies) is a complex registration problem whose solution should match corresponding time-points and trajectories of physical points. We presented a “divide and conquer” method that first decouples the 4D temporal and spatial registrations. The temporal transformation is defined as matching corresponding physiological states and the spatial transformation is defined as matching corresponding anatomical points at each corresponding time-point preserving the homology be-

tween points over time. Second, this “divide and conquer” method decomposes the 4D spatial registration problem into a single 3D inter-sequence anatomical registration and intrasequence motion tracking. First, the newly proposed method has better accuracy than other standard methods. Our registration algorithm showed to be a good solution to solve the 3D inter-subject registration by properly combining information from the whole sequence to obtain a more accurate registration and smoother spatial regularization at the same time. Second, it satisfies by construction the trajectory constraints and thus preserves the homology between physical points over time. The use of the trajectory constraints can be seen as a temporal regularization consistent with the motion occurring in each sequence as opposed to standard regularization methods (for instance, B-Spline or Gaussian smoothing).

Since in this framework the temporal transformation is not solely image-driven (e.g. using electrophysiology like the ECG), we stated that the temporal transformation matching corresponding physiological events could be determined independently from the spatial transformations. Purely image-driven joint spatial and temporal registrations could also have been considered. But as shown in Perperidis *et al.* [Perperidis 2005b], this joint registration increases a lot the computation time. Moreover, the interpretation of the temporal transformation in terms of physiological events is not apparent. But on the other hand, joint spatial and temporal registrations could still be useful when no physiological event has been clearly identified for temporal registration.

This framework also relies on the estimation of the motion transformations used with the trajectory constraints to simplify the registration. Any improvement of the motion tracking algorithm, for instance by including biomechanical constraints such as near incompressibility [Bistoquet 2008, Mansi 2009], would improve the estimation of the inter-sequence anatomical transformations. Furthermore, we use trajectory constraints as hard-constraints. One could think of relaxing these hard-constraints by including uncertainties of motion tracking [Taron 2009].

The 4D registration under trajectory constraints with *Multichannel Diffeomorphic Demons* showed promising results on both real patient data and synthetic data simulated with a physiologically realistic electromechanical cardiac model. A more thorough validation is still necessary on a larger database of patients and with a specific clinical application. Nevertheless our study already showed the new possibilities offered by the 4D spatio-temporal registration method to compare two time-series of cardiac images of different patients (inter-subject comparison of anatomy and function) or of the same patient at different times (intrasubject comparison such as before and after therapy, or at rest and during exercise).

PART IV

CONCLUSION

CONCLUSION AND PERSPECTIVES

Contents

7.1	Synthesis of Contributions	136
7.1.1	A Statistical Atlas of Cardiac Fibre Architecture	136
7.1.2	Registration of 4D Time-Series of Images	137
7.2	Discussion and Perspectives	138
7.2.1	Improvement of the Atlas of Cardiac Fibre Architecture	138
7.2.2	Towards <i>in vivo</i> Imaging of Cardiac Fibre architecture	139
7.2.3	Improvement of 4D Registration Framework	140
7.2.4	Towards a Statistical Atlas of Cardiac Anatomy and Function	141
7.3	Publications	141

Medical image analysis has shown to have a clinical impact, not only for diagnosis and guidance of interventions, but also for therapy planning by helping the personalization of physiological models to a patient. The research work presented in this thesis focused on the comparison of cardiac anatomy and function and can be related to two issues of cardiac therapy using personalized physiological models: the improvement of cardiac fibre architecture models and the evaluation of impact of therapy on the cardiac anatomy and function. Both of these contributions rely on the registration of medical images that gives the opportunity to compare cardiac microstructure, anatomy and function. The groupwise registration of a population of DT-MRIs was used to build an atlas of cardiac fibre architecture. The pairwise registration of 4D cardiac CT sequences, explained as a simultaneous pairwise registration of a collection of 3D images, was used to compare cardiac anatomy and function of different patients and of the same patient before and after intervention to evaluate the effect of therapy.

More generally, these contributions yield computational tools and results that can be used for a better general understanding of cardiac anatomy and function. We first report the contributions and results presented in this manuscript and then conclude by proposing some possible extensions of this research work.

7.1 Synthesis of Contributions

7.1.1 A Statistical Atlas of Cardiac Fibre Architecture

Knowledge about cardiac fibre architecture is essential for a better understanding of electromechanical behavior of the heart either in normal cases or in pathological cases where remodeling processes occur. Moreover including cardiac fibre architecture in electromechanical models of the heart is essential for a realistic simulation of cardiac function. When simulating cardiac function for patient-specific therapy planning, the *in vivo* access to this architecture at a sufficient resolution is still not possible. Hence, cardiac fibre architecture must rely on prior knowledge. Current models are mostly synthetic models, in which generic analytical laws rule the fibre orientation, or realistic single *ex vivo* DT-MRI acquisition that do not capture the possible variability between subjects. Our strategy was to provide a statistical atlas of cardiac fibre architecture from *ex vivo* canine DT-MRI acquisitions to combine the advantages of both approaches being as generic and as realistic as possible. This research work lead to several contributions from methodology to experimental results.

- **Framework to build a statistical atlas of cardiac DT-MRIs :** We detailed a general computational framework to build a statistical atlas of cardiac DT-MRIs. The novelty of this work holds in computing a quantitative average cardiac fibre architecture by processing directly diffusion tensors instead of features extracted from them (e.g. orientation angles or vectors).
- **Decomposition of covariance matrix of diffusion tensors :** We proposed a complete second order statistical analysis of diffusion tensors with a comprehensive analysis of the covariance matrix of diffusion tensors providing the variability of eigenvalues and eigenvectors. This statistical analysis of DT-MRIs provides a novel framework well-suited to study the variability of cardiac fibre architecture within a population.
- **Insight on diffusion tensor reorientation strategies :** We proposed a justification for the choice between the *Finite Strain* (FS) and the *Preservation of the Principal Direction* (PPD) reorientation strategies when registering DT-MRIs. PPD is explained as a mechanical deformation of the space whereas FS preserves the spatial gradient of diffusion tensors.
- **Canine statistical atlas of cardiac fibre architecture :** This framework was applied to a population of nine *ex vivo* canine DT-MRI acquisitions. We obtained a statistical atlas that yields a better description and understanding of cardiac fibre architecture by capturing common features within a population. Results of the intra-species comparison with the analysis of the covariance matrix of diffusion tensors showed that cardiac fibre orientation has low inter-subject discrepancies whereas the laminar sheet orientation has much higher discrepancies within the population of canine hearts.

- **Comparison canine atlas vs. synthetic model :** This comparison showed that synthetic models oversimplify the real cardiac fibre orientation. This was especially true in the apex area where the transmural variation of fibre orientation follows an analytical law different from the one used to create the synthetic model.
- **Comparison canine atlas vs. human heart :** An inter-species comparison between a single human heart and the statistical atlas of canine hearts showed a good consistency of fibre orientation and high discrepancies of laminar sheet orientation. These preliminary results tend to justify the use of a canine atlas of fibre orientation for patient-specific clinical applications.

7.1.2 Registration of 4D Time-Series of Images

The spatio-temporal registration of 4D time-series of images gives the opportunity to compare simultaneously cardiac anatomy and function of different patients (inter-subject comparison of anatomy and function) or of the same patient at different times (intra-subject comparison such as before and after therapy, or at rest and during exercise). Methodological contributions are proposed with the improvement of 4D registration algorithms and with the novel analysis of remodeling after therapy using 4D inter-sequence spatial transformations between pre- and post-operative sequences.

- **Framework for 4D inter-sequence spatio-temporal registration :** We introduced the general setting of 4D inter-sequence spatio-temporal registration that can be decoupled into temporal and spatial registrations. The temporal registration is defined as the mapping of corresponding physiological events and the spatial registration as the mapping of corresponding trajectories of physical points.
- **Trajectory constraints :** To ensure a temporal consistency of transformations by matching trajectories of points, we defined the *trajectory constraints* (TC). These constraints showed to simplify the 4D spatial registration problem to a multichannel 3D registration problem.
- **Multichannel diffeomorphic registration :** We proposed a rigorous extension of 3D *Diffeomorphic Demons* (DD) to vector-valued 3D images, called *Multichannel Diffeomorphic Demons* (MDD), that allows to solve the multichannel 3D registration problem.
- **Evaluation of 4D registration algorithms :** We evaluated the spatio-temporal registration under TC with MDD on electromechanically simulated and real 4D CT sequences of different patients by comparing it to other standard registration methods. It showed that using the trajectory constraints yields a temporal regularization consistent with motion whereas using the

multichannel registration yields a better spatial regularization. The combination of these two showed to be the best compromise between registration accuracy, temporal consistency with motion tracking, spatial smoothness, and computation times.

- **Electromechanically simulated 4D cardiac CT sequences :** We simulated 4D cardiac CT sequences with realistic electromechanical model of the heart including the statistical atlas of cardiac fibre architecture. These simulated sequences have the advantage to be fully controlled and to provide ground truth transformations between frames and sequences. Thus, they are useful data to validate registration algorithms.
- **Application to the analysis of remodeling after therapy :** We also proposed a new possible application of 4D inter-sequence spatio-temporal registration to analyze and quantify the remodeling processes of the heart with atrial fibrillation after radiofrequency ablation. By studying the inter-sequence transformations between a pre-operative and a post-operative sequence over a cardiac cycle, we are able to quantify the anatomical remodeling due to the regression of hypertrophy and the functional remodeling with the improvement of the relaxation stage during diastole.

7.2 Discussion and Perspectives

7.2.1 Improvement of the Atlas of Cardiac Fibre Architecture

The construction of the atlas of cardiac fibre architecture is based on the computation of statistics on diffusion tensors. Basically, we compute a statistical atlas of cardiac DT-MRIs that is then interpreted as cardiac fibre architecture. Another strategy would be to first interpret the diffusion tensors as cardiac fibre architecture described for instance with tensor whose eigenvalues would correspond more specifically to a normalized confidence value in eigenvectors orientation. Still we believe that the difference between the two strategies should not change significantly the results.

The general framework to compute a statistical atlas of cardiac DT-MRIs has been applied to small database of nine canine hearts. The first improvement of the atlas would be to use a larger database. This would make the atlas more reliable in terms of statistics. A second improvement would be to build this atlas from a large database of human data. This would help to have better inter-species comparison between canine and human hearts. But more importantly this would help to confirm (or infirm) that the good consistency of fibre orientation observed within a canine population is also valid for human hearts. Moreover, even if preliminary results show a good correlation between canine and human fibre orientation, it makes more sense to use a human atlas if available. One could also think of using this framework to create atlases of pathological cases to study the remodeling process and include it to patient-specific models.

Adapting the atlas computed in this research work¹ to patient anatomy is a step forward towards bridging the gap between patient-specific information and prior knowledge necessary when simulating cardiac function for diagnosis and planning of therapy [Chinchapatnam 2008, Sermesant 2008, Sermesant 2009] or when caring about the realignment of myocardial fibers orientation in the surgical reconstruction of the left ventricle after infarction [Cirillo 2008, Cirillo 2009].

When using the atlas of fibre architecture for patient-specific electromechanical simulations, the necessary resolution and details of cardiac fibre architecture should be evaluated. It might happen that a canine atlas is sufficient for the desired application. To evaluate this, studying the influence of cardiac fibre architecture on the electromechanical behavior of the heart is essential.

More recently, Q-ball imaging [Tuch 2004] has been used to observe cardiac fibre architecture [Dierckx 2009] with a more detailed directional model of diffusion than diffusion tensors. Preliminary studies have shown that this imaging technique could help to visualize the intra-voxel cardiac fibre structure with for instance two populations of fibres in some area of the hearts. If further studies show a significant advantage of using Q-ball imaging to describe cardiac fibre architecture, the statistical atlas could be computed with this diffusion model. But it would also mean that statistical analysis of Q-ball imaging, already developed for segmentation [Descoteaux 2009] or registration [Chiang 2008], should be extended to be interpreted as cardiac fibre architecture variability.

7.2.2 Towards *in vivo* Imaging of Cardiac Fibre architecture

The construction of the atlas relied on the groupwise registration of anatomical MRIs (T_2 -weighted images) and not the DT-MRIs to avoid to introduce a bias in the statistical analysis of cardiac fibre architecture. Comparing the groupwise registration results and the statistical analysis when registering the anatomical MRIs or directly the DT-MRIs might also help to give insights about the link between cardiac shape and fibre architecture by studying inter-subject transformations.

This link between anatomy and fibre architecture is important since up to now solely the patient cardiac geometry is used to make the atlas patient-specific. One strategy is to create a synthetic model with parametrized analytical laws that will be directly used in any cardiac geometry. The parameters of the analytical laws (mostly the extreme values at epicardium and endocardium of the transmural variation of fibre orientation) can be determined according to the atlas fibre architecture. Another strategy is to deform the atlas geometry to fit the patient geometry. Then the deformed atlas fibre architecture is used to describe the patient fibre architecture in its own geometry. An extension of this strategy would be to couple variability of cardiac geometry and fibre architecture to obtain modes of variation of fibre architecture depending on geometry.

But cardiac fibre architecture might not be dependent only on the geometry of the heart, especially in presence of a pathology. The cardiac fibre architecture and

¹<http://www-sop.inria.fr/asclepios/data/heart/>

cardiac function are also highly interdependent. When cardiac fibre architecture is modified, the cardiac function is modified. And when cardiac function is modified, a remodeling process of cardiac fibre architecture can occur to recover cardiac function. Hence, measurements of the cardiac function obtained *in vivo* might be used to improve the personalization of cardiac fibre architecture. But still some research work remains to determine the correlation between cardiac function parameters that can be measured *in vivo* and fibre architecture.

A more direct way to make another step forward towards bridging the gap between patient-specific information and prior knowledge would be to acquire *in vivo* sparse and/or low resolution DT-MRI data [Reese 1995, Tseng 1999, Dou 2002, Gamper 2007, Frindel 2009a] and fit the atlas of fibre architecture to these data.

7.2.3 Improvement of 4D Registration Framework

The 4D registration framework we proposed highly relies on the determination of the intra-sequence motion transformations that constrain the inter-sequence shape transformations. The 4D spatial registration with trajectory constraints would benefit from any improvement of the motion tracking algorithm for instance by including physical constraints such as elasticity and near incompressibility of cardiac tissue [Mansi 2009] or by making it more robust coupling the registration of all frames at the same time [Ledesma-Carbayo 2005, De Craene 2009, Sundar 2009]. Moreover, since motion tracking is always prone to errors, evaluating uncertainties in the registration algorithms [Taron 2009] either for motion tracking or 4D registration would probably help to soften the hard constraints given by the trajectory constraints.

Robustness of 4D spatial registration could be improved by considering the inter-sequence registration of every possible pair of frames, and not only corresponding frames. But the number of channels would highly increase as well as computation time.

In our 4D spatio-temporal framework, we stated that spatial and temporal transformations can be decoupled when temporal transformation is determined with physiological parameters that are not image-based (e.g. using electrophysiology like the ECG). Purely image-driven joint spatial and temporal registrations could also have been considered. But as shown in Perperidis *et al.* [Perperidis 2005b], this joint registration increases a lot the computation time. Moreover, the interpretation of the temporal transformation in terms of physiological events is difficult. We preferred to perform a temporal registration independently from spatial registration to have a better understanding and control of which physiological states are matched. On the other hand, joint spatial and temporal registrations could still be useful when no physiological event has been clearly identified for temporal registration or when physiological data are not available.

7.2.4 Towards a Statistical Atlas of Cardiac Anatomy and Function

A direct application of this framework would be the construction of a 4D statistical atlas of cardiac anatomy and function. A first work on this topic [Perperidis 2005b] computed a 4D probabilistic atlas that is then used to analyze cardiac function with segmentation and tracking of the endocardium. In our framework, the computation of a 4D statistical atlas would be transformation-based. The average cardiac sequence would be computed by averaging spatial (both intra- and inter-sequences) and temporal transformations.

An atlas of cardiac mechanical function could also be computed by adapting the framework to build the atlas of diffusion tensors to strain tensors with their evolution over a cardiac cycle. In this case, the trajectory constraints satisfied in the 4D registration framework would be particularly important when comparing strain over time between two sequences. If we do not ensure to map the same physical points over time consistently with the motion, we compare the strain of physical points that are not on the same trajectory over the whole sequence.

Both contributions could also be integrated in a single framework to build a joint atlas of cardiac diffusion and strain tensors. Such an atlas would be particularly interesting for studying the link between detailed anatomy with fibre architecture and mechanical function.

7.3 Publications

The research work led to the following publications and submissions:

- JOURNAL ARTICLES -

1 - [Peyrat 2009] **J.-M. Peyrat**, H. Delingette, M. Sermesant, C. Xu and N. Ayache. *Registration of 4D Cardiac CT Sequences Under Trajectory Constraints with Multichannel Diffeomorphic Demons*. IEEE Transactions on Medical Imaging, 2009. Submitted.

2 - [Yeo 2009] B.T.T. Yeo, T. Vercauteren, P. Fillard, **J.-M. Peyrat**, X. Pennec, P. Golland, N. Ayache and O. Clatz. *DT-REFinD: Diffusion Tensor Registration with Exact Finite-Strain Differential*. IEEE Transactions on Medical Imaging, 2009. In press.

3 - [Sermesant 2008] M. Sermesant, **J.-M. Peyrat**, P. Chinchapatnam, F. Billet, T. Mansi, K. Rhode, H. Delingette, R. Razavi and N. Ayache. *Toward Patient-Specific Myocardial Models of the Heart*. Heart Failure Clinics, vol. 4, no. 3, pages 289–301, 2008.

4 - [Peyrat 2007a] **J.-M. Peyrat**, M. Sermesant, X. Pennec, H. Delingette, C. Xu, E.R. McVeigh and N. Ayache. *A Computational Framework for the Statistical Analysis of Cardiac Diffusion Tensors: Application to a Small Database of Canine Hearts*. IEEE Transactions on Medical Imaging, vol. 26, no. 11, pages

1500–1514, 2007.

- INTERNATIONAL CONFERENCE ARTICLES -

5 - [Sermesant 2009] M. Sermesant, F. Billet, R. Chabiniok, T. Mansi, P. Chinchapatnam, P. Moireau, **J.-M. Peyrat**, K. Rhode, M. Ginks, P. Lambiase, S. Arridge, H. Delingette, M. Sorine, A. Rinaldi, Do. Chapelle, R. Razavi and N. Ayache. *Personalised Electromechanical Model of the Heart for the Prediction of the Acute Effects of Cardiac Resynchronisation Therapy*. In Proceedings of Functional Imaging and Modeling of the Heart (FIMH'09), volume 5528 of LNCS, pages 239–248, 2009.

6 - [Mansi 2009] T. Mansi, **J.-M. Peyrat**, M. Sermesant, H. Delingette, J. Blanc, Y. Boudjemline and N. Ayache. *Physically-Constrained Diffeomorphic Demons for the Estimation of 3D Myocardium Strain from Cine-MRI*. In Proceedings of Functional Imaging and Modeling of the Heart (FIMH'09), volume 5528 of LNCS, pages 201–210, 2009.

7 - [Peyrat 2008] **J.-M. Peyrat**, Hervé Delingette, Maxime Sermesant, Xavier Pennec, Chenyang Xu and Nicholas Ayache. *Registration of 4D Time-Series of Cardiac Images with Multichannel Diffeomorphic Demons*. In Proceedings of the 11th International Conference on Medical Image Computing and Computer-Assisted Intervention (MICCAI'08), volume 5242 of LNCS, pages 972–979, 2008.

8 - [Konukoglu 2007] E. Konukoglu, M. Sermesant, O. Clatz, **J.-M. Peyrat**, H. Delingette and N. Ayache. *A Recursive Anisotropic Fast Marching Approach to Reaction Diffusion Equation: Application to Tumor Growth Modeling*. In Proceedings of the 20th International Conference on Information Processing in Medical Imaging (IPMI'07), volume 4584 of LNCS, pages 687–699, 2007.

9 - [Peyrat 2007b] **J.-M. Peyrat**, M. Sermesant, X. Pennec, H. Delingette, C. Xu, E. R. McVeigh and N. Ayache. *Statistical Comparison of Cardiac Fiber Architectures*. In Proceedings of the 4th International Conference on Functional Imaging and Modeling of the Heart (FIMH'07), volume 4466 of LNCS, pages 413–423, 2007.

10 - [Delingette 2007] H. Delingette, M. Sermesant, **J.-M. Peyrat**, N. Ayache, K.S. Rhode, R. Razavi, E.R. McVeigh, D. Chapelle, J. Sainte-Marie, P. Moireau, M. Fernandez, J.-F.c Gerbeau, K. Djabella, Q. Zhang and M. Sorine. *Cardiosense3d: Patient-Specific Cardiac Simulation*. In Proceedings of 4th IEEE International Symposium on Biomedical Imaging (ISBI'07), pages 628–631, 2007.

11 - [Peyrat 2006b] **J.-M. Peyrat**, M. Sermesant, X. Pennec, H. Delingette, C. Xu, E. R. McVeigh and N. Ayache. *Towards a Statistical Atlas of Cardiac Fiber*

Structure. In Proceedings of the 9th International Conference on Medical Image Computing and Computer-Assisted Intervention (MICCAI'06), volume 4190 of LNCS, pages 297–304, 2006.

- OTHERS -

12 - [Peyrat 2006a] J.-M. Peyrat, M. Sermesant, X. Pennec, H. Delingette, C. Xu, E.R. McVeigh and N. Ayache. *Towards a Statistical Atlas of Cardiac Fiber Architecture*. Research Report 5906, INRIA, May 2006.

Affine Transformation of a Plane

The affine transformation of the parameters of a plane is known since a long time. We present here a simple demonstration provided in [Turkowski 1990].

Let P be a plane and its normal \mathbf{n} . The affine transformations preserve the parallelism and therefore the image of a plane is plane. It means that every vector \mathbf{v} in the plane P is transformed through an affine transformation A into a vector $\mathbf{v}' = A\mathbf{v}$ in the image plane P' (see Figure A.1). By definition, every vector \mathbf{v} in the plane P is orthogonal to its normal:

$$\mathbf{n}^\top \mathbf{v} = 0$$

We can reformulate this expression as follows:

$$\mathbf{n}^\top (A^{-1}A)\mathbf{v} = 0$$

From this formulation, we can derive the following expression:

$$((A^{-1})^\top \mathbf{n})^\top A\mathbf{v} = 0$$

Since $\mathbf{v}' = A\mathbf{v}$, we obtain:

$$((A^{-1})^\top \mathbf{n})^\top \mathbf{v}' = 0$$

which is the definition of a vector orthogonal to the plane P' . Finally, the normal \mathbf{n}' of the image plane P' is given by:

$$\mathbf{n}' = \frac{(A^{-1})^\top \mathbf{n}}{\|(A^{-1})^\top \mathbf{n}\|}.$$

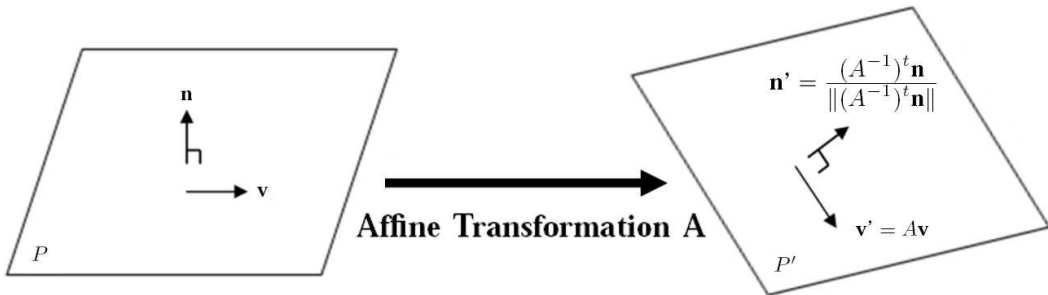


Figure A.1: Affine transformation of a plane P with normal \mathbf{n} into a plane P' with normal \mathbf{n}' .

Covariance Matrix Projections

We present here the projection of the covariance matrix of diffusion tensors onto the orthonormal basis of its tangent space. This decomposition of the covariance matrix gives directly at a first order approximation the variance of eigenvalues and the variance of pair of eigenvectors orientation.

Let us consider the dyadic tensor decomposition of the average diffusion tensor in the Log-Euclidean space:

$$\overline{W} = \log(\overline{D}_{\log}) = \sum_{i=1}^3 \lambda_i \mathbf{v}_i \mathbf{v}_i^\top \quad (\text{B.1})$$

where $\lambda_i = \log(d_i)$ and the $\{d_i\}_{i=1,2,3}$ are the eigenvalues of the diffusion tensor \overline{D}_{\log} .

Considering the deviations $\delta\lambda_i$ and $\delta\mathbf{v}_i$ of the eigenvalues λ_i and the eigenvectors \mathbf{v}_i around the mean diffusion tensor, Equation B.1 becomes:

$$\overline{W} + \delta W = \sum_{i=1}^3 (\lambda_i + \delta\lambda_i) (\mathbf{v}_i + \delta\mathbf{v}_i) (\mathbf{v}_i + \delta\mathbf{v}_i)^\top \quad (\text{B.2})$$

Let us consider the increment ε_{ij} of each vector $\delta\mathbf{v}_i$ in the frame of the mean eigenvectors $\{\mathbf{v}_j\}_{j=1,2,3}$ (see Figure B.1):

$$\delta\mathbf{v}_1 = \varepsilon_{11}\mathbf{v}_1 + \varepsilon_{12}\mathbf{v}_2 + \varepsilon_{13}\mathbf{v}_3$$

$$\delta\mathbf{v}_2 = \varepsilon_{21}\mathbf{v}_1 + \varepsilon_{22}\mathbf{v}_2 + \varepsilon_{23}\mathbf{v}_3$$

$$\delta\mathbf{v}_3 = \varepsilon_{31}\mathbf{v}_1 + \varepsilon_{32}\mathbf{v}_2 + \varepsilon_{33}\mathbf{v}_3$$

These coordinates ε_{ij} in the frame of the mean eigenvectors $\{\mathbf{v}_j\}_{j=1,2,3}$ correspond to the tangent of the angle between $\mathbf{v}_i + \delta\mathbf{v}_i$ and \mathbf{v}_j . Since $\mathbf{v}_1, \mathbf{v}_2$ and \mathbf{v}_3 build an orthonormal frame of \mathbb{R}^3 , $\varepsilon_{ij} = -\varepsilon_{ji}$ at the first order:

$$(\mathbf{v}_i + \delta\mathbf{v}_i)^\top (\mathbf{v}_j + \delta\mathbf{v}_j) = (1 + \varepsilon_{ii})\varepsilon_{ji} + (1 + \varepsilon_{jj})\varepsilon_{ij} = 0$$

$$(1 + \varepsilon_{ii})\varepsilon_{ji} + (1 + \varepsilon_{jj})\varepsilon_{ij} + o(\varepsilon_{ij}, \varepsilon_{ji}) = 0$$

$$\varepsilon_{ij} + \varepsilon_{ji} = o(\varepsilon_{ij}, \varepsilon_{ji})$$

Furthermore, the $\{\mathbf{v}_i + \delta\mathbf{v}_i\}_{i=1,2,3}$ are unit vectors which means there is a relationship between ε_{i1} , ε_{i2} and ε_{i3} :

$$(1 + \varepsilon_{i1})^2 + \varepsilon_{i2}^2 + \varepsilon_{i3}^2 = 1$$

Thus, $\varepsilon_{ii} = -\frac{1}{2}(\varepsilon_{im}^2 + \varepsilon_{in}^2) + o(\varepsilon_{im}^2, \varepsilon_{in}^2)$ which means that at the first order we can consider that $\varepsilon_{ii} = 0$.

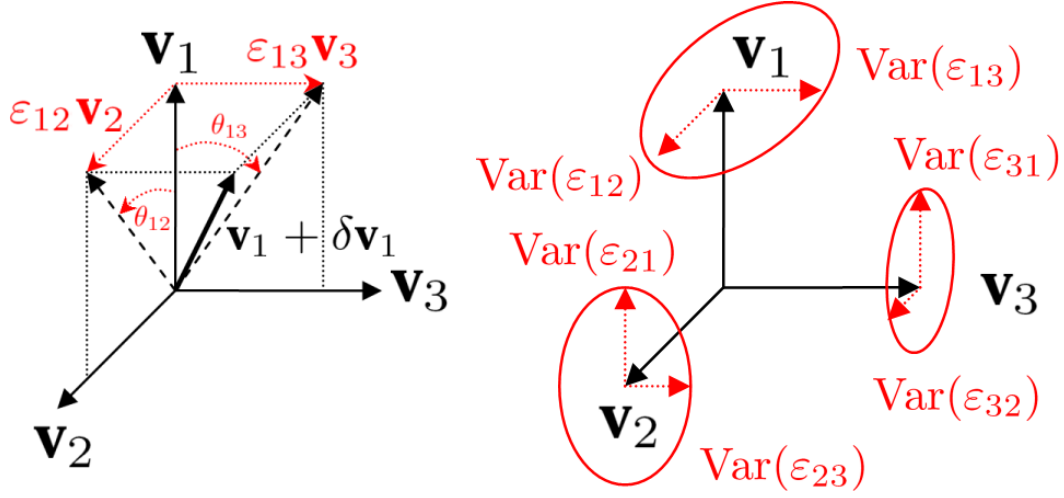


Figure B.1: [First Column] Increment $\delta \mathbf{v}_1$ of the primary eigenvector about its average \mathbf{v}_1 . [Second Column] Orientation variability of the eigenvectors described by an ellipsoidal cone of uncertainty.

Finally, considering only the first order terms of Equation B.2, we obtain the following expression:

$$\begin{aligned} \delta W = & \delta \lambda_1 W_1 + \delta \lambda_2 W_2 + \delta \lambda_3 W_3 + \varepsilon_{23} \sqrt{2} (\lambda_2 - \lambda_3) W_4 \\ & + \varepsilon_{13} \sqrt{2} (\lambda_1 - \lambda_3) W_5 + \varepsilon_{12} \sqrt{2} (\lambda_1 - \lambda_2) W_6 \end{aligned}$$

where the $\{W_i\}_{i=1,2,3}$ form an orthonormal basis of the tangent space at the mean diffusion tensor:

$$\begin{aligned} W_1 &= \mathbf{v}_1 \mathbf{v}_1^\top & W_4 &= \frac{1}{\sqrt{2}} (\mathbf{v}_3 \mathbf{v}_2^\top + \mathbf{v}_2 \mathbf{v}_3^\top) \\ W_2 &= \mathbf{v}_2 \mathbf{v}_2^\top & W_5 &= \frac{1}{\sqrt{2}} (\mathbf{v}_1 \mathbf{v}_3^\top + \mathbf{v}_3 \mathbf{v}_1^\top) \\ W_3 &= \mathbf{v}_3 \mathbf{v}_3^\top & W_6 &= \frac{1}{\sqrt{2}} (\mathbf{v}_2 \mathbf{v}_1^\top + \mathbf{v}_1 \mathbf{v}_2^\top) \end{aligned}$$

Thus, we can formulate the variances of ε_{12} , ε_{13} , ε_{23} , $\delta \lambda_1$, $\delta \lambda_2$ and $\delta \lambda_3$ with respect to the projections of the covariance matrix Σ onto the orthonormal basis $\{W_i\}_{i=1,\dots,6}$ of the tangent space:

$$\begin{aligned} E(\delta \lambda_1^2) &= \mathbf{vec}(W_1)^\top \Sigma \mathbf{vec}(W_1) & E(\varepsilon_{23}^2) &= \frac{1}{2(\lambda_2 - \lambda_3)^2} \mathbf{vec}(W_4)^\top \Sigma \mathbf{vec}(W_4) \\ E(\delta \lambda_2^2) &= \mathbf{vec}(W_2)^\top \Sigma \mathbf{vec}(W_2) & E(\varepsilon_{13}^2) &= \frac{1}{2(\lambda_1 - \lambda_3)^2} \mathbf{vec}(W_5)^\top \Sigma \mathbf{vec}(W_5) \\ E(\delta \lambda_3^2) &= \mathbf{vec}(W_3)^\top \Sigma \mathbf{vec}(W_3) & E(\varepsilon_{12}^2) &= \frac{1}{2(\lambda_1 - \lambda_2)^2} \mathbf{vec}(W_6)^\top \Sigma \mathbf{vec}(W_6) \end{aligned}$$

Atlas and Synthetic Models in AHA Zones

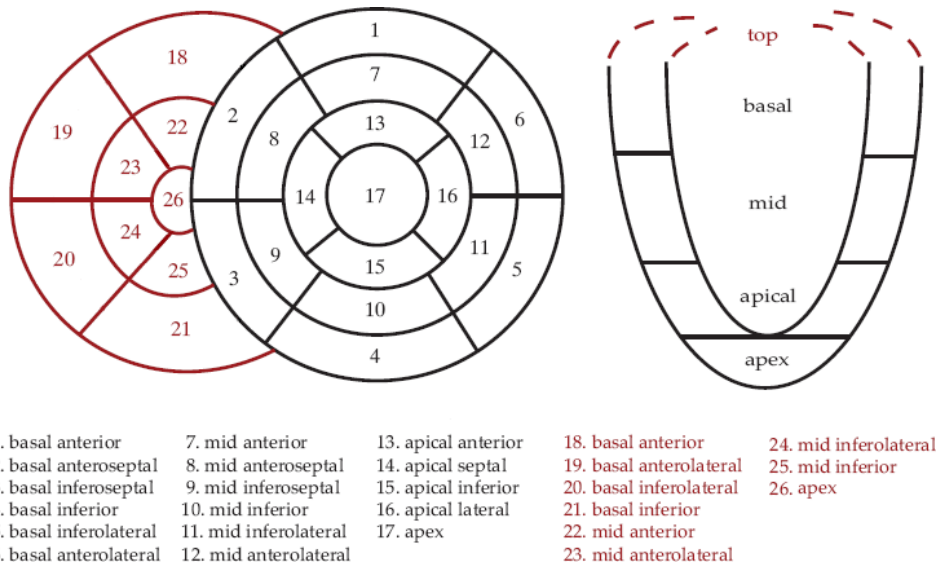


Figure C.1: Bull's eye view of the American Heart Association (AHA) zones of the left ventricle (17 zones) and their extension to the right ventricle (9 more zones) - Adapted from [Moireau 2008].

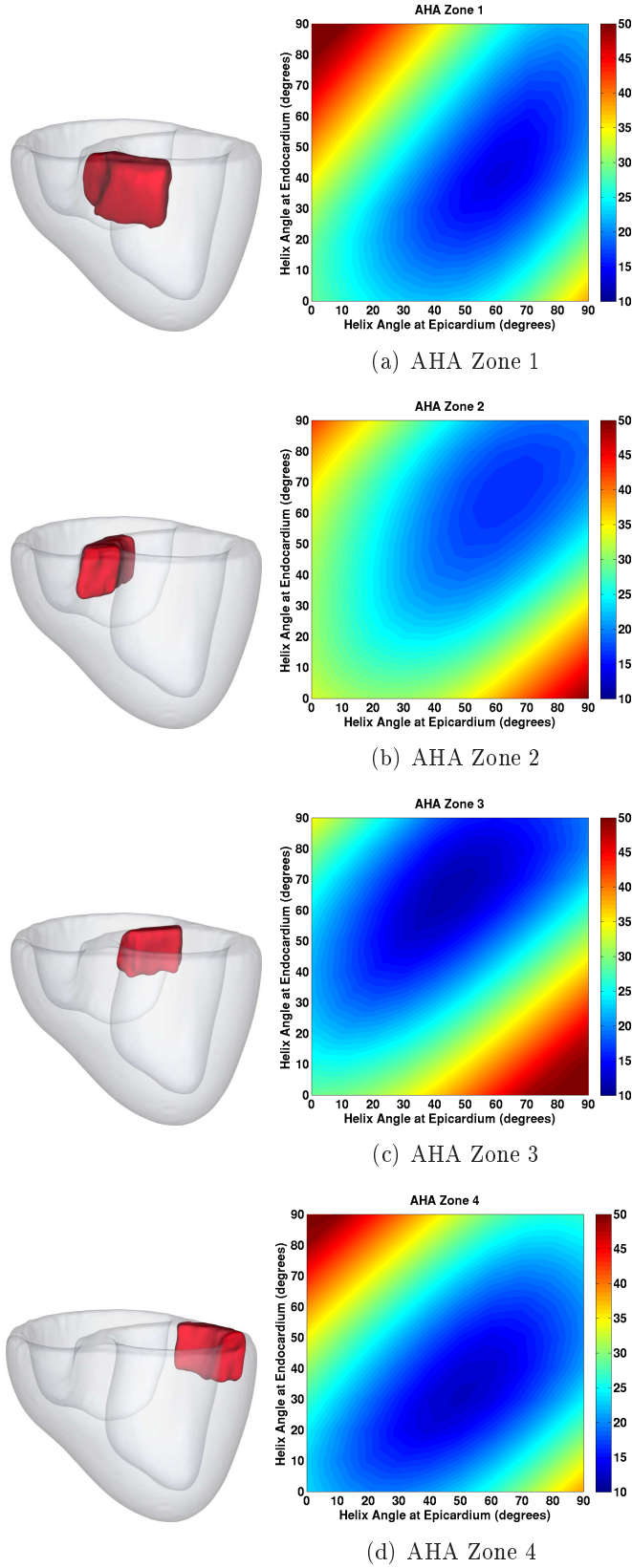
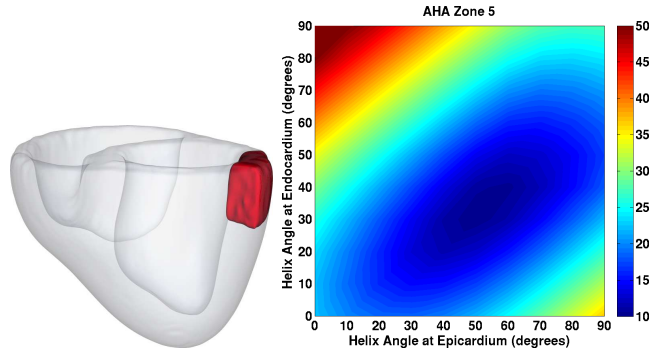
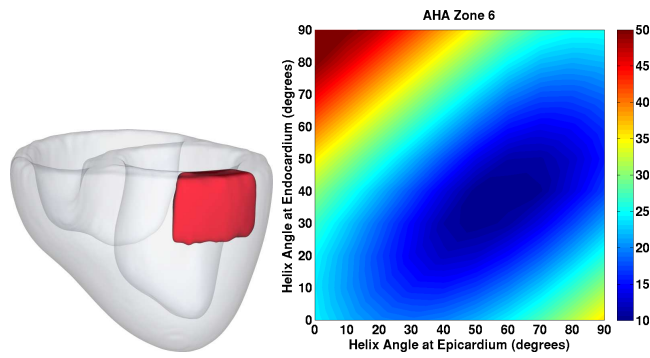


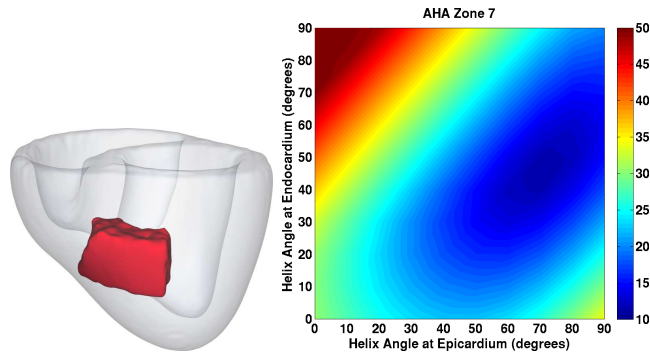
Figure C.2: Average angular difference between the canine atlas and synthetic models with different helix angles at endocardium and epicardium at a given American Heart Association (AHA) zone (colorscale is in degrees).



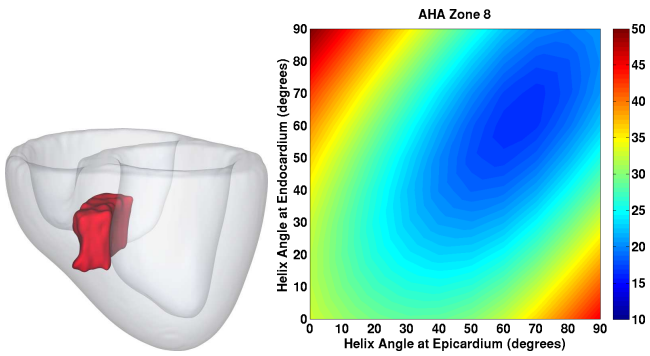
(a) AHA Zone 5



(b) AHA Zone 6

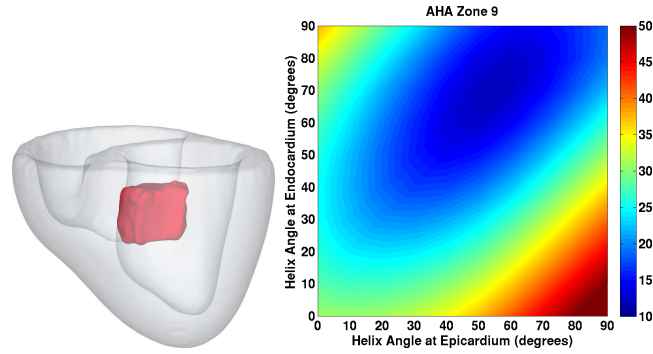


(c) AHA Zone 7

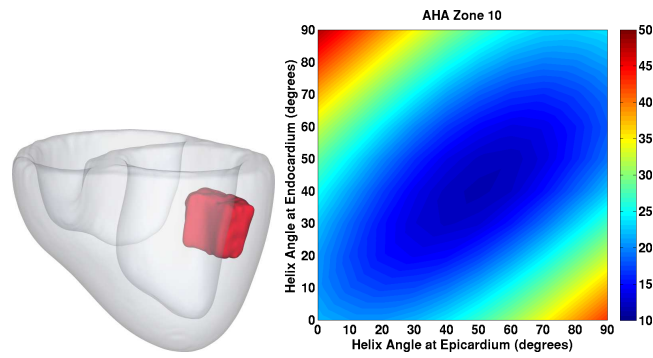


(d) AHA Zone 8

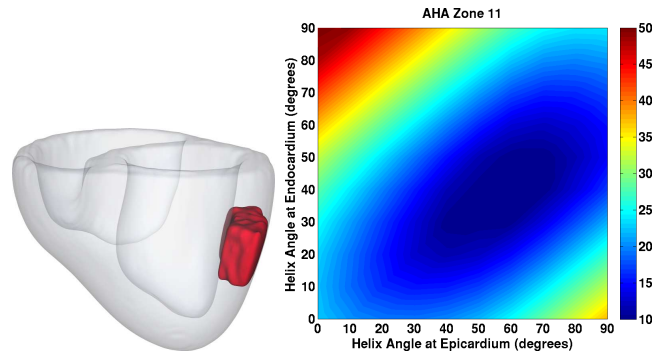
Figure C.3: Average angular difference between the canine atlas and synthetic models with different helix angles at endocardium and epicardium at a given American Heart Association (AHA) zone (colorscale is in degrees).



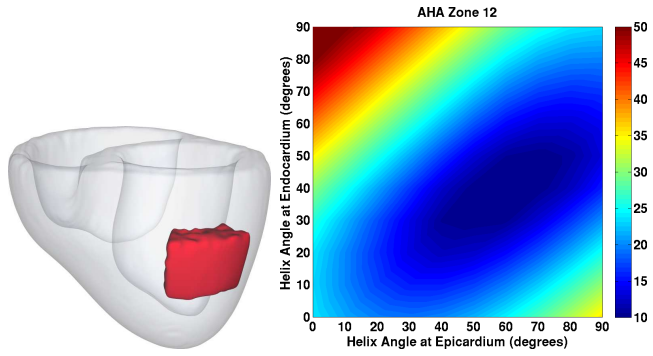
(a) AHA Zone 9



(b) AHA Zone 10

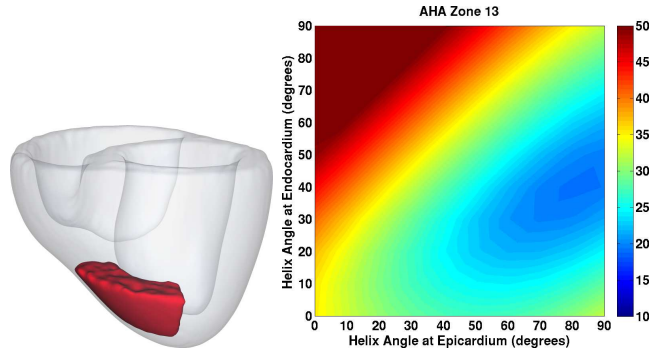


(c) AHA Zone 11

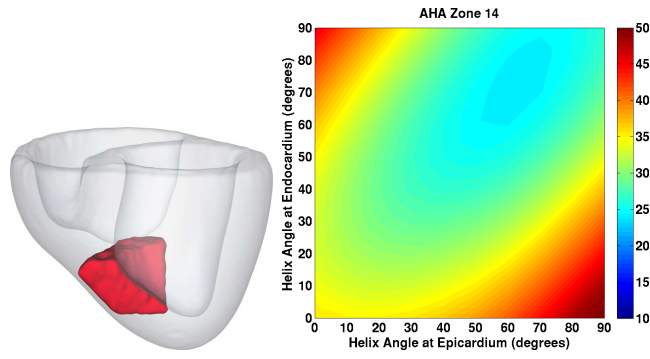


(d) AHA Zone 12

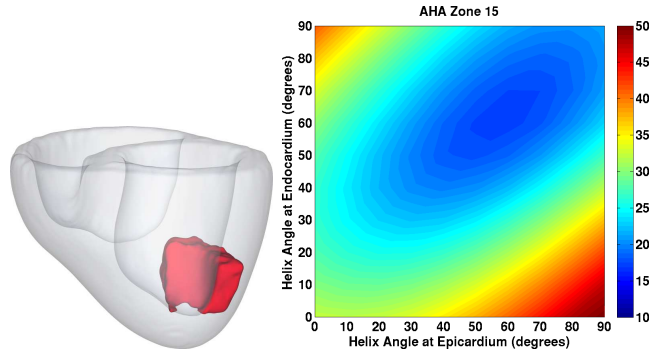
Figure C.4: Average angular difference between the canine atlas and synthetic models with different helix angles at endocardium and epicardium at a given American Heart Association (AHA) zone (colorscale is in degrees).



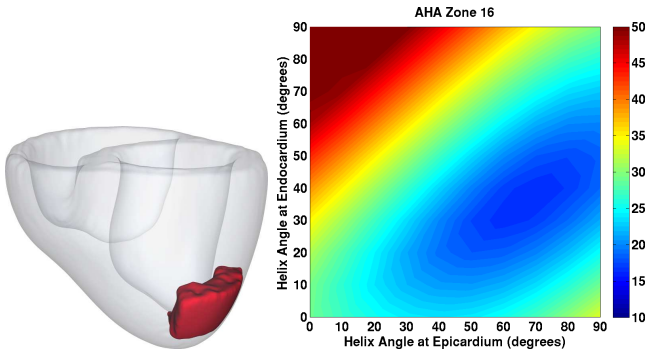
(a) AHA Zone 13



(b) AHA Zone 14

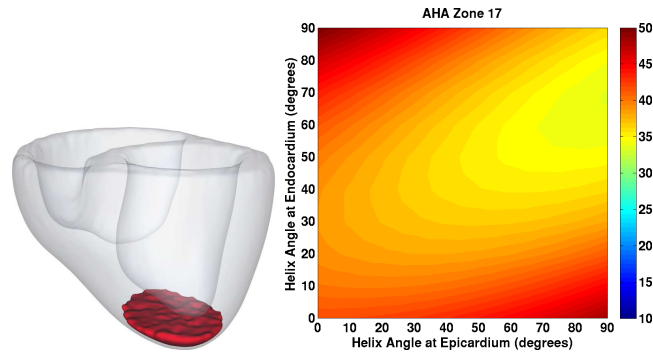


(c) AHA Zone 15

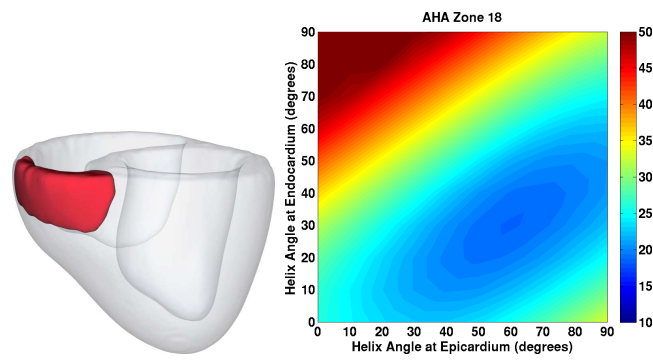


(d) AHA Zone 16

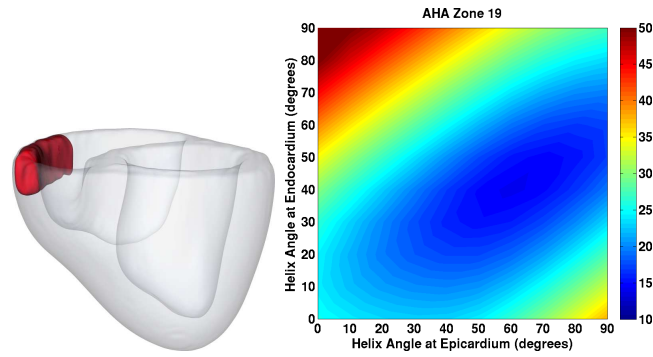
Figure C.5: Average angular difference between the canine atlas and synthetic models with different helix angles at endocardium and epicardium at a given American Heart Association (AHA) zone (colorscale is in degrees).



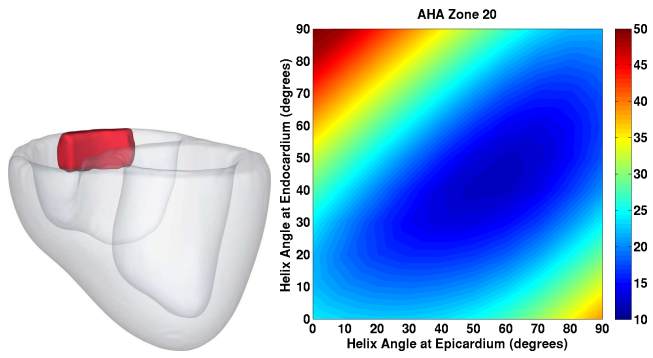
(a) AHA Zone 17



(b) AHA Zone 18

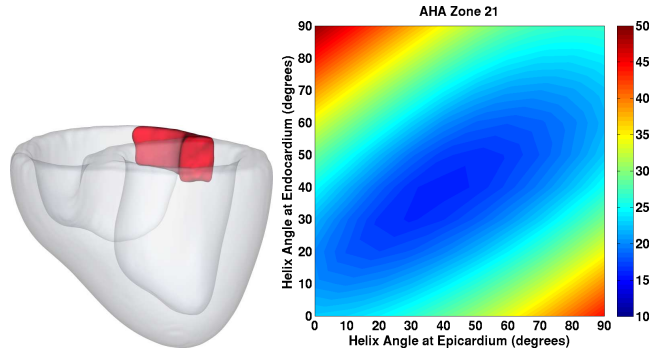


(c) AHA Zone 19

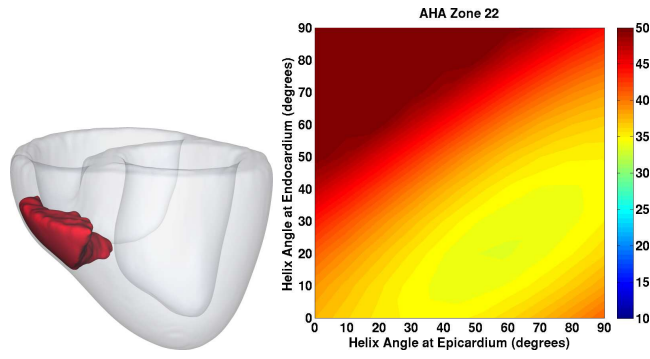


(d) AHA Zone 20

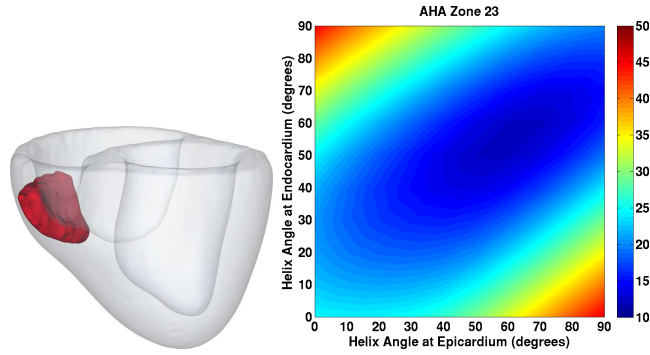
Figure C.6: Average angular difference between the canine atlas and synthetic models with different helix angles at endocardium and epicardium at a given American Heart Association (AHA) zone (colorscale is in degrees).



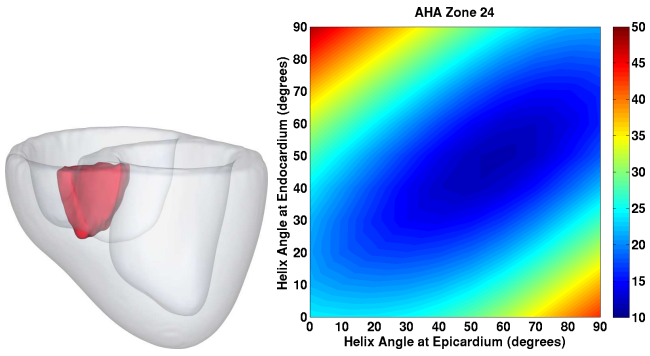
(a) AHA Zone 21



(b) AHA Zone 22

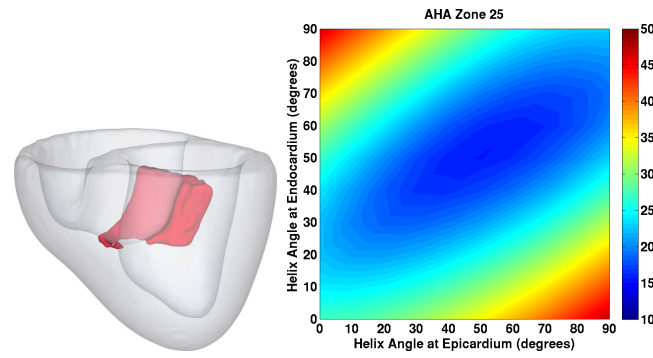


(c) AHA Zone 23

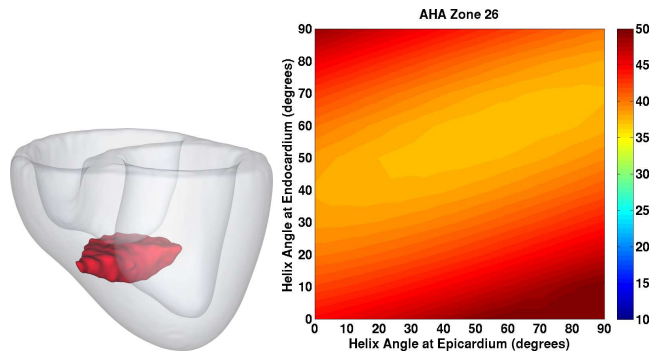


(d) AHA Zone 24

Figure C.7: Average angular difference between the canine atlas and synthetic models with different helix angles at endocardium and epicardium at a given American Heart Association (AHA) zone (colorscale is in degrees).



(a) AHA Zone 25



(b) AHA Zone 26

Figure C.8: Average angular difference between the canine atlas and synthetic models with different helix angles at endocardium and epicardium at a given American Heart Association (AHA) zone (colorscale is in degrees).

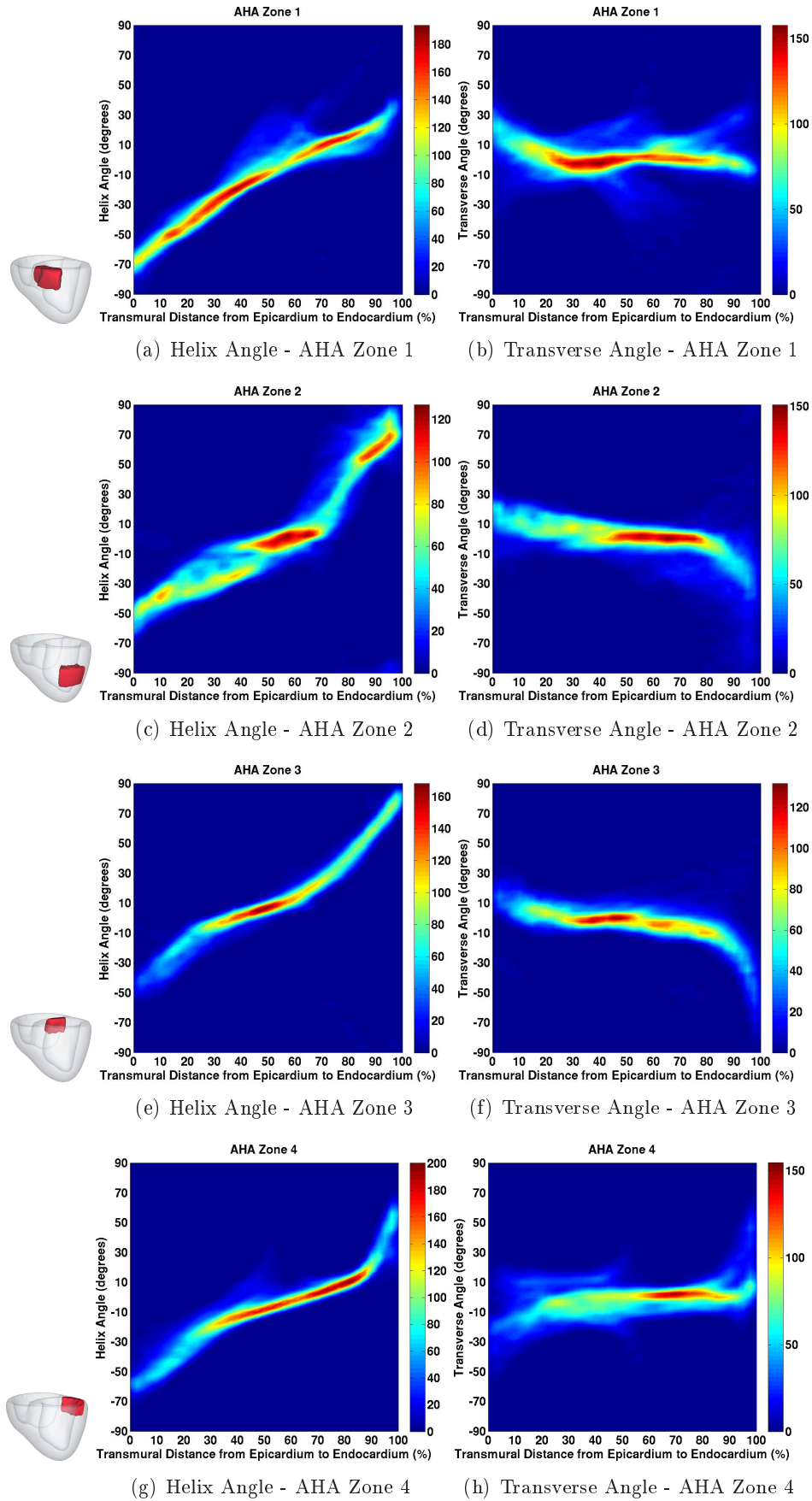


Figure C.9: Histogram of helix and transverse angles with respect to relative transmural distance from epicardium to endocardium at a given American Heart Association (AHA) zone.

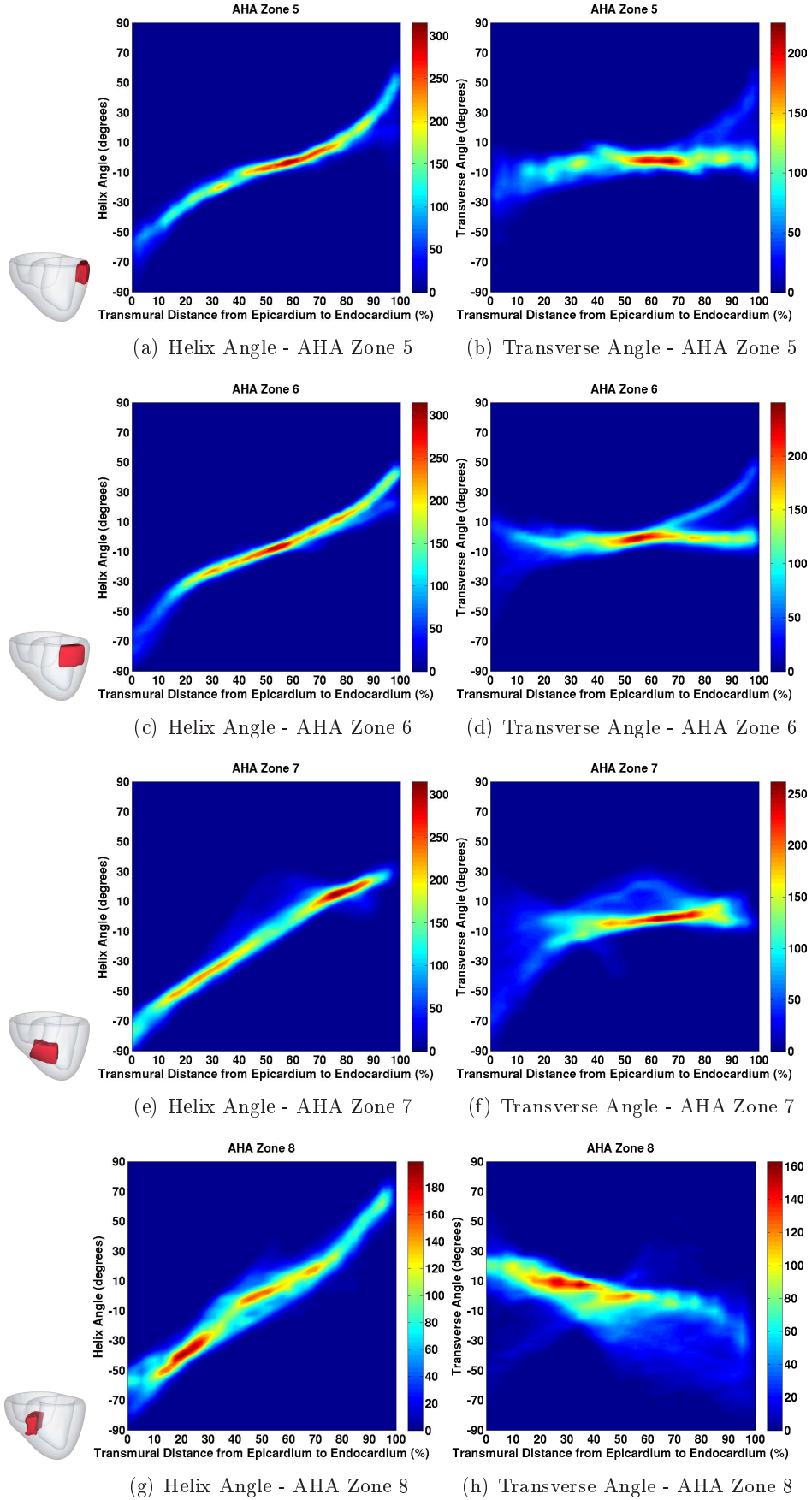


Figure C.10: Histogram of helix and transverse angles with respect to relative transmural distance from epicardium to endocardium at a given American Heart Association (AHA) zone.

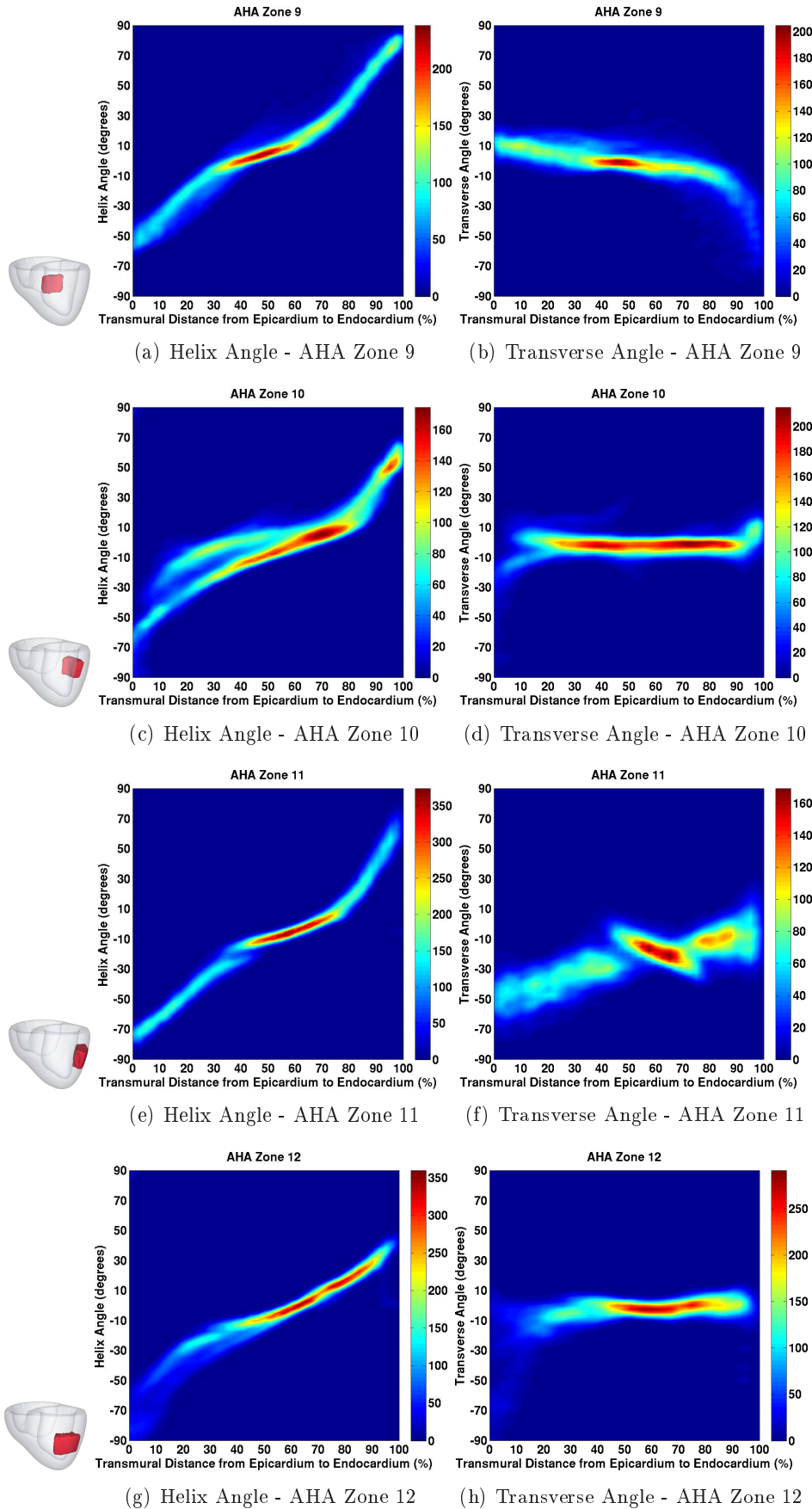


Figure C.11: Histogram of helix and transverse angles with respect to relative transmural distance from epicardium to endocardium at a given American Heart Association (AHA) zone (color represents the number of voxels).

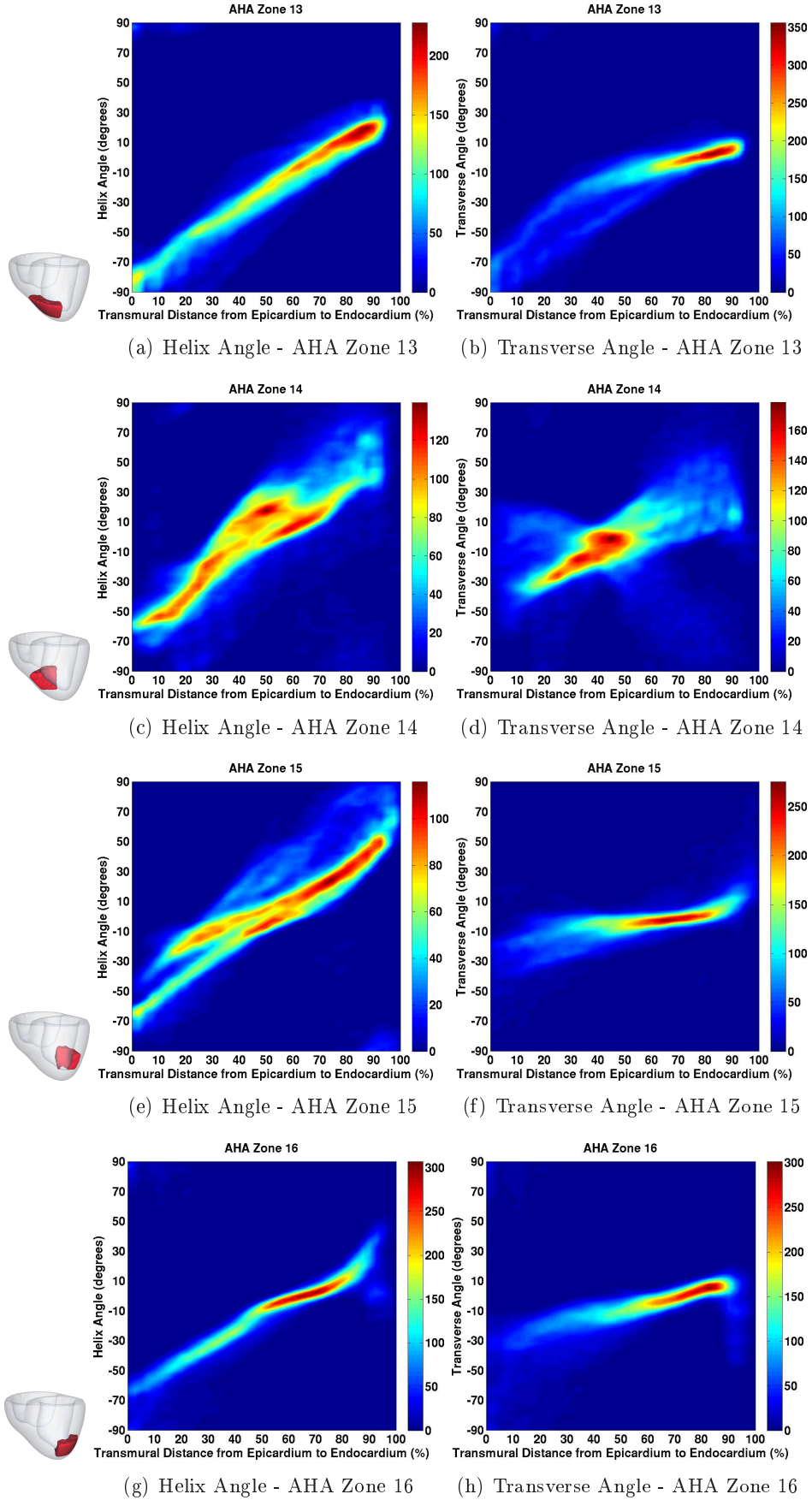


Figure C.12: Histogram of helix and transverse angles with respect to relative transmural distance from epicardium to endocardium at a given American Heart Association (AHA) zone (color represents the number of voxels).

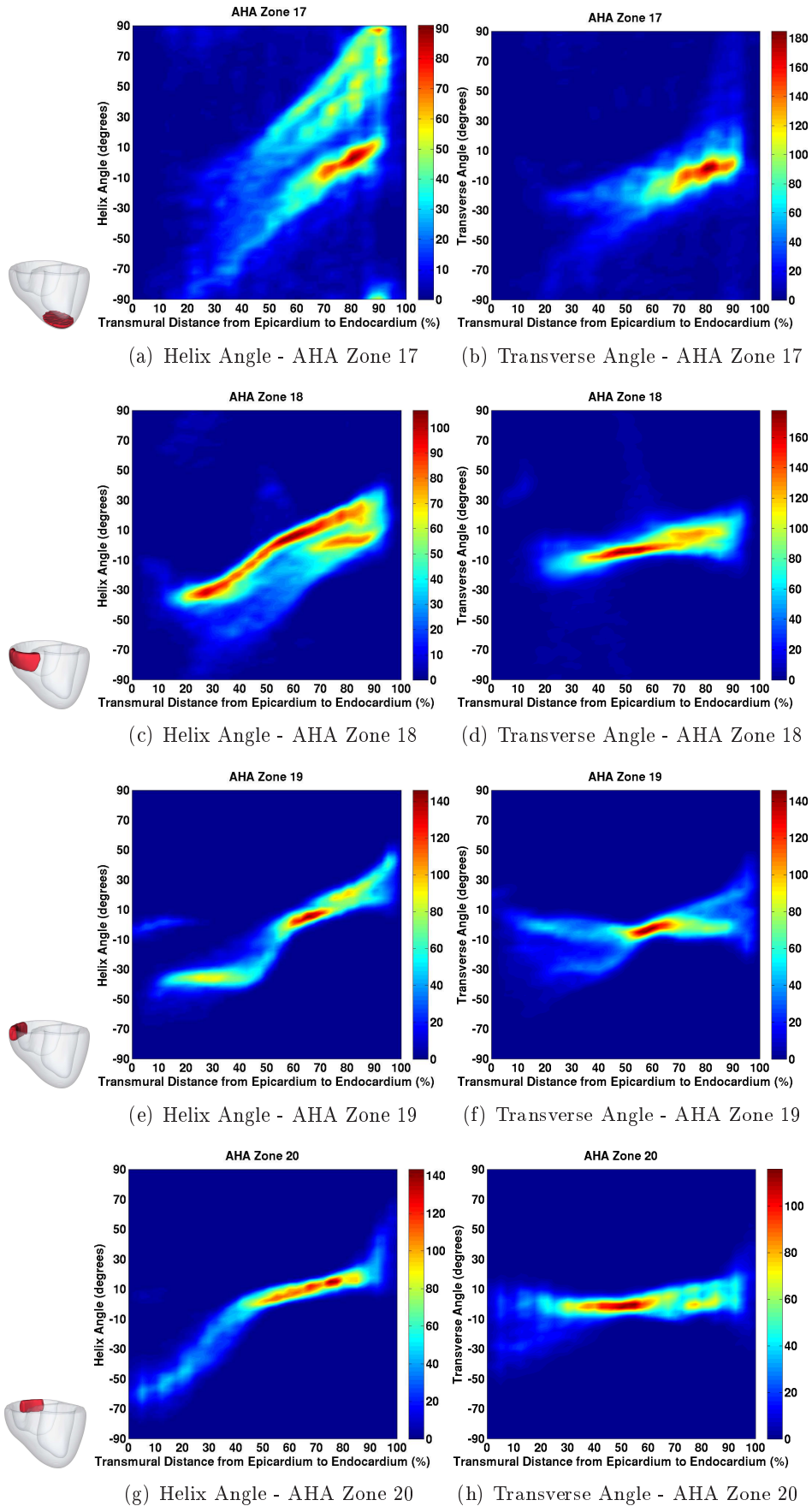


Figure C.13: Histogram of helix and transverse angles with respect to relative transmural distance from epicardium to endocardium at a given American Heart Association (AHA) zone (color represents the number of voxels).

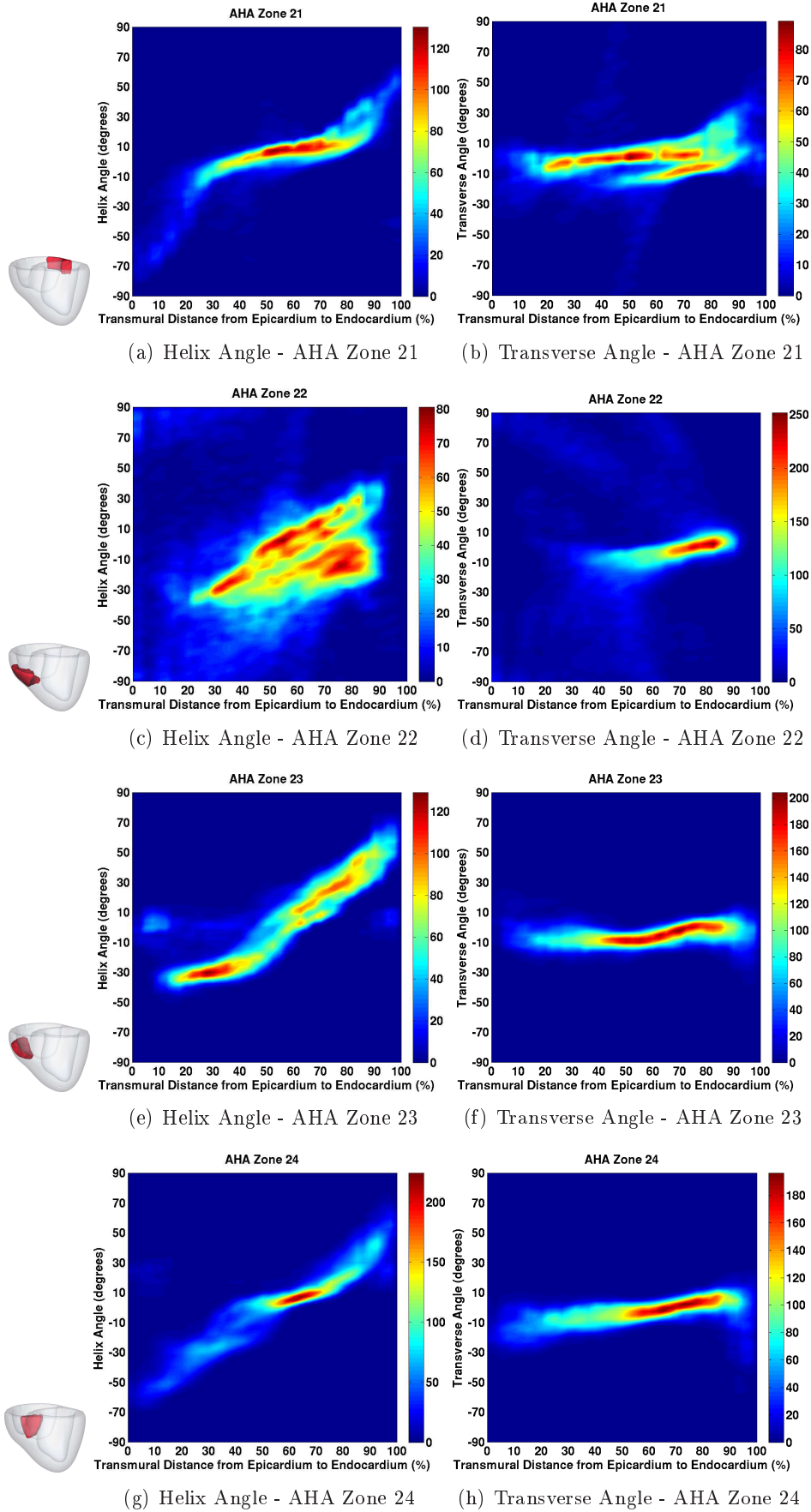


Figure C.14: Histogram of helix and transverse angles with respect to relative transmural distance from epicardium to endocardium at a given American Heart Association (AHA) zone (color represents the number of voxels).

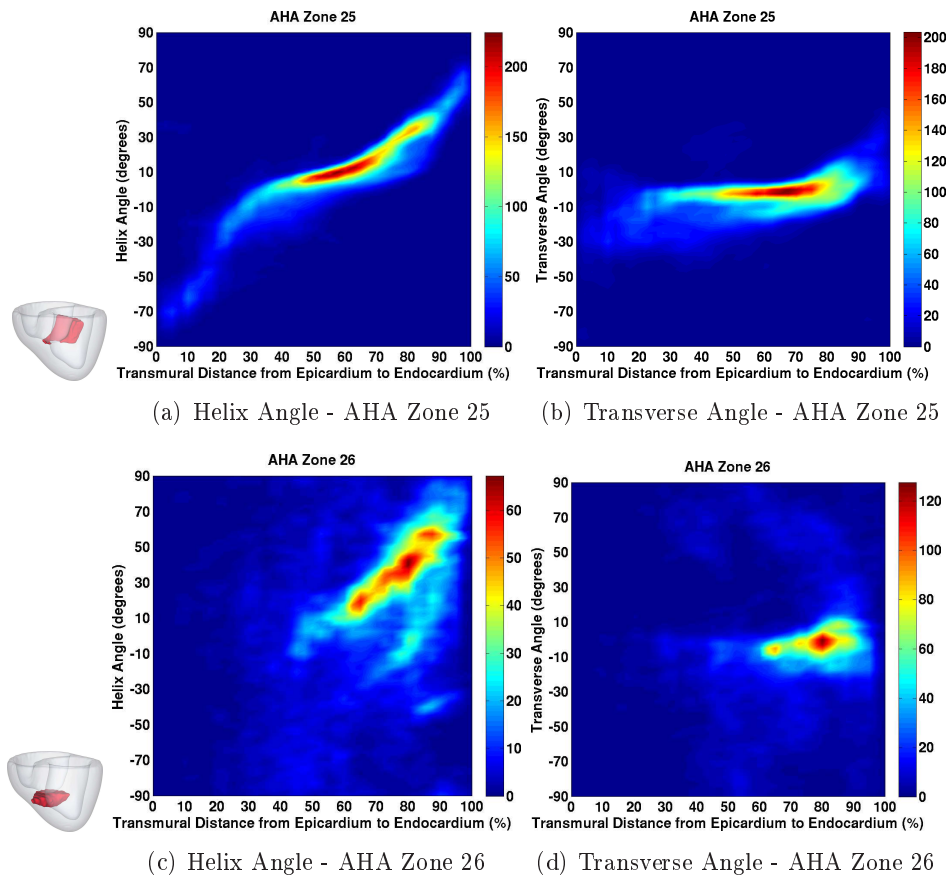


Figure C.15: Histogram of helix and transverse angles with respect to relative transmural distance from epicardium to endocardium at a given American Heart Association (AHA) zone (color represents the number of voxels).

Maximum Step Length

We propose here to determine an upper bound of the norm of the update vector field \mathbf{u} . In the general case, we set the number of space dimensions to d (in our case, we used 3D images so $d = 3$).

$$\mathbf{u} = \sum_{i=1}^d \frac{P_i}{\lambda_i^2 + \sigma^2/\sigma_c^2} \mathbf{e}_i \quad (\text{D.1})$$

where:

$$\begin{aligned} P_i &= - \sum_{j=1}^N \alpha_j (I_j - I'_j \circ S) \mathbf{G}_j^\top \mathbf{e}_i \\ \lambda_i^2 &= \mathbf{e}_i^\top \left(\sum_{j=1}^N \alpha_j \mathbf{G}_j \mathbf{G}_j^\top \right) \mathbf{e}_i = \sum_{j=1}^N \alpha_j (\mathbf{G}_j^\top \mathbf{e}_i)^\top (\mathbf{G}_j^\top \mathbf{e}_i) \\ \sigma^2 &= \sum_{j=1}^N \alpha_j \sigma_j^2 \end{aligned}$$

Let's consider the component u_i of \mathbf{u} in the direction of \mathbf{e}_i :

$$u_i = \frac{P_i}{\lambda_i^2 + \sigma^2/\sigma_c^2}$$

Regarding the numerator P_i , since we use $\sigma_j = |I_j - I'_j \circ S|$, we obtain:

$$|P_i| \leq \sum_{j=1}^N \alpha_j \sigma_j |\mathbf{G}_j^\top \mathbf{e}_i| \quad (\text{D.2})$$

The denominator $\lambda_i^2 + \sigma^2/\sigma_c^2$ can be reformulated as follows:

$$\lambda_i^2 + \sigma^2/\sigma_c^2 = \sum_{j=1}^N \alpha_j \left((\mathbf{G}_j^\top \mathbf{e}_i)^\top (\mathbf{G}_j^\top \mathbf{e}_i) + \sigma_j^2/\sigma_c^2 \right)$$

From the following general inequality for $(a, b) \in \mathbb{R}^2$,

$$\begin{aligned} (a - b)^2 &= a^2 + b^2 - 2ab \geq 0 \\ a^2 + b^2 &\geq 2ab \end{aligned}$$

we obtain this inequality:

$$(\mathbf{G}_j^\top \mathbf{e}_i)^\top (\mathbf{G}_j^\top \mathbf{e}_i) + \sigma_j^2/\sigma_c^2 \geq 2 \frac{\sigma_j}{\sigma_c} |\mathbf{G}_j^\top \mathbf{e}_i|$$

Thus we can find a lower bound of the denominator:

$$\lambda_i^2 + \sigma_j^2/\sigma_c^2 \geq 2 \sum_{j=1}^N \alpha_j \frac{\sigma_j}{\sigma_c} |\mathbf{G}_j^\top \mathbf{e}_i| \quad (\text{D.3})$$

Combining both inequalities D.2 and D.3, we find an upper bound of $|u|$:

$$|u_i| \leq \frac{\sum_{j=1}^N \alpha_j |\mathbf{G}_j^\top \mathbf{e}_i| \sigma_j}{2 \sum_{j=1}^N \alpha_j |\mathbf{G}_j^\top \mathbf{e}_i| \sigma_j / \sigma_c}$$

which simplifies in:

$$|u_i| \leq \frac{\sigma_c}{2} \quad (\text{D.4})$$

The update vector field has d independent components u_i .

$$\mathbf{u} = \sum_{i=1}^d u_i \mathbf{e}_i$$

From the upper bound of each component u_i (inequality D.4) comes the upper bound of the norm of update vector field \mathbf{u} :

$$\|\mathbf{u}\|^2 = \sum_{i=1}^d u_i^2 \leq \sum_{i=1}^d \frac{\sigma_c^2}{4}$$

Finally,

$$\|\mathbf{u}\| \leq \frac{\sqrt{d}}{2} \sigma_c \quad (\text{D.5})$$

BIBLIOGRAPHY

- [Alexander 2001a] A. L. Alexander, K. M. Hasan, M. Lazar, J. S. Tsuruda and D. L. Parker. *Analysis of Partial Volume Effects in Diffusion-Tensor MRI*. Magnetic Resonance in Medicine, vol. 45, no. 5, pages 770–780, 2001. [33](#)
- [Alexander 2001b] D. C. Alexander, C. Pierpaoli, P. J. Basser and J. C. Gee. *Spatial Transformations of Diffusion Tensor Magnetic Resonance Images*. IEEE Transactions on Medical Imaging, vol. 20, no. 11, pages 1131–1139, 2001. [36](#), [47](#), [49](#), [50](#), [51](#), [75](#), [100](#)
- [Allasonnière 2007] S. Allasonnière, Y. Amit and A. Trouvé. *Towards a Coherent Statistical Framework for Dense Deformable Template Estimation*. Journal Of The Royal Statistical Society Series B, vol. 69, no. 1, pages 3–29, 2007. [40](#)
- [Angelini 2001] E.D. Angelini, A.F. Laine, S. Takuma, J.W. Holmes and S. Homma. *LV Volume Quantification via Spatiotemporal Analysis of Real-Time 3-D Echocardiography*. IEEE Transactions on Medical Imaging, vol. 20, no. 6, pages 457–469, 2001. [89](#)
- [Arsigny 2006] V. Arsigny, P. Fillard, X. Pennec and N. Ayache. *Log-Euclidean Metrics for Fast and Simple Calculus on Diffusion Tensors*. Magnetic Resonance in Medicine, vol. 56, no. 2, pages 411–421, 2006. [35](#), [55](#), [57](#), [60](#)
- [Arts 2001] T. Arts, K.D. Costa, J.W. Covell and A.D. McCulloch. *Relating Myocardial Laminar Architecture to Shear Strain and Muscle Fiber Orientation*. American Journal of Physiology - Heart and Circulatory Physiology, vol. 280, pages H2222–H2229, 2001. [15](#), [17](#), [65](#), [71](#), [84](#)
- [Ashburner 2007] J. Ashburner. *A Fast Diffeomorphic Image Registration Algorithm*. NeuroImage, vol. 38, no. 1, pages 95–113, 2007. [98](#)
- [Assaf 2005] Y. Assaf and P. J. Basser. *Composite Hindered and Restricted Model of Diffusion (CHARMED) MR Imaging of the Human Brain*. Magnetic Resonance in Medicine, vol. 27, no. 1, pages 48–58, 2005. [34](#)
- [Avants 2004] B.B. Avants and J.C. Gee. *Geodesic Estimation for Large Deformation Anatomical Shape Averaging and Interpolation*. NeuroImage, vol. 23, no. 1, pages 139–150, 2004. [38](#), [40](#)
- [Avants 2007] B.B. Avants, J. Duda, H. Zhang and J.C. Gee. *Multivariate Normalization with Symmetric Diffeomorphisms for Multivariate Studies*. In Proceedings of the 10th International Conference on Medical Image Computing and Computer-Assisted Intervention (MICCAI’07), volume 4791 of LNCS, pages 359–366, 2007. [100](#)

- [Avants 2008] B.B. Avants, C.L. Epstein, M. Grossman and J.C. Gee. *Symmetric Diffeomorphic Image Registration with Cross-Correlation: Evaluating Automated Labeling of Elderly and Neurodegenerative Brain*. Medical Image Analysis, vol. 12, no. 1, pages 26–41, 2008. [98](#)
- [Ayache 2004] N. Ayache. Computational Models for the Human Body. Handbook of Numerical Analysis (Ed. P. Ciarlet). Elsevier, Amsterdam, The Netherlands, 2004. [5](#), [65](#)
- [Azar 2006] A. Azar, C. Xu, X. Pennec and N. Ayache. *An Interactive Intensity- and Feature-Based Non-Rigid Registration Framework for 3D Medical Images*. In Proceedings of 3rd IEEE International Symposium on Biomedical Imaging (ISBI'06), pages 824–827, 2006. [36](#), [41](#)
- [Bao 2009] L.J. Bao, Y.M. Zhu, W.Y. Liu, P. Croisille, Z.B. Pu, M. Robini and I.E. Magnin. *Denoising Human Cardiac Diffusion Tensor Magnetic Resonance Images using Sparse Representation Combined with Segmentation*. Physics in Medicine and Biology, vol. 54, no. 6, pages 1435–1456, 2009. [76](#)
- [Barmpoutis 2007] A. Barmpoutis, B. Jian, B.C. Vemuri and T. M. Shepherd. *Symmetric Positive 4th Order Tensors & their Estimation from Diffusion Weighted MRI*. In Proceedings of the 20th International Conference on Information Processing in Medical Imaging (IPMI'07), volume 4584 of LNCS, pages 308–319, 2007. [34](#)
- [Basser 1994] P. Basser, J. Mattiello and D. LeBihan. *MR Diffusion Tensor Spectroscopy and Imaging*. Biophysical Journal, vol. 66, pages 259–267, 1994. [28](#), [33](#), [66](#)
- [Basser 1996] P.J. Basser and C. Pierpaoli. *Microstructural and Physiological Features of Tissues Elucidated by Quantitative-Diffusion-Tensor MRI*. Journal of Magnetic Resonance, vol. 111, no. 3, pages 209–219, 1996. [58](#)
- [Basser 2000] P.J. Basser and S. Pajevic. *Statistical Artifacts in Diffusion Tensor MRI (DT-MRI) caused by Background Noise*. Magnetic Resonance in Medicine, vol. 44, no. 1, pages 41–50, 2000. [36](#), [55](#), [58](#), [59](#), [62](#), [63](#)
- [Batchelor 2005] P.G. Batchelor, M. Moakher, D. Atkinson, F. Calamante and A. Connelly. *A Rigorous Framework for Diffusion Tensor Calculus*. Magnetic Resonance in Medicine, vol. 53, pages 221–225, 2005. [35](#), [55](#), [57](#)
- [Beg 2004] M.F. Beg, P.A. Helm, E.R. McVeigh, M. I. Miller and R. L. Winslow. *Computational Cardiac Anatomy using MRI*. Magnetic Resonance in Medicine, vol. 52, no. 5, pages 1167–1174, 2004. [38](#), [40](#), [41](#)
- [Beg 2005] M.F. Beg, M. Miller, A. Trouvé and L. Younes. *Computing Large Deformation Metric Mappings via Geodesic Flows of Diffeomorphisms*. International Journal of Computer Vision, vol. 61, no. 2, pages 139–157, 2005. [98](#)

- [Bhatia 2004] K.K. Bhatia, J.V. Hajnal, B.K. Puri, A.D. Edwards and D. Rueckert. *Consistent Groupwise Non-Rigid Registration for Atlas Construction*. In Proceedings of 2nd IEEE International Symposium on Biomedical Imaging (ISBI'04), volume 1, pages 908–911, 2004. [38](#), [39](#)
- [Bistoquet 2007] A. Bistoquet, J. Oshinski and O.M. Skrinjar. *Left Ventricular Deformation Recovery From Cine MRI using an Incompressible Model*. IEEE Transactions on Medical Imaging, vol. 26, no. 9, pages 1136–1153, 2007. [89](#), [97](#)
- [Bistoquet 2008] A. Bistoquet, J. Oshinski and O.M. Skrinjar. *Myocardial Deformation Recovery from Cine MRI using a Nearly Incompressible Biventricular Model*. Medical Image Analysis, vol. 12, no. 1, pages 69–85, 2008. [122](#), [132](#)
- [Bookstein 1989] F.L. Bookstein. *Principal Warps: Thin-Plate Splines and the Decomposition of Deformations*. IEEE Transactions on Pattern Analysis and Machine Intelligence, vol. 11, no. 6, pages 567–585, 1989. [43](#)
- [Bosch 2002] J.G. Bosch, S.C. Mitchell, B.P.F. Lelieveldt, F. Nijland, O. Kamp, M. Sonka and J.H.C. Reiber. *Automatic Segmentation of Echocardiographic Sequences by Active Appearance Motion Models*. Magnetic Resonance in Medicine, vol. 21, no. 11, pages 1374–1383, 2002. [89](#)
- [Bossa 2007] M. Bossa, M. Hernandez and S. Olmos. *Contributions to 3D Diffeomorphic Atlas Estimation: Application to Brain Images*. In Proceedings of the 10th International Conference on Medical Image Computing and Computer-Assisted Intervention (MICCAI'07), volume 4791 of LNCS, pages 667–674, 2007. [38](#), [40](#)
- [Cachier 2001] P. Cachier, J.-F. Mangin, X. Pennec, D. Rivière, D. Papadopoulos-Orfanos, J. Régis and N. Ayache. *Multisubject Non-Rigid Registration of Brain MRI using Intensity and Geometric Features*. In Proceedings of the 4th International Conference on Medical Image Computing and Computer-Assisted Intervention (MICCAI'01), volume 2208 of LNCS, pages 734–742, 2001. [42](#), [43](#)
- [Cachier 2002] P. Cachier. *Recalage Non Rigide d'Images Médicales Volumiques - Contribution aux Approches Iconiques et Géométriques*. Thèse de sciences, École Centrale des Arts et Manufactures, January 2002. [44](#), [104](#)
- [Cachier 2003] P. Cachier, E. Bardinet, D. Dormont, X. Pennec and N. Ayache. *Iconic Feature Based Nonrigid Registration: The PASHA Algorithm*. Computer Vision and Image Understanding, vol. 89, no. 2-3, pages 272–298, 2003. [99](#)
- [Cachier 2004] P. Cachier and N. Ayache. *Isotropic Energies, Filters and Splines for Vectorial Regularization*. Journal of Mathematical Imaging and Vision, vol. 20, no. 3, pages 251–265, 2004. [122](#)

- [Cao 2006] Y. Cao, M. I. Miller, S. Mori, R.L. Winslow and L. Younes. *Diffomorphic Matching of Diffusion Tensor Images*. In Proceedings of the 2006 Conference on Computer Vision and Pattern Recognition Workshop (CVPRW'06), pages 67–67, 2006. [38](#), [100](#)
- [Casero 2008] R. Casero and J.A. Noble. *A Novel Explicit 2D+t Cyclic Shape Model Applied to Echocardiography*. In Proceedings of the 11th International Conference on Medical Image Computing and Computer-Assisted Intervention (MICCAI'08), volume 5242 of LNCS, pages 527–534, 2008. [89](#)
- [Caspi 2002] Y. Caspi and M. Irani. *Spatiotemporal Alignment of Sequences*. IEEE Transactions on Pattern Analysis and Machine Intelligence, vol. 24, no. 11, pages 1409–1424, 2002. [90](#)
- [Chandrashekara 2004] R. Chandrashekara, R.H. Mohiaddin and D. Rueckert. *Analysis of 3-D Myocardial Motion in Tagged MR Images using Nonrigid Image*. IEEE Transactions on Medical Imaging, vol. 23, no. 10, pages 1245–1250, 2004. [89](#)
- [Chiang 2008] M.-C. Chiang, A.D. Leow, A.D. Klunder, R.A. Dutton, M. Barysheva, S.E. Rose, K.L. McMahon, G.I. de Zubicaray, A.W. Toga and P.M. Thompson. *Fluid Registration of Diffusion Tensor Images using Information Theory*. IEEE Transactions on Medical Imaging, vol. 27, no. 4, pages 442–456, 2008. [38](#), [100](#), [139](#)
- [Chinchapatnam 2008] P. Chinchapatnam, K.S. Rhode, M. Ginks, C.A. Rinaldi, P. Lambiase, R. Razavi, S. Arridge and M. Sermesant. *Model-Based Imaging of Cardiac Apparent Conductivity and Local Conduction Velocity for Diagnosis and Planning of Therapy*. IEEE Transactions on Medical Imaging, vol. 27, no. 11, pages 1631–1642, 2008. [139](#)
- [Cirillo 2008] M. Cirillo and G. Arpesella. *Rewind the Heart: A Novel Technique to Reset Heart Fibers' Orientation in Surgery for Ischemic Cardiomyopathy*. Medical Hypotheses, vol. 70, no. 4, pages 848–854, 2008. [139](#)
- [Cirillo 2009] M. Cirillo. *A New Surgical Ventricular Restoration Technique to Reset Residual Myocardium's Fiber Orientation: the "KISS" Procedure*. Anals of Surgical Innovation and Research, vol. 3, no. 6, 2009. [139](#)
- [Clarysse 2005] P. Clarysse. *Analyse d'Images Cardiaques Assistée par les Modèles*. Habilitation à Diriger des Recherches, INSA Lyon - Université Claude-Bernard Lyon I, 2005. [89](#)
- [Costa 1999] K.D. Costa, Y. Takayama, A.D. McCulloch and J.W. Covell. *Laminar Fiber Architecture and Three-Dimensional Systolic Mechanics in Canine Ventricular Myocardium*. American Journal of Physiology - Heart and Circulatory Physiology, vol. 276, pages H595–H607, 1999. [15](#), [65](#)

- [Costa 2001] K.D. Costa, J.W. Holmes and A.D. McCulloch. *Modelling Cardiac Mechanical Properties in Three Dimensions*. Philosophical Transactions of the Royal Society A: Mathematical, Physical and Engineering Sciences, vol. 359, pages 1233–1250, 2001. 15, 65, 84
- [Cousty 2007] J. Cousty, L. Najman, M. Couprie, S. Clément-Guinaudeau, T. Goissen and J. Garot. *Automated, Accurate and Fast Segmentation of 4D Cardiac MR Images*. In Proceedings of the 3rd International Conference on Functional Imaging and Modeling of the Heart (FIMH'05), volume 4466 of LNCS, pages 474–483, 2007. 89
- [De Craene 2009] M. De Craene, O. Camara, B. Bijnens and A.F. Frangi. *Large Diffeomorphic FFD Registration for Motion and Strain Quantification from 3D-US Sequences*. In Proceedings of Functional Imaging and Modeling of the Heart (FIMH'09), volume 5528 of LNCS, pages 437–446, 2009. 89, 140
- [Declerck 1998] J. Declerck, J. Feldmar and N. Ayache. *Definition of a Four-Dimensional Continuous Planispheric Transformation for the Tracking and the Analysis of Left-Ventricle Motion*. Medical Image Analysis, vol. 2, no. 2, pages 197–213, 1998. 89
- [Delhay 2006] B. Delhay. *Estimation Spatio-temporelle de Mouvement et Suivi de Structures Déformables. Application à l’Imagerie Dynamique du Cœur et du Thorax*. PhD thesis, INSA Lyon, 2006. 89
- [Delingette 2007] H. Delingette, M. Sermesant, J.-M. Peyrat, N. Ayache, K.S. Rhode, R. Razavi, E.R. McVeigh, D. Chapelle, J. Sainte-Marie, P. Moireau, M. Fernandez, J.-F.c Gerbeau, K. Djabella, Q. Zhang and M. Sorine. *Cardiosense3d: Patient-Specific Cardiac Simulation*. In Proceedings of 4th IEEE International Symposium on Biomedical Imaging (ISBI'07), pages 628–631, 2007. 142
- [Descoteaux 2009] M. Descoteaux and R. Deriche. *High Angular Resolution Diffusion MRI Segmentation Using Region-Based Statistical Surface Evolution*. Journal of Mathematical Imaging in Vision, vol. 2, no. 33, 2009. Special Issue on Mathematics in Image Analysis. 139
- [Dierckx 2009] H. Dierckx, A.P. Benson, S.H. Gilbert, M.E. Ries, A.V. Holden, H.Vershelde and O. Bernus. *Intravoxel Fibre Structure of the Left Ventricular Free Wall and Posterior Left-Right Ventricular Insertion Site in Canine Myocardium using Q-Ball Imaging*. In Proceedings of Functional Imaging and Modeling of the Heart (FIMH'09), volume 5528 of LNCS, pages 495–504, 2009. 17, 139
- [Dou 2002] J. Dou, T.G. Reese, W.Y. Tseng and V.J. Wedeen. *Cardiac Diffusion MRI without Motion Effects*. Magnetic Resonance in Medicine, vol. 48, no. 1, pages 105–114, 2002. 65, 76, 140

- [Dou 2003] J. Dou, W.Y. Tseng, T.G. Reese and Van J. Wedeen. *Combined Diffusion and Strain MRI Reveals Structure and Function of Human Myocardial Laminar Sheets in vivo*. Magnetic Resonance in Medicine, vol. 50, no. 1, pages 107–113, 2003. [65](#), [76](#)
- [Durrleman 2009] S. Durrleman, X. Pennec, A. Trouvé and N. Ayache. *Statistical Models on Sets of Curves and Surfaces based on Currents*. Medical Image Analysis, vol. 13, no. 5, pages 793–808, 2009. [40](#)
- [Ehrhardt 2006] J. Ehrhardt, D. Säring and H. Handels. *Optical Flow Based Interpolation of Temporal Image Sequences*. In Proceedings of the Society of Photographic Instrumentation Engineers Conference (SPIE'06), volume 6144, page 61442K, 2006. [89](#), [94](#), [115](#)
- [Einstein 1956] A. Einstein. Investigations on the Theory of the Brownian Movement. New York: Dover, 1956. [28](#), [33](#)
- [Finsterbusch 2009] J. Finsterbusch. *Eddy-Current Compensated Diffusion Weighting with a Single Refocusing RF Pulse*. Magnetic Resonance in Medicine, vol. 61, pages 748–754, 2009. [38](#)
- [Fletcher 2007] P.T. Fletcher and S.C. Joshi. *Riemannian Geometry for the Statistical Analysis of Diffusion Tensor Data*. Signal Processing, vol. 87, no. 2, pages 250–262, 2007. [35](#), [55](#), [57](#)
- [Frindel 2009a] C. Frindel, S. Rapacchi, M. Robini, H. Wen, M. Viallon, L. Fanton and P. Croisille. *In Vivo Cardiac NMR Diffusion Weighted Imaging (DWI) for the Human Heart : Improved Quantification of FA and MD by Edge-Preserving Regularization*. In Proceedings of the International Society of Magnetic Resonance in Medicine (ISMRM'09), volume 17, page 3771, 2009. [140](#)
- [Frindel 2009b] C. Frindel, M. Robini, P. Croisille and Y.-M. Zhu. *Comparison of Regularization Methods for Human Cardiac Diffusion Tensor MRI*. Medical Image Analysis, vol. 13, no. 3, pages 405–418, 2009. [76](#)
- [Fritscher 2005] K.D. Fritscher, R. Pilgram and R. Schubert. *Automatic Cardiac 4D Segmentation using Level Sets*. In Proceedings of the 3rd International Conference on Functional Imaging and Modeling of the Heart (FIMH'05), volume 3504 of LNCS, pages 113–122, 2005. [89](#)
- [Gamper 2007] U. Gamper, P. Boesiger and S. Kozerke. *Diffusion Imaging of the in vivo Heart using Spin Echoes - Considerations on Bulk Motion Sensitivity*. Magnetic Resonance in Medicine, vol. 57, no. 2, pages 331–337, 2007. [65](#), [140](#)

- [Garcia-Barnes 2009] J. Garcia-Barnes. *Statistical Models of the Architecture and Function of the Left Ventricle*. PhD thesis, Universitat Autònoma de Barcelona, 2009. 35, 66
- [Geerts 2002] L. Geerts, P. Bovendeerd, K. Nicolay and T. Arts. *Characterization of the Normal Cardiac Myofiber Field in Goat Measured with MR-Diffusion Tensor Imaging*. American Journal of Physiology - Heart and Circulatory Physiology, vol. 283, no. 1, pages H139–H145, 2002. 66
- [Geerts 2003] Liesbeth Geerts, Roy Kerckhoffs, Peter Bovendeerd and Theo Arts. *Towards Patient Specific Models of Cardiac Mechanics: A Sensitivity Study*. In Proceedings of the 2nd International Conference on Functional Imaging and Modeling of the Heart (FIMH'03), volume 2674 of LNCS, pages 81–90, 2003. 84
- [Gilbert 2007] S.H. Gilbert, A.P. Benson, P. Li and A.V. Holden. *Regional Localisation of Left Ventricular Sheet Structure: Integration with Current Models of Cardiac Fibre, Sheet and Band Structure*. European Journal of Cardiothoracic Surgery, vol. 32, pages 231–249, 2007. 35, 66, 84
- [Goodlett 2009] C.B. Goodlett, P.T. Fletcher, J.H. Gilmore and G. Gerig. *Group Analysis of DTI Fiber Tract Statistics with Application to Neurodevelopment*. NeuroImage, vol. 45, no. 1, pages 133–142, 2009. 36
- [Guimond 2000] A. Guimond, J. Meunier and J.-P. Thirion. *Average Brain Models: A Convergence Study*. Computer Vision and Image Understanding, vol. 77, no. 2, pages 192–210, 2000. 36, 38, 39, 40, 44, 45, 46
- [Haddad 2007] R. Haddad, I.E. Magnin and P. Clarysse. *A New Fully-Digital Anthropomorphic and Dynamic Thorax/Heart Model*. In Proceedings of the 29th Annual International Conference of the IEEE on Engineering in Medicine and Biology Society (EMBS'07), pages 5999–6002, 2007. 107
- [Halpern 2008] E. Halpern. Clinical Cardiac CT: Anatomy and Function. Thieme Medical Publishers, 2008. 22
- [Hashemi 2004] R.H. Hashemi, W.G. Bradley and C.J. Lisanti. MRI: The Basics. Lippincott Williams & Wilkins, 2004. 25
- [Helm 2005a] P.A. Helm. *A Novel Technique for Quantifying Variability of Cardiac Anatomy: Application to the Dyssynchronous Failing Heart*. PhD thesis, Johns Hopkins University, 2005. 16, 35, 66, 67, 71, 84
- [Helm 2005b] P.A. Helm, M.F. Beg, M.I. Miller and R.L. Winslow. *Measuring and Mapping Cardiac Fiber and Laminar Architecture using Diffusion Tensor MR Imaging*. Annals of the New-York Academy of Science, vol. 1047, pages 296–307, 2005. 49, 66

- [Helm 2005c] P.A. Helm, H.J. Tseng, L. Younes, E.R. McVeigh and R.L. Winslow. *Ex Vivo 3D Diffusion Tensor Imaging and Quantification of Cardiac Laminar Structure*. Magnetic Resonance in Medicine, vol. 54, no. 4, pages 850–859, 2005. [17](#), [35](#), [49](#), [66](#)
- [Hermosillo 2002] G. Hermosillo, C. ChéfdâHotel and O. Faugeras. *Variational Methods for Multimodal Image Matching*. International Journal of Computer Vision, vol. 50, no. 3, pages 329–343, 2002. [43](#), [98](#)
- [Hernandez 2007] M. Hernandez, M.N. Bossa and S. Olmos. *Registration of Anatomical Images using Geodesic Paths of Diffeomorphisms Parameterized with Stationary Vector Fields*. In Proceedings of MMBIA Workshop of the IEEE 11th International Conference on Computer Vision (ICCV’07), pages 1–8, 2007. [98](#)
- [Holmes 2000] A. Holmes, D.F. Scollan and R.L. Winslow. *Direct Histological Validation of Diffusion Tensor MRI in Formaldehyde-Fixed Myocardium*. Magnetic Resonance in Medicine, vol. 44, no. 1, pages 157–161, 2000. [15](#), [35](#), [66](#)
- [Hoogendoorn 2009] Corné Hoogendoorn, Federico Sukno, Sebastián Ordás and Alejandro Frangi. *Bilinear Models for Spatio-Temporal Point Distribution Analysis*. International Journal of Computer Vision, pages 1573–1405, 2009. [89](#)
- [Hooks 2002] D.A. Hooks, K.A. Tomlinson, S.G. Marsden, I.J. LeGrice, B.H. Smaill, A.J. Pullan and P.J. Hunter. *Cardiac Microstructure: Implications for Electrical Propagation and Defibrillation in the Heart*. Circulation Research, vol. 91, no. 4, pages 331–338, 2002. [15](#)
- [Hooks 2007] D.A. Hooks, M.L. Trew, B.J. Caldwell, G.B. Sands, I.J. LeGrice and B.H. Smaill. *Laminar Arrangement of Ventricular Myocytes Influences Electrical Behavior of the Heart*. Circulation Research, vol. 101, no. 10, pages 103–12, 2007. [15](#), [65](#)
- [Hsu 1998] E.W. Hsu, A.L. Muzikant, S.A. Matulevicius, R.C. Penland and C.S. Henriquez. *Magnetic Resonance Myocardial Fiber-Orientation Mapping with Direct Histological Correlation*. American Journal of Physiology - Heart and Circulatory Physiology, vol. 274, pages H1627–H1634, 1998. [15](#), [35](#), [49](#), [66](#)
- [Hsu 2001] E.W. Hsu and C.S. Henriquez. *Myocardial Fiber Orientation Mapping using Reduced Encoding Diffusion Tensor Imaging*. Journal of Cardiovascular Magnetic Resonance, vol. 3, no. 4, pages 339–2347, 2001. [15](#), [66](#)
- [Huang 1999] J. Huang, D. Abendschein, V.G. Dávila-Román and A.A. Amini. *Spatio-Temporal Tracking of Myocardial Deformations with a 4-D B-Spline Model from Tagged MRI*. IEEE Transactions on Medical Imaging, vol. 18, no. 10, pages 957–972, 1999. [89](#)

- [Huang 2005] X. Huang, N.A. Hill, J. Ren, G. Guiraudon, D. Boughner and T.M. Peters. *Dynamic 3D Ultrasound and MR Image Registration of the Beating Heart*. In Proceedings of the 8th International Conference on Medical Image Computing and Computer-Assisted Intervention (MICCAI'05), volume 3750 of LNCS, pages 171–178, 2005. [90](#)
- [Hunter 2003] P.J. Hunter, A.J. Pullan and B.H. Smaill. *Modeling Total Heart Function*. Annual Review of Biomedical Engineering, vol. 5, no. 4, pages 147–177, 2003. [5](#), [65](#)
- [Ibanez 2003] L. Ibanez, W. Schroeder, L. Ng, J. Cates, the Insight Software Consortium and R. Hamming. *The ITK Software Guide*, 2003. [114](#)
- [Jezzard 1998] P. Jezzard, A.S. Barnett and C. Pierpaoli. *Characterization of and Correction for Eddy Current Artifacts in Echo Planar Diffusion Imaging*. Magnetic Resonance in Medicine, vol. 39, pages 801–812, 1998. [38](#)
- [Jones 2002] D.K. Jones, L.D. Griffin, D.C. Alexander, M. Catanie, M.A. Horsfield, R. Howarda and S.C.R. Williams. *Spatial Normalization and Averaging of Diffusion Tensor MRI Data Sets*. NeuroImage, vol. 17, pages 592–617, 2002. [36](#), [59](#), [62](#), [63](#)
- [Joshi 2004] S. Joshi, B. Davis, M. Jomier and G. Gerig. *Unbiased Diffeomorphic Atlas Construction for Computational Anatomy*. NeuroImage, vol. 23, no. 1, pages S151–S160, 2004. [38](#), [39](#)
- [Jouk 1995] P.-S. Jouk, Y. Usson, G. Michalowicz and F. Parazza. *Mapping of the Orientation of Myocardial Cells by Means of Polarized Light and Confocal Scanning Laser Microscopy*. Microscopy Research and Technique, vol. 30, no. 6, pages 480–490, 1995. [15](#)
- [Kindlmann 2007a] G. Kindlmann, D.B. Ennis, R.T. Whitaker and C.-F. Westin. *Diffusion Tensor Analysis with Invariant Gradients and Rotation Tangents*. IEEE Transactions on Medical Imaging, vol. 26, no. 11, pages 1483–1499, 2007. [61](#)
- [Kindlmann 2007b] G. Kindlmann, R.S.J. Estepar, M. Niethammer, S. Haker and C.-F. Westin. *Geodesic-Loxodromes for Diffusion Tensor Interpolation and Difference Measurement*. In Proceedings of the 10th International Conference on Medical Image Computing and Computer-Assisted Intervention (MICCAI'07), volume 4791 of LNCS, pages 1–9, 2007. [55](#), [56](#), [58](#)
- [Klein 2009] A. Klein, J. Andersson, B. Ardekani, J. Ashburner, B. Avants, M. Chiang, G. Christensen, D. Collins, J. Gee, P. Hellier, J. Song, M. Jenkinson, C. Lepage, D. Rueckert, P. Thompson, T. Vercauteren, R. Woods, J. Mann and R. Parsey. *Evaluation of 14 Nonlinear Deformation Algorithms Applied to Human Brain MRI Registration*. NeuroImage, 2009. In Press. [98](#)

- [Kocica 2006] M.J. Kocica, A.F. Corno, F. Carreras-Costa, M. Ballester-Rodes, M.C. Moghbel, C. Cueva, V. Lackovic, V.I. Kanjuh and F. Torrent-Guaspa. *The Helical Ventricular Myocardial Band: Global, Three-Dimensional, Functional Architecture of the Ventricular Myocardium*. European Journal of Cardiothoracic Surgery, vol. 29, pages 21–40, 2006. 17
- [Kohlberger 2006] T. Kohlberger, D. Cremers, M. Rousson, R. Ramaraj and G. Funka-Lea. *4D Shape Priors for a Level Set Segmentation of the Left Myocardium in SPECT Sequences*. In Proceedings of the 9th International Conference on Medical Image Computing and Computer-Assisted Intervention (MICCAI'06), volume 4190 of LNCS, pages 92–100, 2006. 89
- [Konukoglu 2007] E. Konukoglu, M. Sermesant, O. Clatz, J.-M. Peyrat, H. Delingette and N. Ayache. *A Recursive Anisotropic Fast Marching Approach to Reaction Diffusion Equation: Application to Tumor Growth Modeling*. In Proceedings of the 20th International Conference on Information Processing in Medical Imaging (IPMI'07), volume 4584 of LNCS, pages 687–699, 2007. 142
- [Lardo 2004] A. Lardo, Z.A. Fayad, N. Chronos and V. Fuster. Cardiovascular Magnetic Resonance: Established and Emerging Applications. Informa Healthcare, martin dunitz édition, 2004. 25
- [Larson 2004] A. Larson, R. White, G. Laub, E.R. McVeigh, D. Li and O. Simonetti. *Self-Gated Cardiac Cine MRI*. Magnetic Resonance in Medicine, vol. 51, no. 1, pages 93–102, 2004. 92
- [LeBihan 1985] D. LeBihan and E. Breton. *Imagerie de Diffusion In Vivo par Résonance Magnétique Nucléaire*. Comptes-Rendus de l'Académie des Sciences, vol. 301, no. 15, pages 1109–1112, 1985. 28, 33
- [Ledesma-Carbayo 2005] M.J. Ledesma-Carbayo, J. Kybic, M. Desco, A. Santos, M. Sühling, P. Hunziker and M. Unser. *Spatio-Temporal Nonrigid Registration for Ultrasound Cardiac Motion Estimation*. IEEE Transactions on Medical Imaging, vol. 24, no. 9, pages 1113–1126, 2005. 89, 140
- [LeGrice 1995a] I.J. LeGrice, B.H. Smaill, L.Z. Chai, S.G. Edgar, J.B. Gavin and P.J. Hunter. *Laminar Structure of the Heart: Ventricular Myocyte Arrangement and Connective Tissue Architecture in the Dog*. American Journal of Physiology - Heart and Circulatory Physiology, vol. 269, no. 2, pages H571–H582, 1995. 15, 35, 65, 66, 80
- [LeGrice 1995b] I.J. LeGrice, Y. Takayama and J.W. Covell. *Transverse Shear Along Myocardial Cleavage Planes Provides a Mechanism for Normal Systolic Wall Thickening*. Circulation Research, vol. 77, no. 1, pages 182–193, 1995. 15

- [LeGrice 1997] I.J. LeGrice, P.J. Hunter and B.H. Smaill. *Laminar Structure of the Heart: a Mathematical Model*. American Journal of Physiology - Heart and Circulatory Physiology, vol. 272, no. 5 Part 2, pages H2466–H2476, 1997. [66](#), [80](#)
- [LeGrice 2001] I. LeGrice, P. Hunter, A. Young and B. Smaill. *The Architecture of the Heart: a Data-Based Model*. Philosophical Transactions: Mathematical, Physical and Engineering Sciences, vol. 359, no. 1783, pages 1217–1232, 2001. [16](#), [65](#), [67](#)
- [Lelieveldt 2006] B.P.F. Lelieveldt, A.F. Frangi, S.C. Mitchell, H.C. van Assen, S. Ordas, J.H.C. Reiber and M. Sonka. *3D Active Shape and Appearance Models in Cardiac Image Analysis*. In Faugeras Paragios Chen, editor, Mathematical Models in Computer Vision: The Handbook, pages 471–485. Springer, 2006 édition, 2006. [89](#)
- [Lenglet 2006] C. Lenglet, M. Rousson, R. Deriche and O. Faugeras. *Statistics on the Manifold of Multivariate Normal Distributions: Theory and Application to Diffusion Tensor MRI Processing*. Journal of Mathematical Imaging and Vision, vol. 25, no. 3, pages 423–444, 2006. [35](#), [55](#), [57](#)
- [Lopez 2008a] A. Lopez, K.D. Fritscher, T. Trieb, R. Schubert and J. Mattes. *3D Inter-Subject Cardiac Registration using 4D Information*. In Proceedings of the Society of Photographic Instrumentation Engineers Conference (SPIE'08), volume 6914, page 691413, 2008. [90](#), [91](#)
- [Lopez 2008b] A. Lopez, K.D. Fritscher, T. Trieb, R. Schubert and J. Mattes. *Cardiac 4D Image Sequence Registration using Bridging Points*. In Proceedings of 32nd Workshop of the Austrian Association for Pattern Recognition (OAGM/AAPR), Challenges in the Biosciences: Image Analysis and Pattern Recognition Aspects, pages 53–62, 2008. [90](#), [91](#)
- [Lorenzo-Valdés 2004] M. Lorenzo-Valdés, G. Sanchez-Ortiz, A. Elkington, R. Mo-hiaddin and D. Rueckert. *Segmentation of 4D Cardiac MR Images using a Probabilistic Atlas and the EM Algorithm*. Medical Image Analysis, vol. 8, no. 3, pages 255–265, 2004. [89](#)
- [Ma 2008] J. Ma, M.I. Miller, A. Trouvé and L. Younes. *Bayesian Template Estimation in Computational Anatomy*. NeuroImage, vol. 42, no. 1, pages 252–261, 2008. [40](#)
- [Mäkelä 2002] T. Mäkelä, P. Clarysse, O. Sipila, N. Pauna, Q.C. Pham, T. Katila and I.E. Magnin. *A Review of Cardiac Image Registration Methods*. IEEE Transactions on Medical Imaging, vol. 21, no. 9, pages 1011–1021, 2002. [105](#)
- [Malvern 1969] L.E. Malvern. Introduction to the Mechanics of a Continuous Medium. Englewood Cliffs, NJ: Prentice-Hall, 1969. [48](#)

- [Mansfield 1977] P. Mansfield. *Multi-Planar Image Formation using NMR Spin Echoes*. J. Phys. C: Solid State Phys, vol. 10, pages 349–352, 1977. [38](#)
- [Mansi 2009] T. Mansi, J.-M. Peyrat, M. Sermesant, H. Delingette, J. Blanc, Y. Boudjemline and N. Ayache. *Physically-Constrained Diffeomorphic Demons for the Estimation of 3D Myocardium Strain from Cine-MRI*. In Proceedings of Functional Imaging and Modeling of the Heart (FIMH'09), volume 5528 of *LNCS*, pages 201–210, 2009. [97](#), [122](#), [132](#), [140](#), [142](#)
- [Marsland 2004] S. Marsland and C. Twining. *Constructing Diffeomorphic Representations for the Groupwise Analysis of Non-Rigid Registrations of Medical Images*. IEEE Transactions on Medical Imaging, vol. 23, no. 8, pages 1006–1020, 2004. [38](#), [40](#)
- [Marsland 2007] S. Marsland and R.I. McLachlan. *A Hamiltonian Particle Method for Diffeomorphic Image Registration*. In Proceedings of Information Processing in Medical Imaging (IPMI'07), volume 4584 of *LNCS*, pages 396–407, 2007. [98](#)
- [Masutani 2006] Y. Masutani, S. Aoki, O. Abe and K. Ohtomo. *Model-Based Tractography Based on Statistical Atlas of MR-DTI*. In Proceedings of 3rd IEEE International Symposium on Biomedical Imaging (ISBI'06), pages 89–92, 2006. [36](#)
- [Mattioli 2005] A.V. Mattioli, S. Bonatti, D. Monopoli, M. Zennaro and G. Mattioli. *Left Atrial Remodelling after Short Duration Atrial Fibrillation in Hypertrophic Hearts*. Heart, vol. 91, no. 1, pages 91–92, 2005. [121](#)
- [McCulloch 1998] A. McCulloch, J.B. Bassingthwaighe, P.J. Hunter, D. Noble, T.L. Blundell and T. Pawson. *Computational Biology of the Heart: From Structure to Function*. Progress in Biophysics and Molecular Biology, vol. 69, no. 2-3, pages 153–155, 1998. [15](#), [66](#)
- [McEachen 2000] J.C. McEachen, A. Nehorai and J.S. Duncan. *Multiframe Temporal Estimation of Cardiac Nonrigid Motion*. IEEE Transactions on Image Processing, vol. 9, no. 4, pages 651–665, 2000. [89](#)
- [Moakher 2005] M. Moakher. *A Differential Geometric Approach to the Geometric Mean of Symmetric Positive-Definite Matrices*. SIAM - Journal on Matrix Analysis and Applications, vol. 26, no. 3, pages 735–747, 2005. [35](#), [55](#), [57](#)
- [Moireau 2008] P. Moireau. *Filtering based Data Assimilation for Second Order Hyperbolic PDE. Applications in Cardiac Mechanics*. Thèse de sciences, École Polytechnique, December 2008. [66](#), [149](#)
- [Montagnat 2005] J. Montagnat and H. Delingette. *4D Deformable Models with Temporal Constraints: Application to 4D Cardiac Image Segmentation*. Medical Image Analysis, vol. 9, no. 1, pages 87–100, 2005. [89](#)

- [Moore 2000] C. Moore, C. Lugo-Olivieri, E. McVeigh and E. Zerhouni. *Three-Dimensional Systolic Strain Patterns in the Normal Human Left Ventricle: Characterization with Tagged MR Imaging*. Radiology, vol. 214, no. 2, pages 453–466, 2000. [123](#)
- [Mori 2007] S. Mori. Introduction to Diffusion Tensor Imaging. Elsevier Science, 2007. [25](#), [28](#)
- [Nash 2001] M.P. Nash and P.J. Hunter. *Computational Mechanics of the Heart*. Journal of Elasticity, vol. 61, pages 113–141, 2001. [65](#)
- [Nielsen 1991] P. Nielsen, I.J. Le Grice, B. Smail and P. Hunter. *Mathematical Model of Geometry and Fibrous Structure of the Heart*. American Journal of Physiology - Heart and Circulatory Physiology, vol. 260, no. 29, pages H1365–H1378, 1991. [17](#), [66](#), [80](#)
- [Ohnesorge 2003] B.M. Ohnesorge, C.R. Becker, T.G. Flohr and M.F. Reiser. *Multislice CT in Cardiac Imaging*. European Journal of Radiology, vol. 47, no. 2, page 174, 2003. [22](#)
- [Osman 1999] N.F. Osman, W.S. Kerwin, E.R. McVeigh and J.L. Prince. *Cardiac Motion Tracking using CINE Harmonic Phase (HARP) Magnetic Resonance Imaging*. Magnetic Resonance in Medicine, vol. 42, no. 6, pages 1048–1060, 1999. [89](#)
- [Park 1996] J. Park, D. Metaxas, A.A. Young and L. Axel. *Deformable Models with Parameter Functions for Cardiac Motion Analysis from Tagged MRI Data*. IEEE Transactions on Medical Imaging, vol. 15, no. 3, pages 278–289, 1996. [89](#)
- [Park 2003] H.-J. Park, M. Kubicki, M. Shenton, A. Guimond, R. McCarley, S. Maier, R. Kikinis, F. Jolesz and C-F. Westin. *Spatial Normalization of Diffusion Tensor MRI using Multiple Channels*. NeuroImage, vol. 20, no. 4, pages 1995–2009, 2003. [38](#), [100](#), [101](#)
- [Park 2005] H. Park, P.H. Bland, A.O. Hero and C.R. Meyer. *Least Biased Target Selection in Probabilistic Atlas Construction*. In Proceedings of the 8th International Conference on Medical Image Computing and Computer-Assisted Intervention (MICCAI'05), volume 3750 of LNCS, pages 419–426, 2005. [38](#)
- [Pennec 1999] X. Pennec. *Probabilities and Statistics on Riemannian Manifolds: Basic Tools for Geometric Measurements*. In A.E. Cetin, L. Akarun, A. Er-tuzun, M.N. Gurcan and Y. Yardimci, editors, Proceedings of IEEE Nonlinear Signal and Image Processing (NSIP'99), volume 1, pages 194–198, 1999. [55](#)
- [Pennec 2005] X. Pennec, A. Roche, P. Cathier and N. Ayache. *Non-Rigid MR/US Registration for Tracking Brain Deformations*. In Multi-Sensor Image Fusion

- and Its Applications, volume 26 of *Signal Processing and Communications*, chapter 4, pages 107–143. CRC Press - Taylor and Francis, 2005. 89, 111
- [Pennec 2006] X. Pennec, P. Fillard and N. Ayache. *A Riemannian Framework for Tensor Computing*. International Journal of Computer Vision, vol. 66, no. 1, pages 41–66, 2006. 35, 48, 55, 57, 60, 80
- [Perperidis 2005a] D. Perperidis. *Spatio-Temporal Registration and Modelling of the Heart using Cardiovascular MR Imaging*. PhD thesis, Imperial College London, 2005. 89, 90
- [Perperidis 2005b] D. Perperidis, R. Mohiaddin and D. Rueckert. *Spatio-Temporal Free-Form Registration of Cardiac MR Image Sequences*. Medical Image Analysis, vol. 9, no. 5, pages 441–456, 2005. 90, 92, 118, 132, 140, 141
- [Peyrat 2006a] J.-M. Peyrat, M. Sermesant, X. Pennec, H. Delingette, C. Xu, E.R. McVeigh and N. Ayache. *Towards a Statistical Atlas of Cardiac Fiber Architecture*. Research Report 5906, INRIA, May 2006. 143
- [Peyrat 2006b] J.-M. Peyrat, M. Sermesant, X. Pennec, H. Delingette, C. Xu, E.R. McVeigh and N. Ayache. *Towards a Statistical Atlas of Cardiac Fiber Structure*. In Proceedings of the 9th International Conference on Medical Image Computing and Computer-Assisted Intervention (MICCAI'06), volume 4190 of LNCS, pages 297–304, 2006. 142
- [Peyrat 2007a] J.-M. Peyrat, M. Sermesant, X. Pennec, H. Delingette, C. Xu, E.R. McVeigh and N. Ayache. *A Computational Framework for the Statistical Analysis of Cardiac Diffusion Tensors: Application to a Small Database of Canine Hearts*. IEEE Transactions on Medical Imaging, vol. 26, no. 11, pages 1500–1514, 2007. 141
- [Peyrat 2007b] J.-M. Peyrat, M. Sermesant, X. Pennec, H. Delingette, C. Xu, E.R. McVeigh and N. Ayache. *Statistical Comparison of Cardiac Fiber Architectures*. In Proceedings of the 4th International Conference on Functional Imaging and Modeling of the Heart (FIMH'07), volume 4466 of LNCS, pages 413–423, 2007. 81, 142
- [Peyrat 2008] J.-M. Peyrat, H. Delingette, M. Sermesant, X. Pennec, C. Xu and N. Ayache. *Registration of 4D Time-Series of Cardiac Images with Multichannel Diffeomorphic Demons*. In Proceedings of the 11th International Conference on Medical Image Computing and Computer-Assisted Intervention (MICCAI'08), volume 5242 of LNCS, pages 972–979, 2008. 142
- [Peyrat 2009] J.-M. Peyrat, H. Delingette, M. Sermesant, C. Xu and N. Ayache. *Registration of 4D Cardiac CT Sequences Under Trajectory Constraints with Multichannel Diffeomorphic Demons*. IEEE Transactions on Medical Imaging, 2009. Submitted. 141

- [Pitiot 2006] A. Pitiot, E. Bardinet, P. M. Thompson and G. Malandain. *Piecewise Affine Registration of Biological Images for Volume Reconstruction*. Medical Image Analysis, vol. 10, no. 3, pages 465–483, 2006. 66
- [Plank 2008] G. Plank, L. Zhou, J.L. Greenstein, S. Cortassa, R.L. Winslow, B. OâRourke and N.A. Trayanova. *From Mitochondrial Ion Channels to Arrhythmias in the Heart: Computational Techniques to Bridge the Spatio-Temporal Scales*. Philosophical Transactions of the Royal Society A: Mathematical, Physical and Engineering Sciences, vol. 366, no. 1879, pages 3381–3409, 2008. 5, 66
- [Plank 2009] G. Plank, R. Burton, P. Hales, M. Bishop, T. Mansoori, M.O. Bernabeu, A. Garny, A.J. Prassl, C. Bollensdorff, F. Mason, F. Mahmood, B. Rodriguez, V. Grau, J.E. Schneider, D. Gavaghan and P. Kohl. *Generation of Histo-Anatomically Representative Models of the Individual Heart: Tools and Application*. Philosophical Transactions of the Royal Society A: Mathematical, Physical and Engineering Sciences, vol. 367, no. 1896, pages 2257–2292, 2009. 66
- [Pop 2008] M. Pop, M. Sermesant, D. Lepiller, M.V. Truong, E.R. McVeigh, E. Crystal, A. Dick, H. Delingette, N. Ayache and G.A. Wright. *Fusion of Optical Imaging and MRI for the Evaluation and Adjustment of Macroscopic Models of Cardiac Electrophysiology: A Feasibility Study*. Medical Image Analysis, vol. 13, no. 2, pages 370–380, 2008. 66
- [Pope 2008] A.J. Pope, G.B. Sands, B.H. Smaill and I.J. LeGrice. *Three-Dimensional Transmural Organization of Perimysial Collagen in the Heart*. American Journal of Physiology - Heart and Circulatory Physiology, vol. 295, no. 3, pages H1243–H1252, 2008. 15
- [Prince 1992] J.L. Prince and E.R. McVeigh. *Motion Estimation from Tagged MR Image Sequences*. IEEE Transactions on Medical Imaging, vol. 11, no. 2, pages 238–249, 1992. 89
- [Prokop 2003] M. Prokop, M. Galanski, C. Schaefer-Prokop, A.J. von der Molen and T.C. Telger. *Spiral and Multislice Computed Tomography of the Body*. Thieme Publishing Group, 2003. 22
- [Reese 1995] T.G. Reese, R.M. Weisskoff, R.N. Smith, B.R. Rosen, R.E. Dinsmore and V.J. Wedeen. *Imaging Myocardial Fiber Architecture In Vivo with Magnetic Resonance*. Magnetic Resonance in Medicine, vol. 34, no. 6, pages 786–791, 1995. 65, 76, 140
- [Relan 2009] J. Relan, M. Sermesant, H. Delingette, M. Pop, G.A. Wright and N. Ayache. *Quantitative Comparison of Two Cardiac Electrophysiology Models Using Personalisation to Optical and MR Data*. In Proceedings of 6th

- IEEE International Symposium on Biomedical Imaging (ISBI'09), pages 1027–1030, 2009. [66](#)
- [Reumann 2007] M. Reumann, D. Farina, R. Miri, S. Lurz, B. Osswald and O. Dossel. *Computer Model for the Optimization of AV and VV Delay in Cardiac Resynchronization Therapy*. Medical and Biological Engineering and Computing, vol. 45, no. 9, pages 845–854, 2007. [5](#), [66](#)
- [Reumann 2008] M. Reumann, J. Bohnert, G. Seemann, B. Osswald and O. Dossel. *Preventive Ablation Strategies in a Biophysical Model of Atrial Fibrillation Based on Realistic Anatomical Data*. IEEE Transactions on Biomedical Engineering, vol. 55, no. 2, pages 399–406, 2008. [5](#), [66](#)
- [Reumann 2009] M. Reumann, V. Gurev and J.J. Rice. *Computational Modeling of Cardiac Disease: Potential for Personalized Medicine*. Personalized Medicine, vol. 6, no. 1, pages 45–66, 2009. [5](#)
- [Richardson 1998] D.R. Richardson, D.C. Randall and D.F. Speck. *Cardiopulmonary System*. Wiley-Blackwell, 1 édition, 1998. [19](#), [93](#)
- [Rijcken 1999] J. Rijcken, P.H.M. Bovendeerd, A.J.G. Schoofs, D.H. van Campen and T. Arts. *Optimization of Cardiac Fiber Orientation for Homogeneous Fiber Strain During Ejection*. Annals of Biomedical Engineering, vol. 27, no. 3, pages 289–297, 1999. [15](#), [65](#)
- [Roche 2001] A. Roche, X. Pennec, G. Malandain and N. Ayache. *Rigid Registration of 3D Ultrasound with MR Images: a New Approach Combining Intensity and Gradient Information*. IEEE Transactions on Medical Imaging, vol. 20, no. 10, pages 1038–1049, 2001. [89](#), [111](#)
- [Rohde 2003] G.K. Rohde, S. Pajevic, C. Pierpaoli and P.J. Basser. *A Comprehensive Approach for Multi-channel Image Registration*. In Proceedings of 2nd International Workshop on Biomedical Image Registration (WBIR'03), volume 2717 of LNCS, pages 214–223, 2003. [38](#), [100](#)
- [Rohde 2004] G.K. Rohde, A.S. Barnett, P.J. Basser, S. Marengo and C. Pierpaoli. *Comprehensive Approach for Correction of Motion and Distortion in Diffusion-Weighted MRI*. Magnetic Resonance in Medicine, vol. 51, no. 1, pages 103–114, 2004. [38](#)
- [Rohlfing 2008] T. Rohlfing, N.M. Zahr, E.V. Sullivan and A. Pfefferbaum. *The SRI24 Multichannel Brain Atlas: Construction and Applications*. In Proceedings of the Society of Photographic Instrumentation Engineers Conference (SPIE'08), volume 6914, page 691409, 2008. [100](#)
- [Romero 2008] D.A. Romero, R. Sebastian, G. Plank, E.J. Vigmond and A.F. Frangi. *Modeling the Influence of the VV Delay for CRT on the Electrical Activation Patterns in Absence of Conduction through the AV Node*. In

- Proceedings of the Society of Photographic Instrumentation Engineers Conference (SPIE'08), volume 6918, page G9182, 2008. [5](#), [66](#)
- [Rosenbloom 2003] M. Rosenbloom, E.V. Sullivan and A. Pfefferbaum. *Using Magnetic Resonance Imaging and Diffusion Tensor Imaging to Assess Brain Damage in Alcoholics*. Alcohol Research and Health, vol. 2, no. 27, 2003. [28](#)
- [Ruiz-Alzola 2002] J. Ruiz-Alzola, C.-F. Westin, S. K. Warfield, C. Alberola, S.E. Maier and R. Kikinis. *Nonrigid Registration of 3D Tensor Medical Data*. Medical Image Analysis, vol. 6, no. 2, pages 143–161, 2002. [38](#), [100](#)
- [Sachse 2004] F. Sachse. Computational Cardiology - Modeling of Anatomy, Electrophysiology, and Mechanics, volume 2966 of *Lecture Notes in Computer Science*. Springer-Verlag Berlin Heidelberg, New-York, 2004. [5](#), [65](#)
- [Sarrut 2007] D. Sarrut, B. Delhay, P.F. Villard, V. Boldea, M. Beuve and P. Clarysse. *A Comparison Framework for Breathing Motion Estimation Methods from 4D Imaging*. IEEE Transactions on Medical Imaging, vol. 26, no. 12, pages 1636–1648, 2007. [89](#)
- [Schreibmann 2008] E. Schreibmann, B. Thorndyke, T. Li, J. Wang and L. Xing. *Four-Dimensional Image Registration for Image-Guided Radiotherapy*. International Journal of Radiation Oncology Biology Physics, vol. 71, no. 2, pages 578–586, 2008. [90](#), [91](#)
- [Schwartzman 2005] A. Schwartzman, R.F. Dougherty and J.E. Taylor. *Cross-Subject Comparison of Principal Diffusion Direction Maps*. Magnetic Resonance in Medicine, vol. 53, no. 6, pages 1423–1431, 2005. [59](#), [62](#)
- [Scollan 1998] D.F. Scollan, A. Holmes, R.L. Winslow and J. Forder. *Histological Validation of Myocardial Microstructure Obtained from Diffusion Tensor Magnetic Resonance Imaging*. American Journal of Physiology - Heart and Circulatory Physiology, vol. 275, pages H2308–H2318, 1998. [15](#), [35](#), [49](#), [66](#)
- [Segars 2008] W.P. Segars, M. Mahesh, T.J. Beck, E.C. Frey and B.M.W. Tsui. *Realistic CT Simulation using the 4D XCAT Phantom*. Medical Physics, vol. 35, no. 8, pages 3800–3808, 2008. [107](#)
- [Sermesant 2005] M. Sermesant, K. Rhode, G. I. Sanchez-Ortiz, O. Camara, R. Andriantsimiavona, S. Hegde, D. Rueckert, P. Lambiase, C. Bucknall, E. Rosenthal, H. Delingette, D.L. Hill, N. Ayache and R. Razavi. *Simulation of Cardiac Pathologies using an Electromechanical Biventricular Model and XMR Interventional Imaging*. Medical Image Analysis, vol. 5, no. 9, pages 467–80, 2005. [5](#)
- [Sermesant 2006a] M. Sermesant, H. Delingette and N. Ayache. *An Electromechanical Model of the Heart for Image Analysis and Simulation*. IEEE Transactions

- in Medical Imaging, vol. 25, no. 5, pages 612–625, 2006. [65](#), [67](#), [80](#), [103](#), [105](#), [107](#), [109](#)
- [Sermesant 2006b] M. Sermesant, P. Moireau, O. Camara, J. Sainte-Marie, R. Andriantsimiavona, R. Cimiran, D.L. Hill, D. Chapelle and R. Razavi. *Cardiac Function Estimation from MRI using a Heart Model and Data Assimilation: Advances and Difficulties*. Medical Image Analysis, vol. 10, no. 4, pages 642–656, 2006. [66](#)
- [Sermesant 2008] M. Sermesant, J.-M. Peyrat, P. Chinchapatnam, F. Billet, T. Mansi, K. Rhode, H. Delingette, R. Razavi and N. Ayache. *Toward Patient-Specific Myocardial Models of the Heart*. Heart Failure Clinics, vol. 4, no. 3, pages 289–301, 2008. [5](#), [66](#), [139](#), [141](#)
- [Sermesant 2009] M. Sermesant, F. Billet, R. Chabiniok, T. Mansi, P. Chinchapatnam, P. Moireau, J.-M. Peyrat, K. Rhode, M. Ginks, P. Lambiase, S. Arridge, H. Delingette, M. Sorine, A. Rinaldi, D. Chapelle, R. Razavi and N. Ayache. *Personalised Electromechanical Model of the Heart for the Prediction of the Acute Effects of Cardiac Resynchronisation Therapy*. In Proceedings of Functional Imaging and Modeling of the Heart (FIMH'09), volume 5528 of LNCS, pages 239–248, 2009. [139](#), [142](#)
- [Simard 1988] P.Y. Simard and G.E. Mailloux. *A Projection Operator for the Restoration of Divergence-Free Vector Fields*. IEEE Transactions on Pattern Analysis and Machine Intelligence, vol. 10, no. 2, pages 248–256, 1988. [122](#)
- [Singh 2007] M. Singh, A. Basu and M. Mandal. *Event Dynamics Based Temporal Registration*. IEEE Transactions on Medical Imaging, vol. 9, no. 5, pages 1004–1015, 2007. [90](#), [92](#)
- [Smith 2004] N.P. Smith, D. Nickerson, E. J. Crampin and P.J. Hunter. *Computational Modelling of the Heart*. Acta Numerica, vol. 13, pages 371–431, 2004. [5](#), [65](#)
- [Streeter 1979] D. Streeter. Handbook of Physiology, chapter The Cardiovascular System: Gross Morphology and Fiber Geometry of the Heart. Williams & Wilkins, 1979. [15](#), [65](#), [66](#), [80](#)
- [Studholme 2004] C. Studholme and V. Cardenas. *A Template Free Approach to Volumetric Spatial Normalization of Brain Anatomy*. Pattern Recognition Letters, vol. 25, no. 10, pages 1191–1202, 2004. [38](#)
- [Sundar 2006] H. Sundar, D. Shen, G. Biros, H. Litt and C. Davatzikos. *Estimating Myocardial Fiber Orientation by Template Warping*. In Proceedings of 3rd IEEE International Symposium on Biomedical Imaging (ISBI'06), pages 73–76, 2006. [35](#), [66](#)

- [Sundar 2009] H. Sundar, H. Litt and D. Shen. *Estimating Myocardial Motion by 4D Image Warping*. Pattern Recognition), vol. 42, no. 11, pages 2514–2526, 2009. [89](#), [90](#), [140](#)
- [Taron 2009] M. Taron, N. Paragios and M.-P. Jolly. *Registration with Uncertainties and Statistical Modeling of Shapes with Variable Metric Kernels*. IEEE Transactions on Pattern Analysis and Machine Intelligence, vol. 31, no. 1, pages 99–113, 2009. [132](#), [140](#)
- [Thirion 1998] J.-P. Thirion. *Image Matching as a Diffusion Process: an Analogy with Maxwell's Demons*. Medical Image Analysis, vol. 2, no. 3, pages 243–260, 1998. [98](#), [99](#)
- [Torrent-Guasp 1980] F. Torrent-Guasp. *La estructuración macroscópica del miocardio ventricular*. Revista Espanola de Cardiología, vol. 33, no. 3, pages 265–287, 1980. [17](#), [18](#)
- [Torrent-Guasp 2005] F. Torrent-Guasp, M.J. Kocica, A.F. Corno, M. Komeda, F. Carreras-Costa, A. Flotats, J. Cosin-Aguillar and H. Wen. *Towards New Understanding of the Heart Structure and Function*. European Journal of Cardiothoracic Surgery, vol. 27, pages 191–201, 2005. [17](#)
- [Tournier 2004] J.-D. Tournier, F. Calamante, D. G. Gadian and A. Connelly. *Direct Estimation of the Fiber Orientation Density Function from Diffusion-Weighted MRI Data using Spherical Deconvolution*. NeuroImage, vol. 23, no. 3, pages 1176–1185, 2004. [34](#)
- [Tseng 1999] W.Y. Tseng, T.G. Reese, R.M. Weisskoff and V.J. Wedeen. *Cardiac Diffusion Tensor MRI In Vivo without Strain Correction*. Magnetic Resonance in Medicine, vol. 42, no. 2, pages 393–403, 1999. [65](#), [76](#), [140](#)
- [Tseng 2003] W.Y. Tseng, V.J. Wedeen, T.G. Reese, R.N. Smith and E.F. Halpern. *Diffusion Tensor MRI of Myocardial Fibers and Sheets: Correspondence with Visible Cut-Face Texture*. Journal of Magnetic Resonance Imaging, vol. 17, no. 1, pages 31–42, 2003. [17](#), [35](#), [49](#), [66](#)
- [Tuch 2002] D.S. Tuch. *High Angular Resolution Diffusion Imaging Reveals Intravoxel White Matter Fiber Heterogeneity*. Magnetic Resonance in Medicine, vol. 48, pages 577–582, 2002. [33](#)
- [Tuch 2004] D.S. Tuch. *Q-Ball Imaging*. Magnetic Resonance in Medicine, vol. 52, pages 1358–1372, 2004. [34](#), [139](#)
- [Turkowski 1990] K. Turkowski. Graphics Gems, chapter Properties of Surface-Normal Transformations, pages 539–547. Academic Press, Inc, 1990. [145](#)
- [Usyk 2000] T. P. Usyk, R. Mazhari and A. D. McCulloch. *Effect of Laminar Orthotropic Myofiber Architecture on Regional Stress and Strain in the Canine Left Ventricle*. Journal of Elasticity, vol. 61, pages 143–164, 2000. [84](#)

- [Uzumcu 2006] M. Uzumcu, R.J. van der Geest, C. Swingen, J.H.C. Reiber and B.P.F. Lelieveldt. *Time continuous Tracking and Segmentation of Cardiovascular MR Images using Multi-Dimensional Dynamic Programming*. Investigative Radiology, vol. 41, no. 1, pages 52–62, 2006. [89](#)
- [Van Hecke 2007] W. Van Hecke, A. Leemans, E. D’Agostino, S. De Backer, E. Vandervliet, P.M. Parizel and J. Sijbers. *Nonrigid Coregistration of Diffusion Tensor Images using a Viscous Fluid Model and Mutual Information*. IEEE Transactions on Medical Imaging, vol. 26, no. 11, pages 1598–1612, 2007. [38](#), [47](#), [51](#), [52](#), [75](#), [100](#)
- [Vercauteren 2009] T. Vercauteren, X. Pennec, A.c Perchant and N. Ayache. *Diffeomorphic Demons: Efficient Non-parametric Image Registration*. NeuroImage, vol. 45, no. 1, pages S61–S72, 2009. [91](#), [98](#), [99](#), [100](#), [101](#), [104](#)
- [Verma 2007] R. Verma, P. Khurd and C. Davatzikos. *On Analyzing Diffusion Tensor Images by Identifying Manifold Structure using Isomaps*. IEEE Transactions on Medical Imaging, vol. 26, no. 6, pages 772–778, 2007. [55](#), [58](#)
- [von Segesser 2005] L.K. von Segesser. *The myocardial band: fiction or fact?* European Journal of Cardiothoracic Surgery, vol. 27, pages 181–182, 2005. [17](#)
- [Wang 2004] Z. Wang, B.C. Vemuri, Y. Chen and T.H. Mareci. *A Constrained Variational Principle for Direct Estimation and Smoothing of the Diffusion Tensor Field from Complex DWI*. IEEE Transactions on Medical Imaging, vol. 23, no. 8, pages 930–939, 2004. [56](#)
- [Wang 2005] Z. Wang and B. Vemuri. *DTI Segmentation using an Information Theoretic Tensor Dissimilarity Measure*. IEEE Transactions on Medical Imaging, vol. 24, no. 10, pages 1267–1277, 2005. [57](#)
- [Wu 2004] Y.C. Wu, A.S. Field, M.K. Chung, B. Badie and A.L. Alexander. *Quantitative Analysis of Diffusion Tensor Orientation: Theoretical Framework*. Magnetic Resonance in Medicine, vol. 52, no. 5, pages 1146–1155, 2004. [59](#), [62](#)
- [Wu 2006] M.T. Wu, W.Y. Tseng, M.Y. Su, C.P. Liu, K.R. Chiou, Van J. Wedeen, T.G. Reese and C.F. Yang. *Diffusion Tensor Magnetic Resonance Imaging Mapping the Fiber Architecture Remodeling in Human Myocardium after Infarction: Correlation with Viability and Wall Motion*. Circulation, vol. 114, no. 10, pages 1036–1045, 2006. [65](#), [76](#)
- [Wu 2009] M.T. Wu, M.Y. Su, Y.L. Huang, K.R. Chiou, P. Yang, H.B. Pan, T.G. Reese, Van J. Wedeen and W.Y. Tseng. *Sequential Changes of Myocardial Microstructure in Patients Postmyocardial Infarction by Diffusion-Tensor Cardiac MR: Correlation with Left Ventricular Structure and Function*. Circulation: Cardiovascular Imaging, vol. 2, no. 1, pages 32–40, 2009. [65](#), [76](#)

- [Xu 2003] D. Xu, S. Mori, D. Shen, P.C. van Zijl and C. Davatzikos. *Spatial Normalization of Diffusion Tensor Fields*. Magnetic Resonance in Medicine, vol. 50, no. 1, pages 175–182, 2003. [49](#)
- [Yeo 2009] B.T.T. Yeo, T. Vercauteren, P. Fillard, J.-M. Peyrat, X. Pennec, P. Golland, N. Ayache and O. Clatz. *DT-REFinD: Diffusion Tensor Registration with Exact Finite-Strain Differential*. IEEE Transactions on Medical Imaging, 2009. In press. [38](#), [100](#), [141](#)
- [Zhang 2006] H. Zhang, P. A. Yushkevich, D. C. Alexander and J. C. Gee. *Deformable Registration of Diffusion Tensor MR Images with Explicit Orientation Optimization*. Medical Image Analysis, vol. 10, no. 5, pages 764–785, 2006. [38](#), [100](#)
- [Zhang 2007] W. Zhang, J.A. Noble and J.M Brady. *Spatio-temporal Registration of Real Time 3D Ultrasound to Cardiovascular MR Sequences*. In Proceedings of the 10th International Conference on Medical Image Computing and Computer-Assisted Intervention (MICCAI’07), volume 4791 of LNCS, pages 343–350, 2007. [90](#)
- [Zollei 2005] L. Zollei, E. Learned-Miller, E. Grimson and W. Wells. *Efficient Population Registration of 3D Data*. In Proceedings of Computer Vision for Biomedical Image Applications, volume 3765 of LNCS, pages 291–301, 2005. [38](#)